DETECTION OF CHIPPING IN CERAMIC CUTTING INSERTS FROM WORKPIECE PROFILE SIGNATURE DURING TURNING PROCESS USING MACHINE VISION

LEE WOON KIOW

UNIVERSITI SAINS MALAYSIA

2017

DETECTION OF CHIPPING IN CERAMIC CUTTING INSERTS FROM WORKPIECE PROFILE SIGNATURE DURING TURNING PROCESS USING MACHINE VISION

by

LEE WOON KIOW

Thesis submitted in fulfillment of the
requirements for the degree of
Doctor of Philosophy

May 2017

ACKNOWLEDGEMENTS

First and foremost, I would like to express my sincere gratitude to my supervisor Professor Dr. Mani Maran Ratnam for his supervision, advice and support since the first beginning of my research. His guidance helped me in all the time of the research and writing of this thesis. Special thanks are also given to my co-supervisor Professor Dr. Zainal Arifin Bin Ahmad for his help and encouragement in my research.

My sincere thanks also goes to the laboratory staffs who have helped me a lot in the laboratory and experimental work. They are Mr. Mohd Shawal Faizal Ismail (Machining laboratory), Mr. Mohd Ashamuddin Hashim (Microscopy and micro analysis laboratory) and Mr. Wan Mohd Amri Bin Wan Mamat Ali (Vibration laboratory) for their support and valuable time to complete this research.

Last but not the least, I would like to thank my parents and family members for their continuous encouragement, support, unlimited dedication and love throughout so many years. My sincere appreciation also extends to all my colleagues and friends who supported me spiritually throughout the entire PhD study.

TABLES OF CONTENTS

LIST OF TABLES

LIST OF FIGURES

LIST OF ABBREVIATIONS

2-D	Two dimensional
3-D	Three dimensional
ACF	Autocorrelation function
AE	Acoustic emission
AFM	Atomic force microscopes
AISI	American Iron and Steel Institute
ASME	American Society of Mechanical Engineers
CCD	Charge coupled device
CPU	Central processing unit
CWT	Continuous wavelet transform
DFT	Discrete Fourier transform
DSLR	Digital single-lens-reflex
DWT	Discrete wavelet transform
FFT	Fast Fourier transform
GLCM	Gray level co-occurrence matrix
ISO	International Organization for Standardization
MVIM	Multi-valued influence matrix
PCBN	Polycrystalline cubic boron nitride
PSD	Power spectral density
RGB	Red Green Blue
RMS	Root mean square
ROI	Region of interest
SEM	Scanning electron microscope

SSA	Singular spectrum analysis
SSD	Sum square of deviation
STFT	Short time Fourier transform
SVM	Support vector machine
TSK	Takagi-Sugeno-Kang

LIST OF SYMBOLS

$*$	Complex conjugation
ϕ	Random dislocation of the workpiece profile caused by chipping
λ	wavelength of the surface waviness
π	Pi
τ	Lag distance
$\Delta\tau$	Lag interval
β	Workpiece rotation angle between successive images
α	Sample variance
γ	Average of amplitude spectrum in a specific spatial frequency band
$\psi(t)$	Mother wavelet
$\psi_{b,a}(t)$	Wavelet basis/ wavelet function
a	Dilation/ scale
a_n	Coefficients of the cosine term
$A(\tau)$	Autocorrelation function coefficient
$A(m\Delta\tau)$	Autocorrelation function coefficient for discrete data
b	Translation
b_n	Coefficients of the sine term
C_n	Amplitude of dislocation in the workpiece profile
$CWT(a,b)$	Wavelet coefficient
d_1, d_2, d_3	Number of pixels between the wavelength
exp	Exponential
f	Feed /feed rate
F_1, F_2	frequency range

$G(x)$	Actual surface profile/ unshifted surface profile
$G(x+\tau)$	Shifted surface profile
$G(i)$	Surface profile at position $m\Delta\tau$
$G(i-m)$	Surface profile at position $(i-m)\Delta\tau$
$G(t)$	Surface profile in time domain
h_1, h_2	Brightness
I_p	Intersection points between the nose profile and workpiece
i	Column in image of workpiece profile
j	Complex number
K	Sub-pixel edge location of the workpiece
L	Total length of workpiece profile
m	Integer number
$\bar{m}_i$	Moments of the input data sequence in the gray-scale image
n	Number of input data
n_R	Number of rotations
N	Total number of pixel/ points in the workpiece profile
O	Centre of the nose profile
$p_1,\ p_2$	densities of the gray level brightness
r_ε	Nose radius
R_a	Arithmetic average height of surface profile
R_t	Peak-to-valley height of the surface profile
R_p	Maximum height of peaks
R_q	Root mean square roughness
R_q^2	Square of root mean square roughness
$RMSW_a$	RMS of CWT coefficient at particular scale of a

s	Skewness
S	capturing time between the successive images
t	Time
$u(x)$	Dislocation profile results from the vibration
$U_{gs}(x)$	Ideal surface profile
V	Spindle rotational speed
V_f	Fundamental feed frequency
V_n	Spatial frequencies
VB	Width of wear land
VB_B	Average flank wear
VB_{max}	Maximum flank wear
w	Length of window
ω	Fundamental angular frequency
x	x vector for x-coordinate of surface profile
x_n	Length of workpiece profile at particular position
x_z	Intensity of the pixel in gray-scale images
(x_i, y_i)	Coordinate of surface profile
y	y vector for y-coordinate of surface profile
$Y(\omega)$	Amplitude of spatial frequencies for continuous Fourier transform
$Y(V_n)$	Amplitude of spatial frequencies for discrete Fourier transform
z	Row in image

PENGESANAN SERPIHAN PADA MATA ALAT SERAMIK DARIPADA TANDA PENGENALAN PROFIL BAHAN KERJA SEMASA PROSES PELARIKAN MENGGUNAKAN PENGLIHATAN MESIN

ABSTRAK

Mata alat seramik lebih cenderung kepada kegagalan menjadi serpihan bukannya kehausan berterusan disebabkan oleh keliatan hentamannya yang rendah. Mata alat menjadi serpihan akan menyebabkan kualiti permukaan dan ketepatan dimensi merosot. Oleh itu, pengesanan dalam proses kegagalan tersebut pada mata alat seramik amat penting terutamanya dalam pengendalian pemesinan tidak berjaga. Kaedah pengesanan kegagalan mata alat dalam proses dengan menggunakan isyarat penderia yang wujud mempunyai had keupayaannya untuk mengesan serpihan mata alat. Pengawasan malat alat daripada profil bahan kerja dengan menggunakan penglihatan mesin mempunyai potensi yang tinggi digunakan semasa proses pemesinan, tetapi tiada percubaan dibuat untuk mengesan kegagalan serpihan mata alat. Dalam kerja ini, kaedah penglihatan mesin dibangunkan untuk mengesan kegagalan serpihan mata alat seramik daripada tanda pengenalan profil 2-D bahan kerja. Profil permukaan bahan kerja bertentangan dengan mata alat dirakam semasa pelarikan dengan menggunakan kamera DSLR. Profil permukaan bahan kerja diekstrak kepada ketepatan sub-piksel dengan menggunakan kaedah momen ketakvarianan. Kesan serpihan mata alat seramik pada tanda pengenalan profil permukaan bahan kerja disiasat dengan menggunakan fungsi autokorelasi (ACF) dan transformasi Fourier cepat (FFT). Pengesanan kegagalan serpihan dijalankan dengan sub-tetingkap FFT dan transformasi gelombang selanjar (CWT). Kegaglan serpihan mata alat seramik menyebabkan puncak ACF profil bahan kerja merosot cepat apabila jarak susul meningkat dan melencong dengan nyata pada sudut putaran bahan kerja yang berlainan. Amplitud frekuensi suapan asas semakin meningkat dengan masa apabila kehausan mata alat berlaku. Akan tetapi amplitud frekuensi suapan

turun naik dengan nyata selepas mata alat gagal menjadi serpihan. Proses pemotongan yang stokastik selepas mata alat menjadi serpihan menyebabkan amplitud frekuensi ruangan yang lebih rendah daripada frekuensi suapan asas meningkat dengan meruncing. Kaedah CWT didapati lebih efektif untuk mengesan permulaan serpihan mata alat dengan tepat pada masa 16.5 s berbanding 17.13 s yang diperolehi daripada sub-tetingkap FFT. Punca min kuasa dua pekali CWT bagi profil bahan kerja pada skala yang lebih tinggi didapati lebih peka bagi mengesan serpihan mata alat seramik dan seterusnya boleh digunakan sebagai petunjuk untuk mengesan kejadian kegagalan serpihan mata alat seramik.

DETECTION OF CHIPPING IN CERAMIC CUTTING INSERTS FROM WORKPIECE PROFILE SIGNATURE DURING TURNING PROCESS USING MACHINE VISION

ABSTRACT

Ceramic tools are prone to chipping due to their low impact toughness. Tool chipping significantly decreases the surface finish quality and dimensional accuracy of the workpiece. Thus, in-process detection of chipping in ceramic tools is important especially in unattended machining. Existing in-process tool failure detection methods using sensor signals have limitations in detecting tool chipping. The monitoring of tool wear from the workpiece profile using machine vision has great potential to be applied in-process, however no attempt has been made to detect tool chipping. In this work, a vision-based approach has been developed to detect tool chipping in ceramic insert from 2-D workpiece profile signature. The profile of the workpiece surface was captured using a DSLR camera. The surface profile was extracted to sub-pixel accuracy using invariant moment method. The effect of chipping in the ceramic cutting tools on the workpiece profile was investigated using autocorrelation function (ACF) and fast Fourier transform (FFT). Detection of onset tool chipping was conducted by using the sub-window FFT and continuous wavelet transform (CWT). Chipping in the ceramic tool was found to cause the peaks of ACF of the workpiece profile to decrease rapidly as the lag distance increased and deviated significantly from one another at different workpiece rotation angles. From FFT analysis the amplitude of the fundamental feed frequency increases steadily with cutting duration during gradual wear, however, fluctuates significantly after tool has chipped. The stochastic behaviour of the cutting process after tool chipping leads to a sharp increase in the amplitude of spatial frequencies below the fundamental feed frequency. CWT method was found more effective to detect the onset of tool chipping at 16.5 s instead of 17.13 s by sub-window FFT. Root mean square of CWT coefficients for the workpiece profile at higher scale band was found to be more

sensitive to chipping and thus can be used as an indicator to detect the occurrence of the tool chipping in ceramic inserts.

CHAPTER ONE

INTRODUCTION

1.1 Background of the study

Tool condition monitoring plays a significant role in machining process because the worn out cutting tool can be identified and replaced in time to avoid the deterioration in the surface quality and dimension accuracy of the machined part. Flank wear is often selected as the tool life criterion in the tool wear monitoring and is accomplished by direct and indirect methods. Direct tool condition monitoring method is usually performed by means of optical devices such as toolmaker's microscope, scanning electron microscope (SEM) and CCD (charge coupled device) camera. Toolmaker's microscope and the SEM are the most popular devices used to measure the flank wear in the past. However, these devices have severe limitation as they can only be used in offline measurement which requires the cutting tool to be removed from the machine for inspection and measurement. Numerous previous works have been conducted to measure the flank wear using CCD camera without the need of dismantling the worn tool from machine. However, this method can only be applied between the cutting operations (Lanzetta, 2001; Wang et al., 2006; Zhang et al., 2012; Chethan et al., 2015).

One major prerequisite of an automated manufacturing system is uninterrupted machining to achieve maximum productivity which require continuous monitoring of the cutting process and cutting tool condition. Most of the in-process tool condition monitoring is conducted by indirect methods. Indirect methods of

monitoring the tool condition depend upon the measurement of sensor signals, which are indirectly related to the condition of the cutting tool edge. With recent advancement in signal processing technology, a large number of indirect methods have been attempted to achieve the in-process tool wear monitoring based on sensor signal features associated with the tool condition such as cutting force, vibration, acoustic emission (AE) and tool temperature (Rehorn et al., 2005; Teti et al., 2010). Many researchers have even combined several sensors to monitor the multitude of information available during machining to assess the tool condition such as the combination of AE and cutting force (Jemielniak et al., 2011a), cutting force and vibration (Kalvoda & Hwang, 2010), AE and vibration (Bhuiyan et al., 2014), cutting forces, vibration and AE (Jemielniak et al., 2011b), AE and cutting sound (Zhang et al., 2015).

The acquired sensor signal obtained from the machining process has been correlated with flank wear by extracting the signal features from any time domain signal using statistical parameters such as the mean value, the root mean square (RMS), kurtosis and skewness. Sensor signals are also transformed into frequency domain and time-frequency domain. The signal features such as the amplitude of the dominant spectral peaks and wavelet coefficient extracted from these transform are used to correlate to the flank wear (Yesilyurt, 2006; Kious et al., 2010; Fang et al., 2011). Other methods such as statistical regression method, neural network, artificial intelligence and pattern recognition have also been widely explored to establish the correlation between the sensor signal and flank wear (Siddhpura & Paurobally, 2013).

The detection of the tool failure by chipping has become more important recently since hard tools such as ceramic cutting tools are commonly used in the

cutting of difficult-to-cut materials such as stainless steel (Lin, 2008; Sobiyi et al., 2015), superalloy (Bushlya et al., 2013), tool steel and hardened tool steel (Özel et al., 2005; Özel et al., 2007; Meddour et al., 2015). Although advances in ceramic processing technology has resulted in high performance tools by improving the toughness, fracture strength and shock resistance, tool chipping and fracture are still serious issues when machining difficult-to-cut material using ceramic cutting tool (Yin et al., 2015). Failure by chipping has more severe effect on the surface finish compared to progressive wear because the cutting forces fluctuates and increases (Liao & Stephenson, 2010). Thus, in-process tool chipping detection as early as possible in ceramic cutting is considered important, in order to stop the machine tool before a catastrophic failure occurs.

Tool chipping occurs when a small piece tool material breaks away from the cutting edge of the tool. The chipped pieces from the cutting edge may vary from microchipping to macrochipping. Breakage of a cutting tool can lead to the total loss of contact between the cutting tool and the workpiece. Chipping and breakage are different from wear which is a gradual process. Chipping and breakage usually occur abruptly resulting in a sudden loss of tool material due to mechanical shocks. The onset of chipping or fracture in a cutting tool results in a change in the contact characteristics between the tool and the workpiece. This in turn results in a significant change in the sensor signals.

Cutting force signal monitoring is one of the most promising methods to detect the precise moment of tool failure. Cutting forces was found to be more effective to detect tool failure than other sensor signals (Li & Mathew,1990). The measurement of cutting force is usually performed by using a dynamometer. When

the tool breaks the cutting force increases slightly above the pre-set threshold and then drops sharply because of the loss of contact between the tool and the workpiece (Cakir & Isik, 2005). However, chipping can also cause failure of a cutting edge without decreasing the cutting force significantly when turning of carbon steel using ceramic insert (Jemielniak, 1992). In addition, tool chipping has been reported to be more difficult to detect using cutting force as the variation of cutting force due to tool chipping may not exceed the threshold limits (Shi & Gindy, 2007).

Previous researchers have reported that AE could be used effectively in detecting tool tip chipping. The AE intensity increases as the tool wear increase and a burst AE signal is produced when the cutting tool has chipped (Jemielniak & Othman, 1998; Wang et al., 2003; Belgassim & Jemielniak, 2011). Strong burst in AE was found after tool fracture because of the sudden increase in the contact area between the workpiece and the chipped cutting tool (Lan & Dornfeld, 1984; Wang et al., 2003). However, these results were contradicted by the recent work of Neslušan et al. (2015) who considered that conventional processing of AE signals does not enable the different phases of the tool wear be clearly recognised during turning of bearing steel using ceramic insert. Besides, most AE sensors have been designed for non-destructive testing and are not suitable for tool wear monitoring as they cannot withstand extreme conditions at the cutting point such as high cutting temperatures and impacts from the chip.

The use of sensors fusion allows more reliable tool failure by chipping detection. Sensor signals from different sources are integrated to provide extended information for tool chipping detection such as the combination of AE and motor power (Wang et al., 2003) and AE and cutting force (Balsamo et al., 2016). However,

previous study have reported that multiple sensor signals used together produced results a little worse than using a single sensor signal during turning of Inconel 625 using ceramic cutting tool (Jemielniak et al., 2011a).

Direct monitoring methods such as vision and optical approaches have been utilized for tool chipping observation on ceramic cutting tool (Patil & Tilekar, 2014). However, this method is only feasible for in-cycle or intermittent observation which requires the machine to be stopped because the continuous contact between the cutting tool and the workpiece does not allow the capture of images of the cutting tool tip during turning. In order to overcome the limitations of the in-process direct observation on cutting tool, identifying the cutting tool condition by analyzing surface texture of machined surface using digital image processing methods from the images of machined surface has been attempted in the past.

The surface texture of machined surface image contains information about the interaction between the tool and the workpiece such as machining conditions (e.g. feed rate, machining speed), waviness, roughness, vibration and chatter. The machined surface image also carries the information about the cutting tool condition by tool imprint on the workpiece. The surface texture of turned workpiece changes remarkably due to the changes in the cutting tool by wear and chipping. For example, previous study has reported that the groves are even and straight with clear ridge lines when the cutting tool is sharp but the groves appear uneven and ridge lines become disjoint when the cutting tool is dull (Kassim et al., 2007). However, the images of workpiece surface were captured between cutting operation using a CCD camera.

Several attempts have been made to evaluate the tool condition by extracting the surface finish descriptors from the images of the freshly machined surface texture to be correlated with the flank wear (Datta et al., 2013; Dutta et al., 2015). The textural analysis methods showed some potential to interpret the tool condition, but they are subject to the changes in illumination condition and the contamination of the dirt and cutting fluid. In addition, their work was conducted offline and no attempt was made to investigate the correlation between the extracted textures features with tool chipping.

According to machining theory, the surface profile of a turned workpiece is formed by the repetition of the nose radius of the cutting insert at a regular interval of feed rate. Thus, nose radius has direct effect on the surface profile of the workpiece and all predominant tool wear such as the flank wear and notch wear can have significant influence on the surface roughness of the workpiece (Penalva et al., 2002; Grzesik, 2008b). An attempt has been made to determine the nose wear and the flank wear from the silhouette of the workpiece profile captured using CCD camera with the aids of backlighting (Shahabi & Ratnam, 2009a; Shahabi & Ratnam, 2009b). However, the work was carried out in-cycle, i.e. in between cutting process.

The development of an effective in-process tool condition monitoring method to detect the onset of tool chipping has not been attempted by previous researches. The case of tool chipping detection in ceramic cutting tool has not been given great attention by the researchers in the past and this is the motivation of the present study.

1.2 Problem statement

Although the vision method has the advantages of capturing the actual geometric changes arising from the wear and chipping of the cutting tool, the direct assessment of the cutting tool using machine vision is not possible during turning. This is because the cutting area is inaccessible due to the continuous contact between the tool and the workpiece as well as presence of coolant and obstruction by chips during turning operation.

In-process tool chipping monitoring is usually performed by using indirect method based on various sensor signals. However, a number of previous studies have shown that tool chipping is hardly detected using sensor signals due to the significant contradictory findings (Jemielniak, 1992; Wang et al., 2003; Cakir & Isik, 2005; Belgassim & Jemielniak, 2011; Neslušan et al., 2015). Thus, there still exists a need to develop a more reliable in-process tool chipping monitoring method.

Previous studies show that with the advancement in image processing technology, the features extracted from the images of the machined surface texture could be used to correlate well with the cutting tool condition. However, this method requires the machine to be stopped before the images of the machined surface can be captured (Datta et al., 2013; Dutta et al., 2015).

Since the cutting tool tip is directly in contact with the workpiece during the turning operation, an imprint of the cutting tool profile is replicated on the machined surface (Kassim et al., 2007). Therefore, the workpiece profile of turned part is directly dependent on the geometry of the cutting tool tip. As the tool chips, the

contact geometry changes, thus affecting the surface being machined. Two dimensional (2-D) image of the surface profile of the turned workpiece has been successfully used for in-cycle nose wear and flank wear measurement in the past (Shahabi & Ratnam, 2009b).

It should be noted from the abovementioned investigations that existing in-process tool condition monitoring method using sensor signals have limitations in detecting tool chipping. The monitoring of tool wear from the turned profile using machine vision shows great potential to be applied in-process. However, to date, no attempt has been made to explore the potential of the 2-D images of the workpiece profile for in-process tool chipping detection in ceramic cutting tool and this has motivated the present study.

1.3 Objectives

The objectives of this research are as follows:

i. To develop a novel approach of in-process tool chipping detection in ceramic cutting insert based on the workpiece profile signature using machine vision.
ii. To investigate the effect of the tool chipping in ceramic cutting inserts on the workpiece profile using autocorrelation function (ACF) and fast Fourier transform (FFT).
iii. To detect the onset of tool chipping by extracting the features from the workpiece profile using sub-window FFT and continuous wavelet transform (CWT).

1.4 Research approach

The approaches of this study are as follows:

i. A 2-D machine vision system consisting of a digital single lens reflex (DSLR) camera and backlighting was developed to capture the images of the edge of the turned workpiece.

ii. Experiments were carried out using aluminium oxide based ceramic cutting insert and the workpiece materials were AISI 01 Arne oil hardening tool steel and SUS 304 stainless steel with diameter of 50 mm.

iii. The condition of the cutting insert was evaluated using the SEM.

iv. Invariant moment method was used to extract the workpiece profile.

v. ACF, FFT and CWT were utilised to extract the features from the 2-D workpiece profile that correlate to tool chipping.

1.5 Scope of study

The scopes of this research are as follows:

i. Proposed tool chipping detection method only considers in turning process.

ii. This study focuses on the tool chipping detection in the aluminium oxide based ceramic cutting insert.

iii. This study distinguishes the sign of tool chipping from gradual wear using 2-D images of turned workpiece.

1.6 Organization of thesis

This thesis is organized into five chapters. The overview of the research is presented in the Chapter One. The background of the research and the existing

problems in similar studies are addressed. The objectives, research approach and the scopes of the research are listed. Chapter Two is about the literature review focusing on the in-process tool condition monitoring methods. The advantages and limitations of the existing in-process tool condition monitoring methods are discussed in detailed. Literature reviews reveal that an effective in-process tool chipping detection methods in ceramic cutting insert has not been thoroughly investigated.

The methodology for in-process detection of tool failure by chipping from the 2-D workpiece profile signature using machine vision method is outlined in Chapter Three. The proposed vision system using high resolution digital camera at high shutter speed has been used in this study for capturing the images of the workpiece profile during turning operation is presented. Detailed workpiece profile extraction method from 2-D images of the workpiece up to sub-pixel accuracy is described in this chapter. Finally, analysis of the 2-D workpiece profile to detect the tool chipping is discussed. The specific procedures in detection of tool chipping in ceramic cutting insert based on the 2-D surface profile extracted from the images of the edge of turned workpiece using ACF, FFT and CWT are discussed.

The results of the simulations and experiments are described in Chapter Four. The effects of the tool chipping on the workpiece surface are discussed. The results on detection of tool chipping in ceramic cutting insert from workpiece profile signature using vision method is presented. Finally, Chapter Five provides conclusion of the thesis and recommendations for future work. The contributions of the proposed method in the field of tool chipping detection are also presented.

CHAPTER TWO

LITERATURE REVIEW

2.1 Introduction

A review of previous research works that are closely related to the studies on the tool failure monitoring in a turning process is presented in this chapter. Firstly, types of tool failure are presented. Previous research works related to the monitoring of tool failure by gradual wear and premature failure by chipping are reviewed in the next section. Emphasis is placed on the in-process detection of the tool chipping for ceramic cutting tool. A summary of the literature review is presented at the end of the chapter.

2.2 Types of tool failure

The turning process is widely used in industry for finish machining of a wide range of components. Tool failure monitoring in turning is essential to achieve not only optimum productivity by reducing machine downtime and unnecessary tool changes, but also to obtain high surface quality and dimensional accuracy as well as minimize the damage to the workpiece or machine tool.

Tool failure can be classified into two groups namely wear and fracture. Wear is generally the removal of material from a cutting tool and is a result of the relative motion between the tool and workpiece. Flank wear at the front edge of the tool flank face and crater wear at the tool rake face are the most typical modes of tool wear in turning (Figure 2.1). Flank wear is mainly caused by the abrasion between the

workpiece and the cutting tool. Crater wear is the formation of a groove on the tool rake face where the chips rubs the tool surface.

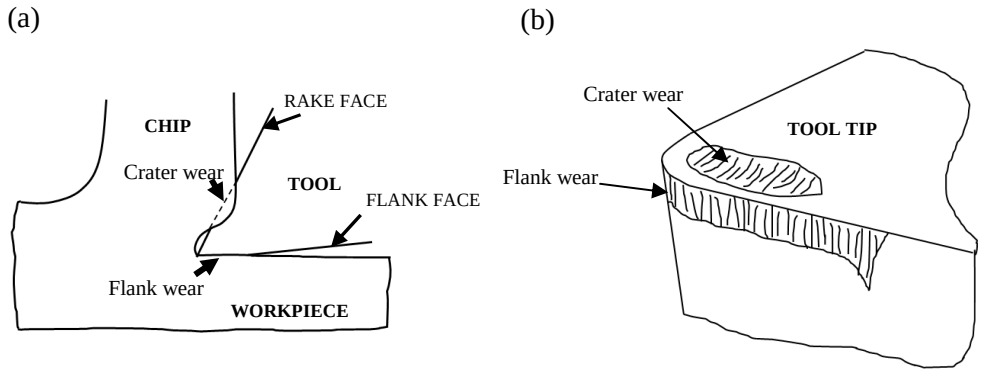

Figure 2.1: (a) Tool-workpiece interaction, and (b) location of crater wear and flank wear (Özel & Davim, 2009)

Directly measured dimensional features of a typical wear pattern have been applied in the past to assess cutting tool's performance which are standardized in International Organization for Standardization (ISO, 1993). Compared to crater wear, flank wear is often used as a criterion to define the end of effective tool life as the wear progresses gradually as shown in Figure 2.2 and thus can be easily monitored.

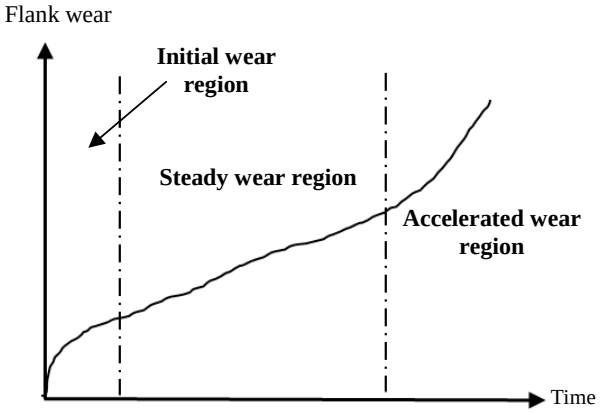

Figure 2.2: Typical flank wear versus time curve (Wang & Gao, 2006)

Flank wear appears in the wear land and is defined by the width of the wear land VB as shown in the Figure 2.3. According to the ISO (1993), the cutting tool is considered to have failed if the average flank wear (VB_B) and the maximum flank wear (VB_{max}) exceeds some critical value such as VB_B> 0.3 mm and VB_{max}> 0.6 mm.

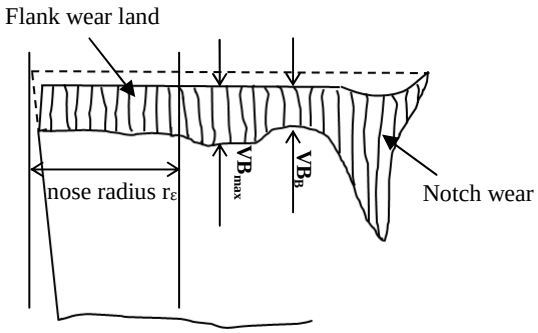

Figure 2.3: Typical wear pattern according to ISO (1993)

Tool fracture is the damage on the cutting edge that range from microchipping to gross chipping. Premature tool failure by chipping refers to the breaking away of small piece from the edge of a cutting tool in micro-scale to massive chipping of cutting edge as shown in Figure 2.4(a) and Figure 2.4(b) respectively. Tool breakage, on the other hand, is the breaking of the entire insert that leads to a total loss of contact between the cutting edge and workpiece as shown in Figure 2.4(c). Chipping of a tool is different from wear, which is a gradual process, premature tool failure by chipping and breakage mostly occur as a sudden and unpredictable breaking away of tool material from the cutting edge. The main reasons for chipping and breakage include brittle nature of the cutting tool materials, the rapid growth of the crater wear, pre-existing potential cracks on the cutting edge, inclusions in the workpiece profile leading to mechanical shocks and impact loading

resulting from the sudden engagement of the cutting tool into the workpiece (Grzesik, 2008a).

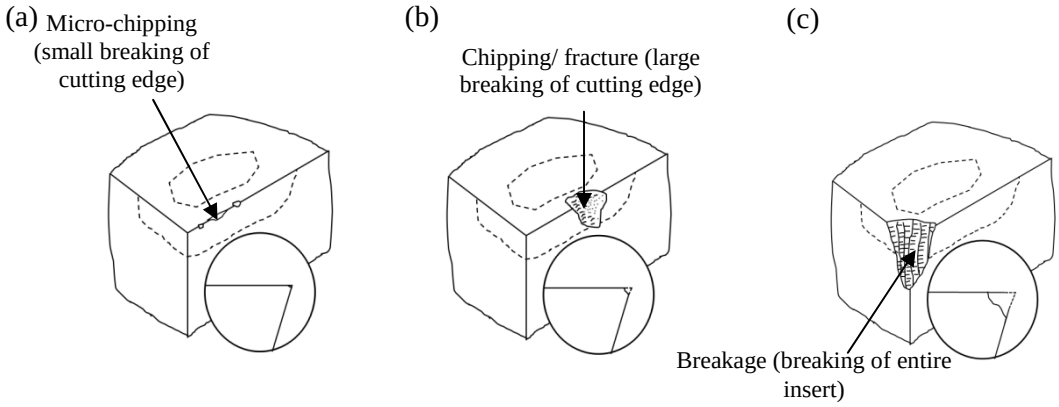

Figure 2.4: Tool failure by chipping and breakage (Grzesik, 2008a)

2.3 Monitoring of gradual wear

Monitoring of gradual wear generally can be divided into two types: direct and indirect method which is explained in Section 2.3.1 and Section 2.3.2, respectively.

2.3.1 Monitoring of gradual wear using direct method

Extensive efforts have been focused on tool wear monitoring using optical methods which is conducted by directly analysing the change in the geometry of the cutting tool. Toolmaker's microscope is the most popular device used to measure wear of cutting tools (Grzesik, 2008a; Čerče et al., 2015). SEM with magnification in the range of several hundred to several thousand is most often used for micro examination. More advanced measuring techniques such as white light interferometry and confocal microscope can be of interest when the analysis in the

nano-scale range is necessary and is useful for crater wear measurement (Devillez et al., 2004; Dawson & Kurfess, 2005). However, the abovementioned direct methods have one main limitation, which is they can only be used for offline measurement. For the offline measurement, the cutting tool has to be dismantled from the machine tool for inspection and this causes interruption to the cutting process as well as is time consuming. Atomic force microscopes (AFM) are powerful tools for 3-D profile measurement with a very high resolution. However, it is very difficult and time consuming to accurately align the AFM cantilever probe with respect to the cutting edge (Cazaux, 2004; Mazzeo et al., 2009).

The past decades has seen the rapid development of tool condition monitoring using machine vision coupled with image processing techniques as direct method in flank wear measurement. In this method, a CCD camera with appropriate lighting reflected in the plane of wear surface is used to acquire the image of the cutting tool. Kurada and Bradley (1997) carried out pioneering work in direct tool condition monitoring by capturing images of flank wear using two fibre optic guided lights and CCD camera. Lanzetta (2001) recognized the types of defects of cutting tool and simultaneously measured the flank wear using a CCD camera equipped with an auto-focus zoom lens for different sizes of cutting tool. However, their study was performed offline.

Pfeifer and Weigers (2000) captured images of tool inserts using CCD camera with a ring light in different angles of incidence for controlled illumination. But there still remain the problem of accuracy because the measurement of flank wear using digital image processing method is highly dependent on the quality of captured images as it is vary considerably although there is a small variation in

illumination. This leads to error in dimensional measurements. Sortino (2003) developed an automated flank wear measurement software by using statistical filtering method from a colour image. However, this measurement method is limited for small flank wear width.

Jurkovic et al. (2005) proposed a vision system which comprised of a CCD camera, laser diod with linear projection as a light, frame grabber for capturing and a personal computer as direct means in flank wear and crater wear measurement. Castejón et al. (2007) and Barreiro et al. (2008) applied machine vision to determine flank wear by means of the discriminant analysis based on geometrical descriptors. The main advantages of their methods is the information about the condition of cutting tool can be obtained without having to remove the cutting inserts from the tool holders. However, the proposed wear measurement techniques using machine vision method were performed between the cutting operation such as in-cycle or intermittent, which requires the machine tool to be stopped. Fadare and Oni (2009) used Canny edge operator to detect significant edges of the worn area of a cutting tool in order to determine the flank wear and notch wear. Although this method is very useful for flank wear determination, but the method is very much sensitive to the fluctuation of ambient light.

Nose wear measurement has also gained attention in the recent years since the machined surface is mainly formed by the tool nose in finish turning. The nose wear can be measured by subtracting the 2-D image of a worn tool from the image of an unworn tool. Kwon and Fischer (2003) determined the nose wear by subtracting the worn tool image from a template after spatial registration of these images. A similar method was also carried out by Shahabi and Ratnam (2009a). The nose wear

was determined by subtracting the 2-D image of a worn tool from the image of unworn tool. The subtraction method can effectively and accurately determine the nose wear, but it requires two images that are aligned precisely before the subtraction. To overcome the limitation, a new approach was proposed by Mook et al. (2009) for measuring nose wear using a single worn cutting tool image. However, this method is not feasible to implement in-process.

In a recent work, Čerče et al. (2015) developed an intermittent 3-D cutting tool wear measurement system using a 2-D profile laser displacement sensor. With movement of the laser displacement sensor across the cutting insert, the sensor measured the distance from the measurement head to the points projected onto the cutting insert and the profile data of cutting insert were grabbed in a matrix form for further evaluation. The depth of flank wear is clearly visible from the comparison of the new and worn cutting inserts cross-sections profiles. Nose wear and crater wear can also be determined by calculating tool wear volume. However, the disadvantage of this method is that it is sensitive to contaminants such as coolant, chips and dust that may remain on the cutting inserts to be measured, which can cause error in the measurement. Chethan et al. (2015) used digital camera with a halogen light to capture the images of cutting insert. The wear region of the cutting insert was estimated using Blob analysis in order to extract the features such as wear area, perimeter and compactness to correlate with the flank wear. However, this method was carried out offline.

2.3.2 Monitoring of gradual wear using indirect method

In-process tool wear monitoring is gaining considerable importance in the manufacturing industry. This can be attributed to the transformation of manufacturing systems from manually operated production machines to highly automated machining centres. In-process tool condition monitoring implies identifying the cutting tool conditions without interrupting the machining process. The direct tool wear evaluation on cutting tool using machine vision system is very simple and accurate, but this method only can be implemented in between cutting operations when the cutting tool is not in contact with the workpiece.

In-process monitoring of tool wear is usually performed by indirect methods that depend upon the measurement of sensor signals which are indirectly correlated to the condition of the cutting tool during the machining operation. Commonly used sensor signal in previous studies including cutting force, AE, vibration, temperature, motor current and power consumption.

Cutting force has been proven to be the one of the significant indicator of tool wear as gradual increase in tool wear during machining causes the cutting force to increase (Gao et al., 2015). The cutting forces generally increases with flank wear because an increase in contact area of the wear land with the workpiece. The use of dynamometer is the most popular method for measurement of cutting forces. It was reported that cutting force currently is the most reliable method employed in in-process tool wear monitoring because cutting force is more sensitive to tool wear than AE and vibration. Thus, many studies have been conducted in the past using

cutting forces to establish the relationship with the flank wear (Sikdar & Chen, 2002; Sick, 2002; Oraby et al., 2005).

Dimla and Lister (2000) used three perpendicular cutting forces to correlate with the flank wear through time series and FFT. They reported that the tangential cutting force is the most sensitive to flank wear while Li (2005) reported that the feed and radial forces are more sensitive to flank wear than tangential cutting force. Fang et al. (2011) concluded that feed force was more sensitive to flank wear. Salgado and Alonso (2007) also found that feed force was more suitable to be applied in tool wear monitoring system because the radial force and tangential force showed greater error in flank wear estimation which reduce the success rate and can cause false alarm. Zhou et al. (2003) indicated that the radial force showed a significant increase when the flank wear increase to 0.2 mm. Penedo et al. (2012) also suggested the radial cutting force to monitor the flank wear by using a hybrid incremental model. In a recent work, Liao et al. (2016) developed a novel approach for flank wear monitoring which is based on the multi-scale hybrid hidden Markov model analysis of cutting force signal. In their study, the instantaneous resultant forces was taken into account because the authors indicated that resultant force signal provides multi-scale information of different directions.

Cutting forces are often used to monitor the flank wear because cutting forces are easy to measure and they have a clear phenomenological relationship with flank wear. However, there is no agreement to which cutting force component has more closer relationship with tool wear. In addition, Liao et al. (2016) reported that the high temperature in tool tip and fast tool material losing rate always result in rapid

tool wear and large fluctuation of cutting force during machining of difficult-to-cut materials.

Ren et al. (2011) applied cutting forces in a Takagi-Sugeno-Kang (TSK) fuzzy approach for tool wear monitoring. Liu et al. (2013a) used several statistical parameters such as average value, RMS, kurtosis and skewness extracted from the cutting forces as input of back-propagation neural network and adaptive neuro-fuzzy inference system for in-process flank wear monitoring. In a recent work, Gao et al. (2015) proposed a data driven modeling framework for flank wear monitoring in turning which is based on statistical processing of cutting force wavelet transform by a hidden Markov tree model. The drawback of these methods is greater computational burden in training phase as a large number of observation samples were used as training data with different machining conditions to build the model to estimate the flank wear.

Ghani et al. (2009) presented a tool wear monitoring method from the cutting forces and cutting parameters using the regression model to predict the flank wear. Camargo et al. (2014) developed a mathematical model based on multiple regression analysis to estimate tool wear during turning of AISI D6 hardened steel using PCBN cutting insert. Although the developed regression model accurately determined the flank wear, the regression based method cannot be extrapolated to different range of cutting condition and to other workpiece and cutting tool materials.

Monitoring cutting tool wear via AE signal analysis has long been practiced. AE can be defined as the transient elastic wave generated by the sudden release of energy in a material. There are several sources of AE signal during machining such

as (i) friction contact between the flank face of cutting tool and workpiece resulting in flank wear, (ii) plastic deformation of cutting tool, (iii) chipping and tool fracture (Li, 2002). The main benefit in the use of AE signal in tool wear monitoring is that the frequency range of the AE signal is much higher than that of the machine vibrations and environmental noises.

Bhaskaran et al. (2012) used skewness and kurtosis of the RMS value of AE signal to monitor flank wear. The kurtosis of RMS value of AE signal increased as the flank wear increased. High skewness of the RMS value of AE signal was found when the flank wear land reached the critical value. Compared to the conventional data processing method, Chen and Li (2007) reported that the wavelet resolution coefficient norm of AE signal is more reliable and useful to estimate tool wear. However, low magnitude of AE signal was generated when the cutting tool undergoes gradual wear compared to the higher magnitude of AE signals which accompanies tool failure by plastic deformation or tool chipping. Thus, AE is not suitable for use as tool wear indicator in gradual wear monitoring applications, but could be used to detect the end of tool life when the tool has deformed due to the excessive wear.

Maia et al. (2015) reported that monitoring the tool wear through the AE signal processed using the average power spectral density (PSD) is sensitive to the wear rate, responding with the high magnitude AE signal value at the beginning of tool life and followed by a decrease at the middle of tool life and increase at the end of the tool life when the wear rate becomes higher. However, monitoring of tool wear using AE signal was difficult because each of the mild wear and severe wear excited a different frequency band (Hase et al., 2012).

During machining, the workpiece and chips rub against the worn tool and produce vibrations which can be used in various ways for tool wear monitoring. Accelerometers are often used to acquire the vibration response. Dimla (2002) reported that vibration increased with flank wear and the vibration signal in the feed and tangential direction were the most sensitive to flank wear. The results showed that time domain analysis of vibration signal to be more sensitive to cutting condition than tool wear, whereas sum total power of vibration signal correlated well with the flank wear. However, the author found that vibration signal can only give better estimation of flank wear in low feed rate because the vibration signal is noisier in higher feed rate.

Chen et al. (2011) monitored flank wear in turning based on logistic regression model by using vibration signals. The wavelet package transform was used to decompose the original vibration signal to find out the frequency bands which well correlated to flank wear and applied the extracted most related features of vibration signals into the logistic regression model to monitor the cutting tool wear. Alonso and Salgado (2008) proposed tool wear monitoring based on longitudinal and transverse vibration signal using singular spectrum analysis (SSA) to decompose the acquired vibration signal. The RMS and variance of the decomposed vibration signals were extracted and the corresponding cutting condition parameters were fed into a back-propagation neural network to determine the flank wear. However, not all the decomposed vibration signals correlated well with the flank wear. The information in the decomposed vibration signals about flank wear is contained mostly in the high frequency components. Alonso and Salgado (2008) indicated that the range of frequencies most correlated with the tool wear changes with the cutting

tool condition and tool wear. For this reason, implementation of the tool condition monitoring based on vibration signal becomes difficult because the frequency range that correlated with the tool wear was difficult to be identified.

Temperature has also been used as a parameter for monitoring tool wear because heat generation is unavoidable in all machining process and it will damage the cutting tool tip due to the effect of diffusion and plastic deformation. Several attempts have been made to monitor the wear of cutting tool based on temperature monitoring. To measure the temperature in the tool tips, thermocouples are the commonly used sensors (O'Sullivan & Cotterell, 2001; Choudhury & Bartarya, 2003; Korkut et al., 2011). However, due to the narrow shear band, chips obstruction and the contact phenomenon between tool and workpiece the measurement of the cutting temperatures closed to tool tip becomes much difficult. In addition, since the temperature varies during machining and cannot be uniquely described by discrete values at a point this can cause error in the tool wear estimation (Sivasakthivel & Sudhakaran, 2013). Infrared thermal cameras have been applied to overcome the limitation of the thermocouple (O'Sullivan & Cotterell, 2001; Davoodi & Hosseinzadeh, 2012). However, the major drawback of the infrared sensor is due the coolant and the chip that may come between the sensor and the surface to be measured thereby causing errors in measurement.

Application of microphone to measure the sound signal for tool condition monitoring has also been attempted in the past. Tekiner and Yesilyurt (2004) used sound signal to assess the flank wear, built up edge, radii of chip curl and surface roughness. Salgado and Alonso (2007) estimated flank wear progression by the emitted sound using singular spectrum analysis in turning of AISI 1040 steel. Samraj

et al. (2011) used singular value decomposition to extract the information regarding flank wear from the emitted sound during turning. Monitoring of flank wear using sound signal has been proven possible, however this method is difficult to implement in the real industry because the noise from adjacent machines and motors can influence the signals.

The use of current and power signal has also been proposed in tool wear monitoring, either from spindle motor or from feed motor. This is because a worn cutting tool require more cutting forces than an unworn cutting tool, thus resulting in more power and current. The major advantage of using current and power signals is its simple hardware implementation that does not interfere with the cutting process. However, current and power signals are not as sensitive to flank wear when compared to cutting forces, AE and vibration signal (Kaye et al., 1995; Silva et al., 1998; Fu & Hope, 2006; Lee et al., 2007).

The need for a more reliable and accurate tool condition monitoring system over a wide range of industrial application is driving the research works towards a multiple sensor approach (known as sensor fusion). This is because signals from a single type of sensor are typically insufficient to provide enough information for tool wear monitoring. The use of several sensors at different locations simultaneously has been proposed for data acquisition in the past. Signals from different sensors are integrated to give the maximum information needed about the tool wear such as the combination of cutting force and vibration (Chelladurai et al., 2008; Chen et al., 2010; Fang et al., 2011), AE and cutting force (Youn et al., 1994; Jemielniak et al., 2011a), AE and vibration (Bhuiyan et al., 2014), cutting forces, vibration and AE (Jemielniak et al., 2011b; Gajate et al., 2012), AE and cutting sound (Zhang et al., 2015).

The strategy of integrating the information from a variety of sensors will increase the accuracy and reliability by resolving the ambiguities about the tool condition. Thus, the most significant advantage of sensor fusion is that sensor fusion enrich information for feature extraction and decision making strategy to correspond to the tool wear. However, this requires complex instrument and extensive data processing makes this method difficult to implement in a real manufacturing environment. Although indirect methods based on various sensor signals have gained a wide interest among researchers in tool wear monitoring, the extraction of the tool condition from the acquired signal is still a challenging task as the detected signals contain noise and other uncertainties (Sanjanwala et al., 1990; Nakao & Dornfeld, 2003; Abellan-Nebot & Subirón, 2010).

2.4 Detection of tool failure by chipping

While tool wear is a slow and progressive process, tool failure by chipping and breakage is a sudden and mostly unexpected event which requires immediate reaction. Tool chipping is a major cause of unscheduled stoppage in a machining operation. It was reported that an average up to 20% of downtime of machine tools resulted from tool failure. Tool failure by chipping on the cutting edge can also cause substantial damages to the workpiece and machine tool. Thus, the ability to detect the occurrence of a tool failure by chipping during machining is much needed and the detection of tool failure must be reliable so as to eliminate machine downtime due to false alarm (Rehorn et al., 2005).

Several signal variables have been reported as good indicators of tool failure by chipping. Among these, cutting force, AE, vibration and motor current have been

investigated intensively in the past for their sensitivity to tool chipping. The effect of the tool chipping on the measured signals must be unique to be distinguishable so that other process irregularities such as hard inclusion in workpiece materials will not be confused with tool chipping.

The use of the cutting force in detecting the tool chipping and breakage has been applied widely in turning process. The effect of the tool chipping is usually revealed from an abrupt change in the signals measured in excess of a threshold value (Kim & Choi, 1996). Cakir and Isik (2005) used cutting forces to detect the precise moment of tool breakage. They found that when a tool breaks the tangential cutting force increases slightly above the pre-set threshold and then drops sharply. This was due to the loss of contact between the tool and the workpiece. The finding is consistent with the findings of past study by Kwak (2006). Cakir and Isik (2005) also reported that cutting force is more sensitive to tool chipping instead of the vibration and motor current. However, tool chipping can also cause failure of a cutting edge without decreasing the cutting force significantly (Jemielniak, 1992; Shi & Gindy, 2007).

A number of studies have also found that monitoring of AE signal to be an effective method to monitor tool chipping. Some previous studies have shown that the level of the RMS of AE signal increases as cutting time and significant burst of AE energy is generated at the instant of tool chipping (Jemielniak & Szafarczyk, 1992; Jemielniak & Othman, 1998; Li et al., 1998). Wang et al. (2003) used time-frequency analysis to process different AE signals emitted from cutting process to estimate the tool state in turning. They found that a burst AE signal in frequency domain was observed after tool chipping because of the sudden increase in the

contact area between the workpiece and the chipped cutting tool. However, contradictory finding was reported by other researchers whereby when tool chipped on a large scale the AE signal reduced due to the decrease in the depth of cut (Li & Mathew, 1990).

Belgassim and Jemielniak (2011) applied statistical method to analyse the AE signal to detect tool failure. They investigated the distribution moments of the AE signal at a predetermined sampling and used the skewness and kurtosis of the distribution to detect tool chipping. They reported that conventional data processing of AE signal features does not enable the different phases of tool wear to be clearly recognised for the detection of tool chipping.

The use of the FFT has been attempted by several researchers in order to detect unusual changes in vibration frequencies due to wear and chipping (Jiang et al., 1987; Colgan et al., 1994). However, the main drawback in the use of vibration signal is their susceptibility to noise and the dependency of the vibration characteristics on combination of machine, tool and workpiece (Wang & Gao, 2006). In addition, as spikes in vibration signals are also generated by hard spots in materials, this can be confused with the spikes generated by chipping.

Tool chipping detection from a single signal variable may lead to misinterpretation of the data due to the complicated dynamic characteristic of machining process. To improve the reliability of tool chipping signature, efforts on integration of multiple sensor signals measurement to detect tool chipping using various pattern classification techniques have been done. Colgan et al. (1994) used multi-valued influence matrix (MVIM) method to determine tool chipping from

vibration and feed motor current signals. However, this detection method result indicated that vibration and feed motor current signal in MVIM were less sensitive to its training environment compared to the neural network. Wang et al. (2003) applied unsupervised neural network to detect tool chipping from AE and motor power signal during turning. However, the ability of neural network method to form a reliable tool chipping signature depends strongly upon their structure and their training inputs. In the case such as machining where adequate data are not available for comprehensive training, neural network may produce false alarms. In a recent work, statistical pattern classification has been also proposed for tool chipping detection in turning using AE and cutting force signal (Balsamo et al., 2016). The authors reported that this method could not correctly detect the tool chipping instant from the recorded signal due to a delay in the instant detection between AE and cutting force signals.

In a recent work, a precision on-machine measurement method of chipping on cutting tool edge which employed a diamond reference edge as a measuring artifact was developed based on a cutting force sensor integrated with the fast tool servo (Chen et al., 2016). The worn tool on the fast tool servo was brought to scan across the diamond reference edge based on the a contact force feedback control loop applied to fast tool servo. The cutting force between the cutting tool edge and the reference edge was kept constant by controlling the tool displacement so that the cutting tool edge contour can be traced by the reference edge. But, this method is strictly feasible for offline measurement only.

2.5 Detection of tool failure in ceramic cutting tool

The use of aluminium oxide based ceramic cutting tools in turning of difficult-to-cut materials is an attractive alternative to replace grinding operation in order to reduce manufacturing costs. Ceramic cutting tools is useful in the cutting of difficult-to-cut materials such as stainless steel (Lin, 2008 ; Sobiyi et al., 2015), superalloy (Bushlya et al., 2013), tool steel and hardened tool steel (Özel et al., 2005; Özel et al., 2007; Meddour et al., 2015).

Interest in ceramics cutting tools in turning of difficult-to-cut material is owing to its favourable materials properties such as high hot hardness, good abrasive resistance and chemical stability. But, the main limitations of ceramic tool materials are due to their low fracture toughness and poor thermal shock resistance, thus resulting in premature tool failure by chipping or catastrophic failure by breakage instead of gradual wear. Continuous machining with a chipped tool can severely deteriorate the surface finish quality and dimensional accuracy of the machined part. Thus, in-process detection of the tool failure by chipping in ceramic is important so that the machine tool to be able stopped immediately to prevent damages to the workpiece and machine tool.

Direct methods using vision system has been attempted to monitor wear in ceramic cutting tool in the past. Patil and Tilekar (2014) proposed an offline tool wear assessment using digital camera and the captured images of cutting tool were processed in *MATLAB*. Cakan (2011) used a laser source that focuses on the workpiece and its reflected ray is captured in-process using a photodiode for accurate measurement of the workpiece diameters to predict the flank wear of alumina based

ceramic cutting tools. The flank wear was indirectly monitored in response to the increases in workpiece diameter. However, no attempts was made to monitor tool chipping in ceramic cutting insert.

Indirect methods using cutting force signal in detecting the tool chipping in ceramic cutting tools have been attempted in the past. Cutting forces are influenced by the tool geometry, as the cutting tool wears, its geometry changes thus impacting over the cutting forces. Jemielniak (1992) used the cutting force in the time domain to detect the tool chipping in ceramic cutting tool. Their results showed that stepwise increase of the average level of the cutting force indicated that tool has chipped.

Shi and Gindy (2007) developed an in-process monitoring method for hard turning using three component force sensors. Experiments were performed for machining Inconel 718 using ceramic tools. The acquired cutting force signals was subsequently processed using wavelet transform. The decomposed signal allows one to distinguish between the static and dynamic components in the force signal and to obtain features of tool malfunctions such as tool wear, tool chipping and tool breakage. The authors found that the use of force signal to detect tool chipping is more difficult compared to the detection of excessive wear and tool breakage because the variation of cutting force caused by tool chipping did not exceed the threshold limit. This study was repeated using multiple sensory signal such as power, force and vibration. The features of each sensor signal were extracted using statistical parameters to correlate with the wear of the ceramic cutting tool. Shi and Gindy (2007) concluded that the extracted statistical parameters from different sensor signal increased with tool wear. Power and force sensor signal were found to be more sensitive in detecting the tool wear compared to the vibration sensor signal.

Neslušan et al. (2015) used an AE method to detect the failure of ceramic tools during hard turning of bearing steel. The authors concluded that the conventional processing of AE signals does not enable the different phases of tool wear to be clearly recognised. It was possible to detect tool failure by chipping and breakage only by recording and analysing the AE features using two different AE sensors at different frequency ranges.

Jemielniak et al. (2011a) applied sensor fusion including vibration, cutting force and AE to monitor the tool condition during turning of Inconel 625 using ceramic cutting insert. The signal features were extracted from time domain signals, frequency domain and time-frequency domain. Cutting force was found to be the most informative parameter for tool wear monitoring compared to the vibration and AE. However, the authors reported that multiple sensor signals used together produced results a little worse than using a single sensor signal.

2.6 Detection of the tool failure from the workpiece surface using machine vision and image processing method

Surface quality has also been used to evaluate the cutting tool condition as the cutting tool operates directly on the workpiece and the machined surface carries valuable information about the machining process. With the rapid development of machine vision and image processing methods, researchers have started using machine vision to investigate tool wear indirectly based on the workpiece surface of a machined part. Kassim et al. (2007) distinguished the sharp and dull tools based on the surface texture of a turned workpiece. The turned workpiece was shaped by cutting tool during machining process which caused ridges and groves formed on the

surface of workpiece. The groves are even and straight with clear ridge lines when the cutting tool is sharp. When the cutting tool is dull, the groves appear uneven and ridge lines become disjointed. However, the images of workpiece surface were captured in-cycle, thus interrupt the machining.

Several researchers have attempted to evaluate the tool condition by extracting the surface finish descriptors from the images of freshly machined surface texture. Dutta et al. (2012) captured images of machined surface in-cycle and analysed them offline using grey level co-occurrence method. The variation of texture descriptors, namely contrast and homogeneity, with machining time were studied and successfully correlated with tool flank wear. However, no attempt was made to investigate the effect of tool chipping on the texture descriptors.

Datta et al. (2013) successfully applied the concept of Voronoi tessellation to extract two texture features, namely the number of polygons with zero cross moment and the total void area of the Voronoi diagram from the machined surface images to be correlated with the flank wear. Voronoi tessellation is a popular method for clustering a set of points into an arrangement of regions defined by the local neighbourhood of each of the points. Voronoi diagram is used to create polygons which provides a description of the neighbourhoods for each of the constituting points. The geometric features of the Voronoi polygons depend on the distribution of points can be used to detect any underlying structural pattern in an image. Non-uniform feed marks is formed in the machined surfaces due to the increase in tool flank wear which results in non-uniform edges in the machined surfaces. Thus, Voronoi polygons becomes non-uniform with the increase in tool flank wear. Dutta et al. (2016) applied texture analyses namely gray level co-occurrence matrix

(GLCM), Voronoi tessellation, and discrete wavelet transform (DWT) based methods to obtain information about the waviness, feed marks, and roughness from the turned surface images for predicting the tool flank wear using support vector machine (SVM) based regression models. However, non-homogeneous illumination due to improper lighting and interference of ambient lighting can affect the reflectance of the workpiece surfaces adversely thus resulting in redundant features from the images of the machined surface.

Recently, Li and An (2016) used machine vision method to acquire the cutting tool images and workpiece surface images simultaneously to monitor tool wear. The automatic focusing and segmentation of the wear region of the cutting tool was determined by using Markov Random Field algorithm while the features of the surface texture of the workpiece surface was obtained using a GLCM to monitor tool wear. Although this proposed method seems promising, images of cutting tool and workpiece only can be captured in between turning operation when the cutting tool is not in contact with the workpiece.

Shahabi and Ratnam (2009b) have successfully applied backlighting to capture the silhouette of workpiece profile to determine the nose wear and flank wear. The proposed method can effectively determine the nose wear by subtracting the images of workpiece profile produced by worn and unworn tool. The maximum flank wear, VB_{max} in the nose radius area can also be determined accurately from the 2-D image of nose radius area of cutting tool using polar coordinate. However, their work was conducted in-cycle and no attempt was made to detect the tool chipping.

2.7 Signal processing method

The signal captured from the machining process are required to be processed and analyzed to obtain the important information about the tool condition. The extraction of signal features related to cutting tool condition is a key issue in tool condition monitoring system. For best performance of tool condition monitoring system, only those signal features which show a high sensitivity to tool condition should be utilized to make the sensing system more efficient. Tool wear monitoring based on sensor signal usually is evaluated through signal processing methods that comprise the steps shown in Figure 2.5. The steps including choice of the measurable sensor signal to be captured, feature extraction and feature classification. The raw sensor signals is processed to extract significant features from the signal in the time domain or frequency domain and to correlate the tool wear or were further fed into a model such as autoregression model, neural network to estimate the tool state (Lauro et al., 2014).

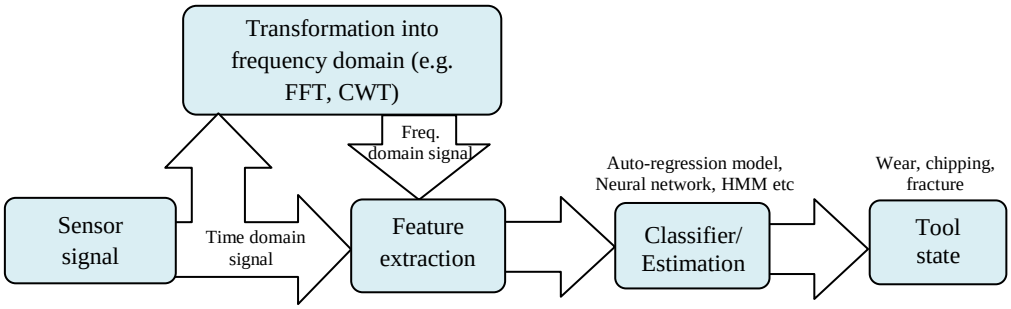

Figure 2.5: The framework of tool condition monitoring using indirect method (Lauro et al., 2014)

2.7.1 Time domain analysis

Signal features need to be derived so that can be used to describe the signal adequately and maintain the relevant information about the process or tool conditions. The most common signal features that can be extracted from any time domain signal are the mean and RMS value of signal. Dimla and Lister (2000), Sikdar and Chen (2002), Cakir and Isik (2005), Sharma et al. (2008) used time domain analysis for force signals and they found that the time domain features of cutting forces correlated well with the tool wear. Guo and Ammula (2005), Bhaskaran et al. (2012), Hase et al. (2014) and Neslušan et al. (2015) used the RMS value of AE signals to estimate the tool condition and found that good correlation exists between the RMS of AE signals and tool wear. Other signal features such as kurtosis, skewness, variance and standard deviation (Bhaskaran et al., 2012; Liu et al., 2013a) are also been adopted for tool condition monitoring. The time domain features have still been widely used in tool condition monitoring as they offer a great deal of simplicity in terms of the extraction. However, these features are susceptible to disturbances so they need to be supplemented with features from other domains (Siddhpura & Paurobally, 2013).

Some previous works have discussed tool wear monitoring by the analysis of surface roughness. The findings agreed that an inherent relation between the surface roughness and tool wear exists. This is because the surface roughness of a workpiece is influenced by the sharpness of the cutting tool. Choudhury and Bartarya (2003) indicated that arithmetic average height of surface profile, R_a decreased when the flank wear increased. However, Lima et al. (2005) found that increased in the flank wear resulted higher value of R_a. Peak-to-valley height of profile, R_t is observed to

decrease as the amount of the flank wear increased (Runola et al., 1994). However, the opposite finding was reported. Penalva et al. (2002) and Grzesik (2008b) found that R_t becomes higher when the tool wear continued increase. Although the use of single parameter of the surface roughness could be used to indicate a change in the machining process, it is difficult to identify where the changes in the machining have been occurred. In addition, surface roughness parameters is also highly dependent on cutting parameters such as cutting speed, feed rate and depth of cut. Thus, it results in different surface roughness when various cutting parameters are adopted.

ACF is an important diagnosis tool which allows to identify the possible random and periodic features buried on generated surface profile. Roy et al. (2007) segregated the relative contribution of the electrolytic dissolution and the mechanical abrasion in electromechanical grinding by evaluating the surface profile using ACF. In a recent work, characteristic of machining process are investigated by extracting the topographical features of electrical discharge machining machined surface through the decomposition of ACF curves (Aich & Banerjee, 2017).

The use of ACF has also been attempted for fault detection and diagnosis. Zubaydi et al. (2000) successfully applied ACF to analyze the vibration response of a structure in order to identify the occurrence of small cracks in the side shell of ship structures. The advantage of using the ACF is that it could be easily obtained from the random vibration response of the structure using a statistical procedure. Rafiee and Tse (2009) introduced ACF of continuous wavelet coefficient of vibration signals as a feature for non-stationary signals in gear fault diagnosis. The ACF plots of synchronized vibration signals is found dies out quickly as with the worn gear. It should be noted from the above literature review, ACF has been successfully applied

for machine surface assessment and machine fault diagnosis. However, limited studies are available on the use of ACF in tool wear monitoring. This has motivated the detection of tool chipping from workpiece profile signature using ACF .

2.7.2 Frequency domain analysis

Frequency domain analysis is a tool of utmost important in signal processing applications. While time domain analysis shows how a signal changes over time, frequency domain analysis shows how the signal's energy is distributed over a range of frequencies. The information that cannot be readily seen in the time domain can be seen in the frequency domain. For this purpose, FFT is the standard method for observing signals in the frequency domain and it has been widely used in tool condition monitoring. The main advantage of frequency domain analysis over time-domain analysis is its ability to identify and isolate certain frequency components of interest and thus extract the features from the signal. For example, Liu et al. (2013b) discovered that the fundamental and third harmonics of frequency of cutting forces are predominantly affected by tool eccentricity, second harmonic of the frequency is caused by the tool wear and fourth harmonic is associated with the chip load.

The signal features extracted from frequency domain are usually considered the amplitude of dominant spectrum peaks and signal power in specific frequency ranges (Teti et al., 2010). Dimla and Lister (2000) used frequency spectrum from vibration and cutting forces signal to correlate with wear. The amplitude of the fundamental frequency peaks of sensor signal was found to increase with tool wear and very slight shift into lower frequency. Similar results was also reported by Kalvoda and Hwang (2010). Haddadi et al. (2008) adopted FFT for vibration signal

for tool condition monitoring in turning operation. The amplitude of the signal spectrum in the range of 0-3.5 kHz was responsive to tool wear and the wear of the cutting tool was accompanied by an increase in the spectrum amplitude of vibration signal in the range of 0-3.5 kHz. In addition, statistic features of the band power spectrum has also been utilized to assess the tool condition. Binsaeid et al. (2009) used mean, variance, kurtosis and skewness of power spectrum in specific frequency band as well as the frequency of maximum peak of band power from multiple sensor signals of force, vibration, AE and spindle power to estimate the wear level.

2.7.3 Time-frequency domain analysis

The band energy in frequency domain allows to predict tool wear, but the main drawback on the use of FFT is lack of time information for detecting transients which include chipping, breakage, collision of a cutting tool. To solve this problem, an attempts has been made through the development of short time Fourier transform (STFT), which is widely applied to tool condition monitoring (Marinescu & Axinte, 2008; Marinescu & Axinte, 2009; Rad et al., 2014) .

In STFT method, the signal is divided into small segment where these segments of the signal is multiplied by a window function to characterize the changes of frequencies at different time intervals. Spectral coefficients are calculated for the short length of data within the window function, the window function is then moved to a new position and the calculation is repeated (Teti et al., 2010) to reveal the variation of the frequency content of signal within the window function. The inherent problem associated with STFT is the trade-off between the time and frequency, which indicates that time and frequency cannot be resolved simultaneously due to

Heisenberg's uncertainty principle (Zhu et al., 2009, Feng et al., 2013). The choice of the window function is found that directly affects the time and frequency resolutions of the analysis result (Gao & Yan, 2010). In addition, the use of the window function in STFT, a part of the window function is attenuated at the boundaries which can cause a loss of frequencies response in the boundaries regions (Pampu, 2011).

In addition to STFT, wavelet transform has been successfully applied and became the most informative approach for time-frequency analysis of signals. Wavelet theory has been developed in the late 1980s by Mallat (1989) and Daubechies (1990) to fulfil the needs for adaptive time-frequency analysis, which can overcome the resolution problem of the STFT. Wavelet transform has been widely applied for tool condition monitoring as its great potential in detecting the abrupt changes of tool condition. Khraisheh et al. (1995) found that CWT is suitable for analyzing the transient in vibration signal during turning process and the transient boundary and the built-up edge were successfully identified. Yesilyurt (2006) used the mean frequency variation of scalogram of vibration signal in end mill tooth breakage detection under varying feed rates. It was found that mean frequency variation of scalogram is quite responsive to the presence of fault.

It was reported that discrete wavelet transform (DWT) is preferable in the time-frequency analysis due to its ability of fast computation. When tool failure occurs, the signals often contain abrupt changes or a sudden shift to a different level, which known as singularity points. Gong et al. (1997) used DWT of cutting forces to monitor flank wear in turning process. Results showed that the fifth level wavelet coefficient were more sensitive to the changes of flank wear states under different depth of cut. However, Kwak (2006) found differences suggesting that the fourth

level approximation coefficient of the cutting force signal increased sharply at onset of tool failure.

Chen and Li (2007) applied DWT for singularity detection from AE signals during turning and found that wavelet coefficient norm was reliable for distinguishing between sharp tool and worn tool. Fang et al. (2012) adopted wavelet decomposition analysis to identify the changes in the vibration signals in different frequency bands and found that third level of wavelet coefficient of the vibration signal was the most sensitive to dynamic tool-edge wear. DWT utilises the sampling of both time data and scale to produce faster algorithm. Scale and time are sampled in power of two (dyadic sampling) to cause some content in scale is loss. Therefore, finest scale in CWT allows for localize the frequency change precisely.

2.8 Chapter summary

Several tool failure monitoring methods including the methods that are still in development progress as well as the commercialized devices are reviewed. A summary of the available methods and their limitations are presented in Table 2.1. From the literature reviewed, it is seen that many optical and vision methods for direct wear assessment on the cutting tool have been developed in the past. Although direct measurement using machine vision have the advantages of capturing the actual geometric changes arising from the wear and chipping of the cutting tool, this methods cannot be applied in-process because the cutting area is inaccessible due to the continuous contact between the tool and the workpiece during machining.

In-process tool failure monitoring is usually performed by indirect method based on various sensor signals. All the indirect methods reviewed in this chapter have their advantages and disadvantages when compared to one another. A number of studies show that a significant contradictory findings do exist. Thus, there still exists a need to develop a more reliable in-process tool failure monitoring method.

Table 2.1: Summary of the methods and their limitations

Method		Limitations
Direct tool condition monitoring method	Tool maker's microscope, SEM, white light interferometry, confocal microscope, AFM, CCD camera	- Offline, intermittent or in-cycle monitoring
Indirect tool condition monitoring method using sensor signal	Cutting forces Vibration AE Sound Temperature Current and Power Sensor fusion	- Highly affected by process parameters, tool and workpiece material - Sensitive to noise - Reliability of the sensor signal to tool failure monitoring still has contradictory findings - Require high computational load
Indirect tool condition monitoring method using workpiece surface	Surface Texture	- Intermittent or in-cycle monitoring - Subjected to illumination and contaminants (e.g. oils, dust) - No attempt was made on tool chipping detection
	Workpiece profile	- Intermittent or in-cycle monitoring on flank wear and nose wear - No attempt made on tool chipping detection

The features extracted from the images of the machined surface texture correlated well with the flank wear. However, this method requires the machine to be stopped before the images of the machined surface can be captured. Previous studies

show that the 2-D workpiece profile possesses a great potential for the indirect assessment of nose wear and flank wear during turning although the previous studies were conducted in-cycle. To date, no attempt has been made to detect the tool chipping based on the workpiece profile in ceramic cutting insert. Thus, the focus of this work is on the development of a novel in-process method for detection of tool failure by chipping from a 2-D workpiece profile signature using machine vision method.

CHAPTER THREE

METHODOLOGY

3.1 Introduction

This chapter outlines the formulation of the methodology to achieve the objectives of the study. The research methodology is discussed in Section 3.2 to Section 3.4 and is summarized in Figure 3.1.

The methodology for in-process detection of tool failure by chipping from the 2-D workpiece profile signature using ACF is presented in Section 3.2. The specific procedures in generating the simulated workpiece profile is presented in the Section 3.2.1 which were used in simulation to demonstrate how ACF method could be used to investigate the effect of tool chipping on the workpiece profile. An experiment, which was carried out to produce the actual workpiece profile on turned part to investigate the capability of the proposed method, is explained in Section 3.2.2. In Section 3.2.3 and Section 3.2.4, experimental setup with a specific image acquisition system for the in-process capturing the images of the workpiece profile during turning operation is presented. Calibration of the image acquisition system such as scaling factor determination (Section 3.2.5), distortion assessment (Section 3.2.6) and motion blurring assessment (Section 3.2.8) are also outlined. A detail description of the workpiece profile detection algorithm in sub-pixel level accuracy edge detection using invariant moment method is explained in Section 3.2.7.

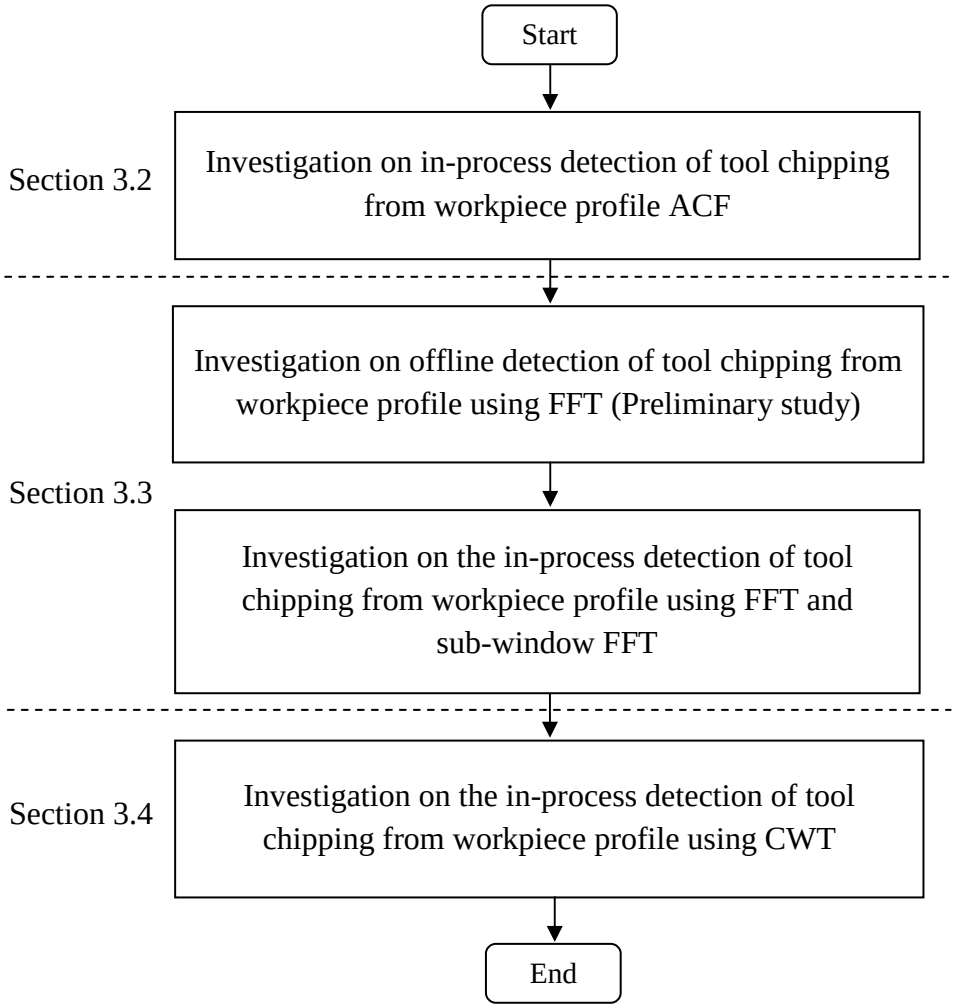

Figure 3.1: Flow of research methodology

Section 3.3 describes the methods for tool chipping detection from the 2-D workpiece profile signature using FFT. The steps in generating the simulated workpiece profile by considering the changes of the tool geometry due to the gradual wear and chipping is presented in Section 3.3.1. An offline preliminary experimental work carried out to capture the images of the turned workpiece profile is presented in Section 3.3.2. In Section 3.3.3, the simulation work on detection of tool chipping based on workpiece profile by considering the presence of tool-workpiece vibration is discussed. In-process experiment to capture the images of the workpiece profile

simultaneously with measurement of tool vibration using accelerometer is presented in Section 3.3.4. To resolve the time resolution of the FFT and drawback of STFT, sub-window FFT was proposed (Section 3.3.5).

Section 3.4 presents the methodology for the detection of tool chipping from workpiece profile using CWT. The reason for applying FFT and CWT is to compare the methods so that a better method in terms of ability of detecting the onset tool failure by chipping is determined. The last section of this chapter is the chapter summary.

3.2 In-process tool chipping detection in ceramic cutting insert from the workpiece profile signature using ACF

Detailed procedure for the simulation work to demonstrate the use of ACF in tool chipping detection based on the workpiece profile signature is explained in Section 3.2.1 while an in-process experimental procedure to investigate the capability of the use of ACF method for detecting the tool chipping in ceramic cutting insert from the actual workpiece profile is presented in Section 3.2.2.

3.2.1 Simulation work

In order to develop an approach capable of detecting the sudden tool failure by chipping in ceramic cutting tool, a simulation work was designed to investigate the potential of ACF in tool chipping detection from the simulated workpiece profile signature. Figure 3.2 shows the specific steps for generating the ideal workpiece profile used in the simulation. In the stage 1, the image of an ideal nose profile (nose

radius, r_ε = 0.8 mm) of the cutting insert was created using *AUTOCAD* software (Version 2013). The created nose profile for simulation is shown in Figure 3.3. The ideal nose profile was drawn according to the designation of the cutting tools used in this study (CNGN 120808 series). The ideal nose profile is formed by a circular edge and two straight lines which represent the major cutting edge and minor cutting edge.

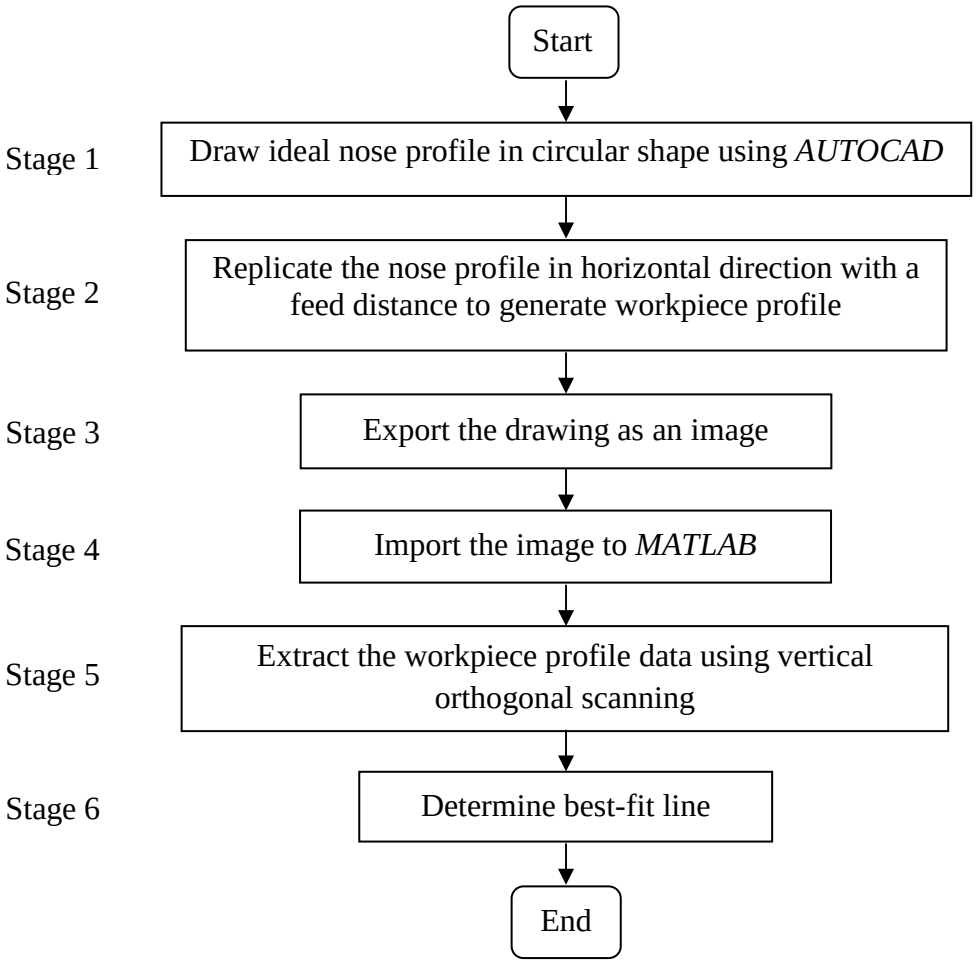

Figure 3.2: The flow chart of the generation of ideal workpiece profile

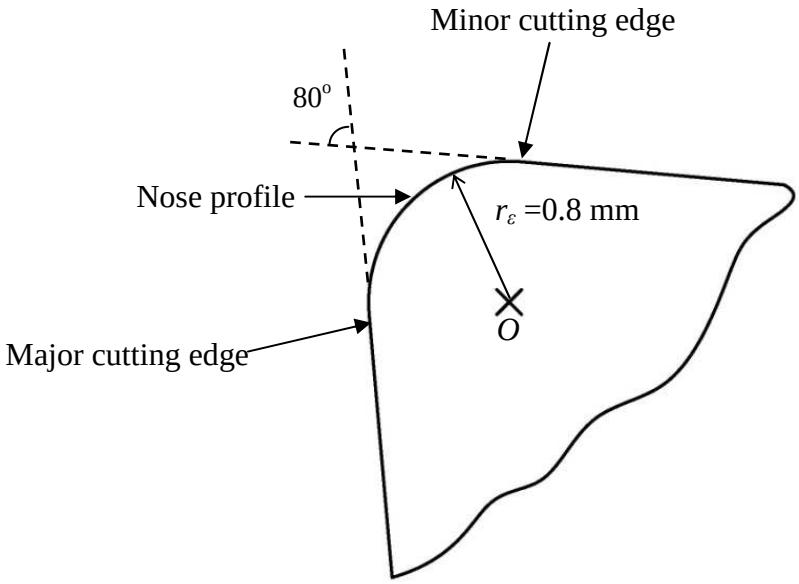

Figure 3.3: Geometry of the nose profile created using *AUTOCAD*

In the stage 2, the nose profile was duplicated horizontally along the feed direction from the centre of the nose profile, *O* with a feed distance f = 0.4 mm as illustrated in Figure 3.4. This is because in a turning process the workpiece is revolved under a moving cutting tool resulting in the tool following a helical path relative to the work surface. Thus, an imprint of the nose profile of a cutting tool is replicated on the machined surface and each imprint is separated from the next by the feed distance f as a result of the feed motion as shown in Figure 3.4. The elements of the vectors that extend beyond the intersection points (I_p) between the nose profile and workpiece were trimmed off in order to produce the workpiece profile shown in Figure 3.5.

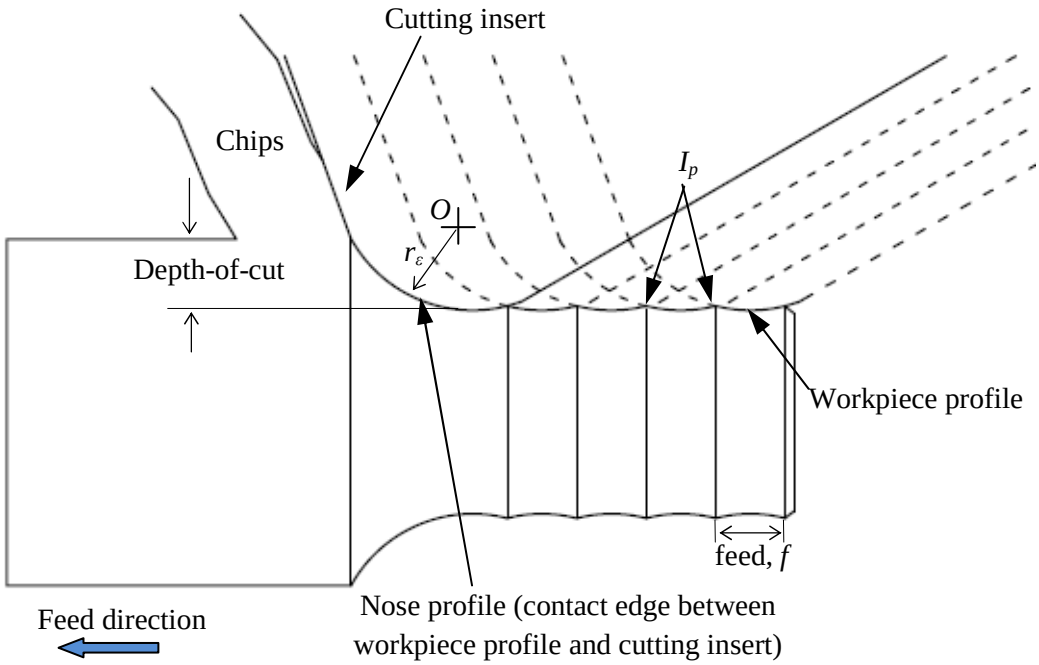

Figure 3.4: Schematic representation of interaction between the cutting tool tip and the formed surface

In the stage 3, a 4 mm length of the simulated ideal workpiece profile was created and exported as an image format. In the next stage, the simulated ideal workpiece profile was read and imported as Red-Green-Blue (RGB) image into *MATLAB*. The RGB image was converted into digitized gray-scale level image, U_{gs} encoded as a 2-D array of pixel in spatial coordinates of x and y. The images of simulated ideal workpiece profile is made up of black and white colours therefore its gray-scale level in each pixel value is either 0 (black) or 255 (white) as shown in Figure 3.5.

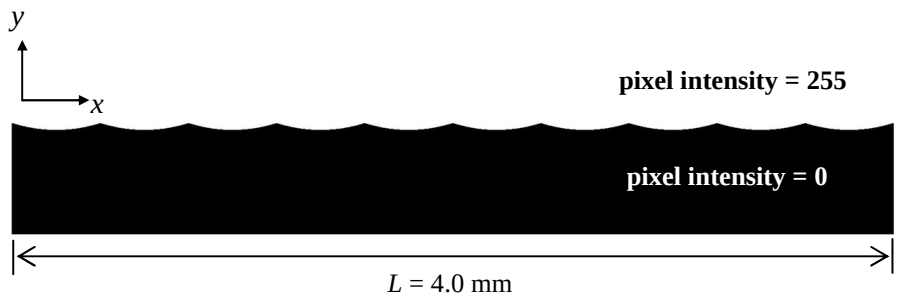

Figure 3.5: Simulated ideal workpiece profile generated from *AUTOCAD*

In stage 5, workpiece profile detection algorithm written in *MATLAB* was applied to extract the surface profile of the simulated ideal workpiece profile. By vertical scanning along each column in the horizontal direction, the *y*-coordinate of the profile was obtained by searching the *y*-coordinate of the pixel that has the first minimum gray-scale level in each column. The *x*-coordinate of the workpiece profile are corresponding to the scanned column values. The algorithms starts scanning the first pixel of the first column of the image to detect the coordinate of the first pixel intensity of 0 (black colour) to form the surface profile data. The scanning continues to search the second column to find the second pixel value of 0. The contour of the workpiece profile was determined by vertical scanning in each column from top to bottom. This step is repeated to detect all the pixels in all the columns that lie on the workpiece profile which reveal the contour of surface roughness of the simulated workpiece profile.

The first pixels with intensity 0 in all columns reveal the contour of the workpiece profile and the typical ideal surface profile is shown in Figure 3.6. The detected surface profile is in pixels value, therefore the scaling factors were used to convert the surface profile in pixels value to metrics value. Since the known border length of the simulated workpiece profile was created from *AUTOCAD*, thus the scaling factor was determined by dividing the length of the simulated workpiece profile with the number of pixels of the images in the horizontal and vertical directions. After that, the best-fit line (known as mean line) of the detected contour of the simulated workpiece was determined. The surface profile can be determined by subtracting the mean value of the roughness profile from each point on the

contour. The coordinates (x_i, y_i) data where *i=1,2,3, ..., N*, were stored into two row vectors denoted as *x* vector and *y* vector, respectively.

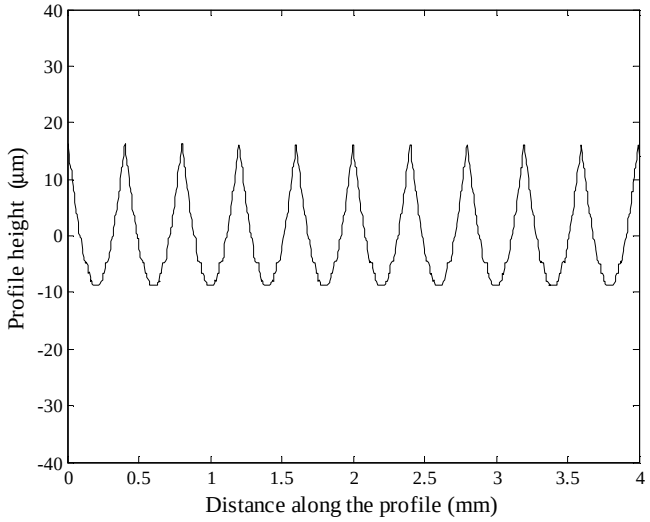

Figure 3.6: Simulated ideal workpiece profile extracted from Figure 3.5 using vertical orthogonal scanning

Unlike in the ideal case the characteristic of a real surface profile is influenced by vibration that occurs during machining. Tool vibration occurs because one of the structural modes of the machine tool and workpiece system is initially excited by cutting forces which are caused by tool failure and corresponding system instability in the machining process, characterized by unwanted excessive vibration between the tool and the workpiece and consequently cause poor quality surface finish. The dynamic force related to the chip-thickness variation acting on the cutting tool is related to the amplitude of tool vibration at resonance and to the variation of the tool's natural frequency while machining (Thomas et al., 1996). As a result tool vibration generates the irregularities seen on the machined surface. Previous work show that the turned surface of a machined workpiece is mainly composed of the

cutting feed component and the vibration component (Sata et al., 1985). Thus, the real surface profile can be expressed as:

$$G(x) = U_{gs}(x) + u(x) \tag{3.1}$$

where $U_{gs}(x)$ is the ideal surface profile and $u(x)$ is the dislocation in the workpiece profile results from the vibration generated during machining. Tool vibrates is mainly as a one degree of freedom system (Thomas et al., 1996). Therefore, the motion equation of the vibrating system can be described as a simple harmonic motion. During stable machining, the vibration signal oscillates with constant frequency and amplitude and the dislocation of workpiece profile due to tool-workpiece vibration can be expressed as:

$$u(x) = \sum_{n=1}^{N} C_n \sin(\omega n x) + \phi \qquad n=1, 2, 3 \ldots \tag{3.2}$$

where C_n is the amplitude of dislocation in the workpiece profile, ω is the fundamental angular frequency and ϕ is the random dislocation of the workpiece profile caused by severe tool chipping.

Since vibration increases as tool flank wear increases due to the increase in the cutting force thus resulting in a periodic variation in depth of cut (Dimla, 2002), the effect of tool wear on the simulated workpiece profile was done by increasing the vibration amplitude. In the simulation, the dislocation in the workpiece profiles that result from the relative tool and workpiece vibration was added into the ideal workpiece profile $U_{gs}(x)$.

For gradual wear the dislocations in workpiece profile caused by vibration is assumed to be low and stable. The random dislocation of vibration is thus neglected. Figure 3.7(a)-(b) shows the simulated workpiece profile produced from the combination of the ideal workpiece profile and dislocation vibration due to gradual wear. The dislocation of vibration were increased by 5% and 10% from the peak-to-valley height of the surface profile (R_t), for a spatial frequency of 100 mm^{-1} which is equivalent to $40V_f$ where V_f is the fundamental feed frequency of the simulated ideal surface profile. The fundamental feed frequency V_f (mm^{-1}) is given by:

$$V_f = \frac{1}{f} \quad \text{where } f \text{ is the feed (mm).} \tag{3.3}$$

A spatial frequency of 100 mm^{-1} was used because previous work has shown that tool wear excites high peaks of vibration signal that appear near a fundamental frequency of 117 Hz in the normal wear stage (Jiang et al., 1987). The maximum peak-to-valley height was determined from the ideal surface profile data which is defined as the vertical distance between the highest peak and the lowest valley along the evaluation length of the surface profile.

Previous study has shown that when a ceramic tool chipped the amplitude of vibration increases sharply reaching 10 times as much as that in normal wear stage (Jiang et al., 1987). Several high peaks were also found in the frequency range 0-117 Hz and the amplitude of peaks fluctuated significantly and randomly as a result of the irregular tool shape after fracture (Jiang et al., 1987). When a tool wears or deforms new sources of vibration are also introduced into the machining due to abnormal cutting conditions (Thomas et al., 1996). Thus, a random dislocation of

workpiece profile with 5 and 10 times higher of the dislocation of surface profile resulted from wear was added as presented in Figure 3.7(c)-(d), respectively.

Relative high amplitude vibration between the tool and the workpiece usually occurs when cutting tool wear increased. Such vibration causes the formation of surface modulation or waviness in both cutting and the tool feed directions (Boryczko, 2011). The surface roughness profile along the axial direction is modulated by a revolution of the spindle within the range of wavelength longer than 2λ, where λ is the wavelength of the workpiece profile (Sata et al., 1985). Therefore, Equation 3.2 was modified and the dislocation of the workpiece profile due to waviness resulting from the tool-workpiece vibration is presented in Equation 3.4. The simulated workpiece profile accompanied with the waviness resulting from the tool-workpiece vibration in Equation 3.4 is shown in Figure 3.7(e). The surface profile presence of waviness resulted from the tool-workpiece vibration aims to observe how does the surface waviness influence the ACF. Thus, the dislocation of vibration in workpiece profile is excluded.

$$u(x) = \sum_{n=1}^{N} C_n \sin\left(\frac{2\pi n x}{\lambda}\right) + \phi \qquad n=1, 2, 3 \ldots \tag{3.4}$$

With the exception of ACF, a common drawback of statistical surface roughness parameters such as mean, RMS, peak-to-valley is that they do not provide information about periodicities. Mean and RMS values are not sensitive to very large impulses. Peak-to-valley height roughness parameter is sensitive to impulses such as tool breakage. However, a single noise spike can throw it off which could lead to false alarm. Therefore, ACF was applied to investigate the effect of the tool chipping on the workpiece profile.

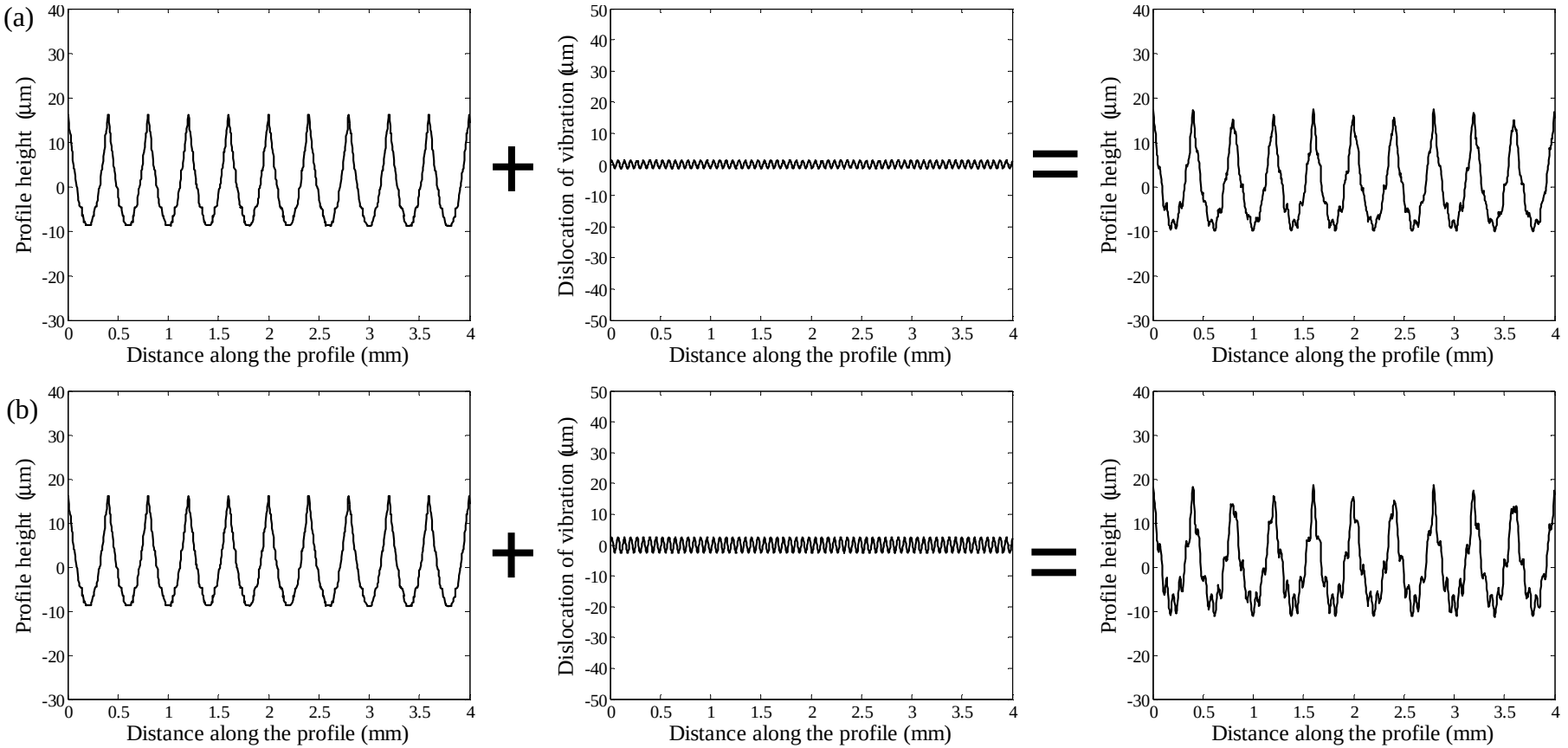

Figure 3.7: (a) simulated surface profile with increasing vibration amplitudes by 5% peak-to-valley height of simulated ideal workpiece profile; (b) simulated surface profile with increasing vibration amplitudes by 10% peak-to-valley height of simulated ideal workpiece profile; (c) simulated surface profile with random vibration with 5 times higher vibration magnitude as in (a); (d) simulated surface profile with random vibration with 10 times higher vibration magnitude as in (a); and (e) simulated surface profile with presence of waviness due to the tool-workpiece vibration by 10 times higher vibration magnitude as in (a) (Continued)

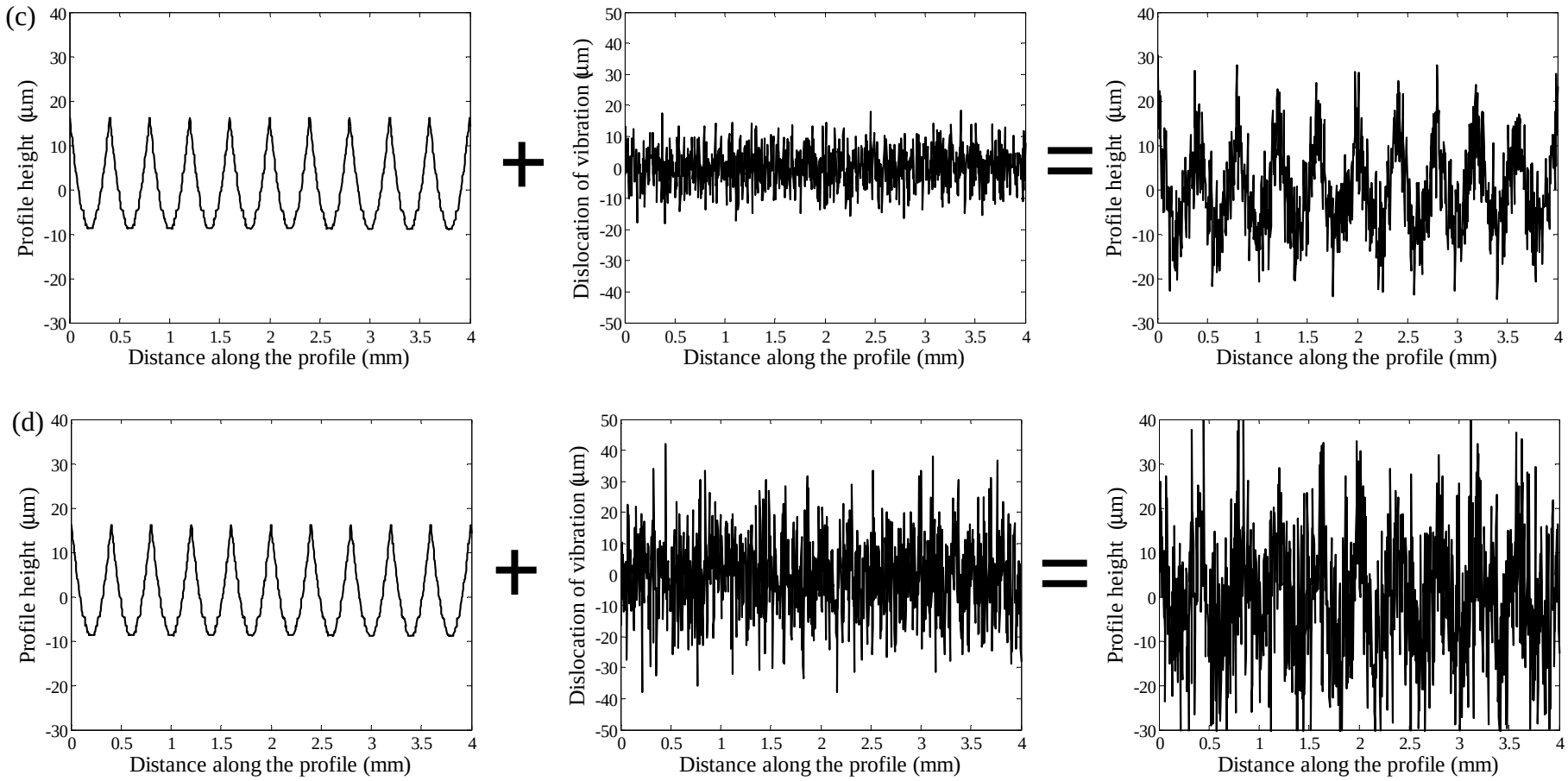

Figure 3.7: Continued

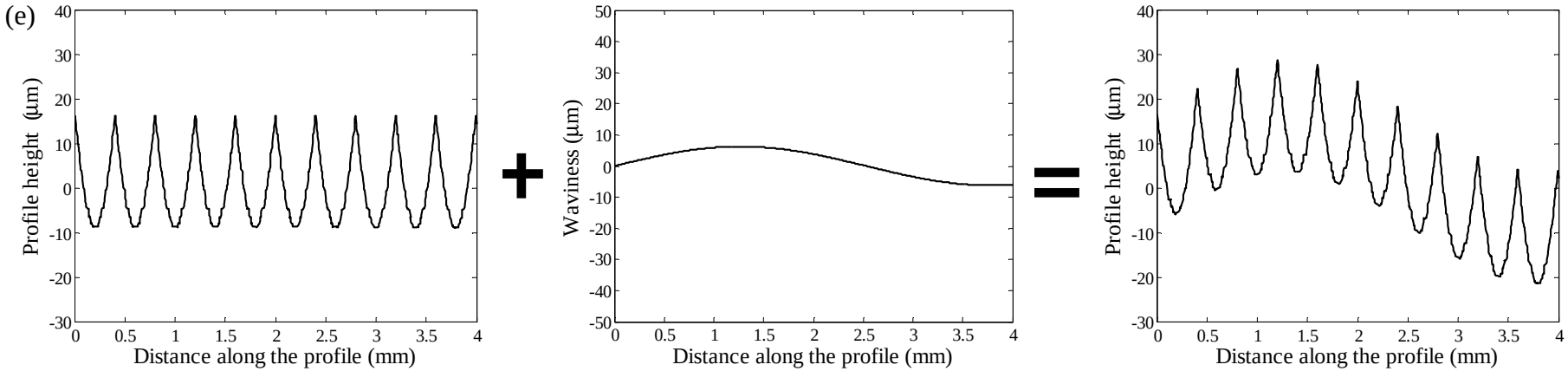

Figure 3.7: Continued

In this work, ACF is chosen because it is capable of detecting the presence of the random noise buried in any periodic surface roughness profile. The flow chart of ACF algorithm written in *MATLAB* is presented in Figure 3.8. The ACF analysis is done by comparing the workpiece profile with a replica of itself whereby the replica is shifted by a lag distance (τ) and is evaluated over the length of the workpiece profile. In other words, for surface profile *G(x)*, the ACF is the average value of product the un-shifted and shifted surface profile, $G(x)G(x+\tau)$ and is given by Equation 3.5 (Bendat & Piersol, 1993):

$$A(\tau) = \lim_{L\to\infty} \frac{1}{L} \int_0^L G(x)G(x+\tau)dx \tag{3.5}$$

For discrete surface profile data the ACF is defined as in Equation 3.6:

$$A(m\Delta\tau) = \frac{1}{N} \sum_{i=1}^{N} G(i)G(i-m) \tag{3.6}$$

where m is an integer, $\Delta\tau$ is lag interval, N is total number of sample points on the workpiece profile, $G(i)$ is the surface profile at position $m\Delta\tau$ and $G(i-m)$ is the surface profile at position $(i-m)\Delta\tau$, i.e. at m sampling intervals earlier. The ACF is then normalized by dividing $A(\tau)$ by the square of RMS roughness (R_q^2). The RMS roughness is defined as the RMS average of the workpiece profile $G(i)$ calculated from the mean line and is expressed in Equation 3.7.

$$R_q = \sqrt{\frac{1}{N} \sum_{i=1}^{N} G(i)^2} \tag{3.7}$$

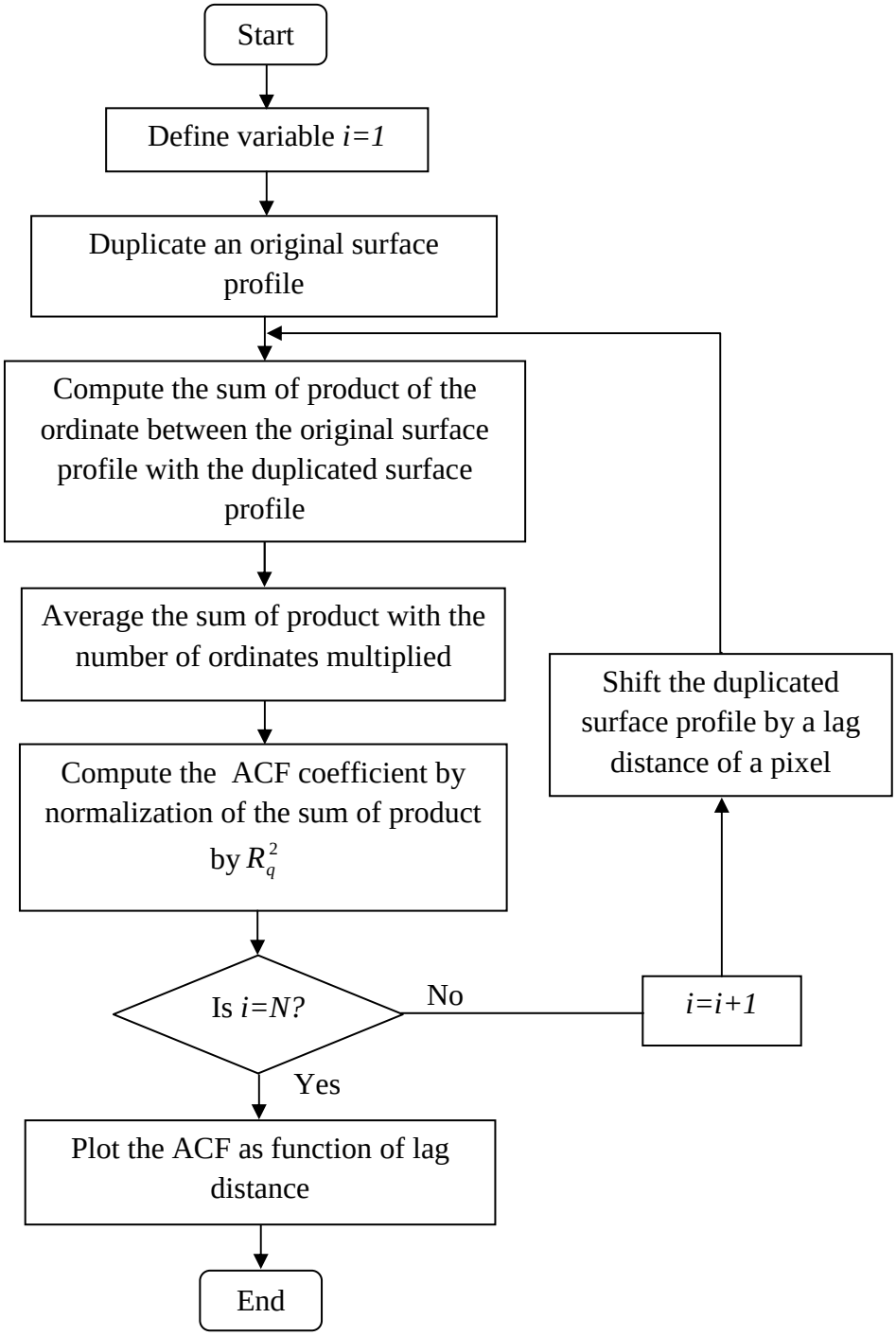

Figure 3.8: Flow chart for ACF algorithm

The mechanism of ACF is depicted in Figure 3.9. Firstly, each ordinate of the workpiece profile was multiplied by itself across the whole workpice profile and the products are add together. After that, the sum of the product is divided by the number of ordinates multiplied and normalized by dividing by R_q^2 to obtain the autocorrelation coefficient to yield a measure of how similar the workpiece profile is at a given distance from the original location. It is always maximum at the origin.

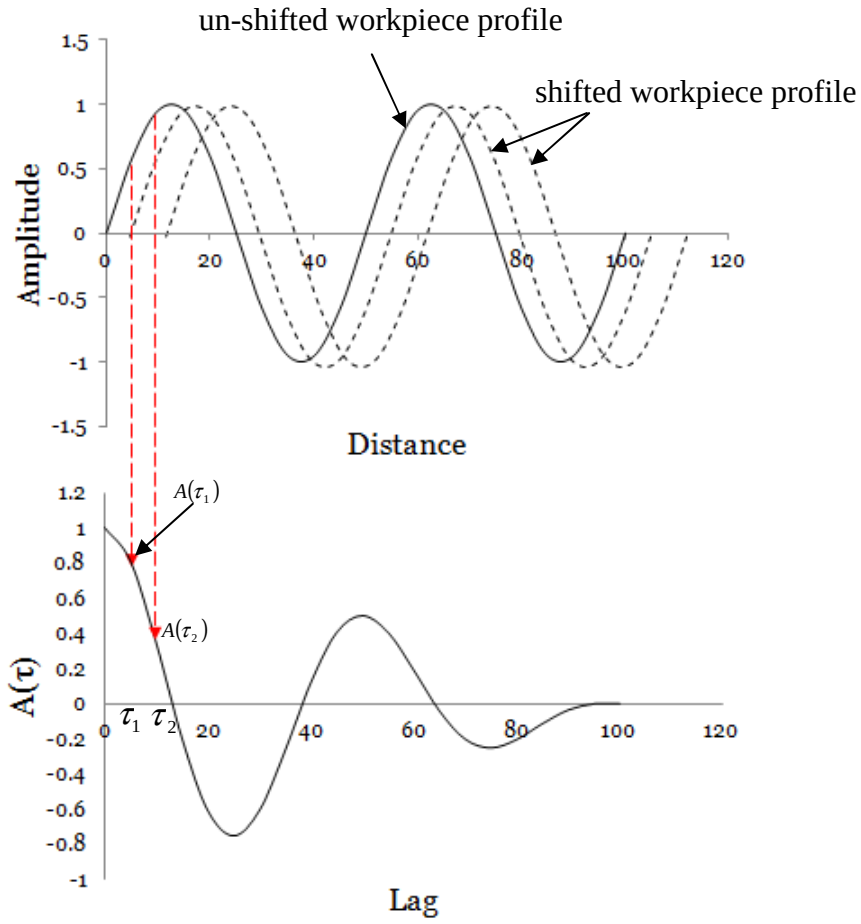

Figure 3.9: Mechanism of ACF

After the autocorrelation has been carried out, the workpiece profile was shifted relative to itself by an amount of τ_1. In this study, each lag distance τ is equivalent to one pixel. The steps abovementioned was repeated by multiplying each ordinate on the un-shifted workpiece profile by the ordinate of shifted workpiece profile and the average of all products are also normalized by dividing by R_q^2 to obtain the second autocorrelation coefficient, $A(\tau_1)$. The process of shifting the workpiece profile by a lag of τ_2 was repeated to obtain autocorrelation coefficient of $A(\tau_2)$ and so on till the end of the workpiece profile is reached. The ACF value between 0 to 1 gives the strength of the relationship between the original profile and shifted profile. Higher ACF value that is close to 1, signifies that there is high correlation between un-shifted surface profiles and shifted surface profile, whereas, close to 0 implies no such significant correlation existed between these surface profiles.

3.2.2 Experimental work

An experimental work was conducted to compare the experimental results with the hypothesis of the simulation. In this section, machining condition and the experimental setup with a specific image acquisition system for capturing the images of the turned workpiece profile during turning operation is presented. Calibration of image acquisition system such as scaling factor determination, distortion assessment and motion blurring assessment was made to ensure a reliable workpiece profile to be used in analysis is obtained. The algorithm for workpiece profile detection in sub-pixel level accuracy edge detection using invariant moment method is also presented.

3.2.3 Machining condition

The turning operation was performed on a *Pinocho S90* conventional lathe machine under dry cutting condition. The workpiece material used in experiments was a cylindrical bar with diameter of 50 mm and a length of 250 mm made of AISI 01 Arne oil hardening tool steel (C: 0.95%, Mn: 1.1%, W: 0.6%, V: 0.1% Cr: 0.6%) with the hardness of 190 HB. The commercially available aluminum oxide based ceramic insert with added zirconia (CNGA 120408T02520 CC620, Sandvik Coromant Ltd., Sweden) was used for the machining experiments. The cutting insert was of rhombic shape. The tool holder used for the turning was DCLNR 2020M (Sandvik Coromant, Sweden).

The cutting conditions were as follows: the spindle rotational speed, 950 rpm; feed rate, 0.4 mm/rev; and depth of cut, 0.5 mm were selected according to the recommendations provided by the cutting tool manufacturer (Sandvik Coromant, 2015). No coolant were employed in the cutting experiment to facilitate the image acquisition of the workpiece profile during turning.

3.2.4 Image acquisition system

The basic components of image acquisition setup consists of 18-megapixel DSLR camera (model: Canon EOS 700D) with a picture resolution of 5184×3456 pixels. The DSLR camera was fitted with Canon EF 100 mm macro lens and connected via USB cable to a personal computer (Intel Pentium Dual CPU E2160 @ 1.80 GHz) for capturing the images of the workpiece profile. Uniform diffused backlighting illumination was obtained by using a high-frequency fluorescent light

(Edmund Optics Pte. Ltd., Singapore) to capture the contour of the workpiece. Backlighting is the suitable type of illumination for this application because only contour of the workpiece surface is needed.

Figure 3.10 shows the in-process image acquisition setup used to capture the images of the workpiece profile during turning operation. When capturing the images of workpiece profile, the intensity of light source and the lens aperture were adjusted to avoid the burnout in the images. The focusing ring on the camera was adjusted so that the edge of the workpiece is sharply in focus. The shutter speed of the DSLR camera was set to 1/4000 s to freeze the motion of the rotating workpiece in order to reduce motion blur in the workpiece images to a minimum. The images of the edge of workpiece were captured diametrically opposite the cutting side during machining as illustrated in Figure 3.11.

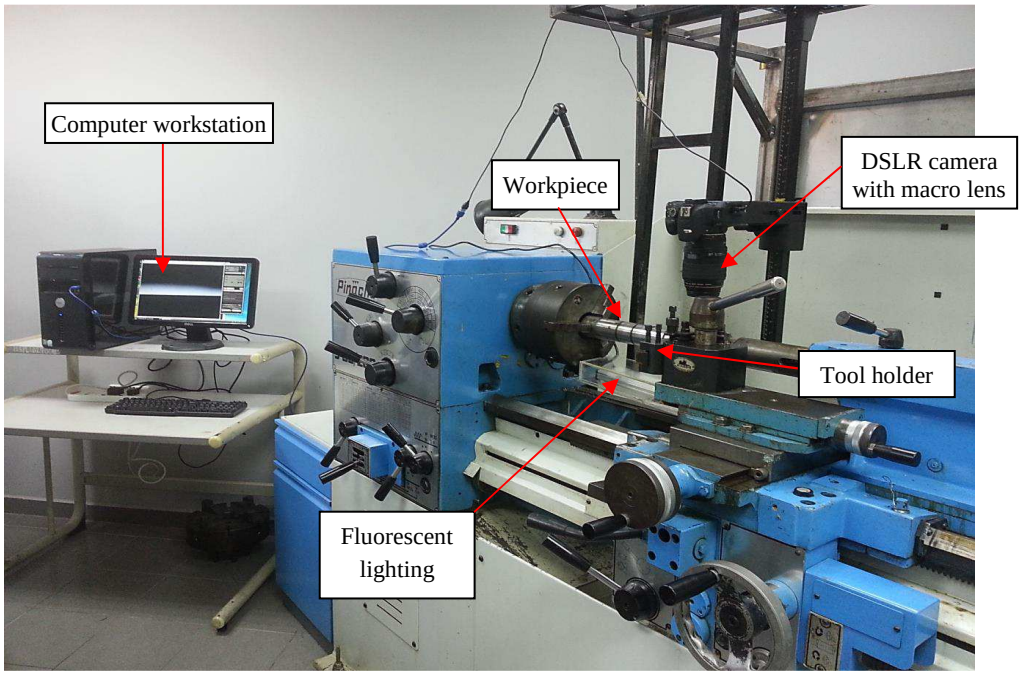

Figure 3.10: Experiment setup for in-process image acquisition during turning operation

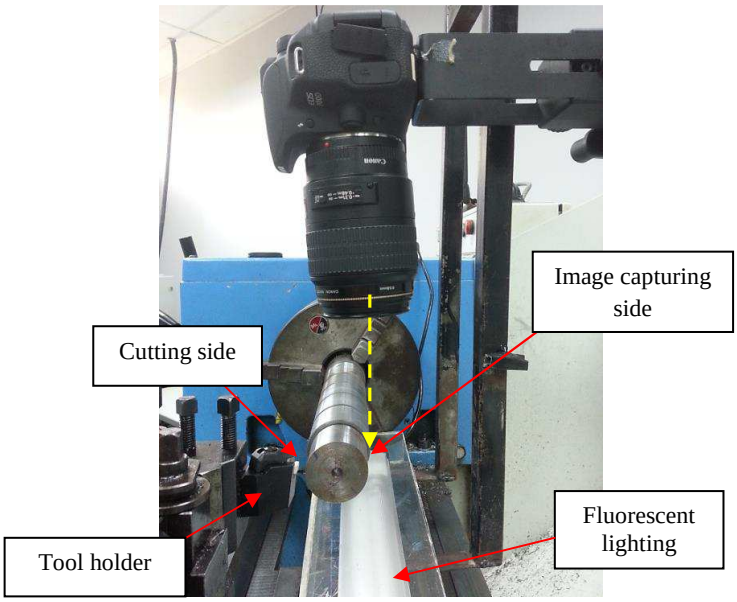

Figure 3.11: Close-up side view of the image acquisition configuration

The images of workpiece profile were captured after the cutting tool has turned the workpice, hence no chip obstruction problem occurred during image acquisition as the chips and cutting tool were beyond the field-of-view. All the images of workpiece were captured using the Canon EOS Utility remote capture software installed in the computer. For each pass of the tool a sequence of six images was capture automatically during each trigger. A sample image of the edge of the workpiece at 950 rpm is shown in Figure 3.12.

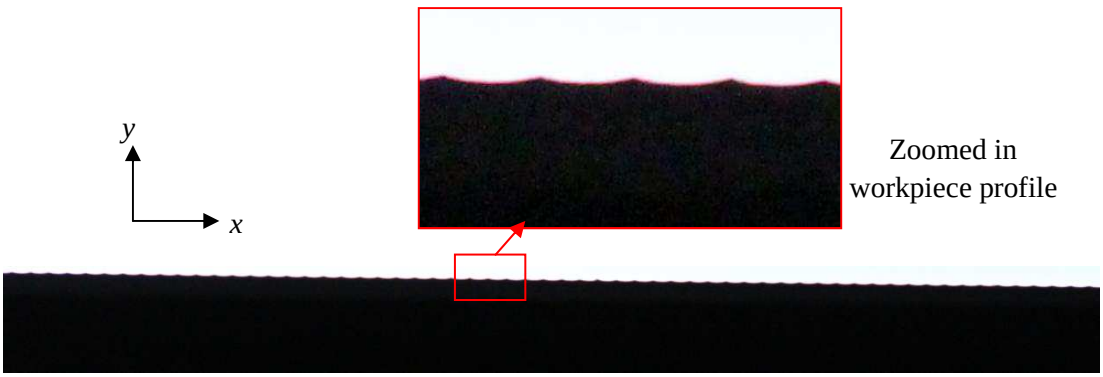

Figure 3.12: Image of the edge of the workpiece captured by DSLR camera

At a spindle speed of 950 rpm the workpiece rotation angle between successive images, β is approximately 60^o. The workpiece rotation angles between successive images was determined using Equation 3.8.

$$\beta = 360[n_R - \text{int}(n_R)] \tag{3.8}$$

where n_R is the number of rotations between the successive images of the workpiece profile and n_R is defined in Equation 3.9.

$$n_R = \frac{V \times S}{60} \tag{3.9}$$

where V is the spindle rotational speed in rpm (rotation per minute) and S (S = 0.2 s) is the capturing time between the successive images (known as frames per second).

As seen in Figure 3.13, when the first edge of the workpiece profile is captured at point Q, the workpiece continues to rotate and the location of P reaches point Q at a rotational angle of β for the next frame.

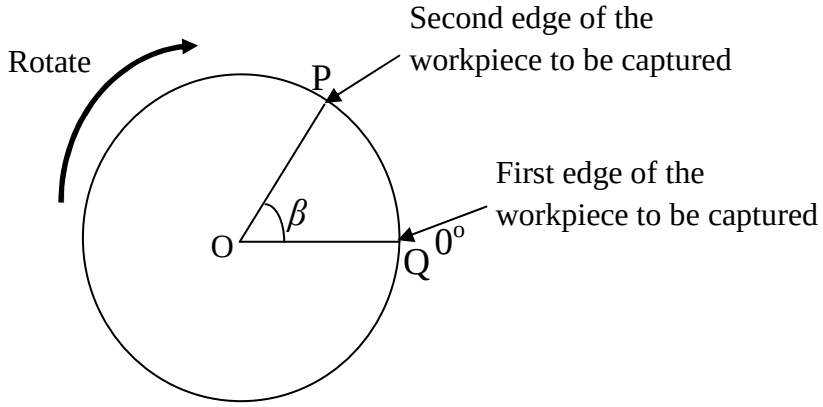

Figure 3.13: Workpiece rotation angle determination

After completion of the image acquisition and analysis of the profile the cutting tool tip was observed under a SEM (Hitachi TM1000) after each pass in order to correlate the condition of cutting tool with the behaviour of each analysis. *Alicona Infinite Focus* (Alicona GmBH Ltd., Austria) was used to obtain 3-D surface of the cutting edge which allows a good visualization of chipping on cutting edge region. The experiment was repeated in order to verify the results to increase the reliability of the proposed method.

3.2.5 Scaling factor determination

The horizontal (*x*-direction) and vertical (*y*-direction) scaling factors for converting the image coordinates in pixels to real world coordinates in metric units were determined using standard *Mitutoyo* pin gages of known diameters, i.e. 0.25 mm, 0.725 mm and 0.895 mm. The pin gage was positioned at the same level as the axis of the workpiece so that the scaling factors can be determined at a position that corresponds to the location of the workpiece edge. The pin gage was positioned horizontally and vertically relative to workpiece in order to determine the corresponding scaling factor in vertical and horizontal direction respectively.

Figure 3.14(a) shows the example of image of pin gage which captured vertically relative to workpiece. The cropped out image of the region of interest (ROI) is shown in Figure 3.14(b). The ROI of pin gage was cropped from the centre of pin gage (e.g. 250 pixels×250 pixels) and the scaling factor is a pre-determined value and is applied in *MATLAB* once for all analysis. The cropped pin gage was binarized to separate the pin gage from the background using Otsu's thresholding method (Otsu, 1979). Firstly, the images of the pin gage was converted from the original

RGB image into digitized gray-scale using command '*rgb2gray*'. After that, the *graythresh* based on Otsu's methods was applied to compute a threshold value to convert the gray-scale image to a binary image using command '*im2bw'*. The Otsu's method is the default thresholding method available in *MATLAB*. Binarization changes the original 8-bit gray scale image into a 2-bit binary image. The binary image of the pin gage is comprised of white pixels (bit value 1) for the background and the black pixels (bit value 0) for the pin gage. This work focuses on tool chipping detection rather than measurement, thus scaling factor determination in pixel level using Otsu's thresholding method was sufficient. The number of pixels occupied by the standard pin gage (e.g. between point *a* and *b*) was calculated and the scaling factor for converting from pixels to micrometers was determined by:

$$Scaling\ factor = \frac{Diameter\ of\ pin\ gage}{Number\ of\ pixels\ occupied\ by\ diameter\ of\ pin\ gage} \tag{3.10}$$

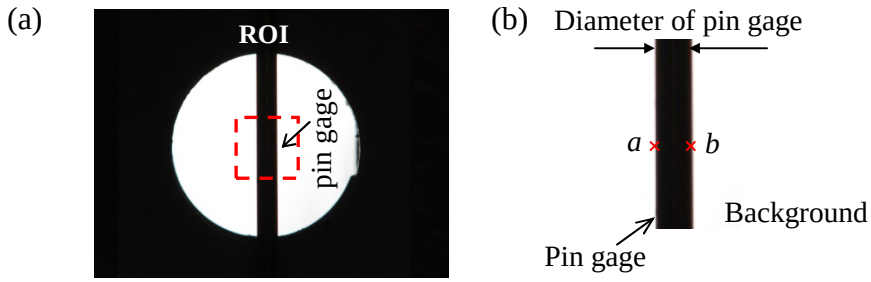

Figure 3.14: (a) Image of pin gage captured vertically, and (b) binarization of cropped ROI to determine the scaling factor

Once the scaling factor in *x*-direction and *y*-direction were defined, the field-of-view can be determined by multiplying the number of pixels of the image in horizontal and vertical direction with the *x*-direction and *y*-direction scaling factor respectively.

3.2.6 Distortion assessment

When the camera was fitted with a closed-up lens, it may introduce some errors in the measurement due to the effect of distortion in the images. The distortion in the images was assessed by using Ronchi ruling (200 lines/4 inches, *Edmund Optics Pte. Ltd.*). The Ronchi ruling was located in the same level of the edge of workpiece and the image of the ruling was captured vertically and horizontally.

The image of the Ronchi ruling in RGB format was binarized to separate the strips from background using Otsu's thresholding method. The binary image of the Ronchi ruling is comprised of the black pixels (bit value 0) for the strips and white pixels (bit value 1) for the background. After that, the distortion of the images was assessed directly from the image by determining the distances between the points as shown in Figure 3.15.

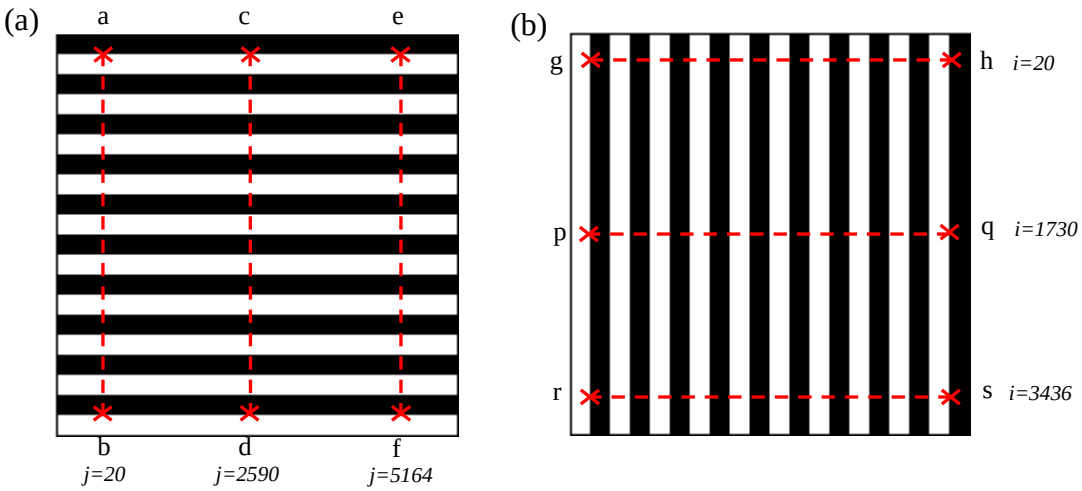

Figure 3.15: Images of Ronchi ruling (a) vertical, and (b) horizontal

The number of pixels between measurement points is tabulated in the Table 3.1. It was found that the maximum deviation in vertical direction and horizontal direction were 5 pixels (0.15%) and 3 pixels (0.06%) respectively. Since the deviation is small, this assures that the image distortion is negligible.

Table 3.1: Number of pixels between measurement points

Points	Number of pixels between the points
a-b	3313
c-d	3308
e-f	3313
g-h	5031
p-q	5028
r-s	5031

3.2.7 Description of workpiece profile detection algorithm in sub-pixel level accuracy edge detection using invariant moment method

The workpiece profile extraction process is the most important step because it determines the accuracy of the subsequent output. Numerous edge detection methods have been developed in the past and generally can be divided into pixel or sub-pixel level method. In order to improve the accuracy of the edge detection, sub-pixel level techniques can be applied to solve the problem of edge detection precision. In this study, an algorithm was developed to extract the workpiece profile with sub-pixel accuracy as illustrated in Figure 3.16 .

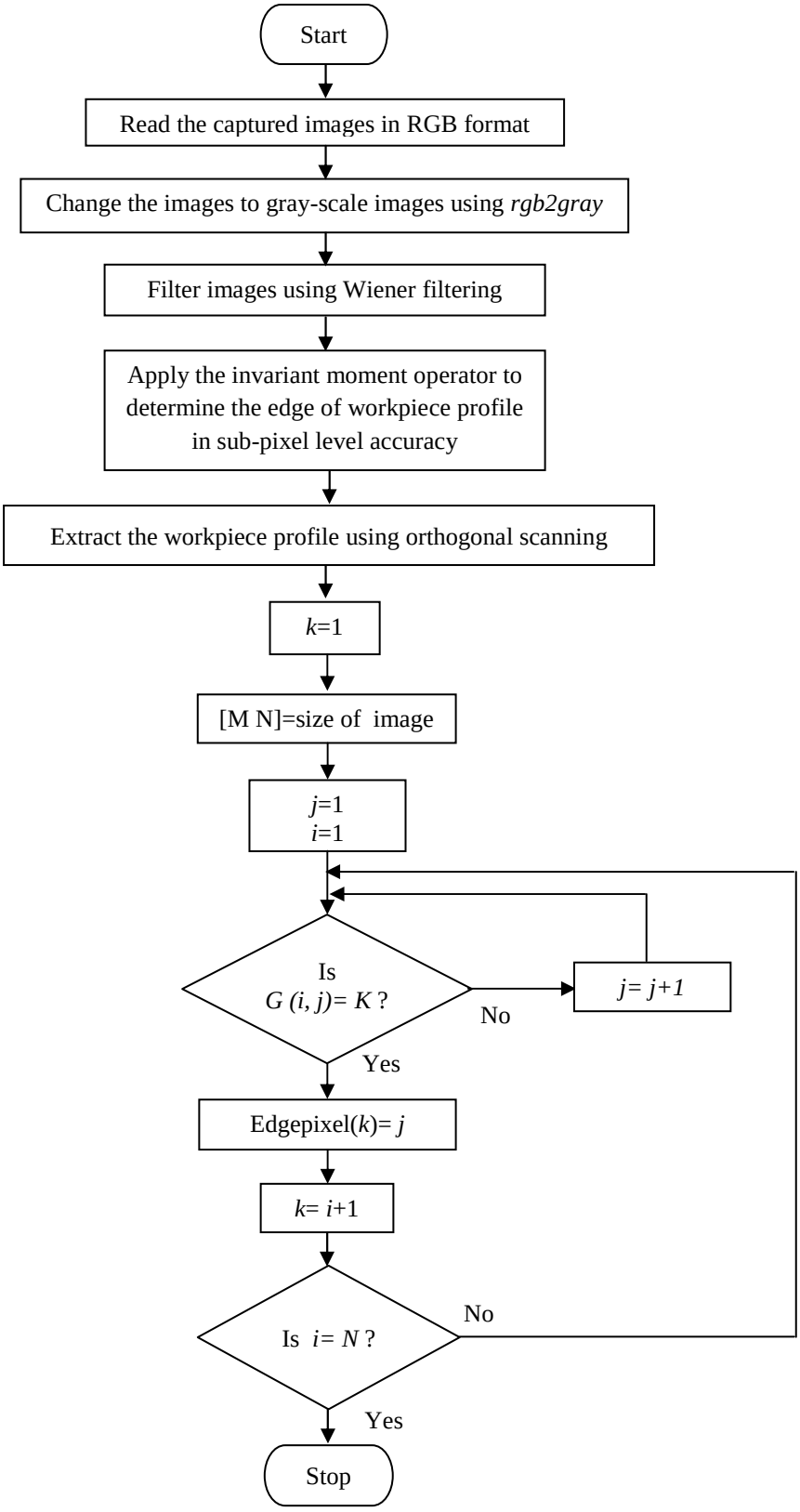

Figure 3.16: Flow chart of algorithm for surface profile detection

Firstly, the captured image was read as a RGB image and was converted to gray-scale using *MATLAB* command '*rgb2gray'*. The workpiece profile in gray-scale is composed of pixel intensity values that range from 0 (black) to 255 (white) bits. The image was then pre-processed to remove noise by using Wiener filtering. Wiener filtering was applied to enhance the image because it allows one to keep the details of the image and remove the effect of the noise in the image.

In the next step, the invariant moment method proposed by Tabatabai and Mitchell (1984) was applied to locate the edge of workpiece profile to sub-pixel accuracy. In the invariant moment method a scan line across a step edge in the absence of noise is characterized by a set of pixel intensity x_z where z = 1, 2, 3 …, n, which are either monotonically non-decreasing or non-increasing. The edge is defined as a sequence of brightness h_1 followed by a sequence of brightness h_2 as illustrated in Figure 3.17, where K denotes the edge location of the workpiece and n is the number of input data. The first three moments $\overline{m}_1$, $\overline{m}_2$ and $\overline{m}_3$ of the input data sequence in the gray scale image were calculated using a threshold independent method based on invariant moment equation:

$$\overline{m_i} = \frac{1}{n}\sum_{z=1}^{n}(x_z)^i \qquad (3.11)$$

where i=1, 2, 3

n = total number of pixel in column i

x_z= intensity of the pixel in gray scale images

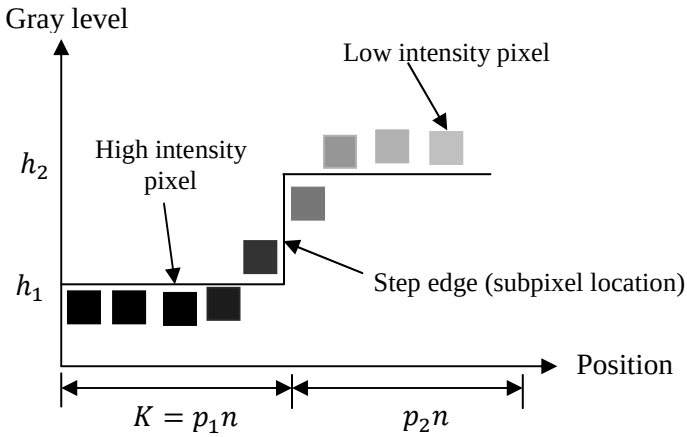

Figure 3.17: Invariant moment method

The first three moments between input data sequence can be solved by:

$$\overline{m_i} = \sum_{j=1}^{2} p_j h_j^i \tag{3.12}$$

The solutions of the edge are calculated by:

$$h_1 = \overline{m}_1 - \alpha\sqrt{\frac{p_2}{p_1}} \tag{3.13}$$

$$h_2 = \overline{m}_1 + \alpha\sqrt{\frac{p_1}{p_2}} \tag{3.14}$$

$$p_2 = \frac{1}{2}\left[1 + s\sqrt{\frac{1}{4+s^2}}\right] \tag{3.15}$$

where p_1 and p_2 are the densities of the gray level brightness value. s is equal to skewness of the input data sequence which is defined in the Equation 3.16.

$$s = \frac{2\overline{m}_1 + \overline{m}_3 - 3\overline{m}_1\overline{m}_2}{\alpha^3} \tag{3.16}$$

where α is sample variance given by:

$$\alpha = \sqrt{\overline{m}_2 - \overline{m}_1^2} \tag{3.17}$$

The densities of the gray level brightness value are related by:

$$p_1 = 1 - p_2 \tag{3.18}$$

Thus, the edge location of the workpiece up to sub-pixel accuracy is determined by:

$$K = p_1 n \tag{3.19}$$

In the next step, the contour of surface roughness profile was detected using orthogonal scanning as illustrated in Figure 3.18(a). The scanning starts from the first point of the first row to locate the sub-pixel profile of *K* value on the workpiece profile which is determined from Equation 3.19. The scanning continues to search the second column to find the second sub-pixel location. The interval along each pair of adjacent scan lines is one pixel apart. This process is repeated to detect all the sub-pixels that lie on the profile thus producing the contour of surface roughness. As seen in Figure 3.18(b), the application of the invariant moment method in sub-pixel edge detection allows more precise edge location.

After that, a best fit line (mean line) of the contour of the surface was determined using least squares fitting. Any tilt that appear in the workpiece profile is removed by subtracting each point on the detected profile from the mean line. Because the profile of the workpiece is in pixel units the roughness profile is converted from pixel unit to metric unit (micrometer) using the scaling factor which is obtained in Section 3.2.5.

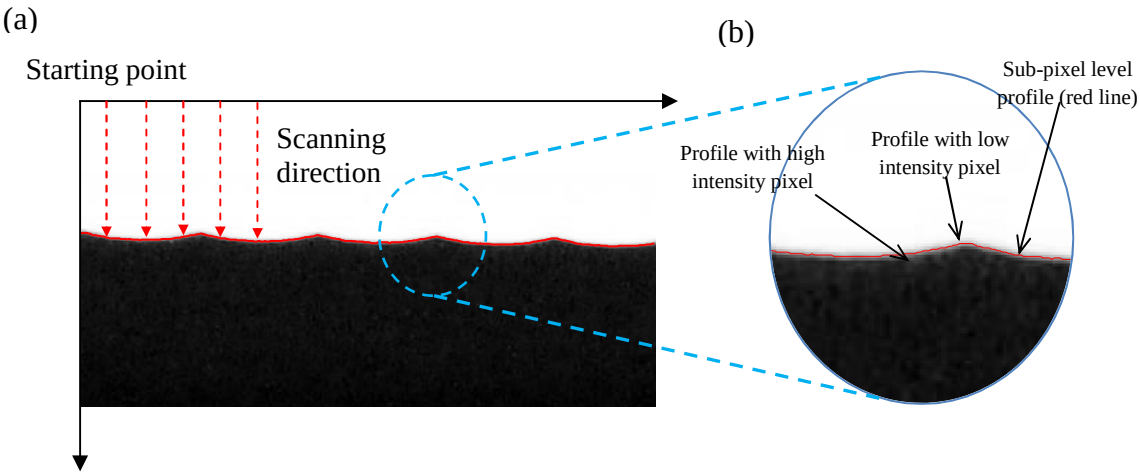

Figure 3.18: Workpiece profile extraction (a) orthogonal scanning, and (b) workpiece profile with sub-pixel edge location.

The surface profile shapes obtained from the abovementioned vision method is very similar when compared to the surface roughness profile measured from the mechanical stylus roughness tester (Mitutoyo SV3100) as shown in Figures 3.19. Three common roughness profile parameters: R_a (Equation 3.20), RMS roughness, R_q (Equation 3.7) and R_t (vertical distance between the highest peak to the lowest valley) were determined from surface profile data extracted from the images. The arithmetic average height of surface profile is given by:

$$R_a = \sum_{i=1}^{n} \frac{G(i)}{N} \quad \text{where } i=1,2,3, \ldots, N \tag{3.20}$$

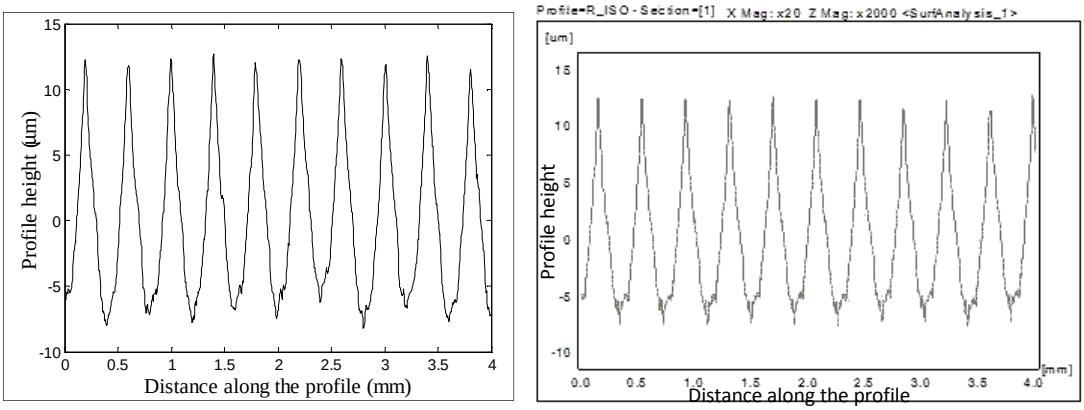

(a) (b)

Figure 3.19: Surface profile obtained from (a) vision method, and (b) stylus method.

Table 3.2 shows the results of surface roughness measurement (R_a, R_q and R_t) using the proposed machine vision method and the comparison with the surface roughness measurement obtained from mechanical stylus method. It can be found that, the comparison of the R_a, R_q and R_t roughness parameters shows an error of only 2.07%, 1.93% and 1.96%, respectively. An acceptable error range depends on the application (e.g. 5-10% error). An error with 0-5% exceptionally good. The comparison shows the error is small (less than 5%) and thus the proposed machine vision method is able to provide a reliable workpiece profile to be used for analysis.

Table 3.2: Validation of the roughness values (R_a, R_q and R_t) obtained from vision method by comparing the roughness values(R_a, R_q and R_t) obtained from stylus method

Roughness parameter (μm)	Stylus method				Vision method				Error (%)
	1	2	3	Average	1	2	3	Average	
R_a	4.99	4.95	5.06	5.00	4.86	4.85	4.98	4.90	2.07
R_q	5.67	5.63	5.72	5.67	5.53	5.51	5.66	5.56	1.93
R_t	21.50	20.89	19.77	20.72	20.25	21.12	22.05	21.14	1.96

3.2.8 Motion blurring effect assessment

Motion blurring can occur when capturing a rotating workpiece. The motion blurring effect can be eliminated by maximizing the shutter speed in order to keep the edge of workpiece profile sharp. The shutter speed of the DSLR camera was set to 1/4000 s to freeze the motion of the rotating workpiece in order to reduce motion blur in the workpiece images to a minimum. The surface profile detection in sub-pixel accuracy level algorithm presented in Section 3.2.7 was used to extract the workpiece profile. After that, the command '*findpeaks*' in *MATLAB* was applied to locate the peak between the wavelength of the workpiece profile. The motion blurring effect in the rotating image was determined by comparing the number of pixels between the wavelength of the workpiece profile under various spindle rotational speeds with the number of pixels between the wavelength of the static workpiece profile as illustrated in Figure 3.20.

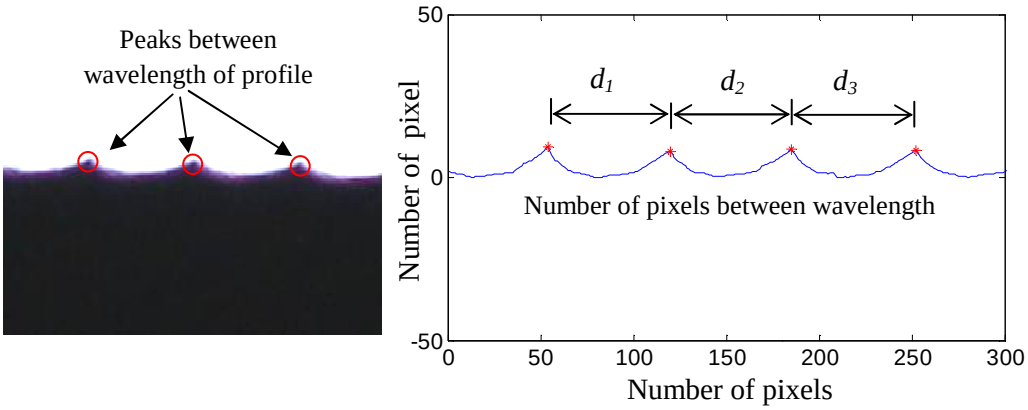

Figure 3.20: Motion blurring assessment by comparing the number of pixels between the wavelength of workpiece profile

The number of the pixels between the wavelength of the workpiece profile under various spindle rotational speed is tabulated in Table 3.3. The maximum

deviation of the number of pixels between the wavelength for the static and rotating images was found to be only 3.4%, thus the motion blurring effect could be neglected.

Table 3.3: Number of pixels between the wavelength

Rotational Speed	Number of pixels between the wavelength		
RPM	d_1	d_2	d_3
0	65	66	66
625	66	66	68
1150	66	66	67
1750	66	67	67

3.3 Detection of tool chipping in ceramic cutting insert from the workpiece profile signature using FFT

This section is divided into five sub-section. Section 3.3.1 explains the simulation work on tool chipping detection from the 2-D workpiece profile signature using FFT by considering the geometry changes of the tool nose due to wear and chipping while an offline experimental work used to validate the simulation work is presented in Section 3.3.2. Simulation work on detection of tool chipping based on workpiece profile by considering the presence of tool-workpiece vibration resulting from wear and chipping is outlined in the following section. In-process experiment setup to capture the images of the actual workpiece profile simultaneously with measurement of tool-workpiece vibration using accelerometer is presented in Section 3.3.4. In order to further assess the applicability of FFT method in onset tool

chipping detection, sub-window FFT method was proposed aims to resolve the time resolution of the FFT and the drawback of STFT is presented in Section 3.3.5.

3.3.1 Simulation work on detection of tool chipping from surface profile signature using FFT by considering the geometry changes of the tool nose

The surface profile of the turned workpiece is the imprint of the cutting tool nose profile replicated on the machined surface and each imprint is a periodic pattern separated by the feed distance *f* as a result of the feed motion as illustrated in Figure 3.21(a). Thus, the interaction between the cutting tool tip and the workpiece clearly shows that the tool nose region plays an important role in shaping the surface profile. If the cutting tool is used in finish turning, whereby the depth-of-cut is smaller than radius of cutting insert r_ε, the cutting process occurs in the nose radius of the cutting tool between points P to Q as shown in Figure 3.21(b).

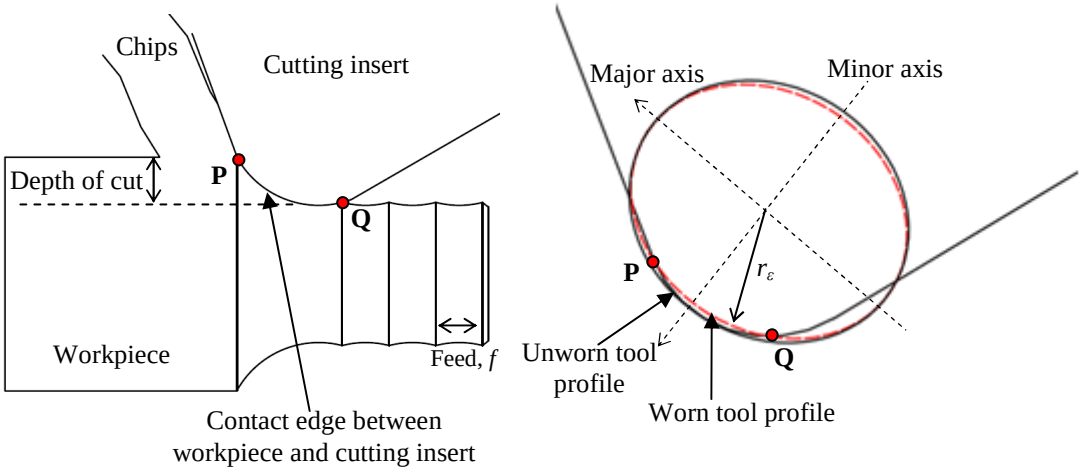

(a) (b)

Figure 3.21: (a) Schematic representation of interaction between the cutting tool tip and the formed surface, and (b) formation of tool wear by increasing the radius in minor axis.

Gradual wear occurs from the outer point P to the inner point Q due to the loss of material from the cutting tool tip caused by abrasion between the tool and the workpiece. Consequently, the radius r_ε increases. This gradual wear was simulated by generating an ellipse on the contact edge between cutting insert tip and workpiece. The gradual wear was approximated by increasing the radius of the minor axis of the ellipse as shown in Figure 3.21(b). Figure 3.22 shows examples of the gradual wear generated on the cutting tool by increasing the nose radius r_ε. The black shaded region indicate the loss of tool material due to the abrasion between the cutting tool and the workpiece during machining.

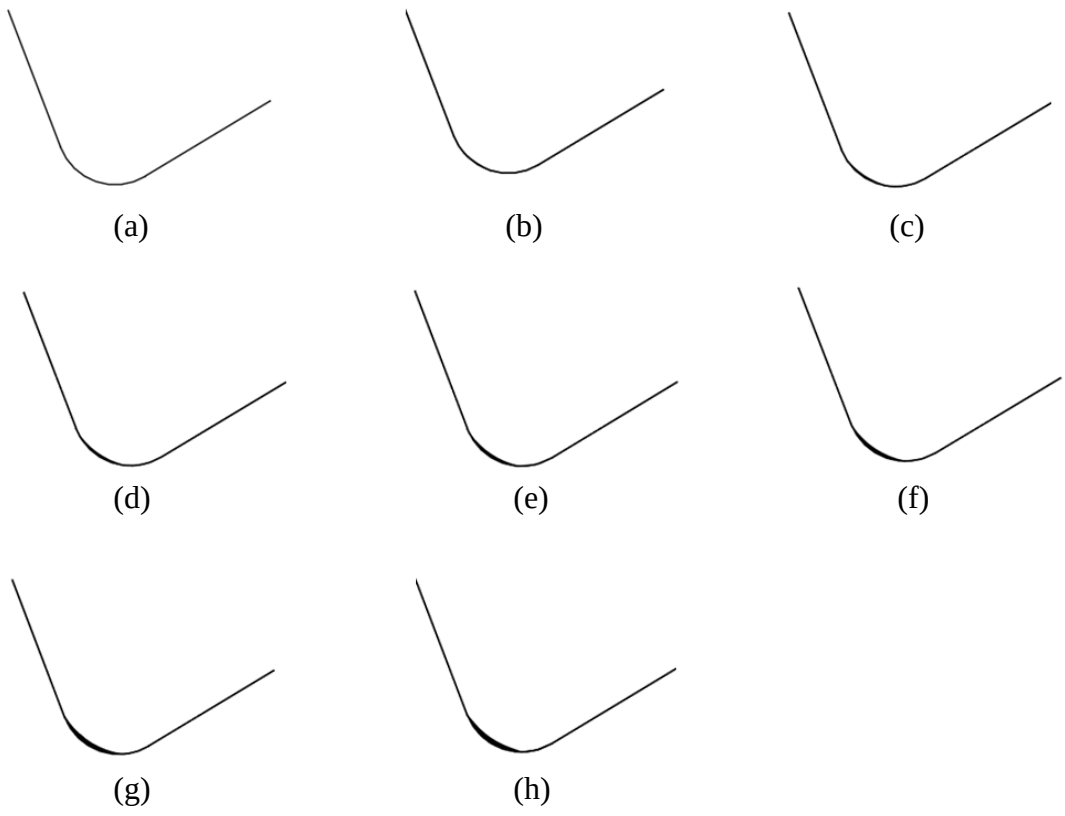

Figure 3.22: Simulated cutting tool (a) unworn, (b) gradual wear by increase 1% of r_ε in the minor axis, (c) gradual wear by increase 2% of r_ε in the minor axis, (d) gradual wear by increase 3% of r_ε in the minor axis, (e) gradual wear by increase 4% of r_ε in the minor axis, (f) gradual wear by increase 5% of r_ε in the minor axis, (g) gradual wear by increase 6% of r_ε in the minor axis, and (h) gradual wear by increase 7% of r_ε in the minor axis

Figure 3.23 shows the simulated workpiece profile corresponding to the simulated worn tool generated in Figure 3.22. The simulated worn cutting tools and their surface profiles were constructed using *AUTOCAD* (Version 2013). For the fresh cut shown in Figure 3.23(a) the turned surface profile similar to a very fine circular thread was observed. As the 'tool wear' increases it was observed that the peaks of the thread generated by the tool feed tend to become higher. This is because the steep groove on the tool nose due to the gradual wear leads to the sharp peaks on the workpiece profile signalled by the higher value of R_t which is illustrated in Figure 3.24. This behaviour is in agreement with the evolution of the tool wear and explains the significant increase of the maximum peak-to-valley height (R_t) of surface profile (Pavel et al., 2005; Nabil and Mabrouk, 2006).

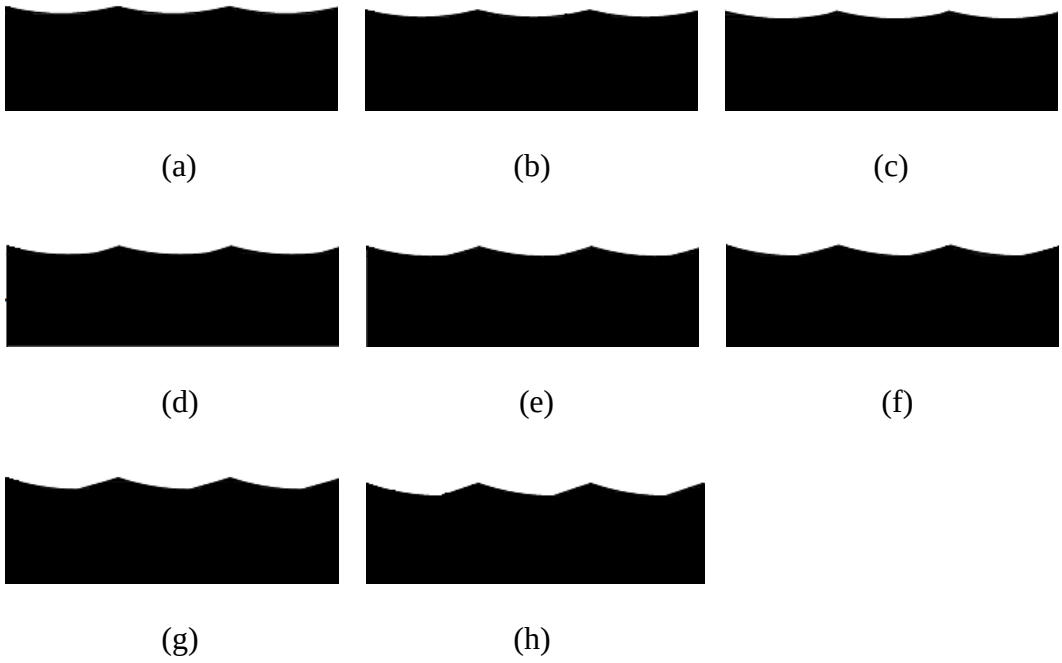

Figure 3.23: Simulated workpiece profile corresponding to the simulated worn tool in Figure 3.22

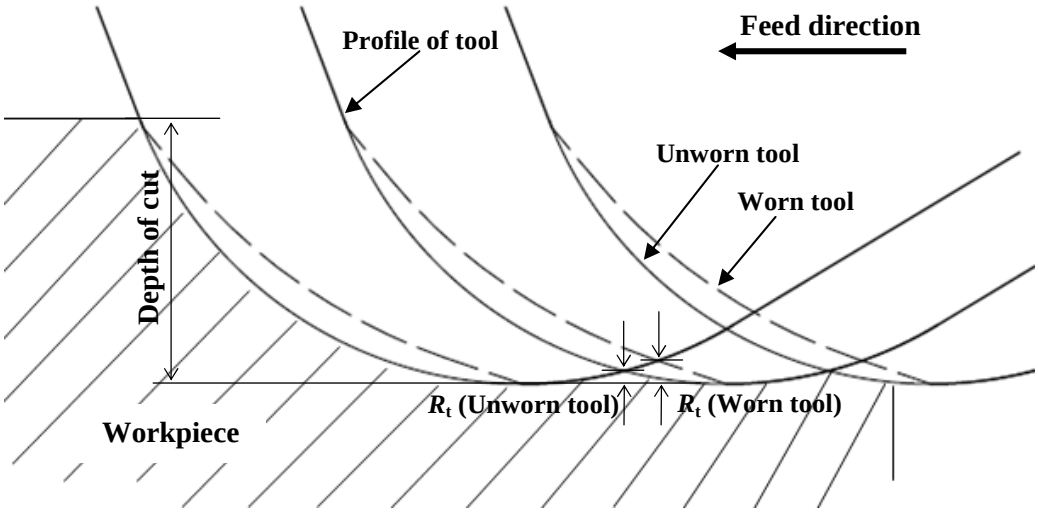

Figure 3.24: Tool nose area showing the maximum peak-to-valley height R_t of workpiece profile generated from worn and unworn tool profile.

Chipping of cutting inserts was simulated by generating a cavity or depression on the cutting tool tip. Figure 3.25 demonstrates the generation of the chipping on the tool nose region. The tool nose has a radius r_ε between the points *P* and *Q*, which lie at the ends of the major cutting edge. The simulation of chipping was carried out by forming an irregularly shaped cavity manually and randomly on the nose region cutting tool and the chipping is demonstrated by removing a cavity or depression (chipped area of A mm^2) from the sector subtending an angle θ at the center. The successive simulated worn tools by chipping were obtained by enlarging the chipped area of A mm^2. Figure 3.26 shows the simulated chipped tool where the chipping occurred at the early stage of cutting operation. The size of chipping is enlarged for the successive chipped tool from Figure 3.26(a) to Figure 3.26(h). The corresponding simulated workpiece profile is shown in Figure 3.27.

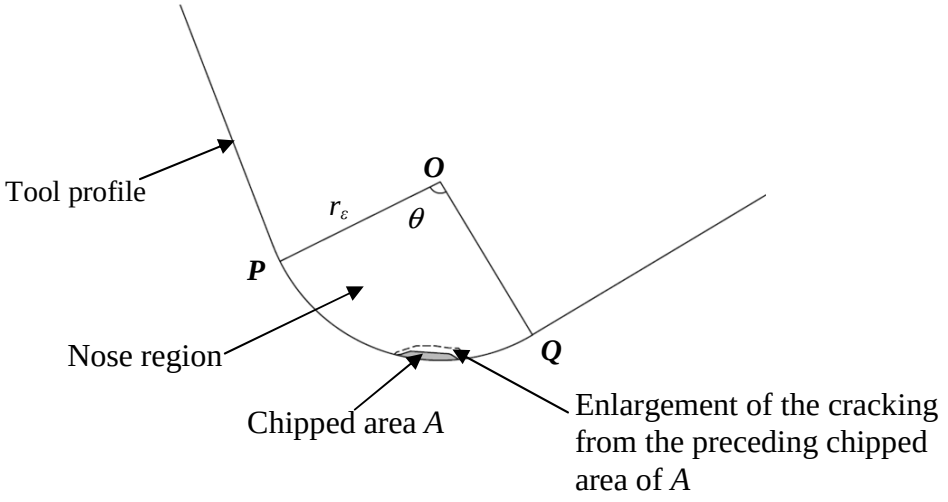

Figure 3.25: Formation of chipping by removing a cavity from tool nose region.

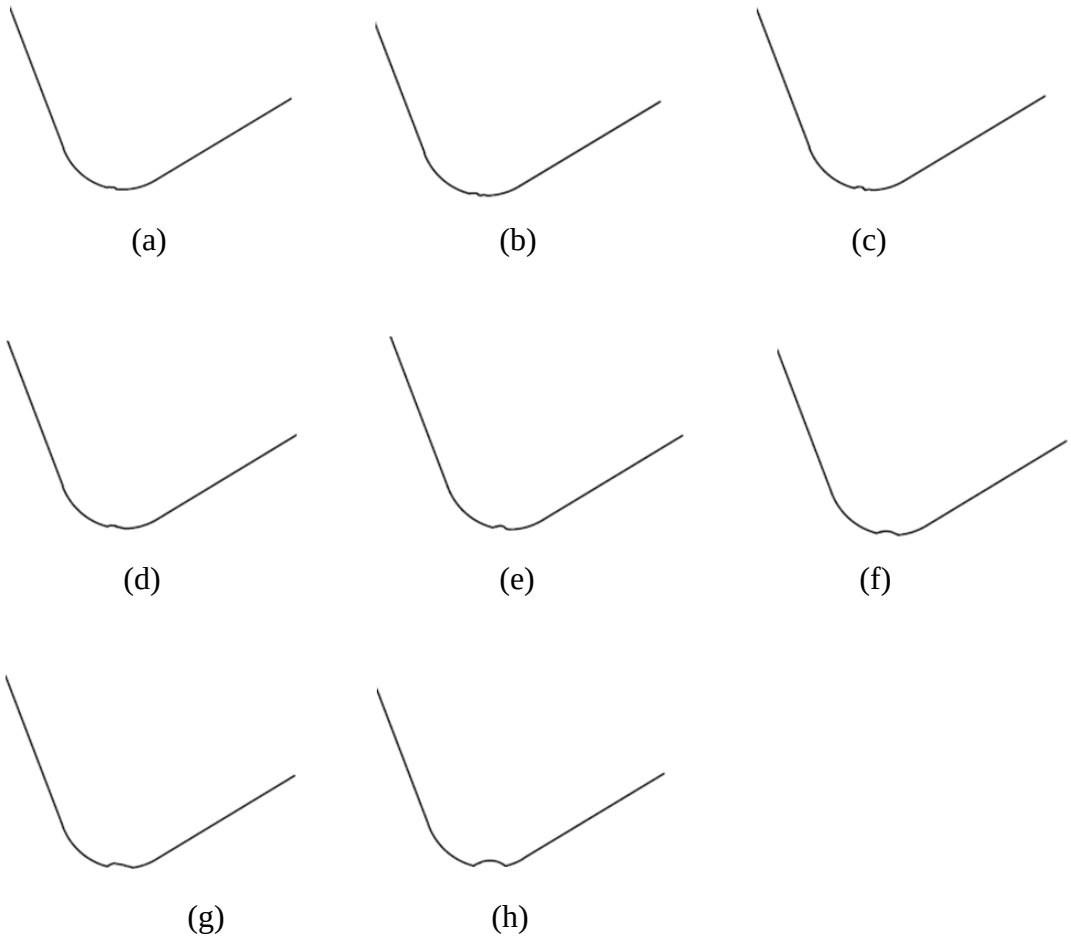

Figure 3.26: Simulated worn tool for chipping

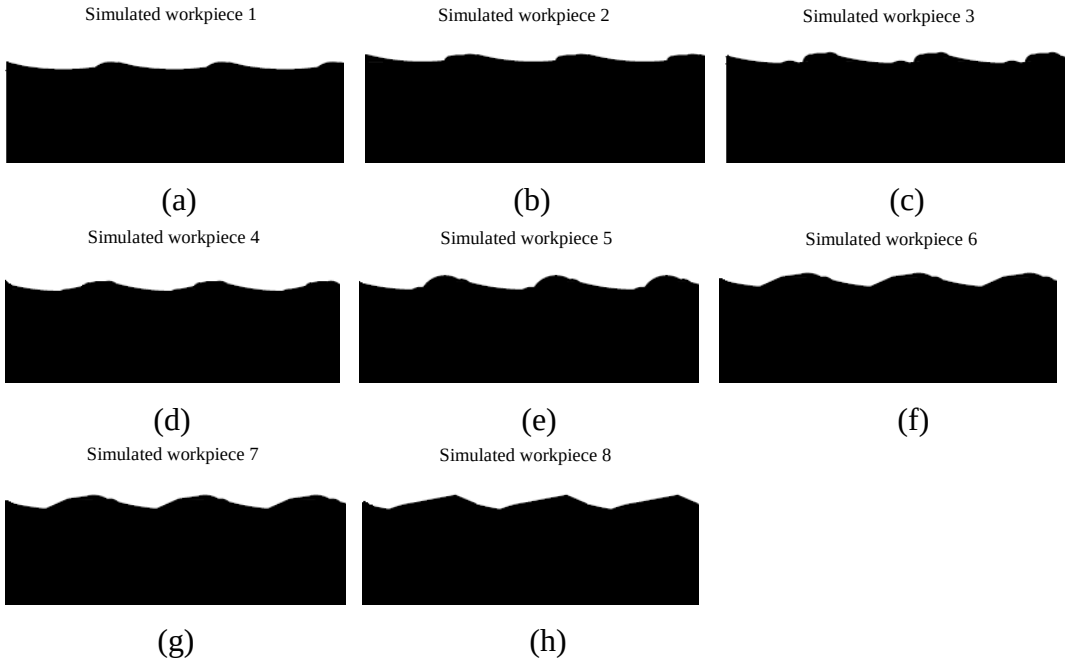

Figure 3.27: Simulated workpiece profile corresponding to the simulated chipped tool in Figure 3.26

Figure 3.28 shows examples of replicated simulated worn tools by wear (Figure 3.28(a)-(c)) and chipping (Figure 3.28(d)-(h)) which demonstrated the evolution of the simulated worn tool from gradual wear to chipping and their corresponding workpiece profiles are presented in Figure 3.29. To produce the corresponding simulated workpiece profile resulted from gradual wear and chipping (Figure 3.23, Figure 3.27 and Figure 3.29), the procedure of Stage 2 to Stage 6 shown in Figure 3.2 were repeated. The simulated workpiece profiles were generated by replicating the nose profile of simulated worn cutting tool by a feed distance of 0.4 mm for a length of 4 mm. The simulated workpiece profiles created by *AUTOCAD* were exported to JPEG format and converted from RGB to gray-scale in *MATLAB*. The simulated workpiece profile in gray-scale image was detected when the intensity values changes from 255 to 0 using vertical scanning algorithm written in *MATLAB*. The algorithm start scanning from the first pixel of the first column. If

the first pixel value is 0 the scanning begins at the second column. This operation is repeated for all the columns to detect the contour of the surface profile.

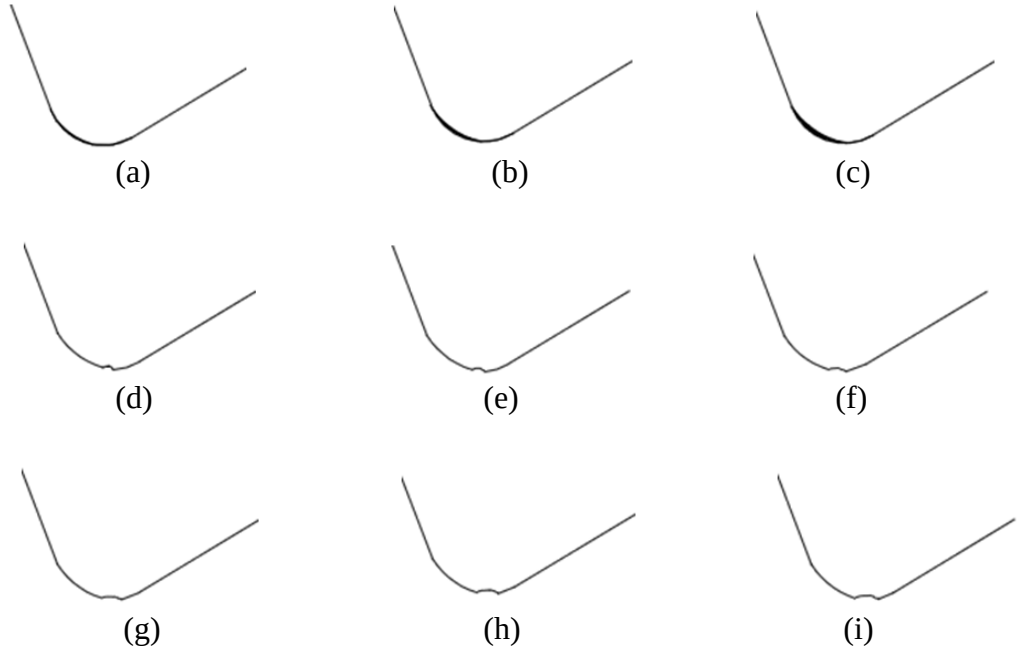

Figure 3.28: Simulated worn tool from evolution of gradual wear to chipped tool

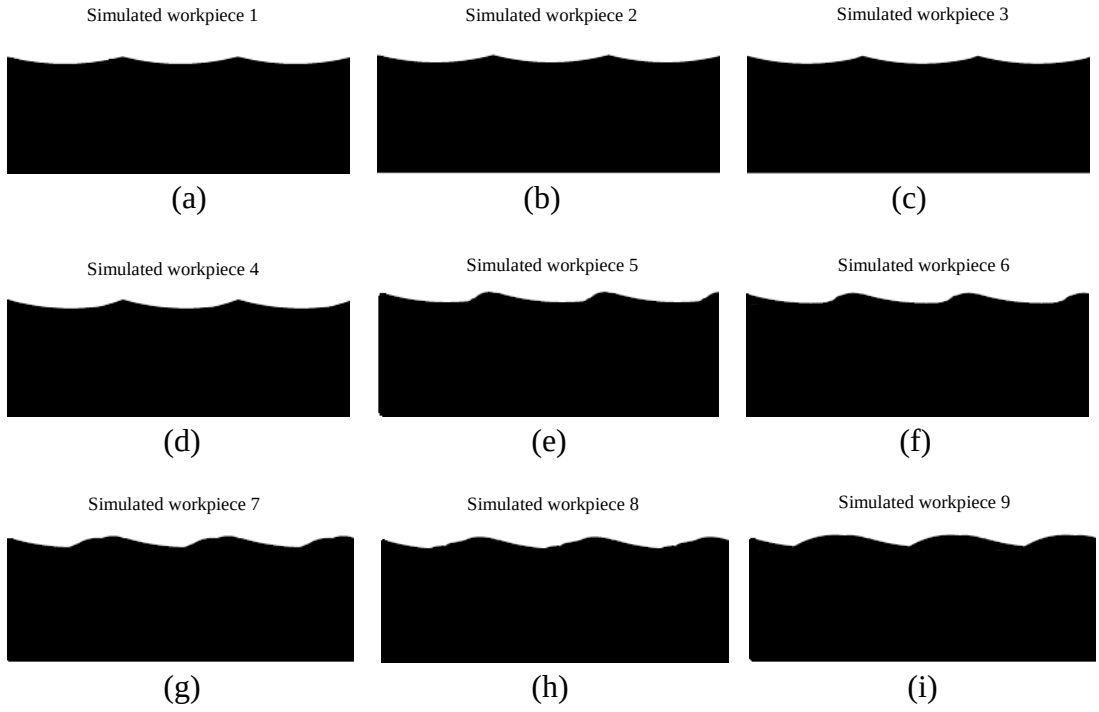

Figure 3.29: Simulated workpiece profile corresponding to the simulated worn tool in Figure 3.28

The extracted simulated workpiece profile was expressed as a function of position along the simulated workpiece distance. By vertical scanning along the column (x-coordinate), the y-coordinate of the surface profile $G(x)$ was obtained by extracting the y-coordinate of the pixel that has 0 value in each column. The x-coordinate of surface profile $G(x)$ correspond to the scanned column. The simulated workpiece profile in the spatial domain was then converted into the frequency domain using FFT. Since the surface profile of the turned part is essentially periodic it can be expressed as a Fourier series given by:

$$G(x) = \sum_{n=1}^{N} \left[a_n \cos(\omega n x) + b_n \sin(\omega n x) \right] \tag{3.21}$$

where $G(x)$ is the workpiece profile height as a function of distance x, n is an integer, ω is the angular frequency, a_n and b_n are the coefficients of the cosine and sine terms respectively. Thus , a finite Fourier transform can be written as:

$$Y(\omega) = \int_{0}^{L} G(x) \exp(-j\omega x) dx \tag{3.22}$$

The resulting transformed workpiece profile gives an expression of the frequency components that contribute to the workpiece profile when a spectrum plot of amplitude versus frequency is constructed. The amplitude of $Y(\omega)$ is the magnitude of the complex number in the frequency domain and is represented by the vertical axis. The workpiece profile was extracted at discrete points over a finite length interval, L. For data taken at discrete points over a finite length interval the spectrum amplitude of the roughness profile is determined by the discrete Fourier

transform (DFT). The amplitude of the spectrum of workpiece profile $Y(V_n)$ at spatial frequency of V_n is given by (Wheeler and Ganji, 2010):

$$Y(V_n) = \left| \sum_{n=0}^{N-1} G(x_n) e^{\left(\frac{-2\pi j n}{L} x_n \right)} \right| \qquad n = 0, 1, 2, 3, \ldots, N\text{-}1 \tag{3.23}$$

where j is a complex number defined by $j = \sqrt{-1}$ and V_n represents a discrete spatial frequency of the workpiece profile which expresses the number of roughness wavelengths within a unit of length x_n. V_n is given by:

$$V_n = \frac{1}{x_n} = \frac{n}{L} \tag{3.24}$$

The workpiece profile extracted from the 2-D image of workpiece was read as RGB image when it was imported to *MATLAB* and was converted into digitized gray-scale image in spatial coordinates of x and y. Thus, the workpiece profile data set consists of N values of $G(x)$ measured at equal intervals of Δx within a total length of workpiece profile, L, i.e.:

$$N = \frac{L}{\Delta x} = \frac{L}{x_{n+1} - x_n} \tag{3.25}$$

The fundamental feed frequency V_f (mm^{-1}) represented in the spectrum analysis is determined by $\frac{1}{f}$ (Equation 3.3).

The discrete surface profile data extracted from vertical scanning was loaded into *MATLAB*. The FFT algorithm in the *MATLAB* was used to compute the DFT of the surface profile $G(x)$. *MATLAB* uses the *fft* command to determine the amplitude of each spatial frequency components of a discrete workpiece profile. The effects of tool wear and chipping on the amplitude of fundamental feed frequency and its harmonic was investigated.

3.3.2 Offline experimental work

Preliminary study on tool chipping detection was carried out offline whereby the workpiece was removed from the turning machine for image acquisition. The image of the edge of workpiece was captured offline after machining. Figure 3.30 shows the offline image acquisition configuration. The DSLR camera was positioned overhead to capture the edge profile clearly with the aid of the backlighting system. The camera was mounted on a linear translation stage and tracks in order to move the camera along the workpiece to capture the images continuously.

Machining experiments were carried on 50 mm diameter SUS304 stainless steel workpiece of length 255 mm. An in-house fabricated cutting inserts made from zirconia-toughened alumina (ZTA) + magnesium oxide (MgO) was used to turn the workpiece. The ceramic inserts consists of 79.2 wt. % aluminium oxide, 19.7 wt. % yttria stabilized zirconia and 1.1 wt. % of magnesium oxide (Azhar et al., 2010). A commercially available carbide tool (TNMG 160404 MF – Sandvik Ltd.) was used because carbide insert has better fracture toughness than ceramic to prevent chipping which could be used for studying the effect of gradual wear on the amplitude of fundamental feed frequency and its harmonics in a separate experiment. Stainless

steel was used instead of tool steel because carbide insert was not suitable for cutting tool steel as tool steel is harder compare to SUS304 stainless steel (Tsao, 2002). The machining was conducted using a *Pinocho S90* conventional lathe machine under dry cutting. Spindle rotational speed of 625 rpm, feed rate of 0.4 mm/rev and 0.5 mm depth of cut were used in the machining experiments. Observation on the cutting tool tips were carried out by means of a SEM (*Hitachi TM1000*).

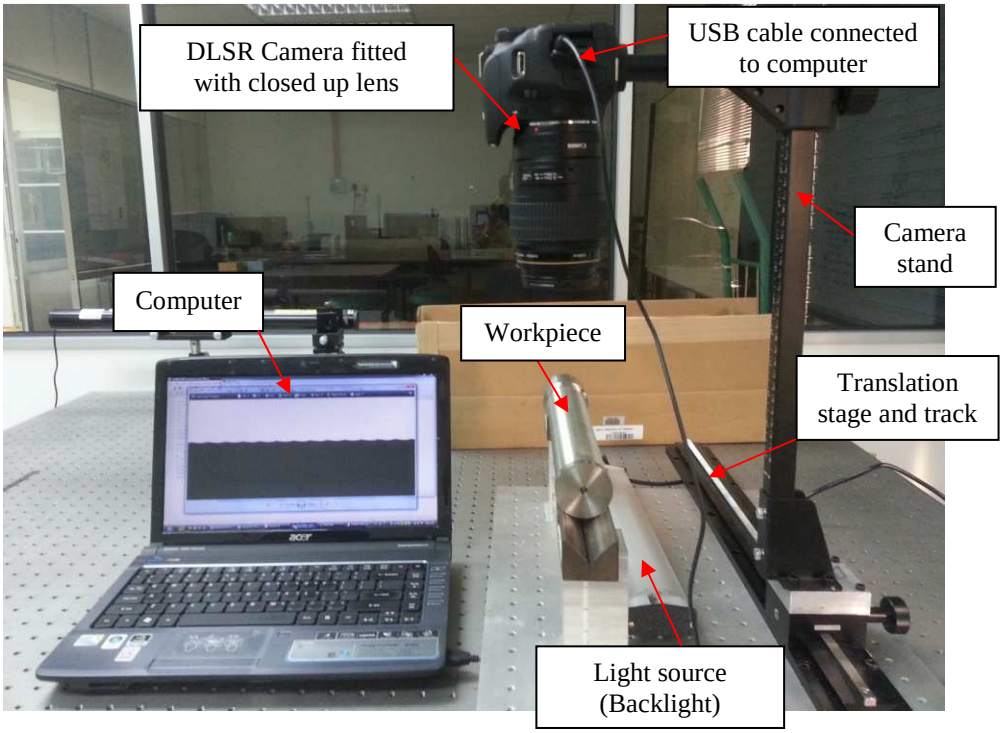

Figure 3.30: Offline image acquisition configuration.

3.3.3 Simulation work on detection of tool chipping from surface profile signature using FFT by considering the presence of tool-workpiece vibration

The generation of the simulated workpiece profile in Section 3.3.1 only considered the effects of tool nose geometry changes due to tool wear and chipping on the amplitude of fundamental feed frequency and its harmonic. Tool-workpiece

vibration was not taken into consideration. However, in fact various factors affect the surface profile of turned workpiece. The dominant factors are the tool geometry, feed rate and chatter vibration. Thus, investigation on detection of tool chipping from the simulated surface profile in the presence of the tool-workpiece vibration results from wear and chipping using FFT was carried out. The simulated workpiece profile generated in Section 3.2.1 was applied in this simulation. In Section 3.3.1, only the amplitude of fundamental feed frequency and its harmonics were used to correlate to the cutting tool condition while other spatial frequencies were excluded. Thus, an in-process investigation on tool chipping detection from the distribution of the spatial frequencies along the workpiece profile signature was carried out.

3.3.4 In-process experimental work

The experimental setup (image acquisition system configuration during turning operation) was same in the Section 3.2.2 but with the addition of tool-workpiece vibration measurement. Accelerometer sensors (*Dytran 3055B2T*) were mounted on the cutting tool holder in the axial, radial and tangential direction as shown in Figure 3.31 in order to measure the tool-workpiece vibration during turning operation. The main interest of the study is not on the vibration signal. The purpose of the tool-workpiece vibration measurement is to observe the effect of tool chipping on the vibration signal between the tool and the workpiece as well as how does the tool-workpiece vibration affects the surface profile.

A turning machine (*Pinocho S90*) was used to perform finish turning experiments on AISI 01 Arne oil hardening tool steel using aluminium oxide based ceramic cutting insert with added zirconia (CNGA120408T02520 CC620, Sandvik

Coromant Ltd., Sweden). The cutting condition including the spindle rotational speed, feed rate and depth of cut were set as 950 rpm, 0.4 mm/rev and 0.8 mm, respectively. To obtain the actual surface profile from the images of turned workpiece in both offline and in-process experiments, steps in Section 3.2.5 and Section 3.2.7 were repeated before applying FFT analysis as summarized in the Figure 3.32.

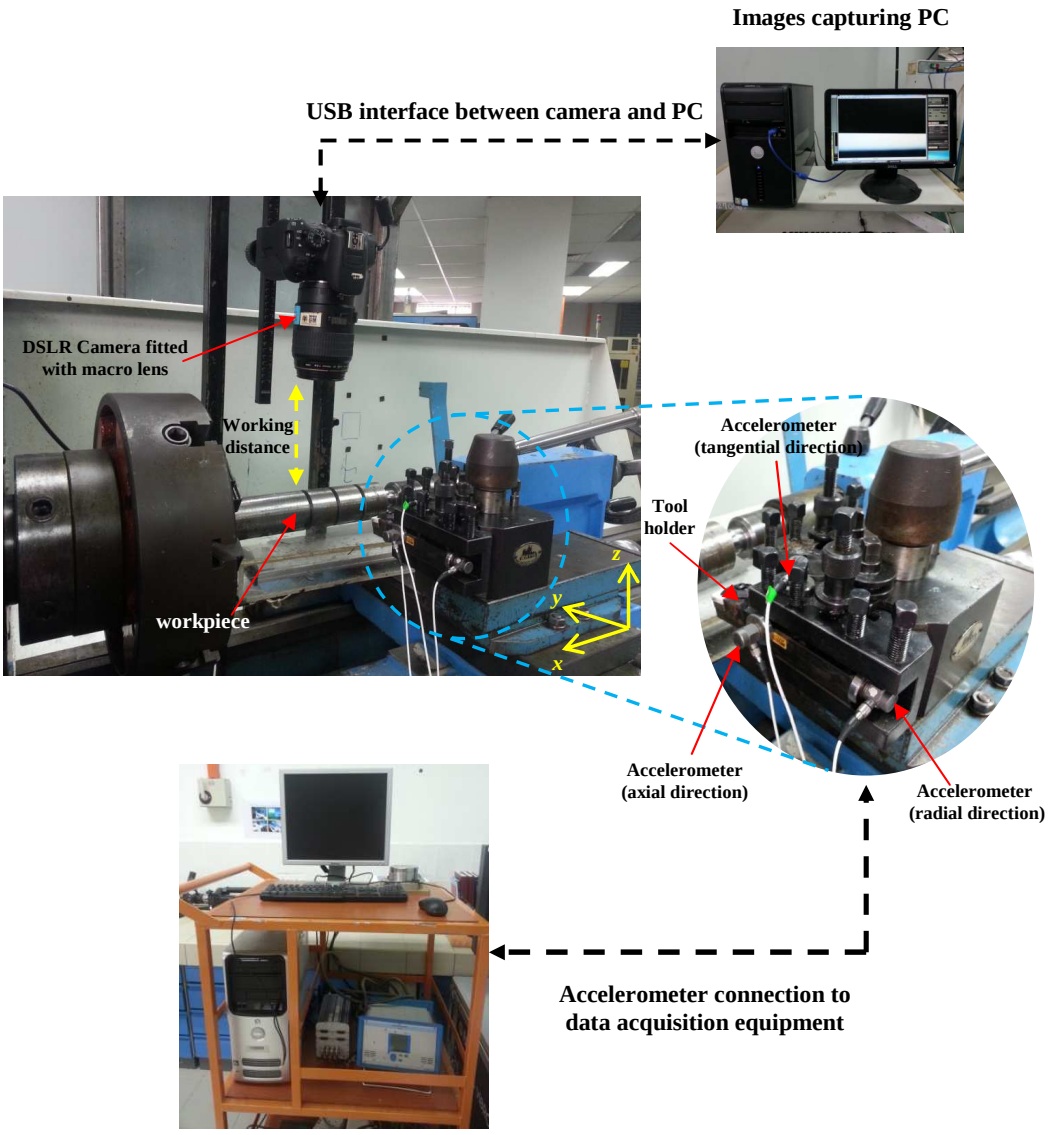

Figure 3.31: In-process experiment setup with vibration measurement

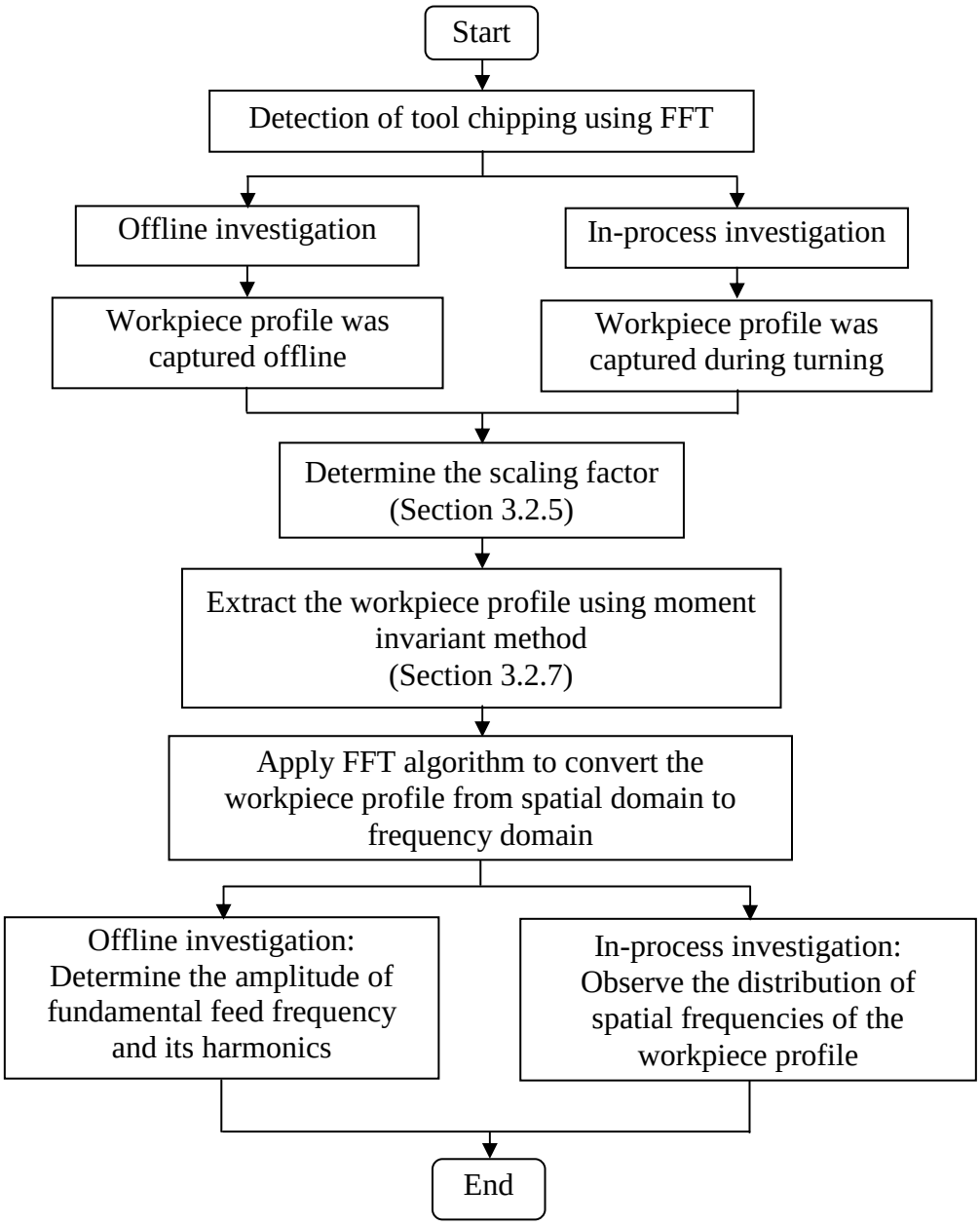

Figure 3.32: Flow chart for FFT analysis of actual workpiece profile for offline and in-process tool chipping detection in ceramic cutting tool

Results obtained from Section 3.2.2 was used as a control experiment with the following cutting condition: rotational speed 950 rpm, feed rate 0.4 mm/rev and depth-of-cut 0.5 mm. The purpose of the control experiment is to validate the reliability of the proposed method on the detection of tool chipping in ceramic cutting insert when one of the cutting condition was changed. The cutting parameter

was not our main concern in the study. The study focus on the tool chipping detection method during turning and the developed tool chipping detection method could be applied no matter what cutting parameters used in machining.

3.3.5 In-process detection of tool chipping from surface profile signature using sub-window FFT

The major drawback of STFT is that analysis result is highly dependent on window function. The attenuation effect in the window function cause a loss in spectral estimate. Therefore, in this study, a novel sub-window FFT method that independent of window function is proposed. Similar to STFT, sub-window FFT uses small time-shifted window to approximate the time-frequency information, providing bands of frequencies over time increments. The procedure for computing the sub-window FFT of a workpiece profile waveform is to divide a longer workpiece profile waveform into shorter segments equal to the evaluation length of 4.0 mm according to ASME B46.1 (2009) standard and then to compute the FFT of the workpiece profile separately on each shorter segment. The time resolution of sub-window FFT was determined by:

$$\text{Sub-window time resolution} = \frac{w}{fV} \tag{3.26}$$

where w is the length of the window, f is feed rate and V is spindle rotational speed.

Statistical features from the sub-window FFT of workpiece profile was extracted. Only amplitude of spatial frequency in a particular spatial frequency component provide information pertaining to failure of cutting tool. Average of

amplitude spectrum in a specific spatial frequency band, γ which is defined as (Binsaeid et al., 2009):

$$\gamma = \frac{1}{n}\int_{F_2}^{F_2} Y(V_n) \tag{3.27}$$

where $Y(V_n)$ is spectrum amplitude at a specific spatial frequency components and F_1, F_2 is the frequency range.

3.4 In-process detection of tool chipping from workpiece profile signature using CWT

The actual workpiece profile obtained from experiment in Section 3.3 was further analysed using CWT. This is because one drawback of FFT is that it is not possible to simultaneously examine time (or spatial) and frequency. That is, the analysed surface profile can only be observed over time (or spatial), or over frequency. Sub-window FFT was proposed to solve the time resolution problem. However, the determination of window size is difficult and the time domain resolution is highly dependent on the size of the window and machining parameters. For this reason, wavelet transform was applied in this work.

CWT allows for analyzing and displaying the characteristics of signal waveform that are dependent on time and scale. Therefore, CWT is potentially a useful tool to detect the workpiece waveform with exotic spectral contents and transient information content due to tool failure. Furthermore, FFT is more appropriate to be applied to stationary signals whereas CWT allows the components of a non-stationary waveform to be analyzed.

Figure 3.33 shows the flow chart for CWT algorithm written in *MATLAB* applied in this study. Before a transform can be performed an appropriate wavelet function must be selected. The shape of the wavelet function is one of the most important considerations in the selection of a basis. Generally, the shape of the wavelet function should show similar characteristics to the signal being analyzed.

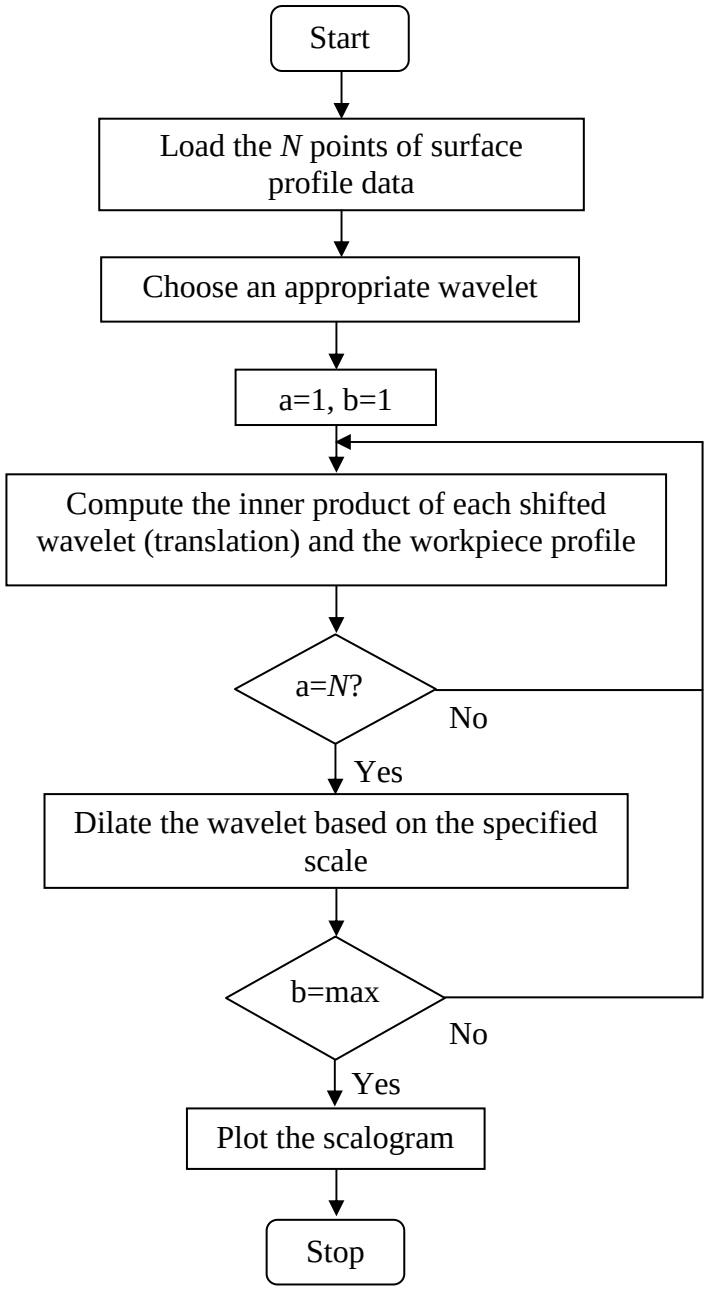

Figure 3.33: Flow chart for CWT algorithm

Several wavelets have been applied in previous works to study the surface roughness characterization including Morlet (Josso et al., 2002; Grzesik and Brol, 2009), Mexican hat (Grzesik and Brol, 2009), Daubechies (Chen et al., 1999) etc. In this study, the Morlet wavelet was chosen which is excellent in frequency distribution analysis. Further, the Morlet wavelet has been consistently used in the previous work for surface profile analysis, thus making it appropriate for interpreting the surface profile result.

In the next stage, the inner product of wavelet and the workpiece profile waveform was computed. The wavelet transform performs decomposition of a waveform into a wavelet of functions localized in both time and frequency, defined by Leavey et al. (2003):

$$CWT(a,b) = \int_{-\infty}^{\infty} G(t)\psi_{b,a}^{*}(t)dt \tag{3.28}$$

where $CWT(a,b)$ is the wavelet coefficient, $G(t)$ is the workpiece profile in time domain, $\psi_{b,a}(t)$ is the wavelet basis, a and b are denoted as dilation (scaling) and translation (time) factors, respectively, and $*$ represents the complex conjugation. The translation and scaling operations on mother wavelet $\psi(t)$ constructs a family of function as:

$$\psi_{b,a}(t) = \frac{\psi}{\sqrt{a}}\left(\frac{t-b}{a}\right) \tag{3.29}$$

The analysing wavelet applied in this study, i.e. Morlet wavelet is shown in Figure 3.34(a). The scaling or dilation controls the width of the wavelet while the translation parameter controls the location of the wavelet. The interpretation of

Equation 3.29 is that the size of the wavelet function $\psi_{b,a}(t)$ varies with the dilation or scaling. Wavelet transform usually starts by using low scale wavelet functions progressing to higher scales. When the scale increases the wavelet is stretched in the horizontal *x*-axis direction while it is squashed in the vertical *y*-axis direction as shown in Figure 3.34(b).

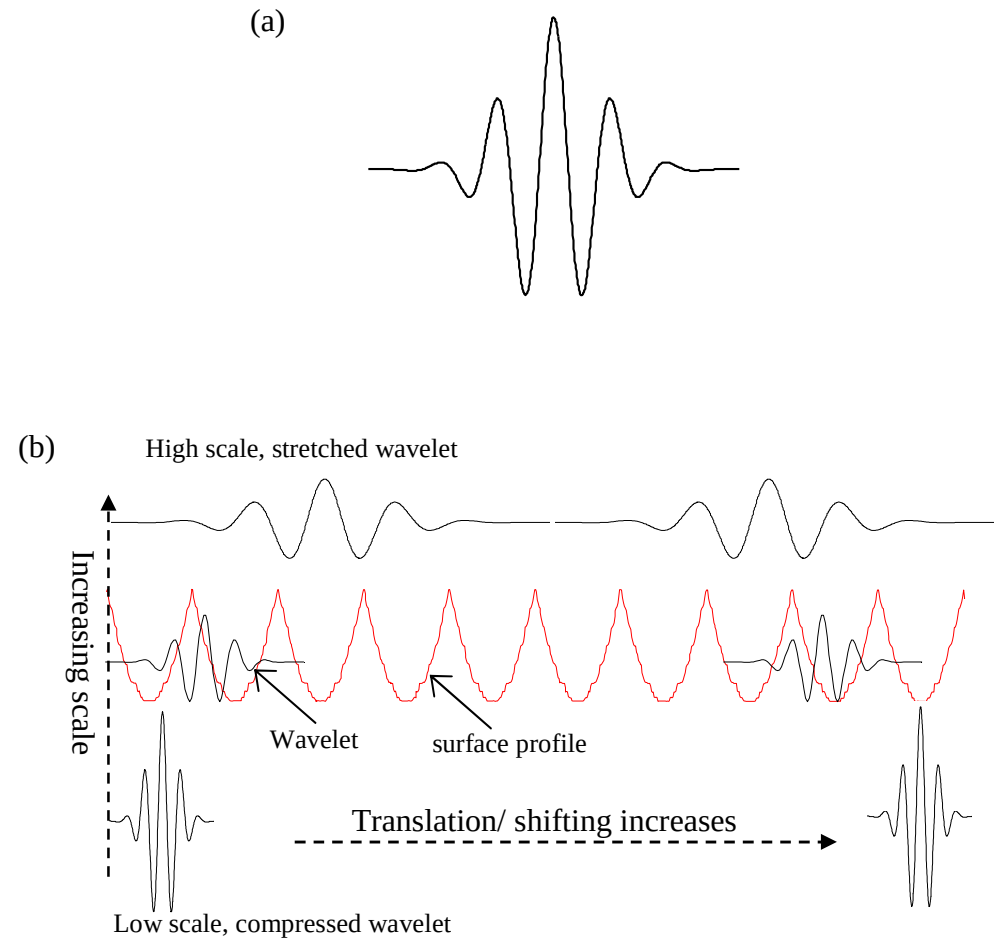

Figure 3.34: (a) Morlet wavelet, and (b) wavelet analysis overview

The analyzing wavelet is placed at the beginning of the signal (t=0). The wavelet is then moved by a small increment of pixel in the positive time direction. The wavelet is multiplied by the workpiece profile waveform and integrated to calculate a new wavelet coefficient. This process is continued until the end of the workpiece profile is reached. At this point the scale is increased, the wavelet being stretched and dilated, and the wavelet is returned to the starting point of the workpiece profile waveform to calculate the new wavelet coefficient.

This transformation is repeated until the workpiece profile waveform has been analyzed for all the scales to produce the squares of the CWT coefficients and form a scalogram as illustrated in Figure 3.35. The scales over which to compute the CWT could be any real positive numbers. For DWT the scale are sampled in power of two (dyadic sampling). In this study, the determination of scale range in the CWT is based on the dyadic sampling (2^1, 2^2, 2^3,... etc).

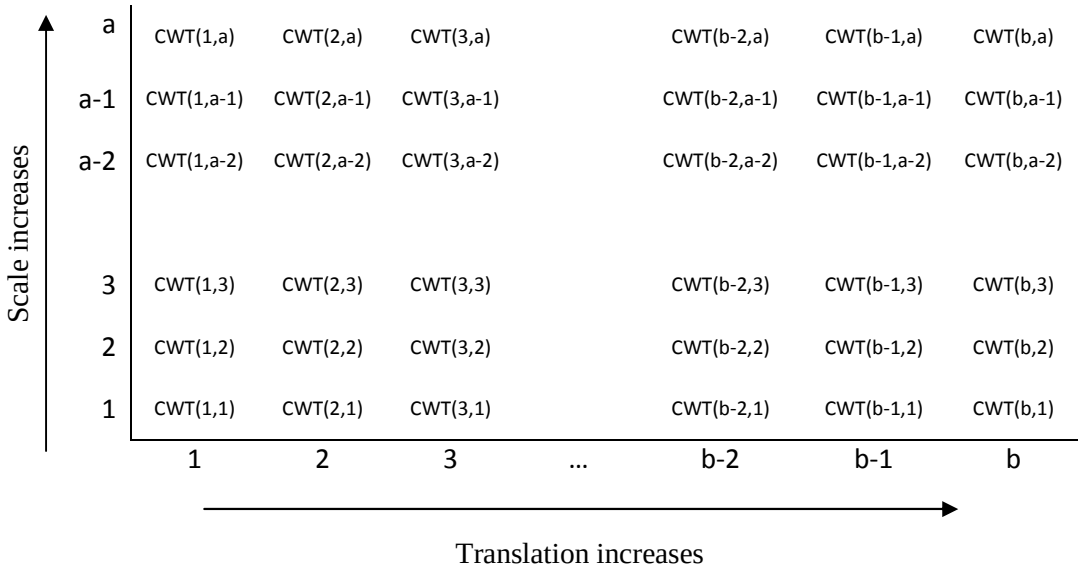

Figure 3.35: Wavelet analysis to produce scalogram

The CWT allows the localization of frequency components in the analyzed workpiece profile. The CWT performs a comparison of the wavelet to the workpiece profile waveform. Large CWT coefficients at that translation and scale indicate that high degree of similarity exists between the wavelet function and workpiece profile waveform. If the wavelet function and workpiece profile are dissimilar, small CWT coefficients are found. Therefore, the wavelet transform is a measure of how much the workpiece profile waveform resembles the wavelet at a particular position and scale.

The scale is usually correlated to the frequency of the wavelet function. Scale is inversely proportional to the frequency. Low scale is usually associated with the most tightly packed wavelet (high frequency) and vice versa. This wavelet transform process provides an indication of the frequency contents of the workpiece profile waveform. A large CWT coefficients at a particular scale implies the presence of a particular frequency because an approximate relationship exists between the scale and the frequency.

3.5 Chapter summary

In this chapter, the simulation method and experimental method to detect tool chipping in ceramic cutting inserts based on the 2-D images of workpiece profile in turning are outlined. The simulated workpiece profiles with the presence of the vibration due to wear and chipping were generated in order to demonstrate the application of ACF in detection of tool chipping based on the workpiece profile signature. In-process experiment was conducted to investigate the capability of the proposed ACF method for detecting the tool chipping in ceramic cutting insert from

the workpiece profile signature. The results obtained from experiments was used to compare the results from simulations which are presented in the next chapter.

Simulation work was conducted to investigate the capability of the FFT method in tool chipping detection based on the workpiece profile signature. An offline preliminary experimental work was carried out to investigate how amplitude of fundamental feed frequency of the workpiece profile and its harmonics could be used to correlate with the tool chipping while other spatial frequencies were ignored. An in-process experiment on tool chipping detection was conducted to investigate the effect of tool chipping on the distribution of spatial frequencies of workpiece profile when the workpiece profile in spatial domain was transformed into frequency domain. The results of experiments and simulations were discussed in the next chapter.

The sub-window FFT method was introduced to resolve the limitation in STFT which is highly dependent of window function. CWT method was applied to overcome the limitation of the sub-window FFT method as CWT allows to decompose the workpiece profile in time domain and frequency domain simultaneously. The results and discussions as well as the comparison for both methods are detailed out as well in the next chapter.

CHAPTER FOUR

RESULTS AND DISCUSSIONS

4.1 Introduction

The results and discussions of the research work are presented in this chapter. Section 4.2 presents the results of simulation on the detection of tool chipping from workpiece profile signature using ACF followed by a discussion of the results obtained from an in-process experiment. The analysis of the effect of the tool chipping on the workpiece surface using ACF is discussed. The findings obtained from the simulation and experiments are compared.

Section 4.3 discusses the results of the simulation works on detection of the tool chipping from the workpiece profile signature using FFT are compared with the findings obtained from the experiments. The effect of tool chipping on the amplitude of spatial frequencies of workpiece profile is explained. In addition, the results on detection of onset tool chipping in ceramic cutting insert using proposed sub-window FFT is also discussed.

In Section 4.4, discussions on the capability of the CWT for detecting the tool chipping in ceramic cutting insert based on the workpiece profile signature is presented. Tool chipping detection methods by using sub-window FFT and CWT are compared so that a better method in terms of the ability of detecting the onset tool failure by chipping can be determined. Finally, the chapter summary is presented in the Section 4.5.

4.2 In-process detection of chipping in ceramic cutting insert based on the surface profile signature using ACF

In this section, the outcomes of simulation (Section 4.2.1) and experimental work (Section 4.2.2) on the detection of tool chipping from workpiece profile signature using ACF are discussed in details. The comparison for results obtained from simulation and experimental work were made and the effect of the tool chipping on the workpiece profile using ACF is also discussed.

4.2.1 Simulation results

Simulated workpiece profiles were used to demonstrate how the ACF can be applied to identify subtle changes in the turned workpiece profile caused by tool chipping. Figure 4.1(a)(i) shows the simulated ideal workpiece profile generated at tool nose radius of 0.8 mm and a feed rate of 0.4 mm per revolution. The peak of the ACF decreases uniformly and linearly as the lag distance increases due to the periodic workpiece profile as shown in Figure 4.1(a)(ii). When the cutting tool undergoes gradual wear, the peak of ACF show a slight deviation from the ideal plot (without vibration) and the deviation increases as shown in Figure 4.1(b)(ii) and Figure 4.1(c)(ii). This is because the amplitude of dislocation in workpiece results from the tool and workpiece vibration generated during machining increases.

When a tool has chipped the peaks of the ACF decrease rapidly as the lag distance increases as shown in Figures 4.1(d)(ii)-(e)(ii). The plot of the peaks also deviates significantly from the envelope of the autocorrelation peaks for a surface produced by an ideal simulated (chipping-free) tool. This behavior is due to the

random variation in the workpiece profile that results from the increased vibration after tool chipping. When the randomness of the surface profile increases the deviation becomes more prominent. Figure 4.1(f)(ii) shows a rapid decline in the peak of ACF as the lag distance increases due to the presence of waviness in the surface profile. The undulations of the surface waviness in the simulated workpiece profile leads to the profile is lack of autocorrelation with increasing lag distance.

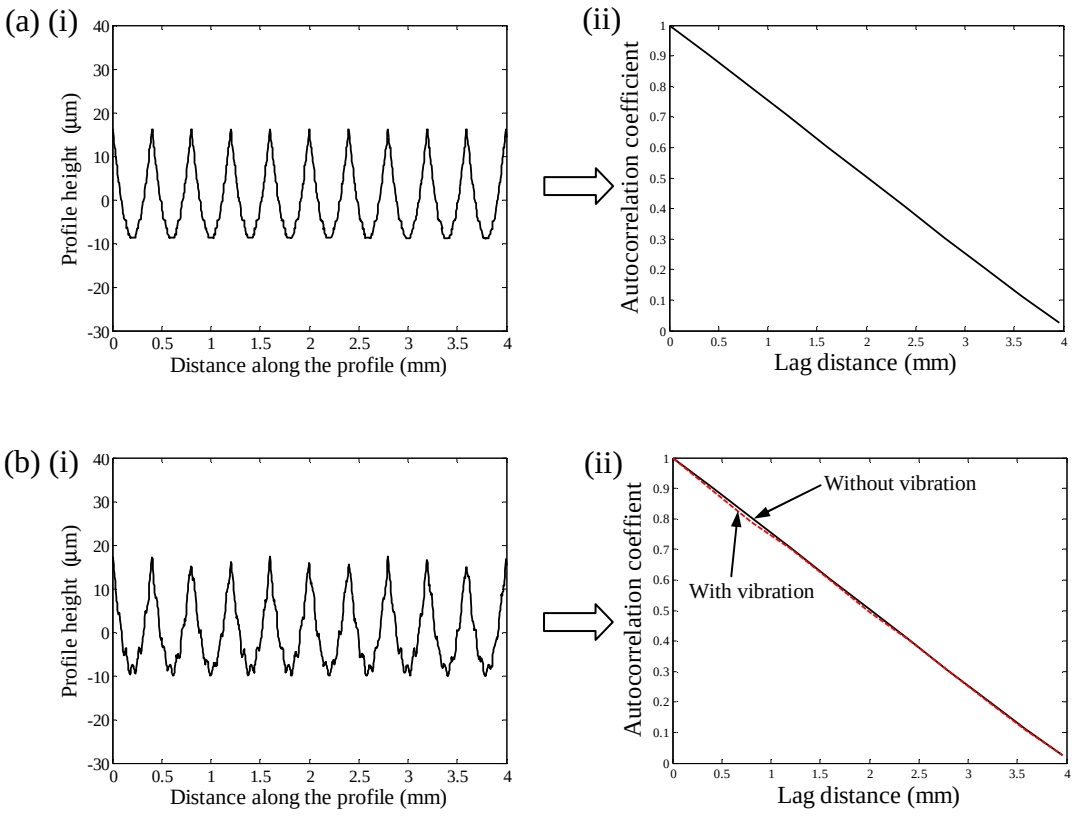

Figure 4.1: (a)(i) Ideal workpiece profile and (ii) corresponding peak of ACF plot; (b)(i) simulated surface profile with increasing vibration amplitudes by 5% peak-to-valley height of simulated ideal workpiece profile and (ii) corresponding peak of ACF plot; (c)(i) simulated surface profile with increasing vibration amplitudes by 10% peak-to-valley profile height of simulated ideal workpiece profile and (ii) corresponding peak of ACF plot (ii); (d)(i) simulated surface profile with random vibration with 5 times higher magnitude as in (b) and (ii) corresponding peak of ACF plot; (e)(i) simulated surface profile with random vibration with 10 times higher magnitude as in (b) and (ii) corresponding peak of ACF plot; and (f) simulated surface profile with presence of waviness due to the tool-workpiece vibration by 10 times higher vibration magnitude as in (b) and (ii) corresponding peak of ACF plot (Continued)

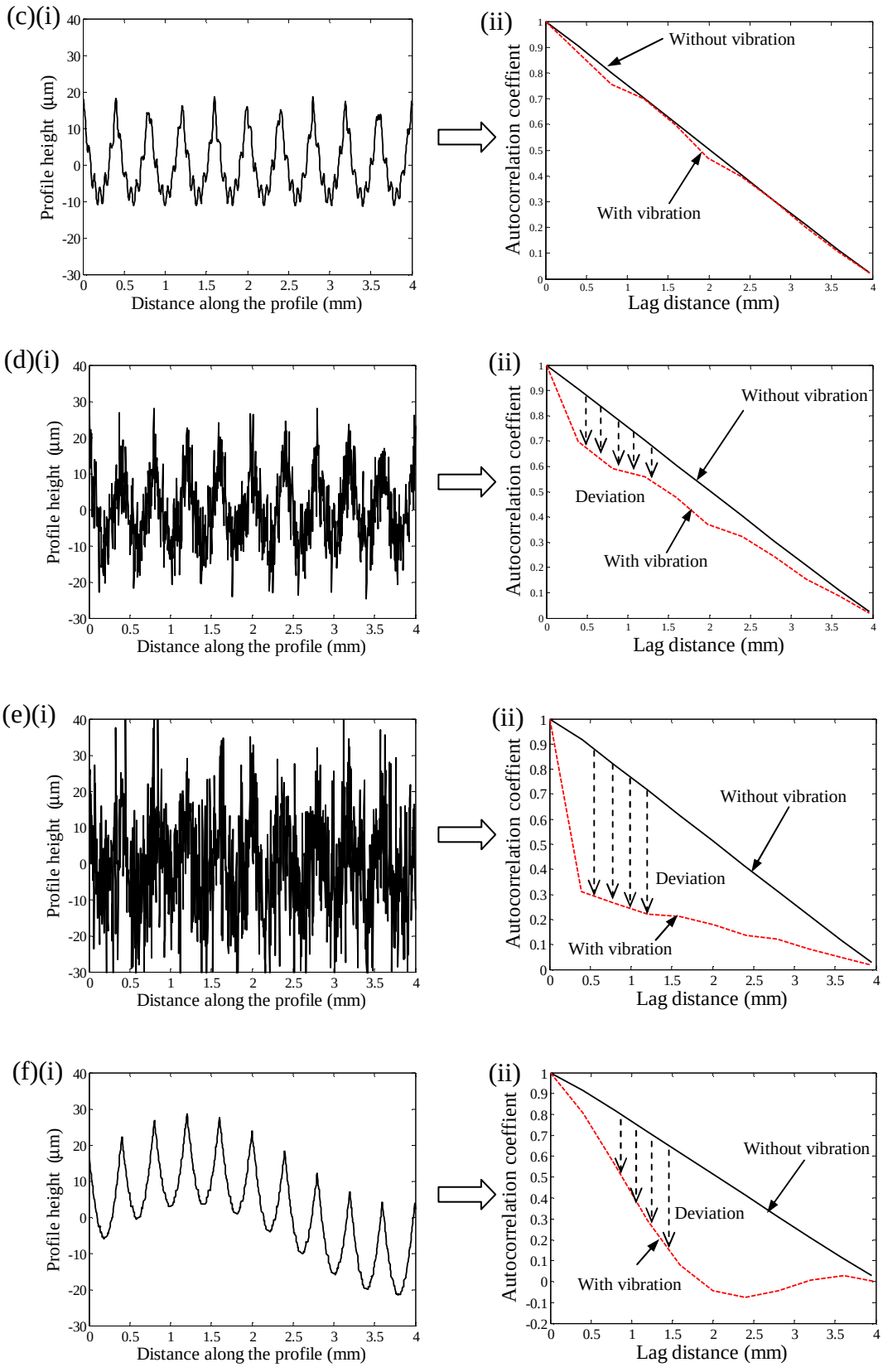

Figure 4.1: (continued)

4.2.2 Experimental results

Figures 4.2 shows the peaks of the ACF against the lag distance at different rotational angles of the workpiece. Based on the experiment results in the Figures 4.2(a) and Figure 4.2(b), it can be noticed that the envelope of the peaks of ACF decreased gradually with the lag distance along the workpiece profile. The trends of the peak of the ACF are almost the same at different rotation angles of the workpiece. Figure 4.2(c), however, shows a rapid decrease in the peak of ACF between lag distances of 0 mm to 8 mm for the cutting interval between 11.1 s to 16.5 s. In Figures 4.2(d) to Figure 4.2(f), the envelopes of the peak of ACF for workpiece profile at different rotational angles deviate significantly from one another. Simulation and experiment results show that ACF is capable of detecting the random features buried in the surface profile by determining the correlation coefficient between the pairs of shifted and un-shifted surface profile at a separation distance called lag distance (each lag is equivalent to 1 pixel value) regardless of the total length of workpiece profile.

Figures 4.3(a) and Figure 4.3(b) show the SEM images of the cutting inserts after the machining operation for the peak of ACF plot in Figure 4.2(b) and Figure 4.2(c), respectively. As seen in Figures 4.3(a), abrasion grooves are formed on the flank face of the cutting insert due to the tool and workpiece abrasion in the early machining time interval of 5.6 s to 11.0 s. Figure 4.3(b) shows chipping that appeared on the cutting edge of the ceramic inserts after machining time duration of 16.5 s. Figure 4.4 shows a 3-D view of the cutting edge using *Alicona InfiniteFocus* where the chipping is clearly visible. The chipping in Figure 4.4 occurred on the nose area which falls in the flank wear land as shown in Figure 2.3.

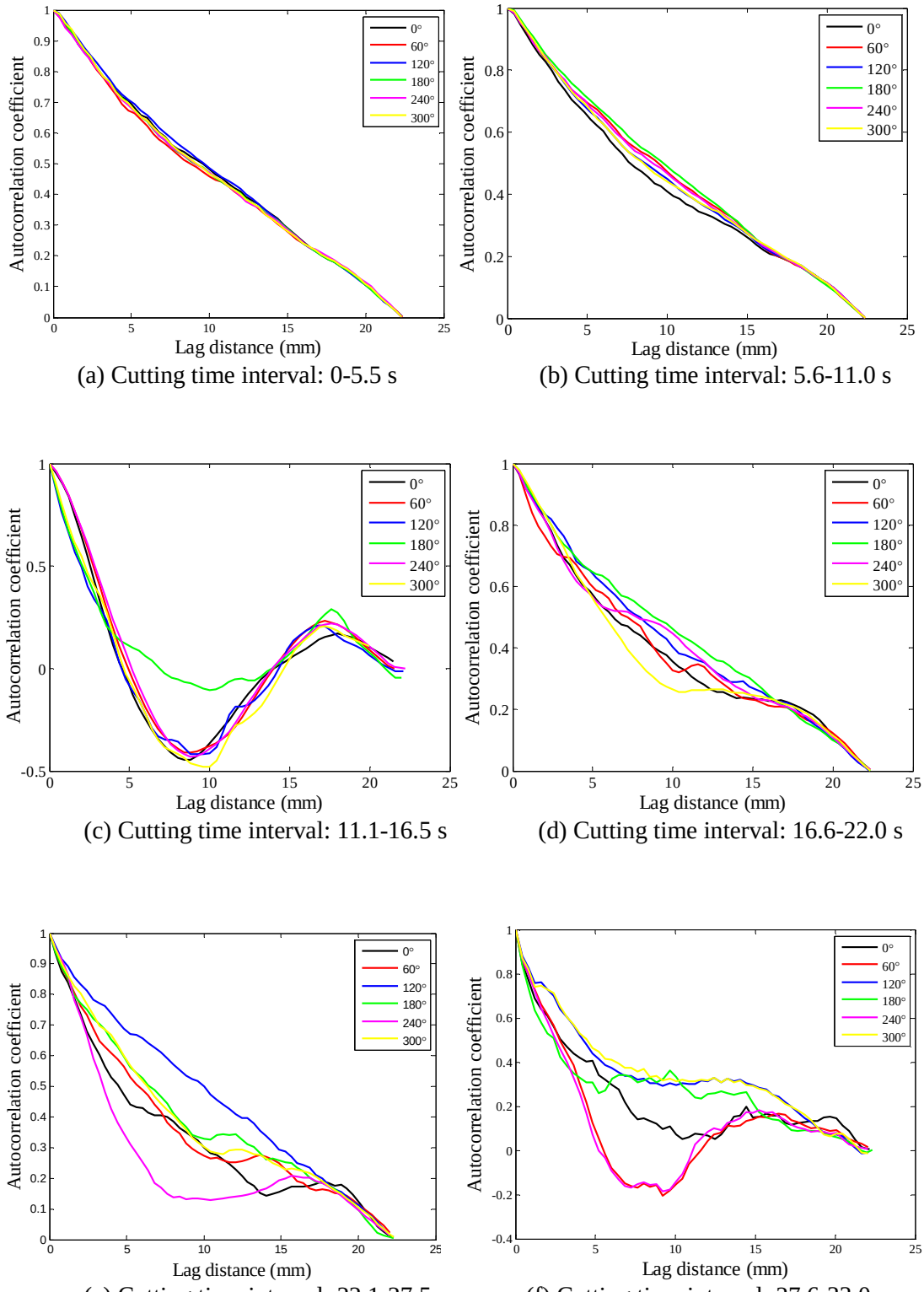

(a) Cutting time interval: 0-5.5 s

(b) Cutting time interval: 5.6-11.0 s

(c) Cutting time interval: 11.1-16.5 s

(d) Cutting time interval: 16.6-22.0 s

(e) Cutting time interval: 22.1-27.5 s

(f) Cutting time interval: 27.6-33.0 s

Figure 4.2: ACF plot of workpiece profile generated by aluminium oxide ceramic cutting insert at different rotational angles within cutting time interval of (a) 0-5.5 s, (b) 5.6-11.0 s, (c) 11.1-16.5 s, (d) 16.6-22.0 s, (e) 22.1-27.5 s, and (f) 27.6-33.0 s

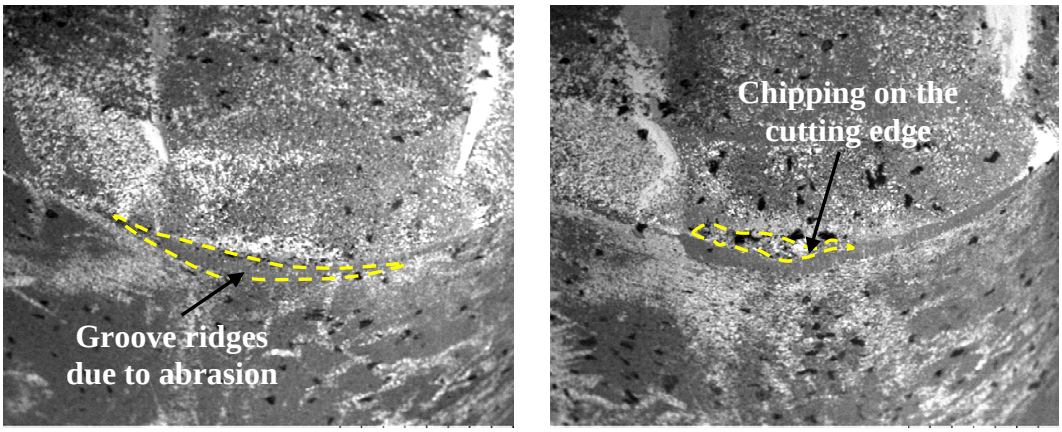

(a) (b)

Figure 4.3: SEM micrographs of aluminium oxide ceramic cutting insert after machining (a) before chipping, and (b) after chipping.

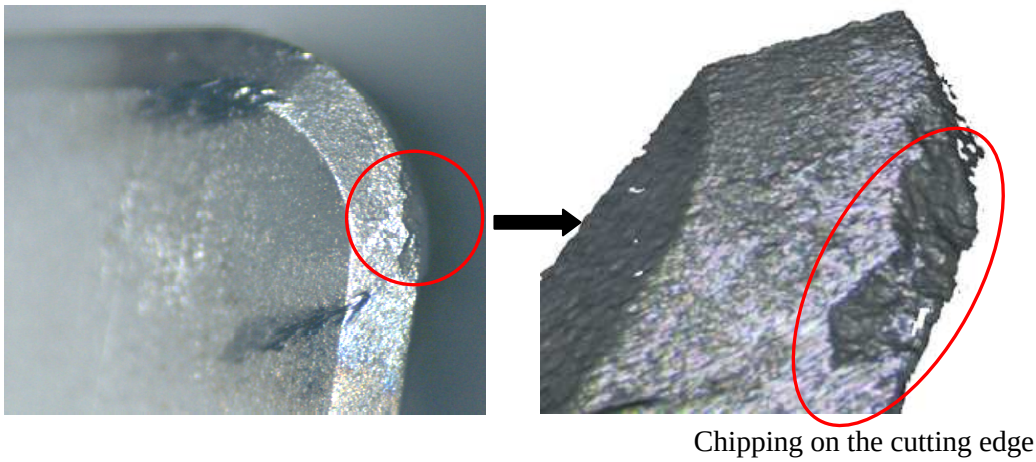

Figure 4.4: 3-D observation of the chipping on the cutting edge by *Alicona Infinite Focus*.

In the early machining stage the ceramic cutting insert produces a periodic profile with almost constant wavelength along the workpiece. The peak-to-valley height of the surface roughness profile is approximately constant up to a machining time of 11 s (at various rotation angles) as shown in Figure 4.5 and Figure 4.6.

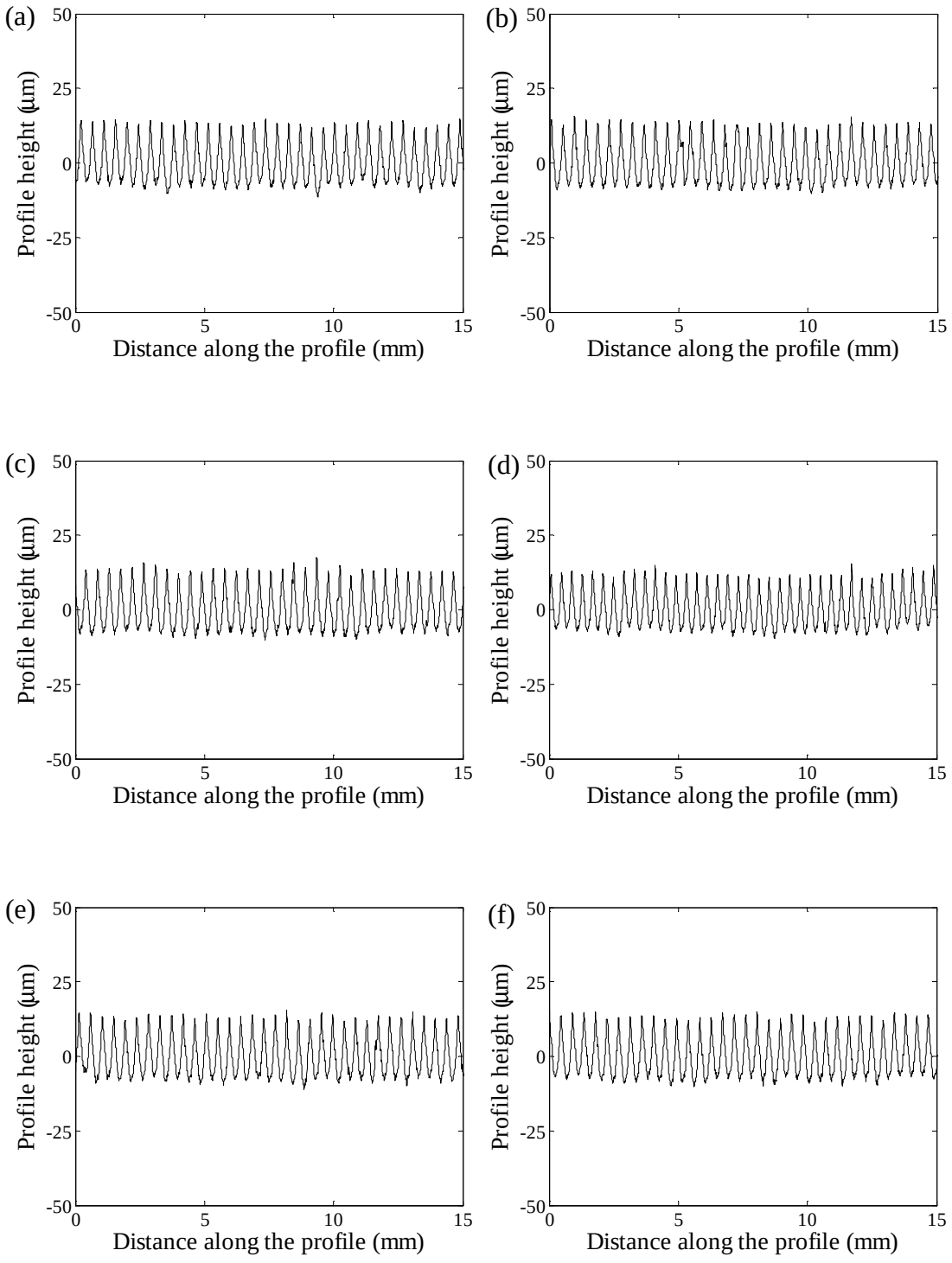

Figure 4.5: Extracted surface roughness profile from 2-D workpiece images at different rotational angles (a) 0^o, (b) 60^o, (c) 120^o, (d) 180^o, (e) 240^o, and (f) 300^o in cutting time interval of 0-5.5 s.

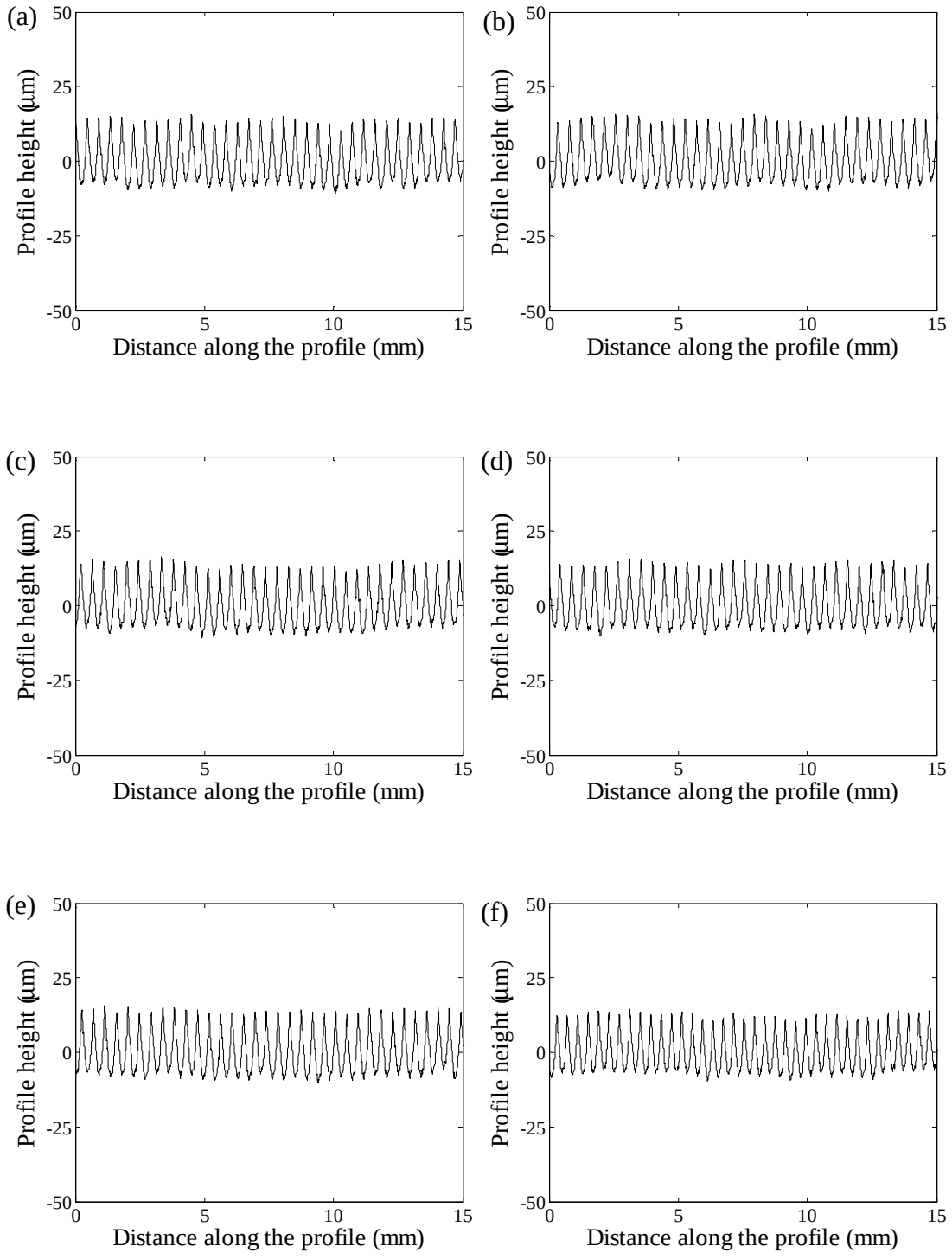

Figure 4.6: Extracted surface roughness profile from 2-D workpiece images at different rotational angles (a) 0^o, (b) 60^o, (c) 120^o, (d) 180^o, (e) 240^o, and (f) 300^o in cutting time interval of 5.6-11.0 s.

Figure 4.7 shows the zoomed in 2-D workpiece profiles and their corresponding surface roughness profiles before tool chipping. The peaks of the ACF for a workpiece profile generated from an unworn or progressively worn cutting tool decreases gradually as a function of lag distance and are almost identical at different rotational angles as shown in Figure 4.2(a) and Figure 4.2(b). This is due to the uniform and repeatable profile which shows good replication of the workpiece profiles as the lag distance increases.

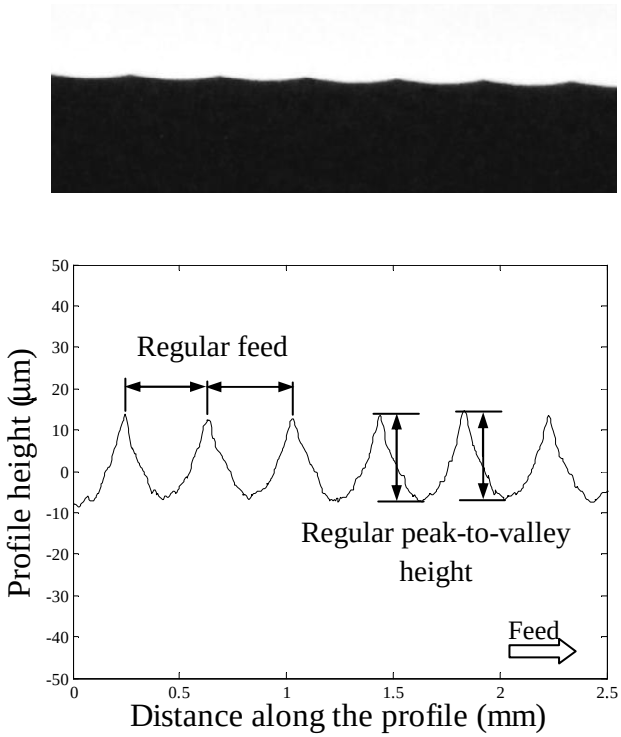

Figure 4.7: Zoomed view of 2-D images of the workpiece profile and the corresponding extracted surface roughness profile before tool chipping

Figure 4.8 to Figure 4.11 show the surface profiles at selected cutting intervals of time and corresponding workpiece profile to the peak of ACF plot in Figure 4.2(c) to Figure 4.2(f) respectively. The sharp decrease and the significant deviation in the peaks of the ACF plots at different rotational angles observed in Figure 4.2(c) to Figure 4.2(f) are attributed to the variation in the workpiece profile

caused by the tool chipping. Figure 4.12 illustrates the zoomed view of 2-D images of the workpiece profile and their corresponding extracted surface roughness profile after tool chipping. After tool chipping the surface roughness profiles do not repeat periodically compared to the profiles at the initial cutting stages. The peak-to-valley heights of the surface roughness profile change irregularly.

When the turning of workpiece was continued by using the chipped cutting insert this could lead to continuous failure of the cutting insert by tool chipping because the workpiece profile generated in the subsequent passes show significant and distinct undulations of the surface waviness at different rotational angles observed in Figure 4.8 to Figure 4.11. As the ceramic tool material is brittle and once it has been chipped or broken, the bonding between the grains are weakened due to the mis-orientation of the neighbouring grains abutting chipping. Continuous tool chipping could be the result of propagation of chipping initiated at the edge of the cutting insert under the action of cyclic load due to the instability of cutting process caused by the tool-chip abrasion.

When the cutting tool has chipped or continue to chip its effects on the cutting force variation can sometime cause severe vibration during machining. This is because the chipped cutting tool and workpiece contact area increases and this causes the cutting force to increase and in turn excite the tool and workpiece to vibrate during machining. Consequently, the vibration between the chipped cutting tool and the workpiece leads to the tool movement with respect to the workpiece which become unstable during cutting operation.

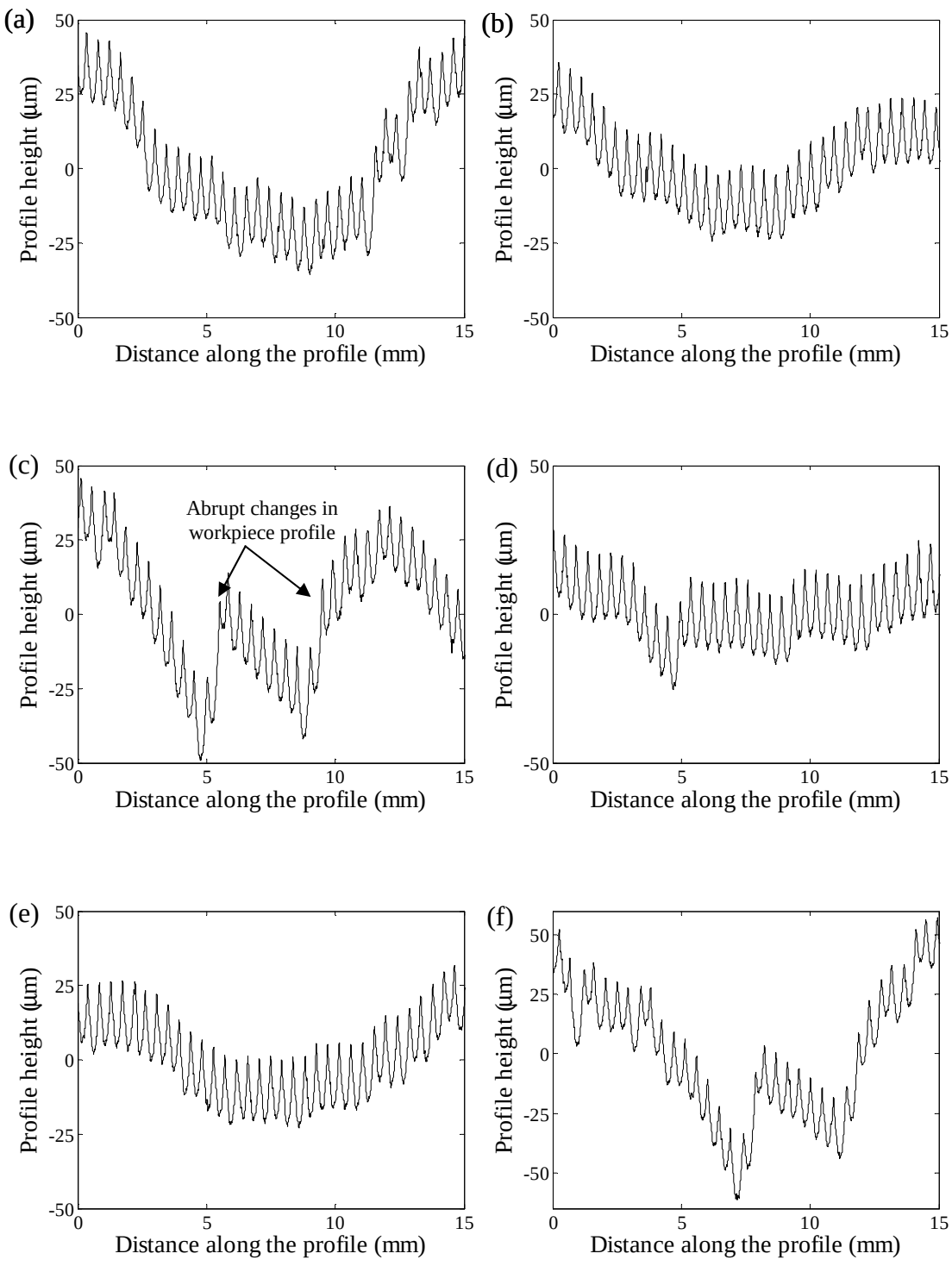

Figure 4.8: Extracted surface roughness profile from 2-D workpiece images at different rotational angles (a) 0^o, (b) 60^o, (c) 120^o, (d) 180^o, (e) 240^o, and (f) 300^o in cutting time interval of 11.1-16.5 s

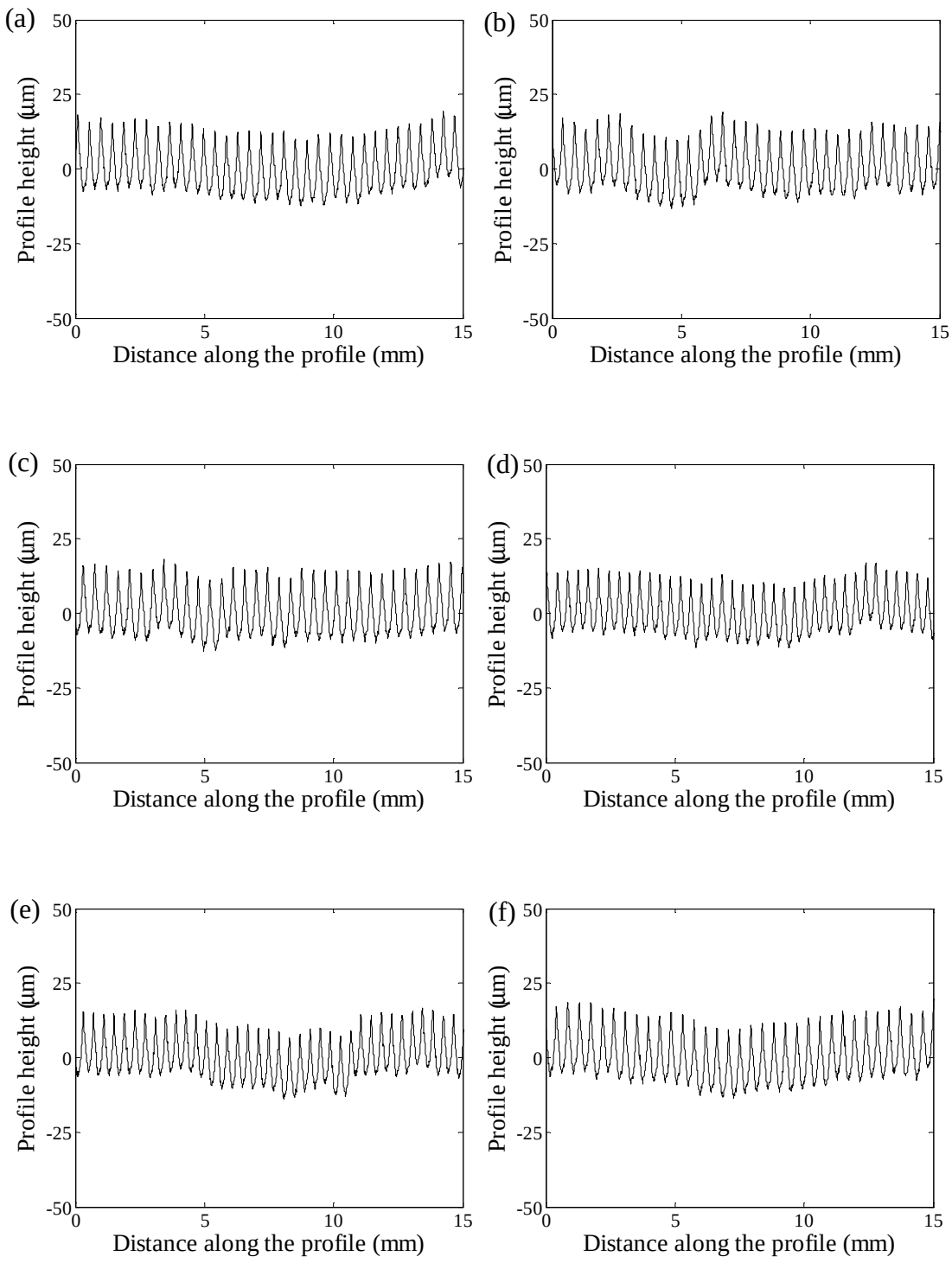

Figure 4.9: Extracted surface roughness profile from 2-D workpiece images at different rotational angles (a) 0^o, (b) 60^o, (c) 120^o, (d) 180^o, (e) 240^o, and (f) 300^o in cutting time interval of 16.6-22.0 s

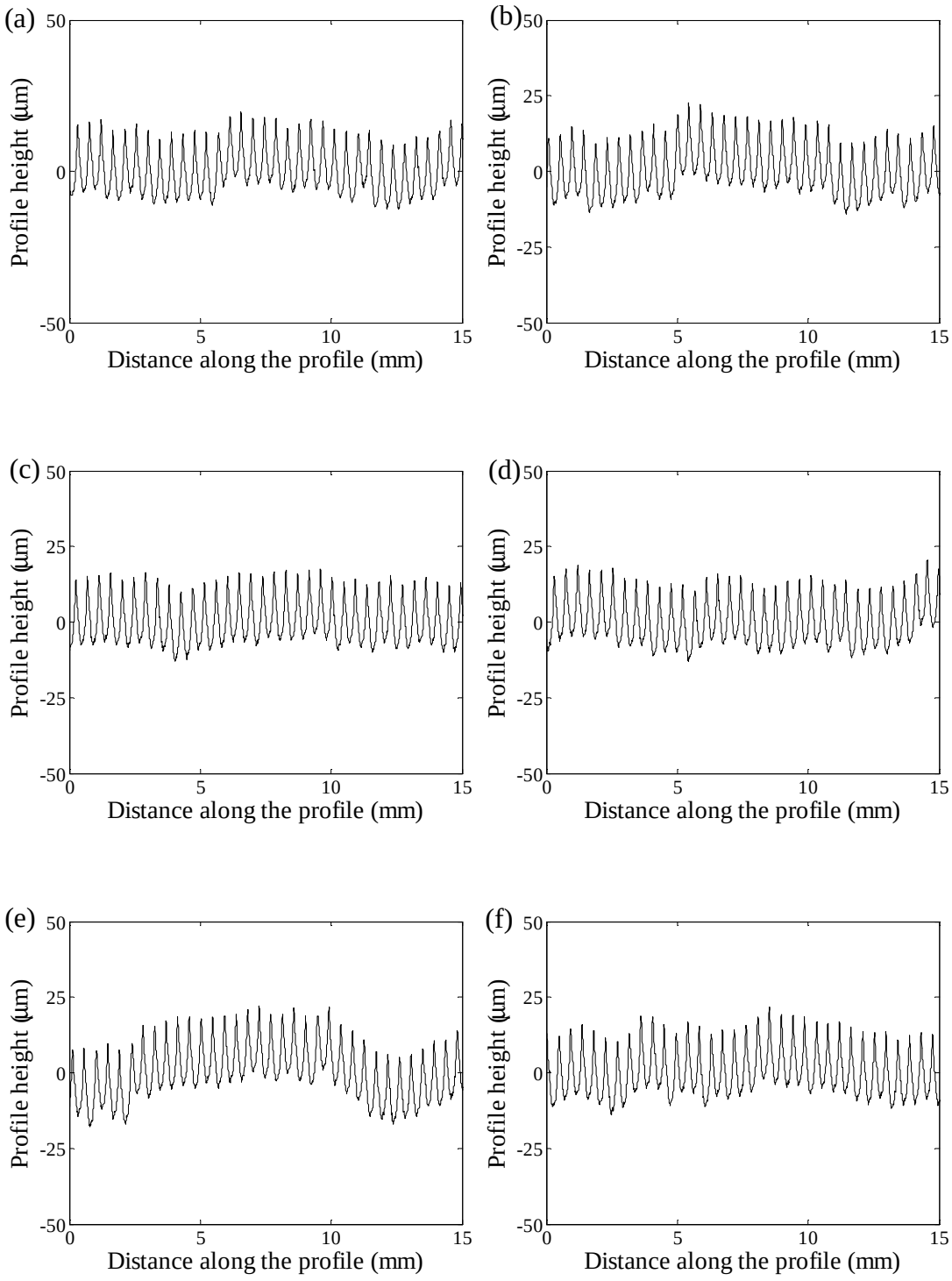

Figure 4.10: Extracted surface roughness profile from 2-D workpiece images at different rotational angles (a) 0^o, (b) 60^o, (c) 120^o, (d) 180^o, (e) 240^o, and (f) 300^o in cutting time interval of 22.1-27.5 s

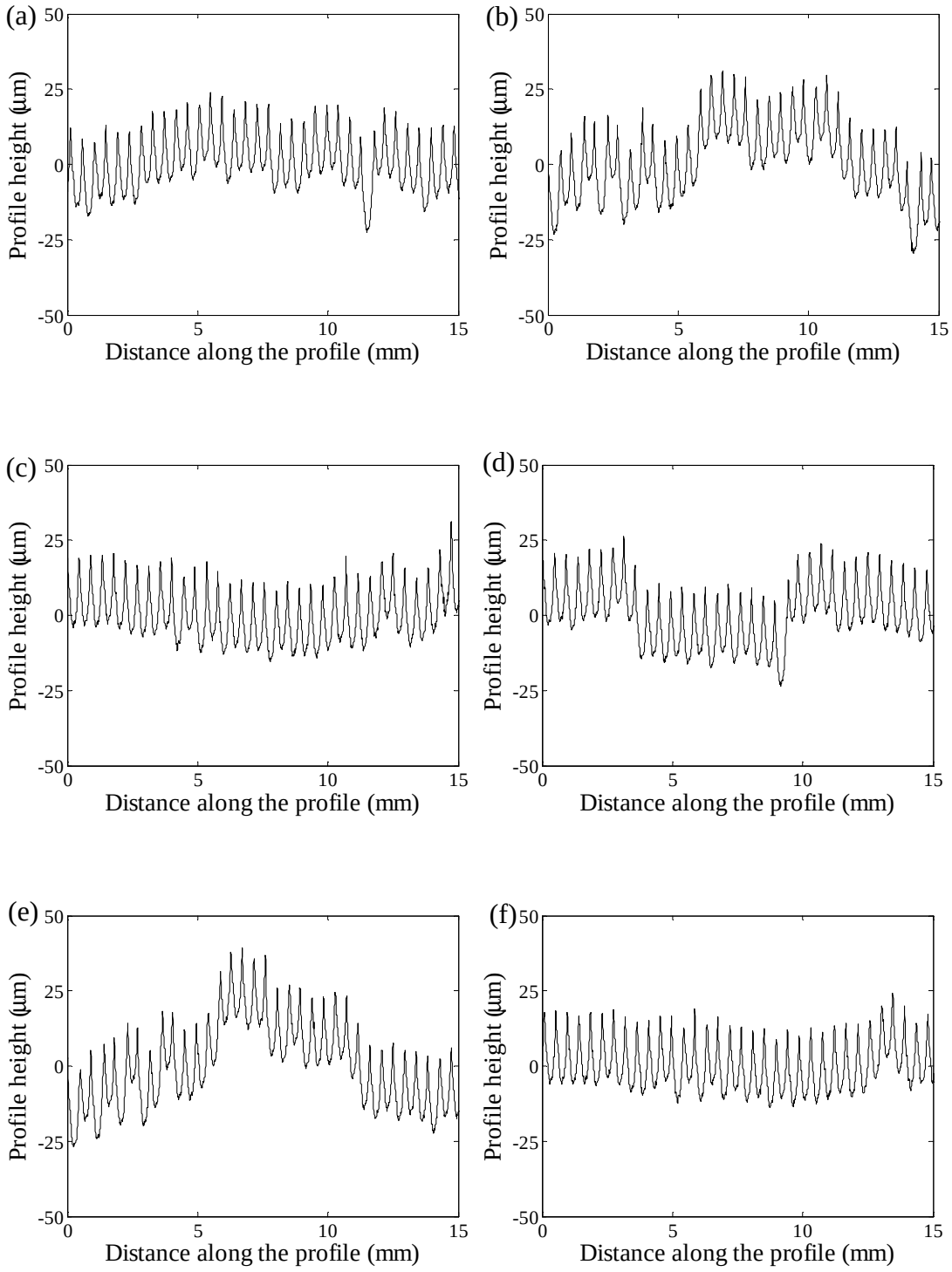

Figure 4.11: Extracted surface roughness profile from 2-D workpiece images at different rotational angles (a) 0^o, (b) 60^o, (c) 120^o, (d) 180^o, (e) 240^o, and (f) 300^o in cutting time interval of 27.6-33.0 s

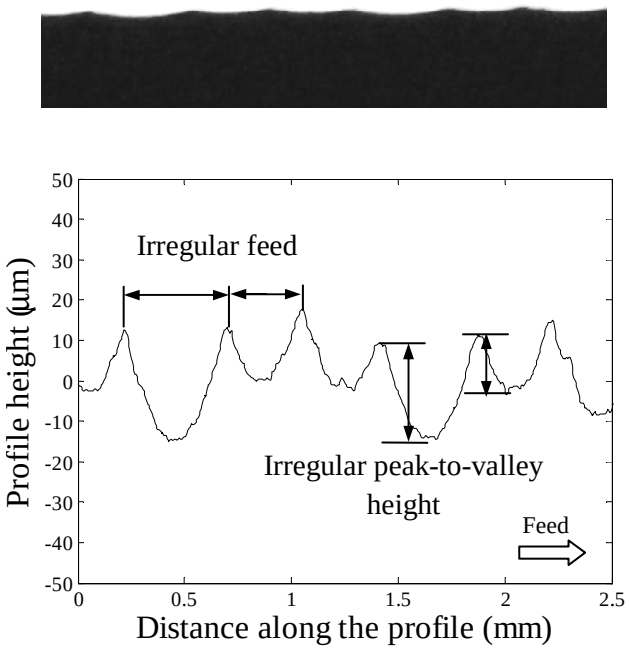

Figure 4.12: Zoomed view of 2-D images of the workpiece profile and the corresponding extracted surface roughness profile after tool chipping.

According to Boryczko (2011) unstable tool movement results in non-uniform distribution of the height of irregularities and wavelengths in the transverse direction in the workpiece profiles. The effect of chipped tool and workpiece vibration leads to the dislocation in workpiece profile and the dislocation of the tool edge perpendicular to the workpiece results from the vibration generated during its successive revolutions. The irregular profile height is observed due to the inconsistent tool movement whether the tool approaches or moves away from the workpiece. The resulting profile differs from the theoretical profile to a significant extent due to the unpredictable interaction between the chipped tool and the workpiece.

Since the unstable cutting process arising from the chipped tool and workpiece contact is not absolutely predictable, random features appear in the

workpiece profiles and the workpiece profile differ from one another at various rotation angles as observed in Figure 4.8 to Figure 4.11. Due to this reason, the sharp decrease and the significant deviation in the peaks of the ACF plots at different rotational angles were observed. The trends of the peak of ACF obtained from the experiments before and after tool chipping are consistent with the results from the simulation study. The peaks of ACF obtained in the experiments (Figure 4.2(c)-(f)) decrease rapidly in the presence of tool-workpice vibration and explicit surface waviness appear after tool chipping as observed in the simulation.

The sum square of deviation (SSD) from the peak of ACF of the ideal workpiece profile for each workpiece rotation angle was determined to correlate with the tool condition. Figure 4.13 shows the ACF for a simulated ideal workpiece profile with a feed of 0.4 mm and length equal to the actual length of image of the workpiece profile. As seen in Figure 4.13, the ACF is maximum and equal to 1 for zero spatial separation ($\tau = 0$) and then decays gradually with increase in the lag distance. As the lag distance increases the correlation diminishes because the original profile and shifted profile have increasingly smaller overlapping areas. The slope and the rate of decrement of the peak of ACF plot are known as indicators of randomness of the surface. The ACF attains a peak when the lag is a multiple of wavelength which means that the surface replicates itself at a spatial separation of wavelength.

The peak of ACF and the lag distance were correlated using Pearson's *r* value in linear regression. Pearson's *r* is a measure of the strength of the linear relationship between two variables. Pearson's *r* of approximately -1 indicates that a perfect but negative linear relationship exists between the peak of ACF and lag distance. The residual sum-of-square for the regression was used to determine the coefficient of

determination (R^2). A high value of adjusted R^2 shows a significant linear relationship between the peaks of ACF and lag distance. The linear relationship between the peak of ACF and distance is used as datum to estimate the tool state by determining the SSD from the peak of ACF of ideal workpiece profiles as shown in Figure 4.1(d) to Figure 4.1(f).

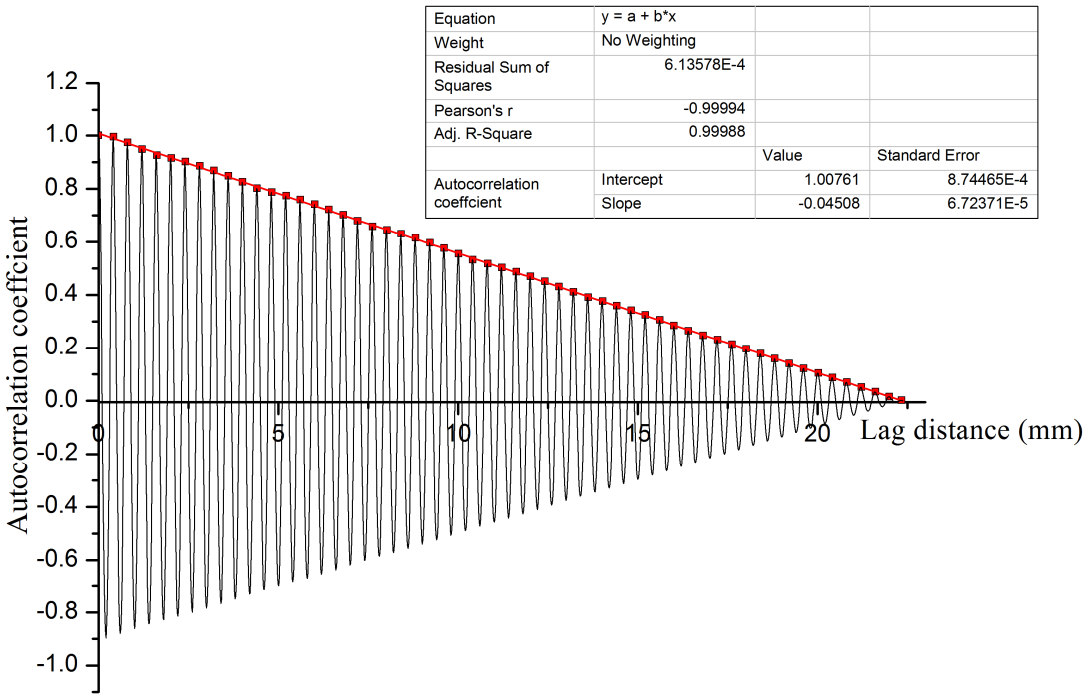

Figure 4.13: Peak of ACF of the simulated ideal workpiece profile against with the lag distance.

A 3-D plot of the SSD from ideal workpiece profiles at different workpiece rotation angles within different cutting interval is presented in Figure 4.14. As seen in this figure there is no obvious change in the SSD value before cutting time of 11.1 s. This indicates that the machined profiles have good replication and are highly correlated at different rotational angles of the workpiece. The SSD increased sharply after tool chipping at cutting time interval of 11.1 s to 16.5 s. This is due to the non-

uniform and abrupt changes in the workpiece profile generated at different workpiece rotation angles.

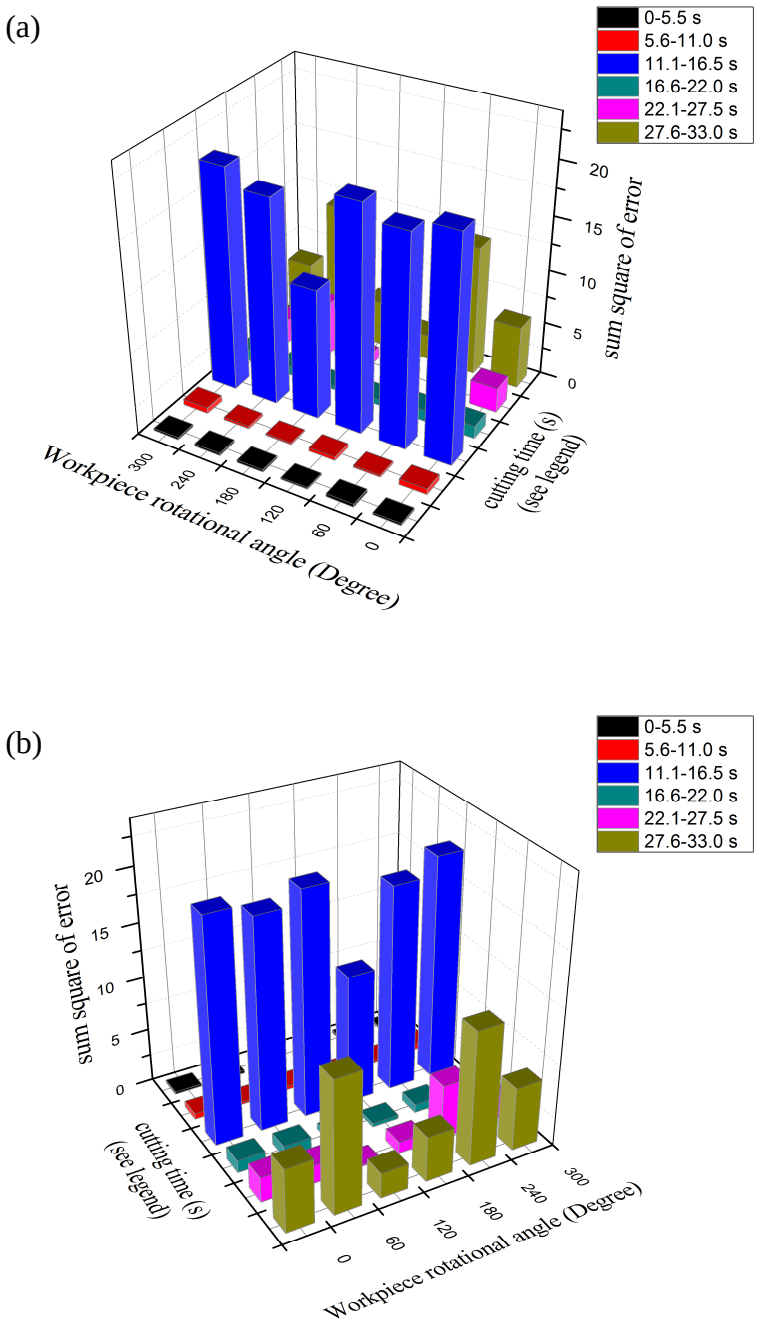

Figure 4.14: 3-D bar plot of SSD from the ACF peak for the ideal workpiece profile:(a) front view, and (b) back view.

A small SSD value was again observed at cutting time interval of 16.6-22.0 s. This is because when the chipped cutting tool is repositioned and continues to move it touches the workpiece again thus closing the gap to continue the cutting. However, the SSD value is generally high after tool chipping and has significant fluctuation at different cutting time intervals. The SSD of the peak of ACF of the workpiece profile with different workpiece rotation angles also show significant fluctuation at the onset of cutting time of 11.1 s. It seems reasonable to expect the fluctuation as the surface roughness profiles shown in Figure 4.8 to Figure 4.11 change in various ways as the dislocation profile resulting from the tool-workpiece vibration generated during machining when the tool chipping or more severe chipping of tool insert occurs.

When the experiment was repeated similar results were found as shown in Figure 4.15. Once again, the envelope of the peaks of the ACF was found to deviate significantly from one another at different angles when the tool has chipped as evident in Figure 4.15(b).

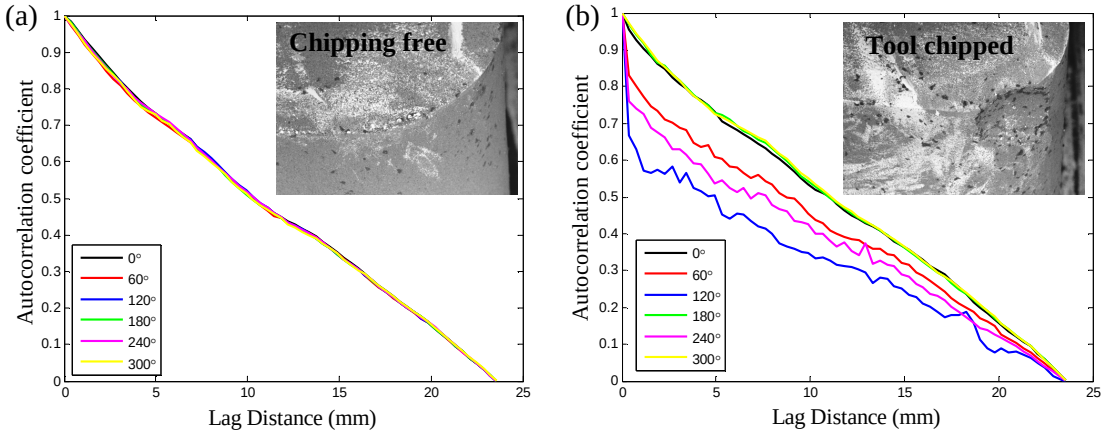

Figure 4.15: ACF plot of workpiece profile generated by aluminium oxide ceramic cutting insert at different rotational angles for repeat experiment (a) before tool chipping, and (b) after tool chipping

4.3 Detection of tool chipping in ceramic cutting insert from the surface profile signature using FFT

In this section, the results of using FFT method to analyze the surface profile to detect tool chipping are presented. Two simulation works on detection of tool chipping from surface profile signature using FFT by considering (i) the changes of the tool nose, and (ii) the presence of the tool-workpiece vibration were conducted. The results of each simulation work is presented and followed by the results obtained from the experiments. The effect of tool chipping on the amplitude of spatial frequencies of the workpiece profile is discussed. The results on detection of onset tool chipping in ceramic cutting insert using proposed sub-window FFT method is presented in the final part of this section.

4.3.1 Simulation results on detection of tool chipping from surface profile signature using FFT by considering the changes of the tool nose

Figure 4.16 presents the example of the spectrum analysis of the simulated ideal surface profile with feed rate of 0.4 mm/rev. As seen in the figure a strong fundamental feed frequency (V_f) of 2.5 mm^{-1} (1/0.4 mm) appears at a wavelength equal to the feed. Under ideal conditions the surface roughness profile is generated by the repetition of the tool tip profile at intervals of feed per revolution. This is based on the assumption that the tool is ideally positioned relative to the workpiece. Since the ideal surface produced by the tool nose is periodic several harmonics given by mV_f where m = 2, 3, 4…. appear together with the fundamental feed frequency V_f. As seen in Figure 4.16 the fundamental feed frequency and its harmonics are

prominent. Thus, the amplitude of the fundamental feed frequency and its harmonics were extracted to correlate with the cutting tool condition.

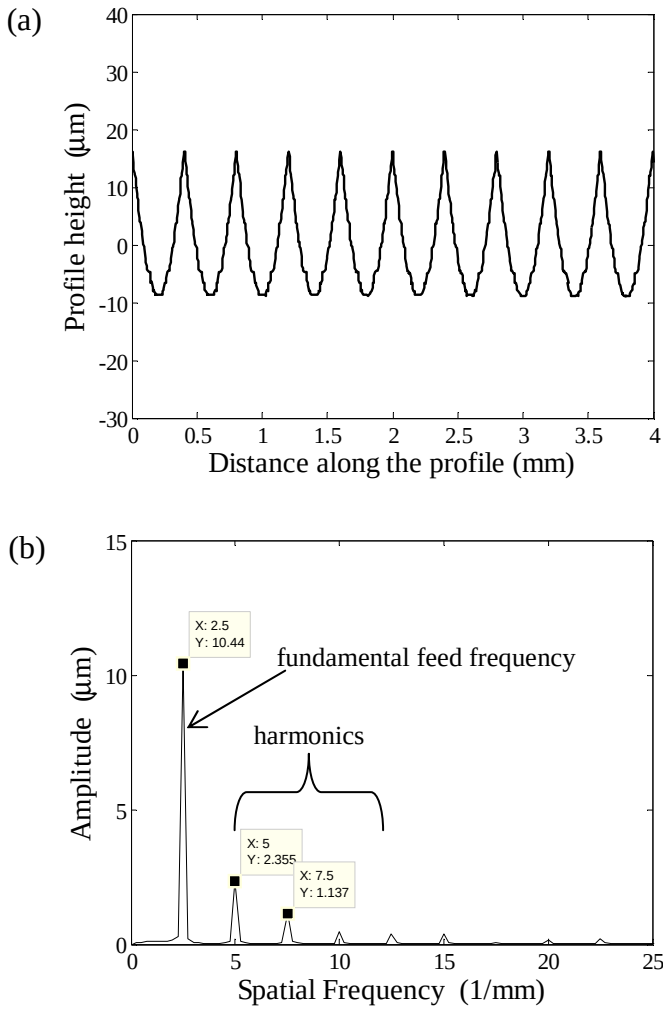

Figure 4.16: (a) Simulated ideal workpiece profile, and (b) FFT analysis for simulated ideal workpiece profile

Figure 4.17 illustrates the evolution of amplitude of the fundamental feed frequency and its harmonics for the simulated gradual wear on cutting tool in Figure 3.23 (represented by % increase of nose radius in minor axis length). It was noted that the amplitude of fundamental feed frequency increases with the increase of gradual wear. The second and third harmonics of fundamental feed frequency did not show any significant trend.

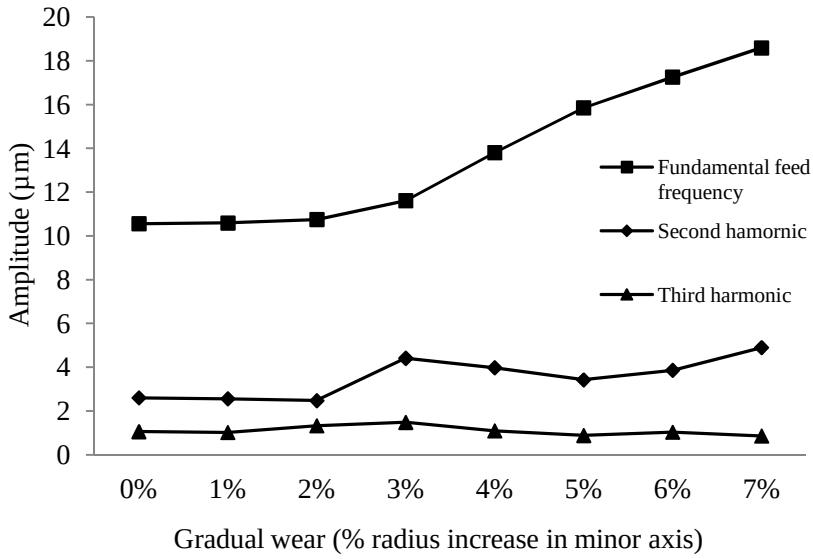

Figure 4.17: Variation of the amplitude of fundamental feed frequency, second harmonic and third harmonic of the simulated surface profile for gradual wear

Figure 4.18 shows simulation results where the chipping occurred at the early stage of cutting operation as shown in Figure 3.27. It can be noted from Figure 4.18 the spectrum amplitude of fundamental feed frequency start fluctuating from beginning of the simulated chipped cutting tool. Again, the second and third harmonics of fundamental feed frequency did not show any significant trend. Since the fundamental feed frequency is predominant with tool geometry in the FFT analysis, the fundamental feed frequency was employed to correlate with the cutting tool condition. Figure 4.19 presents the evolution of the amplitude of the fundamental feed frequency for the corresponding simulated workpiece profile due to gradual wear and chipping on cutting tool shown in Figure 3.29. As seen in Figure 4.19 the amplitude of the fundamental feed frequency increased uniformly during gradual wear and starts fluctuating once chipping occurred.

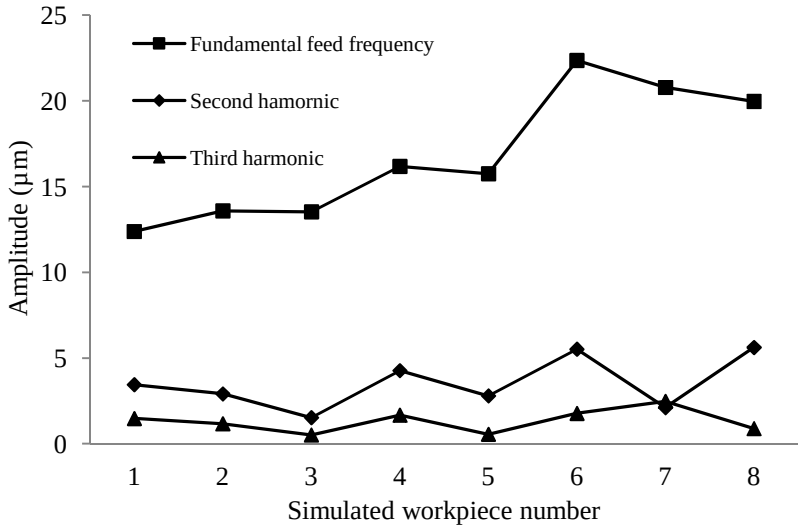

Figure 4.18: Variation of the amplitude of fundamental feed frequency, second harmonic and third harmonic of simulated surface profile for chipping

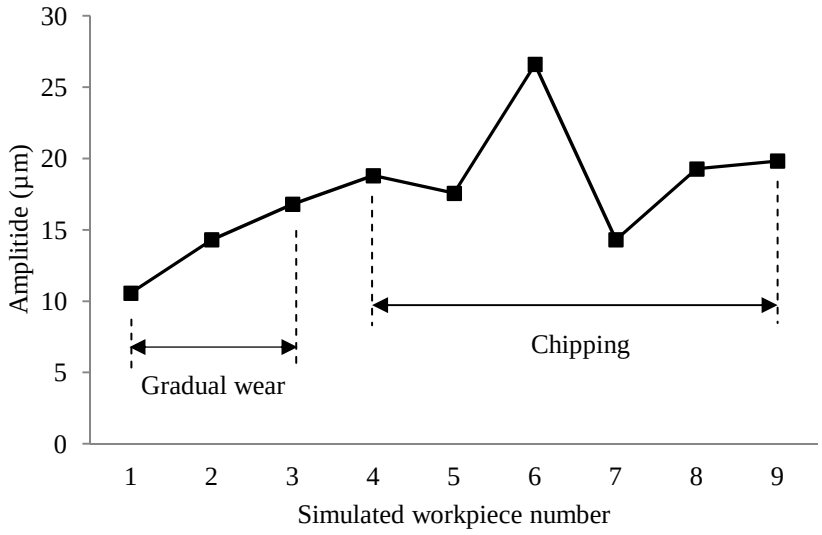

Figure 4.19: Variation of the amplitude of fundamental feed frequency of the simulated surface profile from gradual wear to chipping

As shown in Figure 4.20, when the cutting tool has chipped, it was observed that the R_t decreased due to the depth of cut reduced. When the cutting tool undergoes continuous chipping on the steep groove of the tool nose, this leads to the workpiece profile signalled by the higher value of R_t. This behaviour explains the

significant fluctuations of the R_t of surface profile and consequently leads to the fluctuations in amplitude of the fundamental feed frequency.

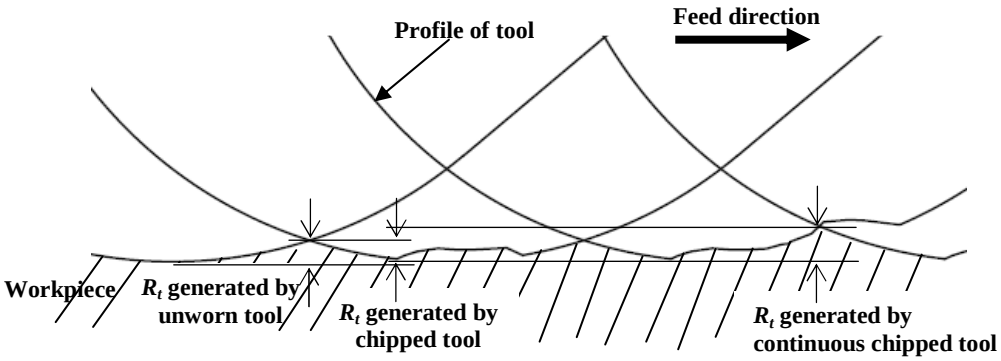

Figure 4.20: Tool nose area showing the maximum peak-to-valley height R_t of workpiece profile generated from unworn and chipped tool profile

4.3.2 Results of offline experiment

An offline preliminary study on detecting the tool chipping in ceramic insert was conducted. A commercially available carbide cutting tool (TNMG 160404 MF – Sandvik Ltd.) was used for studying the effect of gradual wear on the amplitude of fundamental feed frequency and its harmonics in a separate experiment. The carbide cutting insert was observed using a SEM after machining as shown in Figure 4.21. It can be seen that there was no chipping or breakage on the edge of cutting insert after eight minutes of machining. Thus, the wear pattern on the carbide insert can be considered as gradual wear which mainly due to the abrasion.

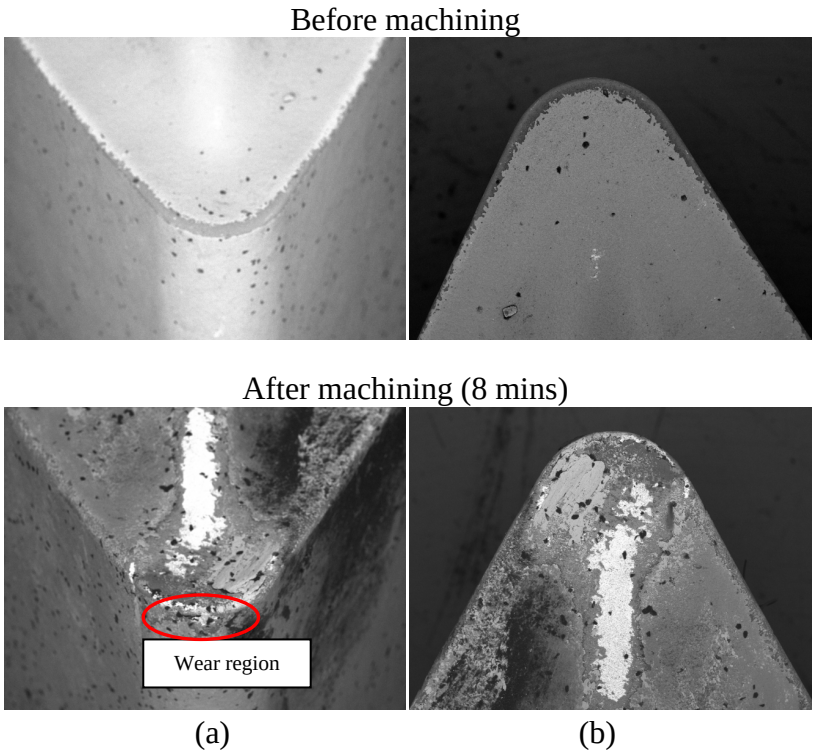

Figure 4.21: SEM observation of carbide cutting insert before and after machining (a) isometric view, and (b) top view.

Figure 4.22 shows the evolution of the amplitude of fundamental feed frequency and its harmonics as a function of cutting time for the carbide cutting insert. Figure 4.22(a) shows the amplitude of the fundamental feed frequency is constant as the cutting tool undergoes minimum wear within a short cutting duration of 76.3 seconds. Gradual wear progresses slowly, therefore to demonstrate the effect of gradual wear on the amplitude of fundamental feed frequency and its harmonics the workpiece profile images were captured at the end of each cutting interval of 2 minutes. The result in Figure 4.22(b) shows that the amplitude of the feed frequency increased gradually with tool wear for a cutting duration of 8 minutes. As seen in Figure 4.22, there was no distinctive trend observed in the harmonics of the feed fundamental frequency. These results agree closely with those from the simulation study shown in the Figure 4.17.

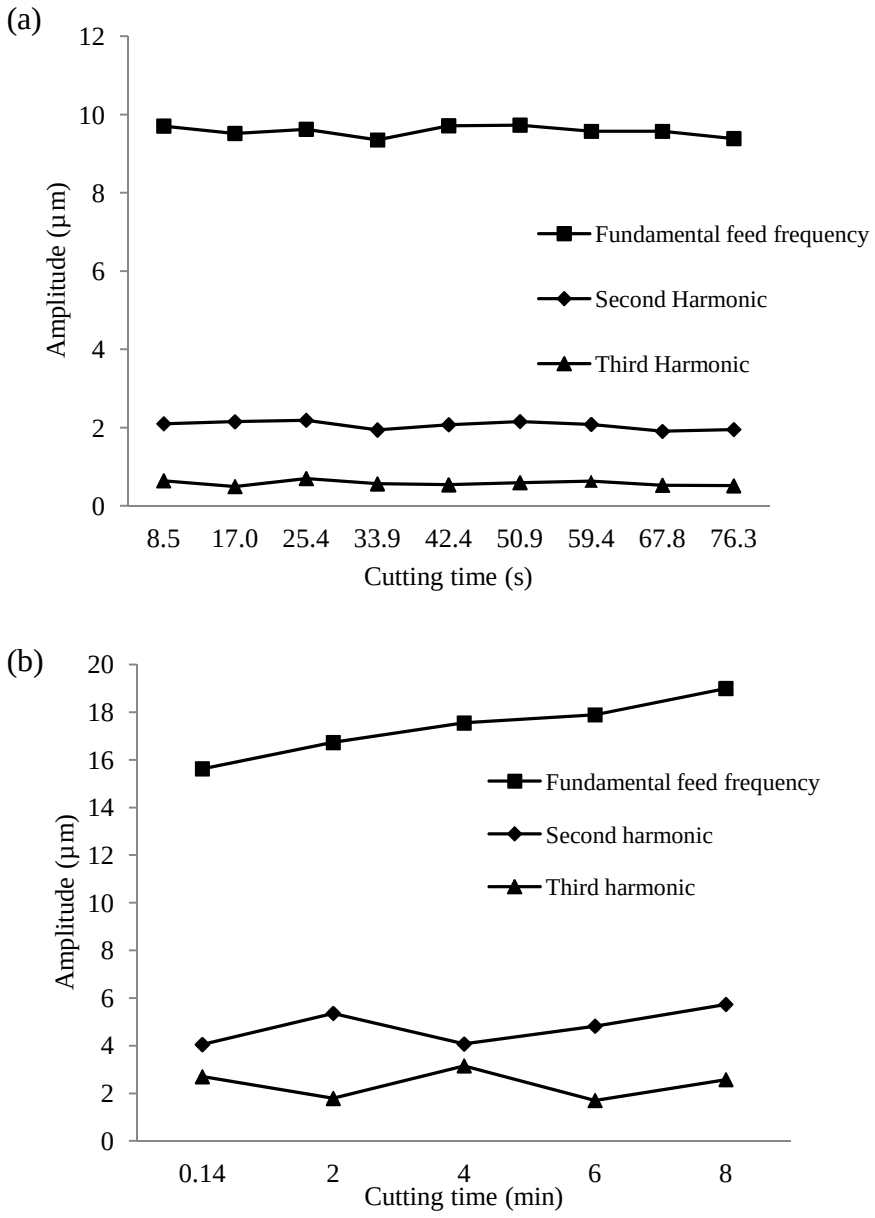

Figure 4.22: Variation of the amplitude of fundamental feed frequency, second harmonic and third harmonic of actual surface profile from turning stainless steel work piece using carbide insert in (a) cutting time duration of 76.3 s, and (b) cutting time duration of 8 minutes

Figure 4.23 shows an example of zoomed in spectrum analysis for actual surface profile obtained from experiment using carbide cutting insert. It can be found that the amplitude spectrum for the workpiece surface machined using the carbide insert exhibits a strong fundamental feed frequency of 2.538 mm^{-1} and frequencies that are nearly multiplies of the fundamental feed frequency, i.e. harmonics. There is

always a constant fundamental feed frequency for any cutting conditions because the surface profile along the axis of the workpiece is generated by the tool geometry forming one feed groove for each rotation of the workpiece. The fundamental feed frequency V_f is represented in FFT analysis as described in Equation 3.3, where f is the tool feed. Since the feed used in this experiment was 0.4 mm a fundamental feed frequency of 2.5 mm^{-1} in an ideal workpiece profile is expected as seen in Figure 4.16. The deviation between the theoretical fundamental feed frequency (2.5 mm^{-1}) and the actual (2.538 mm^{-1}) is due to the inconstancies in tool movement per object rotation or uneven movement of the tool feed system in the lathe.

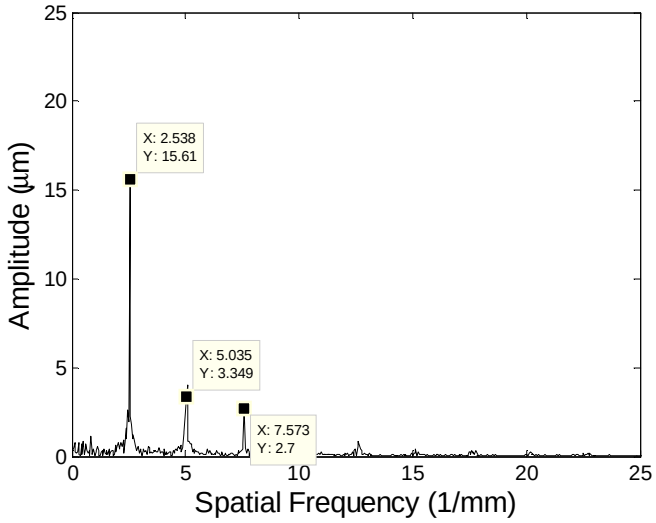

Figure 4.23: Example of FFT analysis for actual surface profile obtained from the experiment using carbide cutting insert

The profile of the turned surface was analyzed further to better understand increase in surface roughness is due to the increase of tool wear. Figure 4.24 shows the images of workpiece profile and the roughness profile extracted from the 2-D images of the edge of workpiece. From the figure, it was observed that for fresh tool the workpiece profile of the turned surface closely resembles the ideal geometrical shape of the tool as in the simulated turning process. As seen in the figure, the

surface roughness profile is repeating periodically as expected and the length of each cycle (wavelength) is nearly equal to the machining feed per revolution (0.4 mm).

(a) Cutting time: 0.14 min

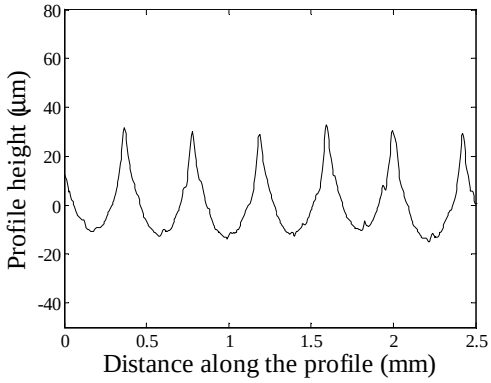

(b) Cutting time: 4 min

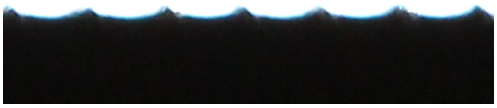

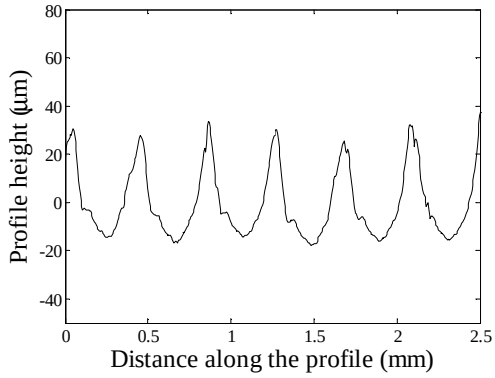

(c) Cutting time: 8 min

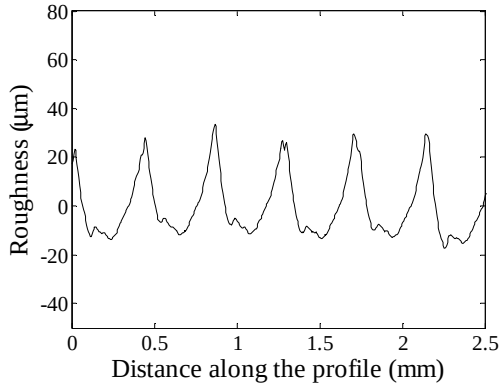

Figure 4.24: 2-D images of the workpiece profile from turning with carbide cutting insert and their corresponding surface roughness profile at cutting time duration of (a) 8.5 s, (b) 50.9 s, and (c) 84.8 s

The maximum peak-to-valley height of the surface profile (R_t), which is the vertical distance between the highest peak and the lowest valley within the evaluation length, was determined from the images of the workpiece profile. The changes in R_t for the roughness profile are shown in Figure 4.25. The amplitude of peak-to-valley of the surface profile at the initial cutting stage is lower and increased with cutting time. Grzesik and Zalisz (2008) and Penalva et al. (2002) reported similar findings that when tool wear increases, i.e. the maximum peak-to-valley of the roughness profile also increased. They explained that the increase of R_t is due to the peak of the workpiece profile tend to be higher (maximum height of the surface profile peak (R_p) increases) as the tool wear increases.

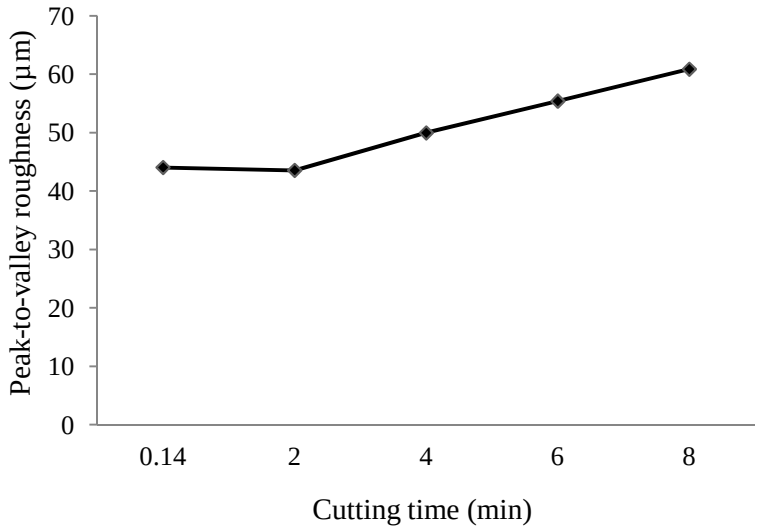

Figure 4.25: Peak-to-valley roughness parameter (R_t) as a function of cutting time for carbide insert

An in-housed fabricated ceramic cutting insert (zirconia-toughened alumina (ZTA) + magnesium oxide (MgO)) was used for studying the effect of chipping on the amplitude of fundamental feed frequency of workpiece profile and its harmonics. From the SEM images shown in Figure 4.26, it was observed that the ceramic cutting

insert chipped severely on the rake face at the end of the turning process. Since ceramic is a brittle material, friction between the tool-workpiece interfaces caused premature tool failure by chipping instead of gradual wear. The detection of these failure modes in ceramic cutting insert is important since chipping may occur early during the turning.

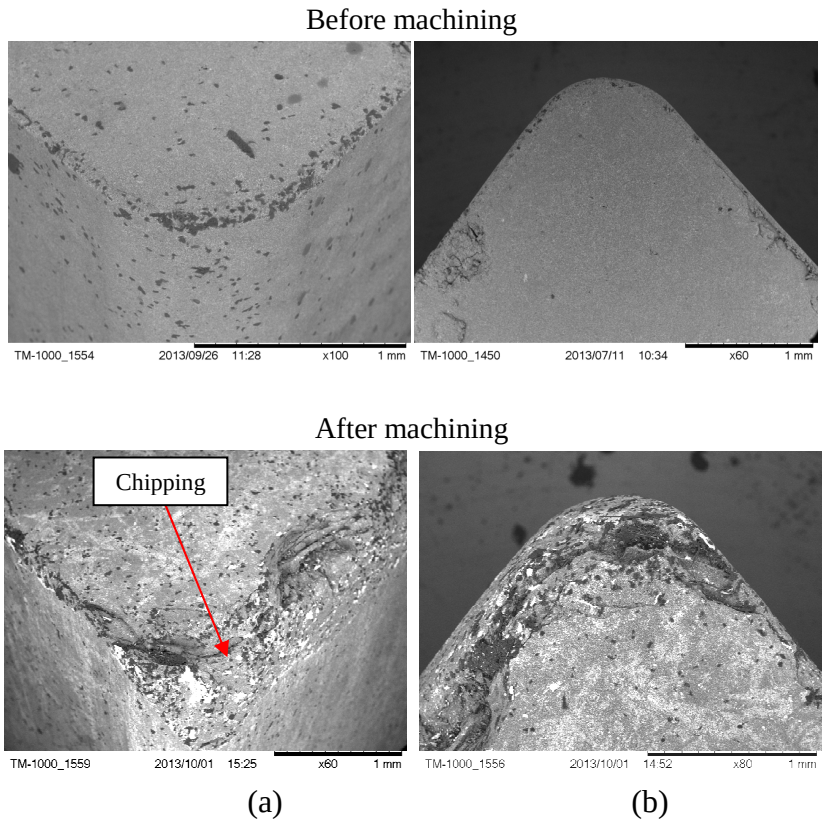

Figure 4.26: SEM observation of the ceramic cutting insert before and after machining (a) isometric view, and (b) top view

According to the result shown in Figure 4.27, it can be seen that there was a drop to nearly 14.1% in amplitude of fundamental fed frequency and was remained stable from 17.0 s to 42.4 s. After 42.4 s. the amplitude of fundamental feed frequency fluctuated significantly, the trend was clearly upward and downward in between 19.7% and 27.9%. Figure 4.28 shows the 2-D images of workpiece profile at selected intervals of cutting time and their corresponding roughness profile plots.

It can be observed that the workpiece profile at the end of cutting process (cutting time of 84.8 s) has irregular peak-to-valley heights compared to the profile from the fresh cut at cutting time of 8.5 s due to the severe chipping of the cutting tool edge. Figure 4.28(a) shows that the surface profile was close to the theoretical profile at the initial cutting stage at 8.5 s. However, when severe chipping has taken place the amplitude of roughness profile is not uniform but fluctuates as seen in Figure 4.28(c).

Figure 4.29 shows that there is significant fluctuation in the peak-to-valley height of surface profile which explains the fluctuation in the amplitude of fundamental feed frequency in cutting time interval of 42.4 s to 84.8 s was observed. Ideally, when the cutting tool edge is still intact the surface profile of the workpiece is predominantly affected by the feed. When the edge of cutting insert has been damaged by chipping the surface of workpiece will not be affected by the tool nose and the feed only but many other influencing factors will be introduced.

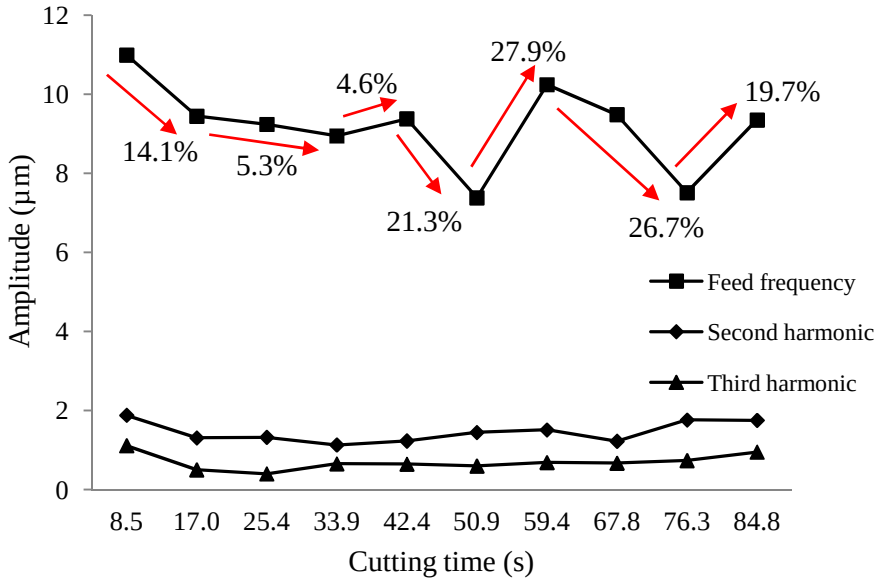

Figure 4.27: Variation of the amplitude of fundamental feed frequency, second harmonic and third harmonic of actual surface profile from turning stainless steel workpiece using ceramic insert.

(a) Cutting time: 8.5 s

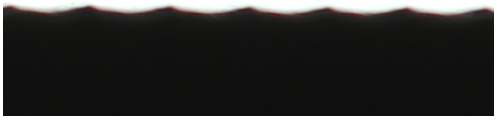

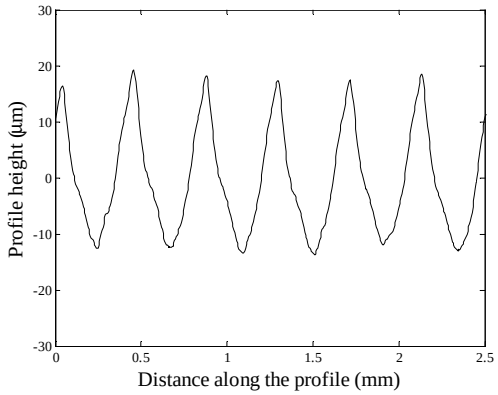

(b) Cutting time: 50.9 s

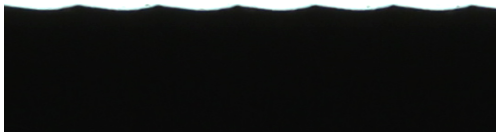

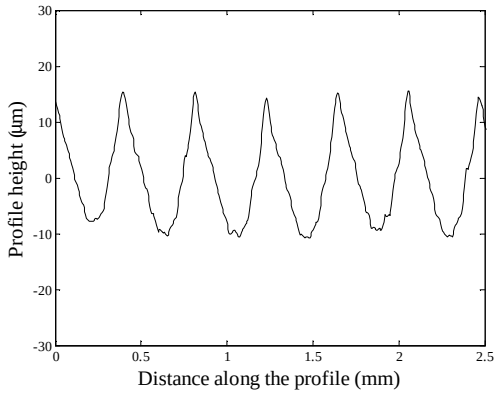

(c) Cutting time: 84.8 s

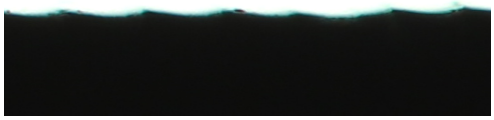

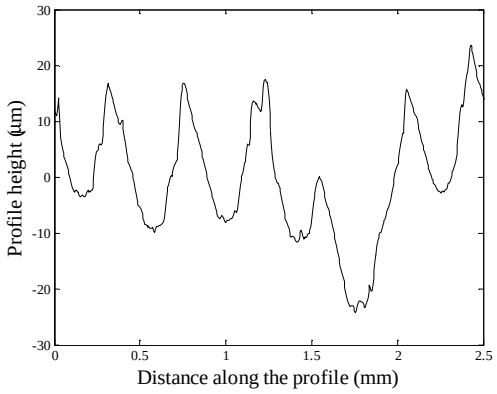

Figure 4.28: 2-D images of the edge of workpiece from turning with ceramic cutting insert and their corresponding surface roughness profile at cutting time duration of (a) 8.5 s, (b) 50.9 s, and (c) 84.8 s

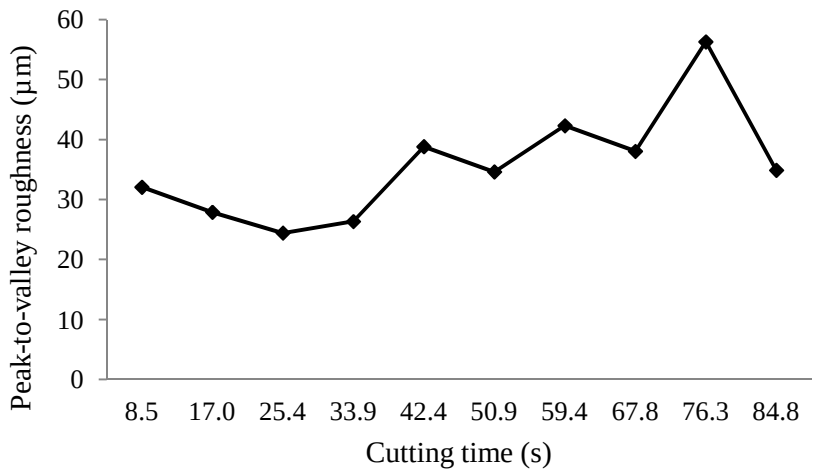

Figure 4.29: Peak-to-valley roughness parameter (R_t) as a function of cutting time for ceramic insert.

Previous experimental work (Lan & Dornfeld, 1984) showed that cutting forces increase suddenly due to tool fragments being squeezed between the tool and workpiece when tool is chipped, and subsequently decline. The level of cutting force may increase or decrease due to chipping of the cutting tool depending on the degree and type of chipping. The force level change after the cutting tool chipped off is caused by a loss of the depth of cut and accompanying decrease in the chip load on the tool. Thus the machining process become unstable as the cutting forces excites the tool and workpiece to vibrate significantly when the cutting tool has chipped. The effect of the relative tool and workpiece vibration leads to instability in the machining process and determine whether the tool cuts deeper or shallower from the surface of workpiece. Consequently the peak-to-valley height of the workpiece profile fluctuates. Oraby and Alaskari (2008) also reported that consistent correlation was found between surface roughness and cutting force. When the cutting forces fluctuate the surface roughness of the work material also fluctuated, thus leading to a sudden drop and increase in the amplitude of the fundamental feed frequency.

4.3.3 Simulation results on detection of tool chipping from surface profile signature using FFT by considering the presence of tool-workpiece vibration

Results of simulation study on the detection of tool chipping from surface profile signature in Section 4.3.1 only considered the change on the tool nose profile due to gradual wear and chipping. Vibration between the tool and the workpiece was excluded. Since the simulated workpiece profile produced by the worn and chipped tool are periodic, the fundamental feed frequency is predominant and is accompanied with small amplitude spatial frequencies at harmonics of the fundamental feed frequency. Thus, the offline study only considered the amplitude of fundamental feed frequencies and its harmonics, while the amplitudes in other frequencies were not investigated.

When the workpiece profile was turned with a worn cutting tool caused by gradual wear, a new spatial frequency of around 16 mm^{-1} was found as shown in Figure 4.30(a)(ii)-(b)(ii). This is due to the presence of irregularities in the workpiece profile due to a regular vibration between the cutting tool and the workpiece. When a tool has chipped the surface profile is accompanied by random dislocation of vibration as shown in Figure 4.30(c)(i)-(d)(i). From the corresponding FFT plot shown in Figure 4.30(c)(ii)-(d)(ii) little ripples in frequencies was observed due to the sudden changes from one frequency component to another due to the randomness of the dislocation in surface profile. Presence of the waviness in surface profile as shown in Figure 4.30(e)(i) results in a conspicuous low spatial frequency as shown in Figure 4.30(e)(ii).

The amplitude of fundamental feed frequency are almost equal because the periodic simulated workpiece profile with wavelength of 0.4 mm contributes a strong fundamental feed frequency of 2.5 mm^{-1}. There was no obvious impact of the

dislocation of workpiece profile due to vibration on periodic ideal surface profile at wavelength of feed. Therefore, the amplitude of the fundamental feed frequency was approximately same. The dislocation in workpiece profile due to regular and random tool-workpiece vibration with the wavelength that not equal to feed distance excites other spatial frequencies that beyond the fundamental feed frequency.

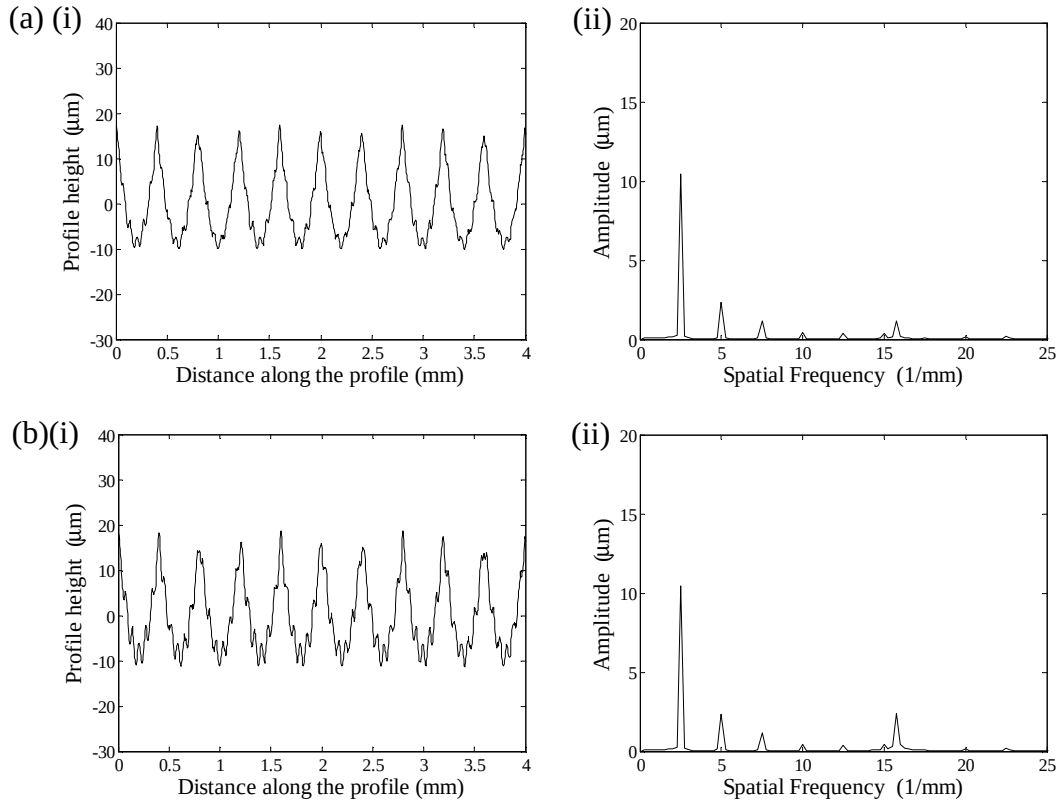

Figure 4.30: (a)(i) Simulated surface profile with increasing vibration amplitudes by 5% peak-to-valley height of simulated ideal workpiece profile and (ii) corresponding FFT plot; (b)(i) simulated surface profile with increasing vibration amplitudes by 10% peak-to-valley height of simulated ideal workpiece profile and (ii) corresponding FFT plot (ii); (c)(i) simulated surface profile with random vibration with 5 times higher vibration magnitude as in (a) and (ii) corresponding FFT plot; (d)(i) simulated surface profile with random vibration with 10 times higher vibration magnitude as in (a) and (ii) corresponding FFT plot; and (e) simulated surface profile with presence of waviness due to the tool-workpiece vibration by 10 times higher vibration magnitude as in (a) and (ii) corresponding FFT plot (Continued)

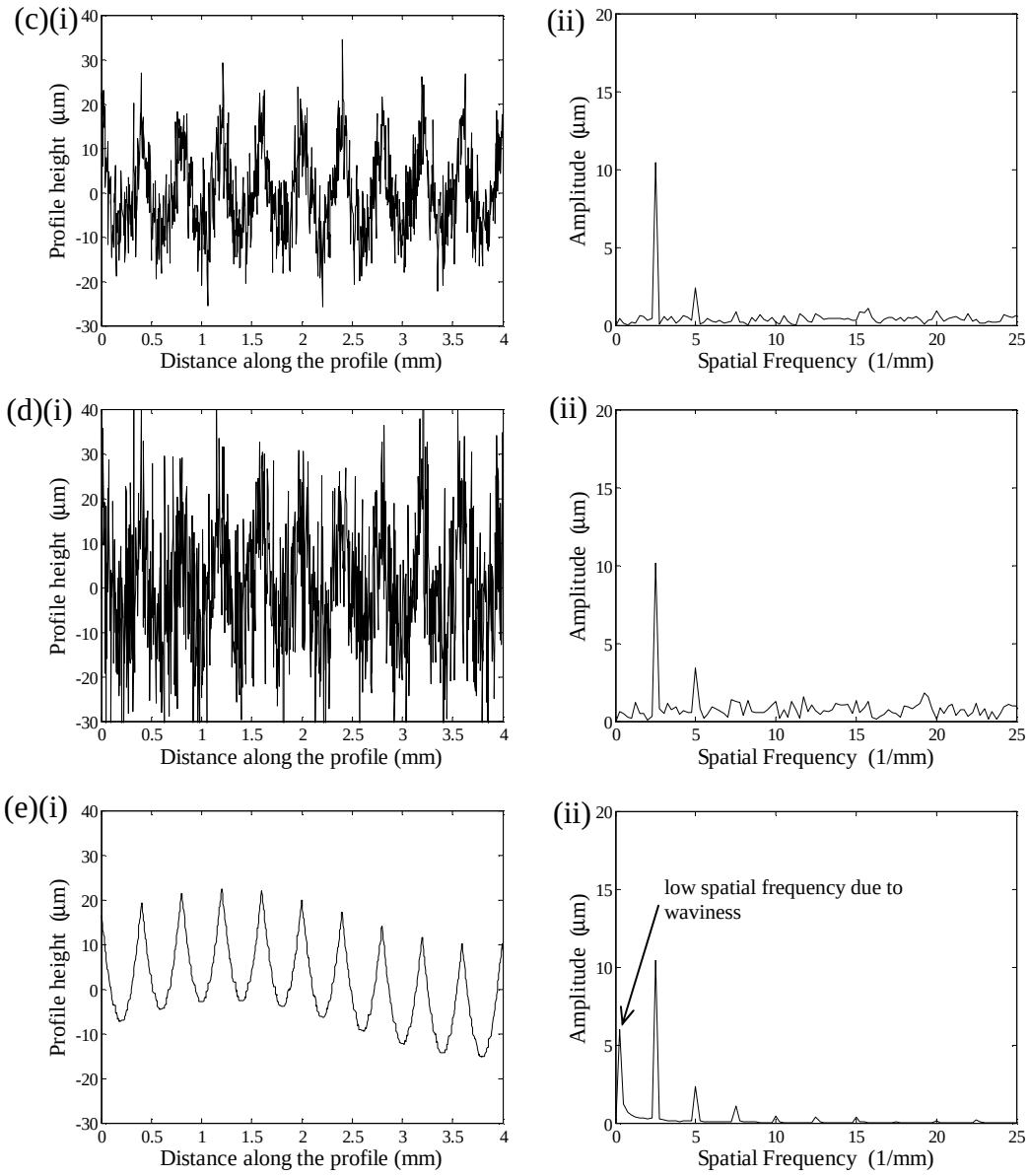

Figure 4.30: continued

4.3.4 Results of in-process experiment

The offline results have shown that the fundamental feed frequency extracted from the FFT of the workpiece profile can be used to detect the tool chipping in ceramic insert. The experimental work was conducted in-process to detect the tool chipping during turning of AISI 01 oil hardening tool steel using a commercial aluminium oxide based ceramic insert by investigating the distribution of the spatial frequencies along the workpiece profile. Figure 4.31 to Figure 4.34 show the zoomed

actual workpiece profile captured during turning for each pass and their corresponding extracted sub-pixel profile at six workpiece rotation angles. Figures 4.35(a)(i)-(d)(i) show the FFT for the actual workpiece profile obtained from the experiment (Figure 4.31 to Figure 4.34) after each pass for different workpiece rotation angles. It should be pointed out that the rotation angles of the workpiece at different cutting durations do not correspond to one another since the start of capturing of the profiles is random during the turning. The corresponding cutting inserts for each pass are shown in Figures 4.35(a)(ii)-(d)(ii).

Before tool chipping the amplitude of the fundamental feed frequency approximates to 2.5 mm^{-1} at various rotation angles of the workpiece is predominant as seen in Figures 4.35(a)(i), Figure 4.35(b)(i) and Figure 4.35(c)(i). This observation agrees with the FFT of the simulated ideal workpiece profile. When the machining process is stable the tool produces a periodic profile with almost constant wavelength at various rotation angles of the workpiece (Figure 4.31 to Figure 4.33). After a machining duration of 22.0 s severe chipping on the cutting edge of the ceramic inserts was observed (Figure 4.35(d)(ii)). Since ceramic is brittle, friction between the tool-workpiece interfaces causes premature tool failure by chipping instead of gradual wear. After the cutting insert has chipped the amplitude of the spatial frequencies lower than fundamental feed frequency increased sharply for all workpiece rotation angles as seen in Figure 4.35(d)(i). Figures 4.36 shows examples of zoomed-in FFT plot at workpiece rotation angles of 60^{o} before and after tool chipping. The results of experiment consistent with results of simulation, because of irregular surface profile introduced other spatial frequencies due to the random features exist in the surface profile after tool has chipped. Low spatial frequencies was observed was due to presence of the waviness.

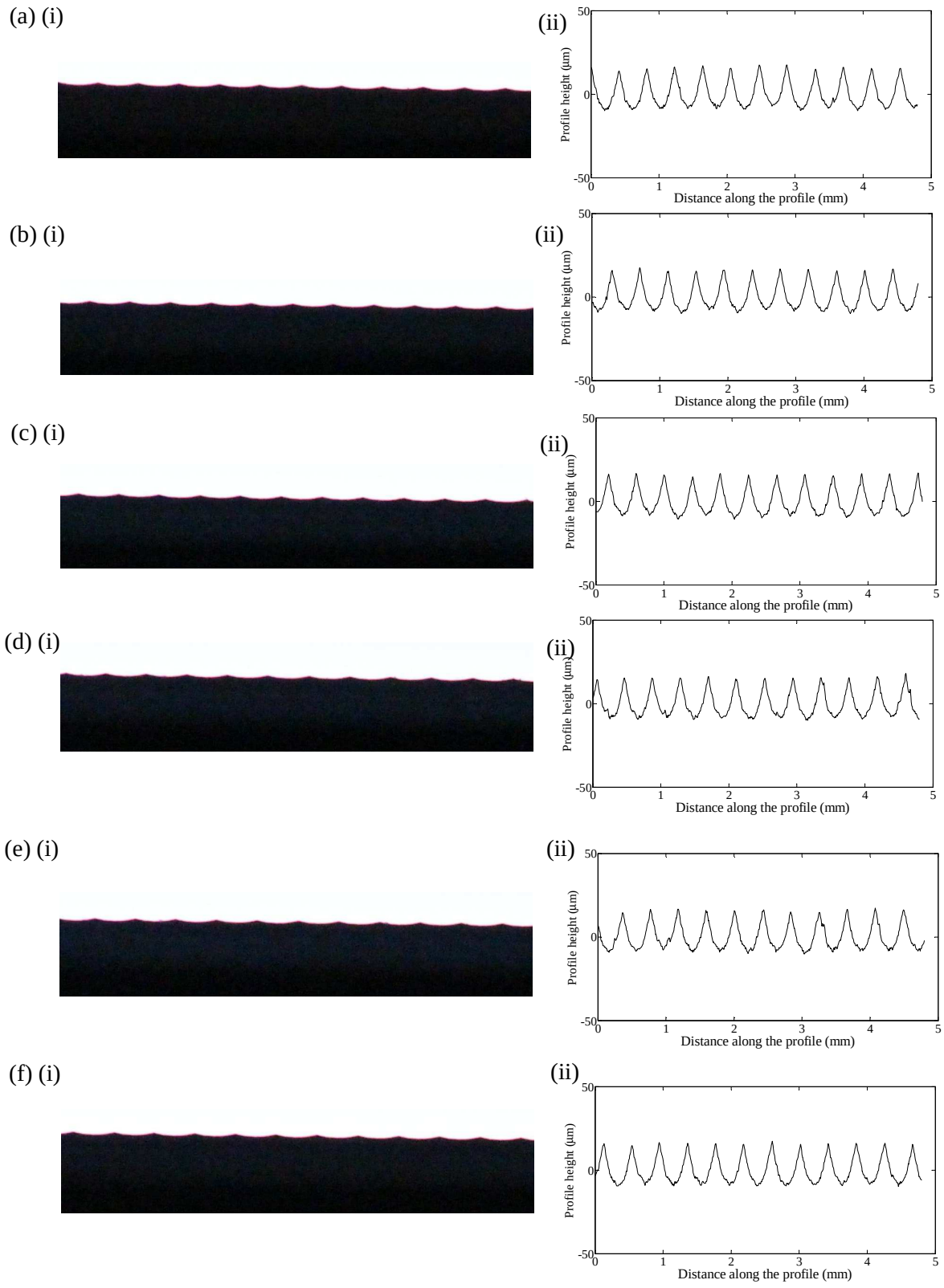

Figure 4.31: Zoomed in actual workpiece profile at different rotation angles (a) 0^o, (b) 60^o, (c) 120^o, (d) 180^o, (e) 240^o, (f) 300^o and their corresponding extracted sub-pixel profile at cutting duration of 5.5 s

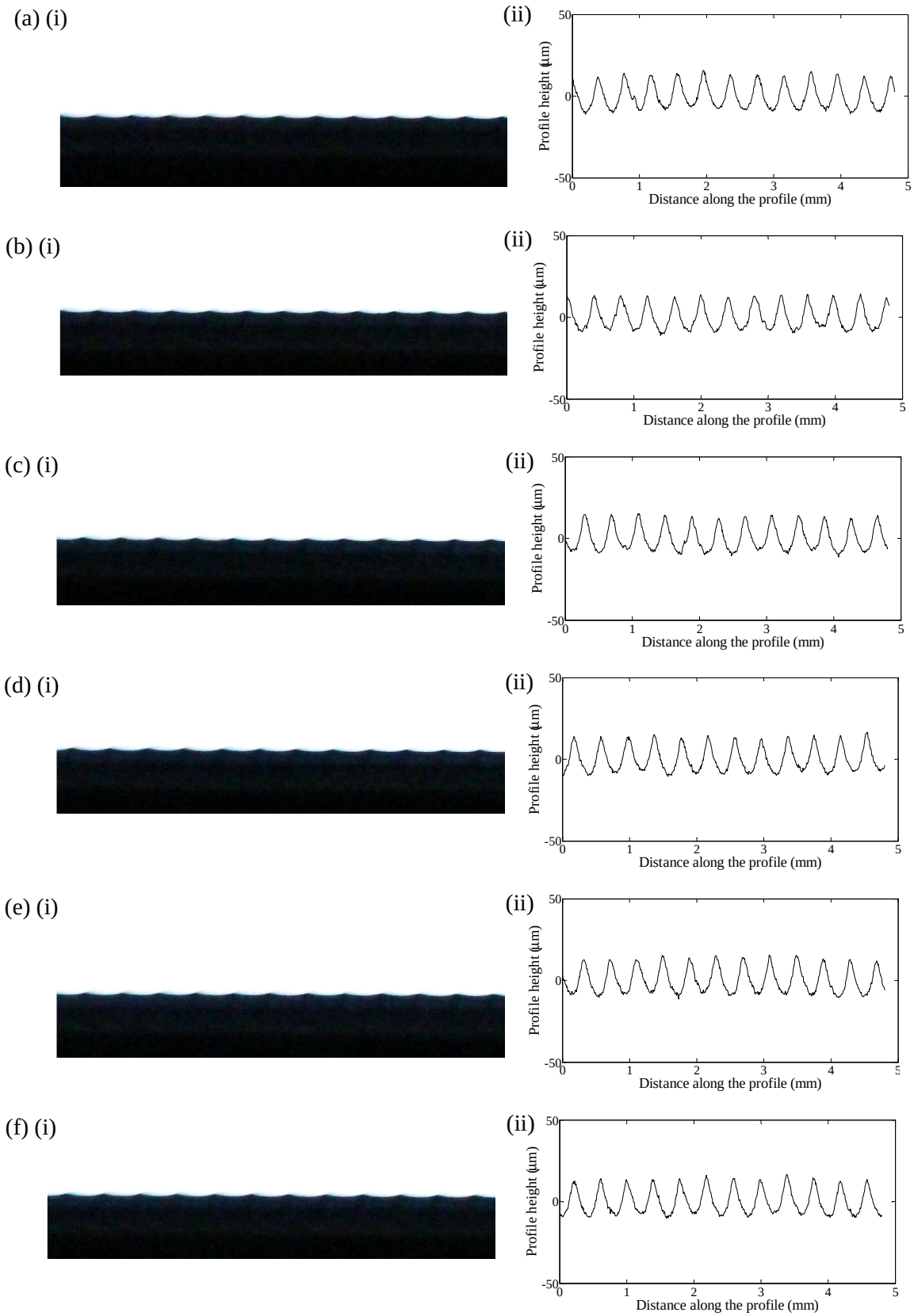

Figure 4.32: Zoomed in actual workpiece profile at different rotation angles (a) 0^o, (b) 60^o, (c) 120^o, (d) 180^o, (e) 240^o, (f) 300^o and their corresponding extracted sub-pixel profile at cutting duration of 5.6-11.0 s

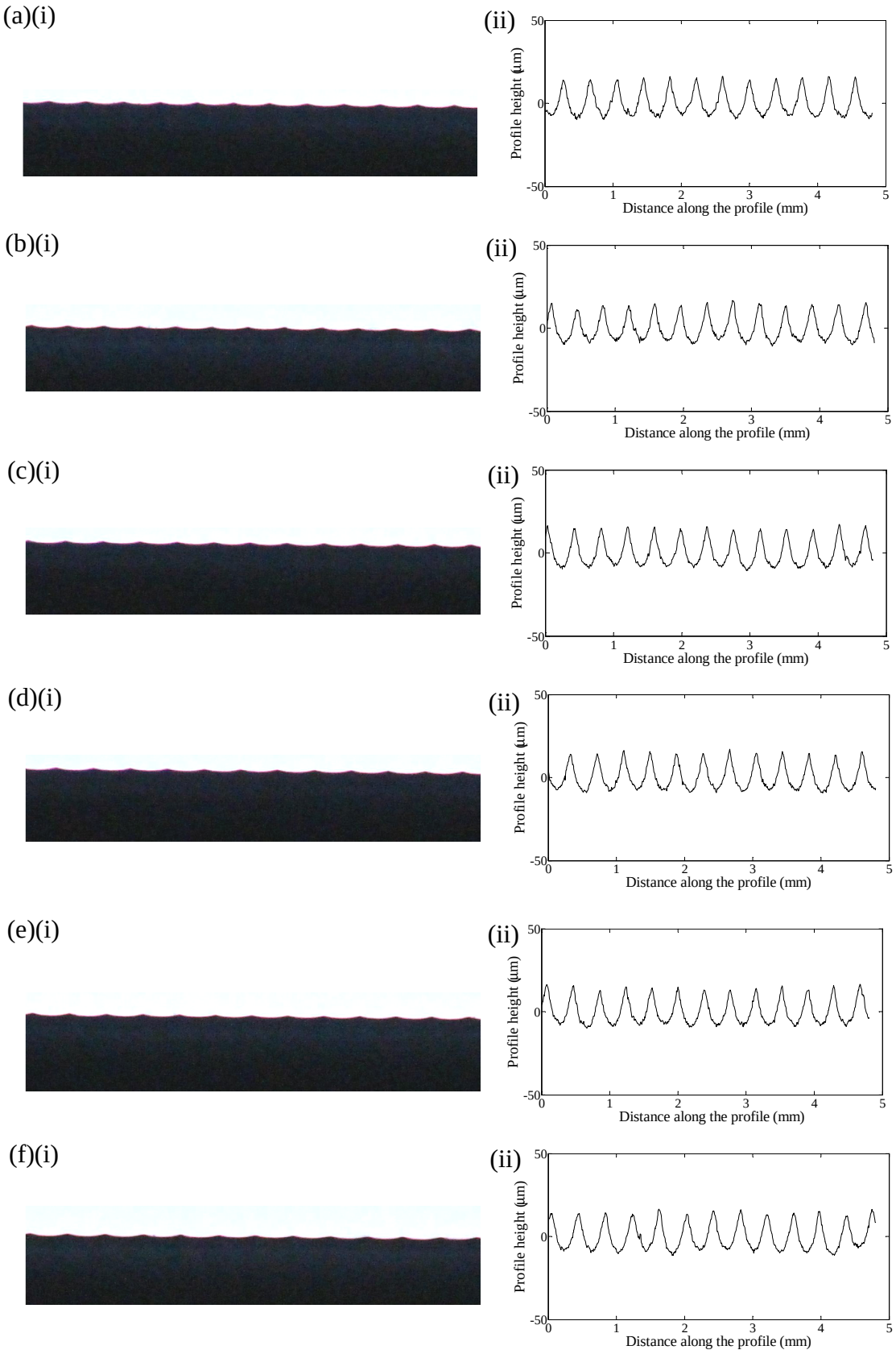

Figure 4.33: Zoomed in actual workpiece profile at different rotation angles (a) 0^o, (b) 60^o, (c) 120^o, (d) 180^o, (e) 240^o, (f) 300^o and their corresponding extracted sub-pixel profile at cutting duration of 11.1-16.5 s

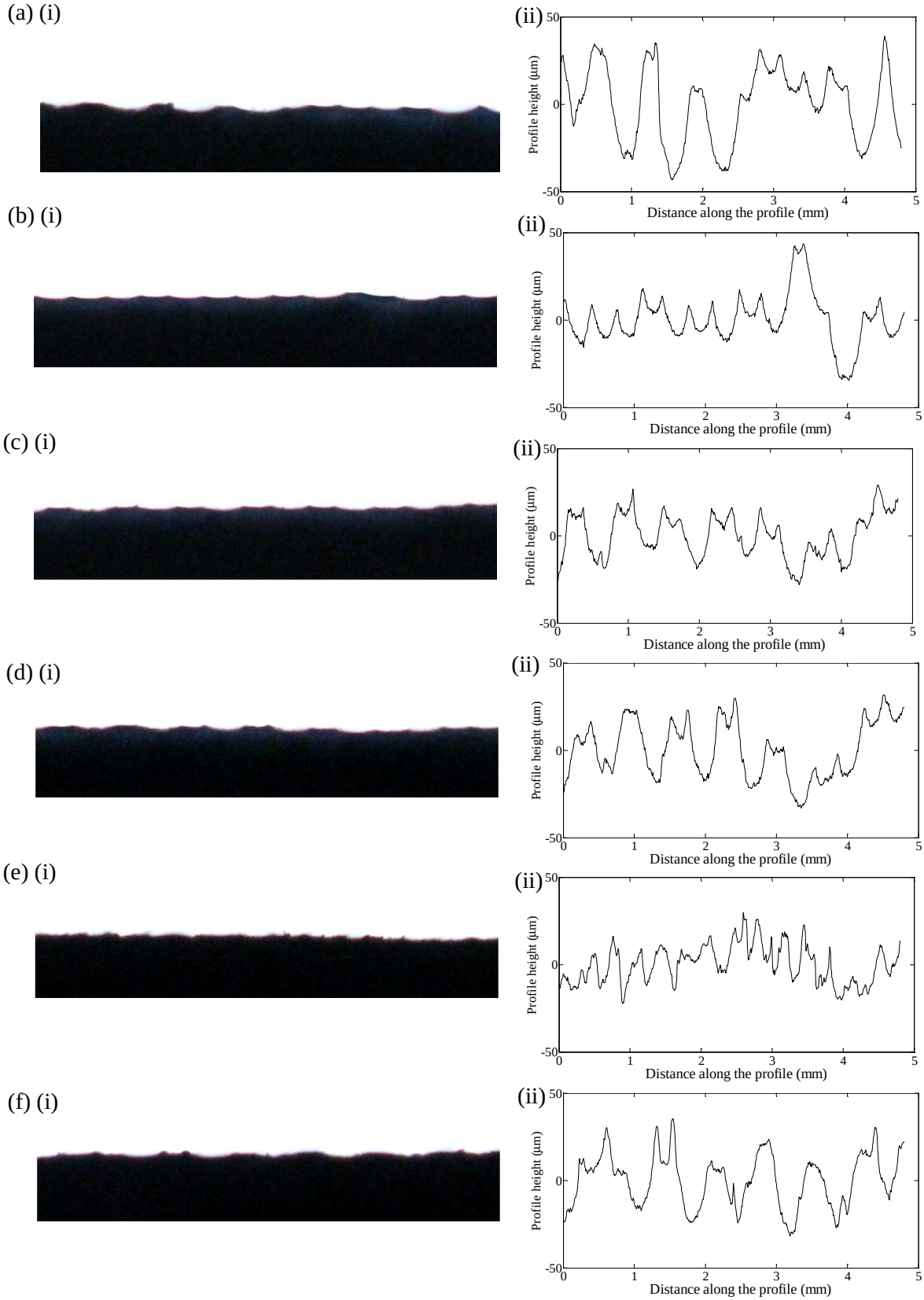

Figure 4.34: Zoomed in actual workpiece profile at different rotation angles (a) 0^o, (b) 60^o, (c) 120^o, (d) 180^o, (e) 240^o, (f) 300^o and their corresponding extracted sub-pixel profile at cutting duration of 16.6-22.0 s

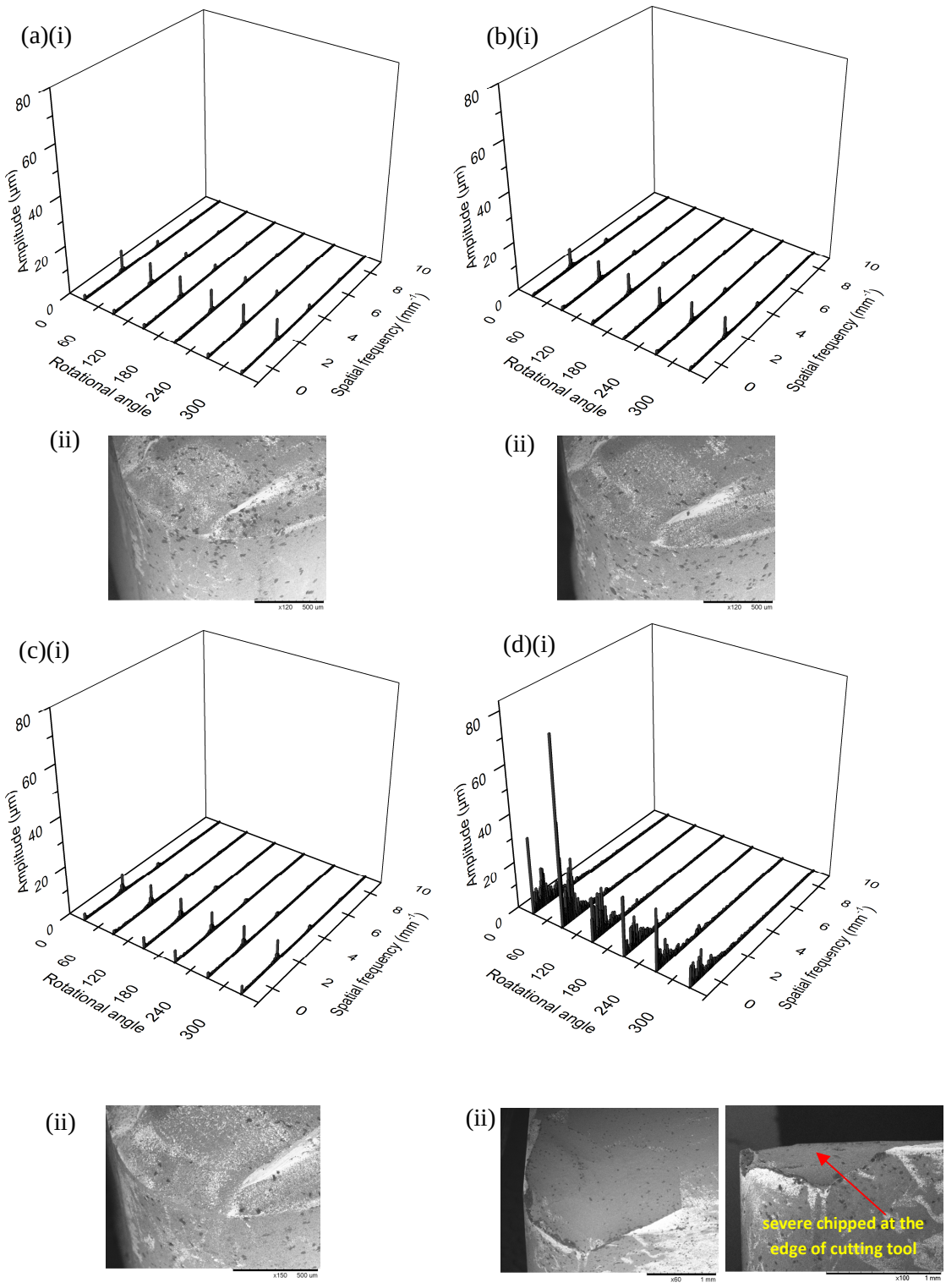

Figure 4.35: FFT of the actual workpiece profile for each pass and their corresponding cutting tool condition at cutting time duration of (a) 5.5 s, (b) 11.0 s, (c) 16.5 s, and (d) 22.0 s

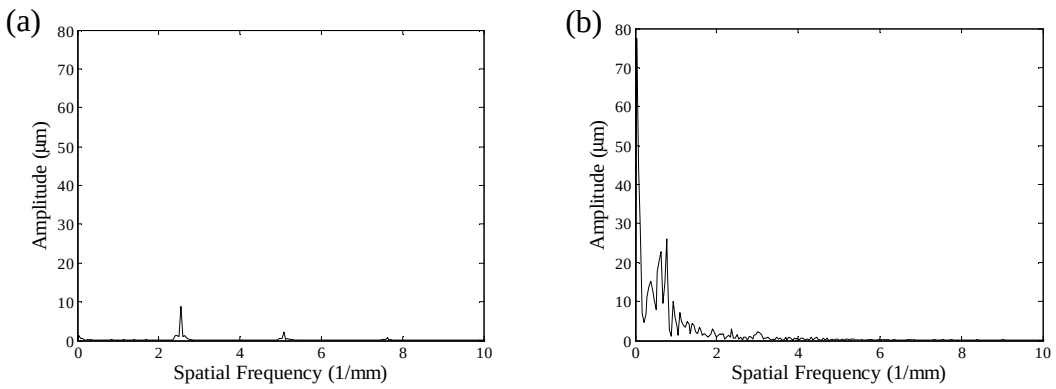

Figure 4.36: Examples of zoomed in FFT plot (a) before, and (b) after tool chipping

Figure 4.37 shows the variation in the amplitude of the fundamental feed frequency of the workpiece profile with cutting duration. The amplitude of the fundamental feed frequency remained almost constant with minimum gradual wear within a cutting duration of 16.5 s but decreased abruptly after the tool insert has chipped (Figure 4.37). This repeated result shows that the result obtained from offline and in-process experiments are in agreement which confirmed that the amplitude of fundamental feed frequency could be used to detect the tool chipping.

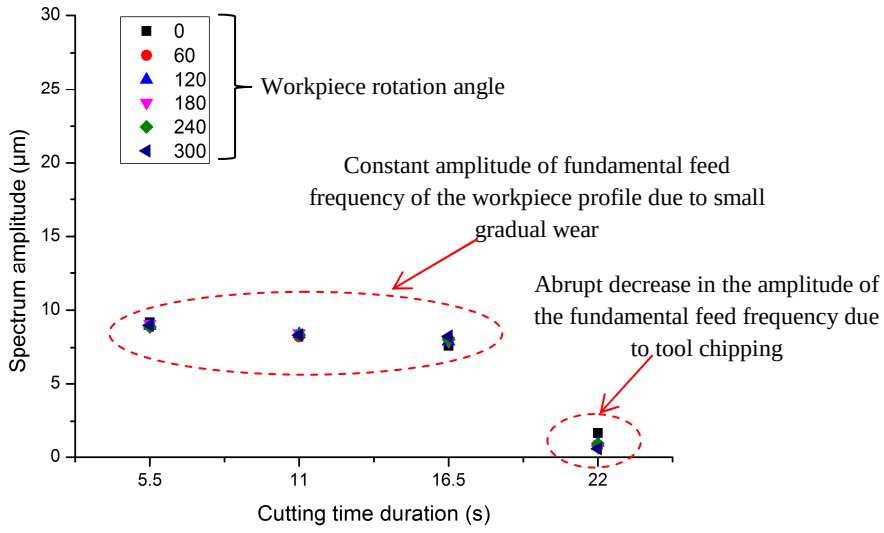

Figure 4.37: Variation in the amplitude of the fundamental feed frequency of the workpiece profile with cutting duration at various workpiece rotation angles.

4.3.5 Results of in-process onset detection of tool chipping from surface profile signature using sub-window FFT

As STFT analysis is highly dependent on window function and selection of window function is difficult as it affect accuracy due to attenuation effect in the window function cause a loss in spectral estimate. For this reason, attempt has been made to solve the problem by sub-window FFT that independent of window function. Figure 4.38 to Figure 4.40 show the sub-window of the FFT along the workpiece profile at different rotational angles for cutting duration of 16.5 s where the cutting tool undergoes gradual wear. As seen in Figure 4.38(a)(i)-(c)(i) to Figure 4.40(a)(i)-(c)(i), the sub-window of FFT for each workpiece profile shows a constant dominant peak appearing at the fundamental feed frequency of around 2.45 mm^{-1} which is approximately equal to the fundamental feed frequency of the ideal workpiece profile (reciprocal of the feed rate of 1/0.4 =2.5 mm^{-1}). In addition, the spectrum amplitude of each FFT window along the workpiece profile is similar to one another. This is because a periodic profile with almost constant wavelength along the workpiece was produced as shown in Figure 4.38(a)(ii)-(c)(ii) to Figure 4.40(a)(ii)-(c)(ii) at different rotational angles of the workpiece.

Figure 4.41(a)-(c) shows the sub-window and their corresponding workpiece profile for the subsequent pass at the time interval of 16.5 s to 22.0 s. The workpiece profile is divided into smaller length's window viz 4 mm equally for 5 sub sections and each of the sub window length's interval duration is 0.63 s. As seen in Figure 4.35 when the tool has chipped severely after a cutting duration of 22.0 s, the amplitudes at spatial frequencies lower than the fundamental feed frequency increase sharply starting from the first FFT sub-window for all rotation angles which was

thereafter cutting time duration of 16.5 s. Since each sub-window approximate to 0.63 s increment along the workpiece profile it can be concluded that the cutting tool chipped at cutting time of approximately 17.13 s.

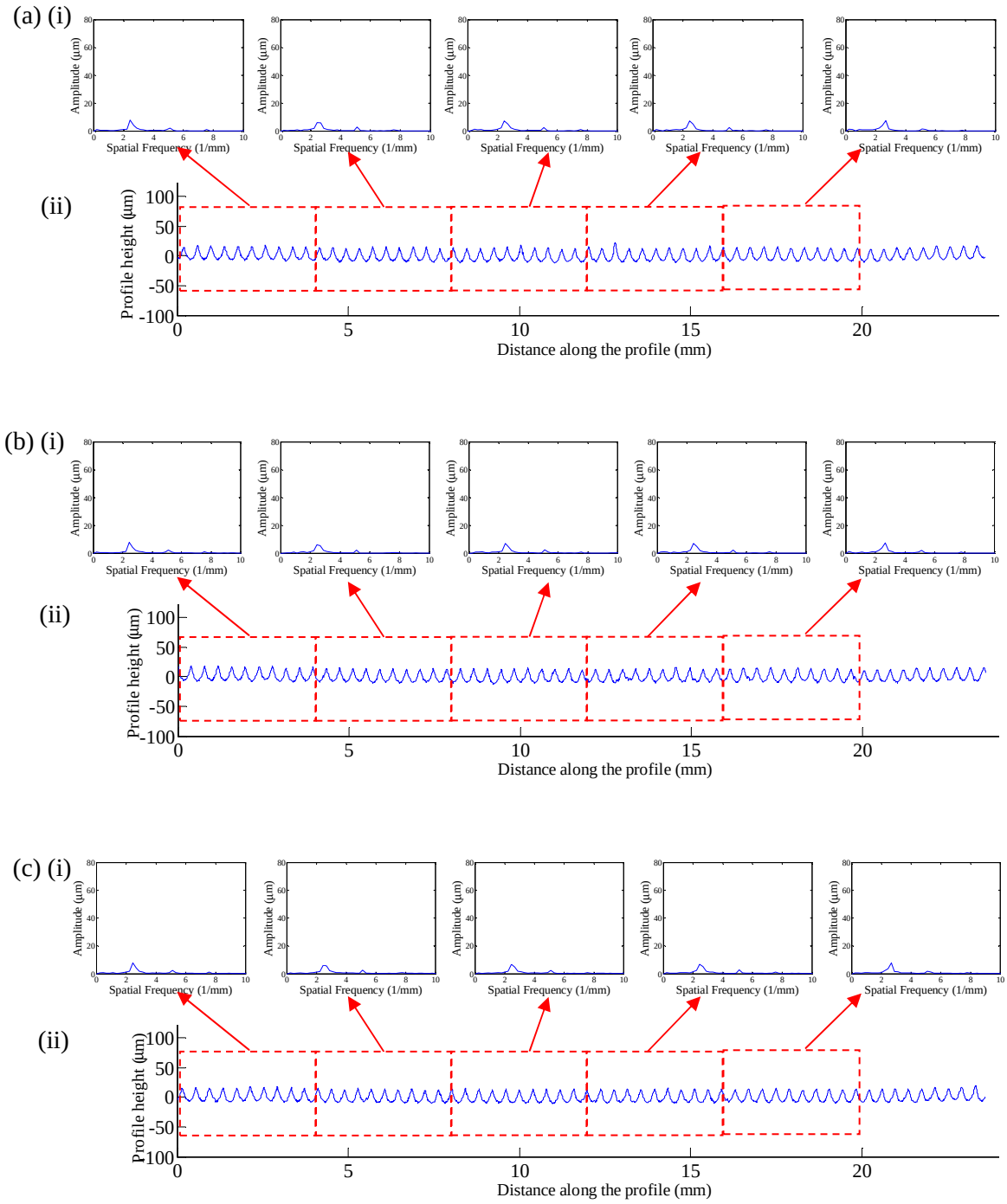

Figure 4.38: Sub-window of the FFT along the workpiece profile at different rotational angles (a) 0^o, (b) 120^o, and (c) 240^o in cutting time duration of 0-5.5 s

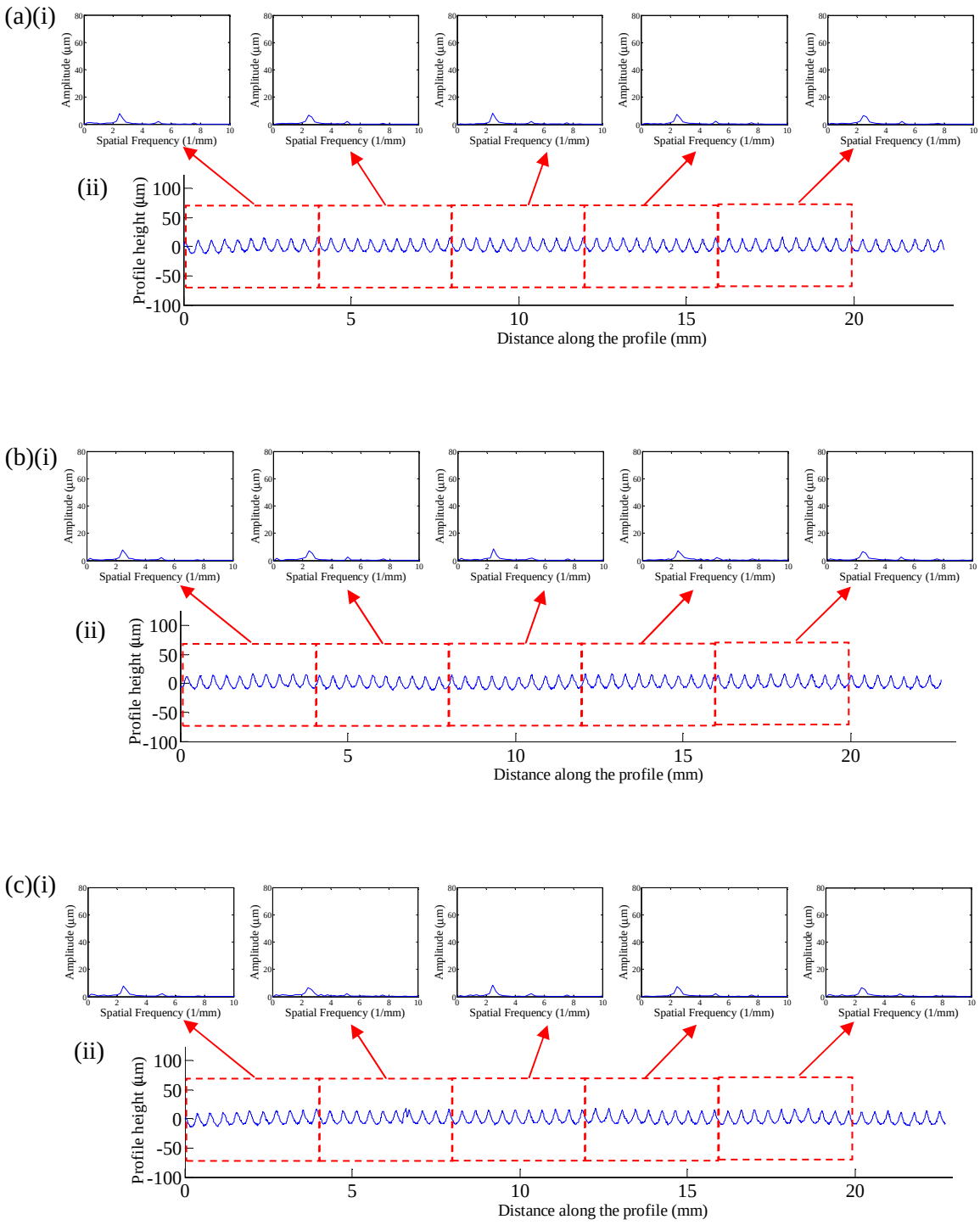

Figure 4.39: Sub-window of the FFT along the workpiece profile at different rotational angles (a) 0^{o}, (b) 120^{o}, and (c) 240^{o} in cutting time duration of 5.6-11.0 s

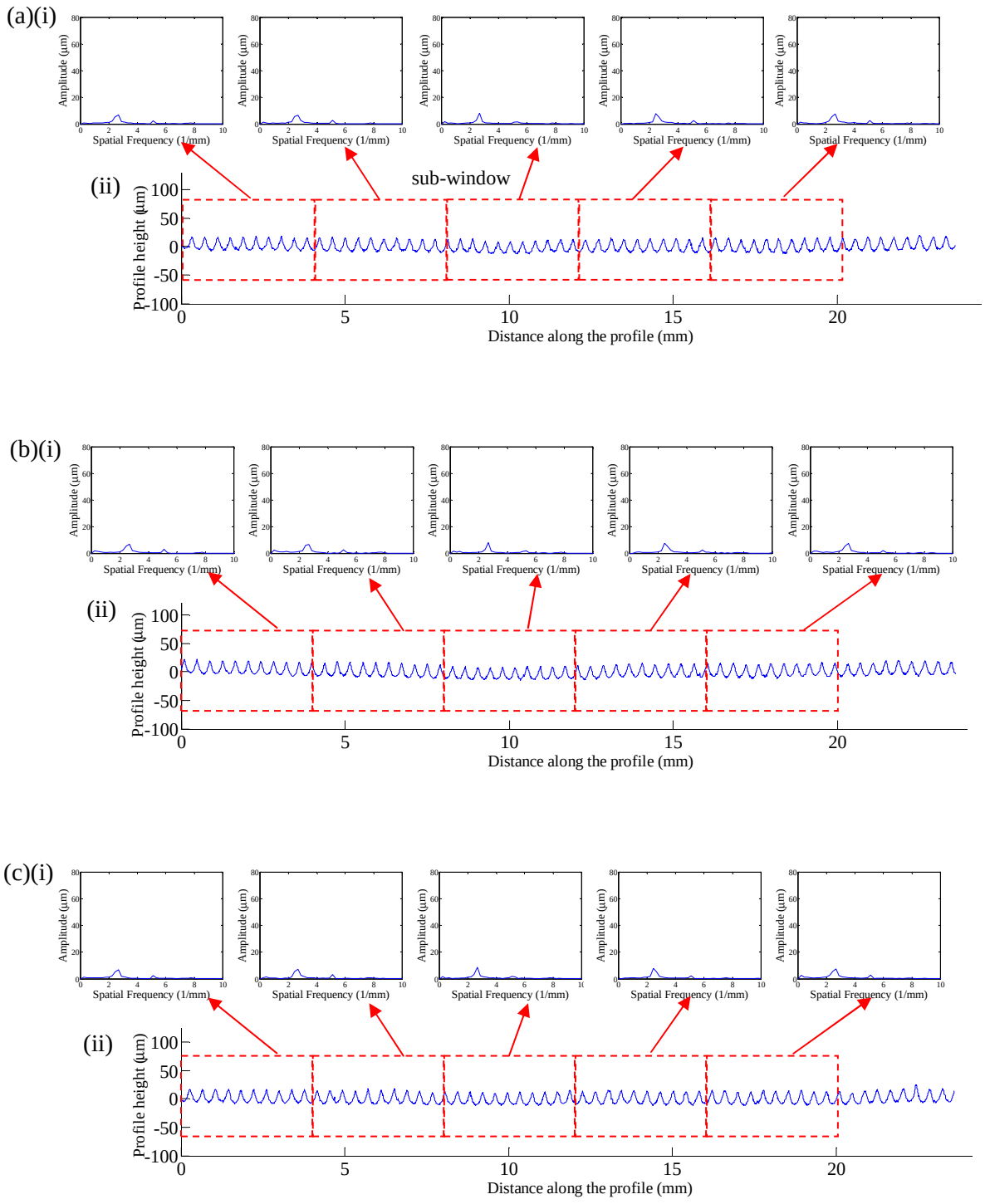

Figure 4.40: Sub-window of the FFT along the workpiece profile at different rotational angles (a) 0^o, (b) 120^o, and (c) 240^o in cutting time duration of 11.1-16.5 s

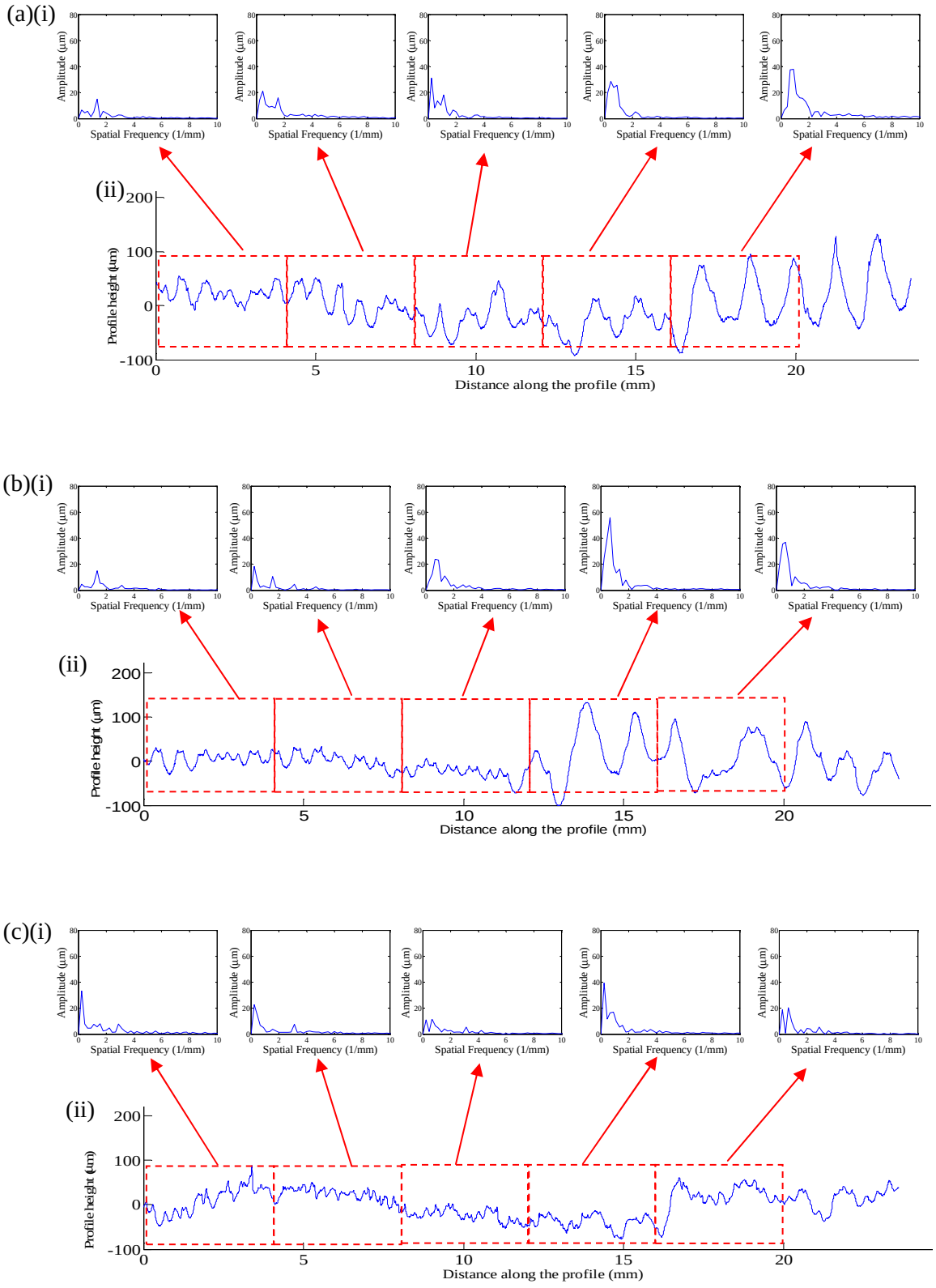

Figure 4.41: Sub-window of the FFT along the workpiece profile at different rotational angles (a) 0^o, (b) 120^o, and (c) 240^o in cutting time duration of 16.5-22.0 s

Figures 4.41(a)(ii)-(c)(ii) display the fact that after tool chipping the peak-to-peak distance is not always equal to the feed and the peak-to-valley heights of the surface roughness profile changes irregularly and fluctuate significantly, thus introducing other spatial frequencies and reducing the amplitude contributed by the feed wavelength. This is because when the cutting tool has chipped its effects on the cutting force variation can cause severe vibration between the tool and the workpiece during machining.

Figure 4.42 shows the tool-workpiece vibration in the axial, radial and tangential directions, respectively, during the turning at various cutting durations. In Figure 4.42(a) to Figure 4.42(c), small amplitudes of the tool-workpiece vibration in the axial, radial and tangential directions within cutting time duration of 16.5 s were observed as the cutting tool edge is still intact and the cutting process is steady and stable. Thus, only a very small amplitude of spatial frequency beyond the fundamental feed frequency appear due to the small chatter excited during the turning process when the cutting tool is still new is observed.

Measurements of the tool vibration have confirmed that the tool vibrates significantly during cutting time duration between 16.5 s to 22 s as large amplitudes of the tool-workpiece vibration in three directions was found after the tool has chipped (Figure 4.42(d)). Babouri et al. (2016) also found that when the cutting insert undergoes accelerated wear caused by chipping is accompanied by an increase in vibration. The machining process becomes unstable as the vibration between the tool-workpiece interfaces increased significantly when the tool edge has failed. As a result the vibration between the chipped tool and workpiece leads to unstable cutting and to the random fluctuations in the workpiece profile (Boryczko, 2011).

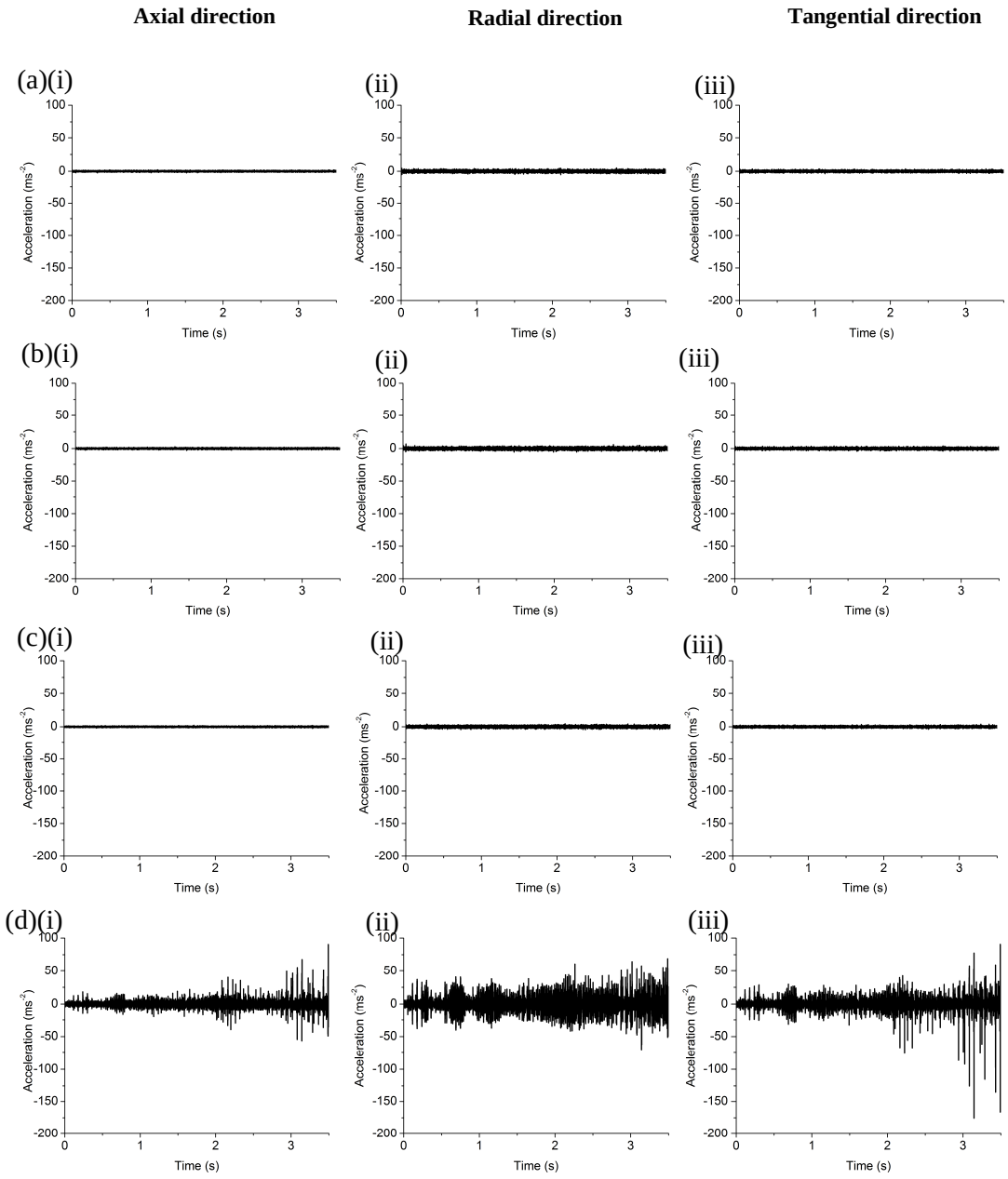

Figure 4.42: Vibration measurement within cutting time duration of (a) 5.5 s, (b) 11.0 s, (c) 16.5 s, and (d) 22.0 s

The tool-workpiece vibration also causes waviness in both the cutting and the tool feed directions. Because of the long wavelength and periodicity of waviness along the tool feed direction the waviness manifests as a sharp peak in the spectrum at lower spatial frequencies. Figure 4.41(a)(ii)-(c)(ii) and Figure 4.42(d) integrally show that tool-workpiece vibration leading to the occurrence of the significant

undulation of the surface waviness. Therefore, it was evident that the spatial frequencies lower than the fundamental feed frequency in the workpiece profile is mainly due to tool-workpiece vibration which caused by the tool chipping. The past research work by Cheung and Lee (2000) also have shown that the chatter vibration and rotational spindle error could be identified in the low spatial frequencies from the result of the spectrum analysis of the surface profile.

Figure 4.43 shows the one of example of zoomed sub-window FFT plot to show spatial frequencies around the fundamental feed frequency before and after tool chipping. When the cutting tool has chipped, the amplitudes of the spatial frequencies lower than the fundamental feed frequency increase for different rotation angles of the workpiece. FFT allows to identify certain spatial frequency components of interest to correlate to tool chipping. Therefore, the average of the amplitude of the spatial frequencies lower than the fundamental feed frequency in each sub-window was calculated as an indicator of tool chipping and are tabulated in Table 4.1.

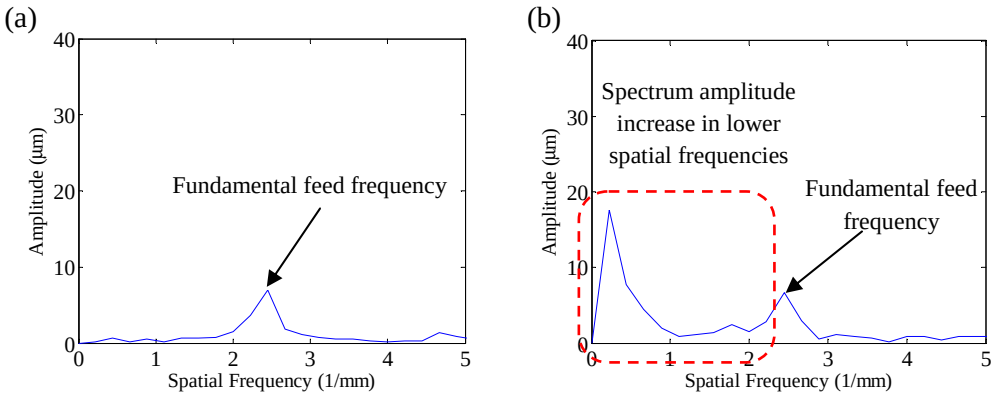

Figure 4.43: Zoomed sub-window of FFT of the workpiece profile for (a) before tool chipping, and (b) after tool chipping

Table 4.1: Average of spectrum amplitude at spatial frequencies lower than the fundamental feed frequency.

Duration (s)	Rotational angle	Sub-window				
		1	**2**	**3**	**4**	**5**
5.5	0	0.6993	0.7620	0.9144	0.8930	0.9601
	60	0.7751	0.7421	0.6497	0.7042	0.6739
	120	0.6212	0.7000	0.7947	0.8801	0.8147
	180	0.7857	0.7578	1.6125	0.7039	0.7489
	240	0.6830	0.5847	0.6349	0.7844	0.7275
	300	0.6297	0.6698	0.6663	0.6850	0.7741
11.0	0	0.9892	0.8445	0.5525	0.7122	0.9083
	60	0.8955	0.7825	0.8669	0.8264	1.0742
	120	0.8423	0.9315	0.9108	0.6753	0.7733
	180	0.9858	0.7850	0.7332	0.9580	1.0510
	240	1.0574	1.1974	0.8707	0.6070	0.9996
	300	0.8263	0.8401	0.7943	0.8098	1.1629
16.5	0	0.8266	0.8098	0.7362	0.6675	0.7671
	60	1.2783	0.6537	0.6612	0.8959	1.2237
	120	1.0443	1.2350	0.7487	0.7610	1.1360
	180	0.7167	0.7907	0.6748	0.9815	1.2032
	240	0.9475	0.6158	0.7018	0.7897	1.2136
	300	1.1428	0.8482	0.5136	0.8340	0.9094
22.0	0	4.6717	9.0307	9.1889	11.3930	14.8924
	60	3.2714	8.2668	16.9896	19.0731	22.6823
	120	4.0822	4.5554	9.1238	16.8191	13.5248
	180	5.5554	6.4563	6.7220	10.4054	9.8891
	240	5.5554	6.4563	6.7220	10.4054	9.8891
	300	4.2321	5.3848	7.8268	8.8003	6.7615

Low average values of the sub-window amplitude at spatial frequencies lower than the fundamental feed frequency were observed before tool chipping. The standard deviation of the average amplitude for each sub-window for various rotational angles in Table 4.1 is presented in Figure 4.44. The low standard deviation in the average sub-window amplitude at spatial frequencies lower than the fundamental feed frequency indicates that the workpiece profiles at different rotational angles are highly similar to one another before tool chipping. However, the standard deviation of the average sub-window amplitude at the spatial frequencies lower than the fundamental feed frequency for various workpiece rotational angle increased sharply at cutting duration of approximate to 17.13 s due to the non-

uniform workpiece profile generated at different rotational angle when the severe chipping has taken place.

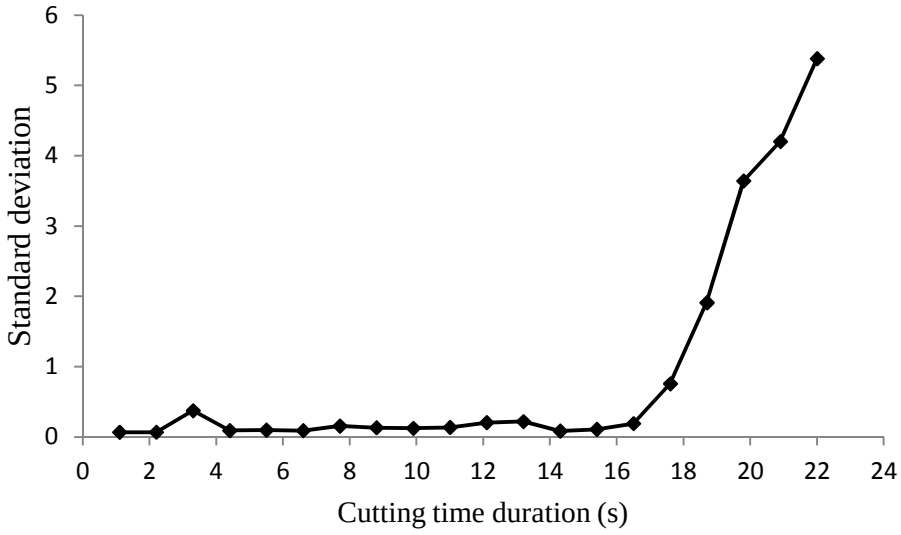

Figure 4.44: Standard deviation of the amplitude of FFT for each sub-window at various rotational workpiece angle.

4.4 Results of in-process onset detection of chipping in ceramic cutting tools based on the surface profile signature using CWT

Although the sub-window FFT of the workpiece profile was successfully applied to detect the tool chipping at cutting time duration of 17.13 s, the accuracy of the sub-window method is highly dependent upon the size of the window. Moreover, the FFT method is designed for the use with stationary signal. Since the waveform of the workpiece is non-stationary the wavelet analysis was applied to overcome the limitations of FFT (Josso et al., 2002; Grzesik and Brol, 2009).

Figure 4.45 shows the scalogram for the simulated ideal workpiece profile. Scale in CWT can be any real positive number. In this study, scale in the CWT is

determined based on the dyadic sampling (2^1, 2^2, 2^3,... etc) which is used in DWT. As shown in CWT of ideal profile, scale corresponding to feed frequency is ranging in between 60 to 80 (nearest power of two is 2^6). Higher scale should be used to detect the lower frequencies, thus the scale of 120 (approximate to 2^7) was applied to localize the lower frequencies. Figures 4.46 to Figure 4.48 show the corresponding scalograms for workpiece profile in Figures 4.38(a)(ii)-(c)(ii) to Figures 4.40(a)(ii)-(c)(ii) using Morlet wavelet at the cutting duration of 16.5 s where the ceramic cutting tool undergoes gradual wear. It can be seen that before the cutting tool has chipped, smooth and periodic workpiece profile waveform features are visible in Figures 4.38(a)(ii)-(c)(ii) to Figures 4.40(a)(ii)-(c)(ii) at various rotational angles. Their corresponding scalograms in Figure 4.46 to Figure 4.48 show that the highest magnitude of the CWT coefficients display an oscillatory pattern at scales between 60-80 (within the same spatial frequency band) where the oscillation in the wavelet correlates best with the wavelet feature. The highest CWT coefficient values oscillate within the same scale band (frequency band) are associated with the regular feed of the workpiece profile which show an agreement with the result of scalogram for simulated ideal workpiece profile.

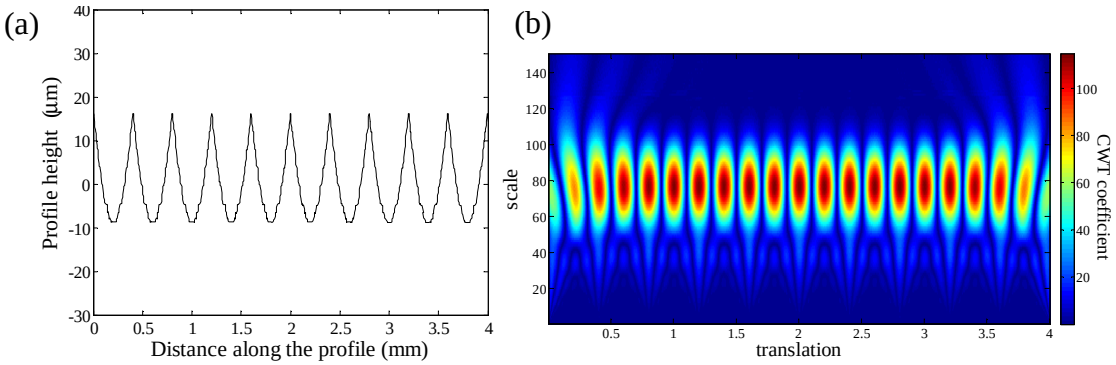

Figure 4.45: (a) simulated workpiece profile, and (b) scalogram for simulated ideal workpiece profile

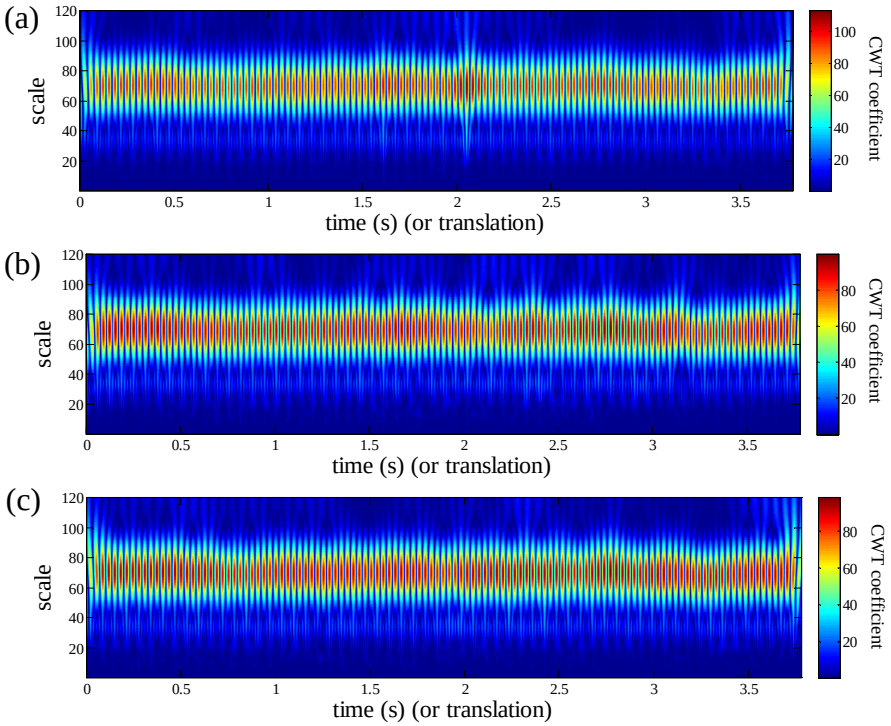

Figure 4.46: Scalograms corresponding to the workpiece profile in Figure 4.38(a)(ii)-(c)(ii)

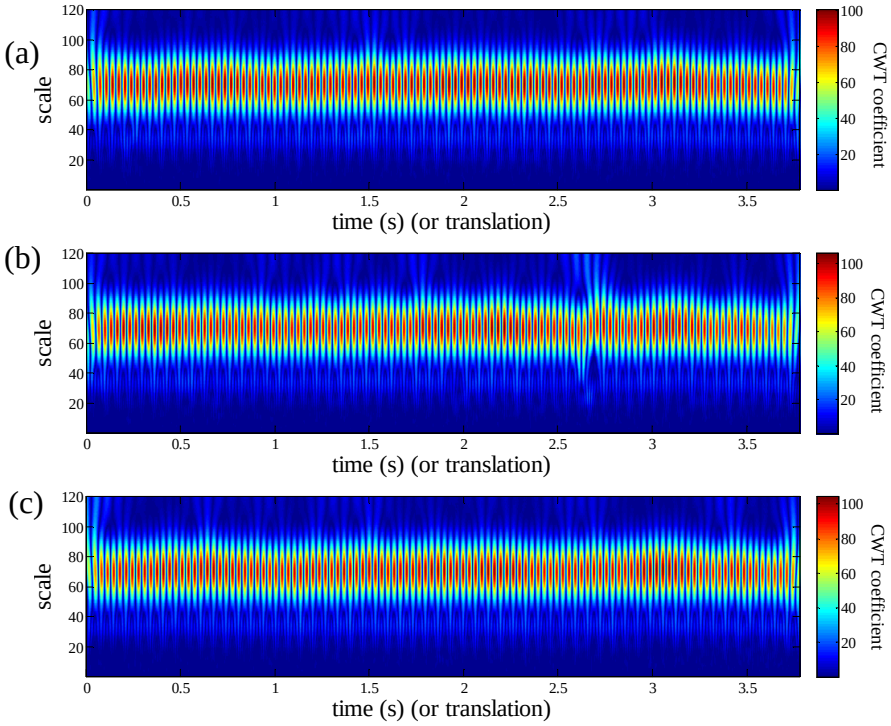

Figure 4.47: Scalograms corresponding to the workpiece profile in Figure 4.39(a)(ii)-(c)(ii)

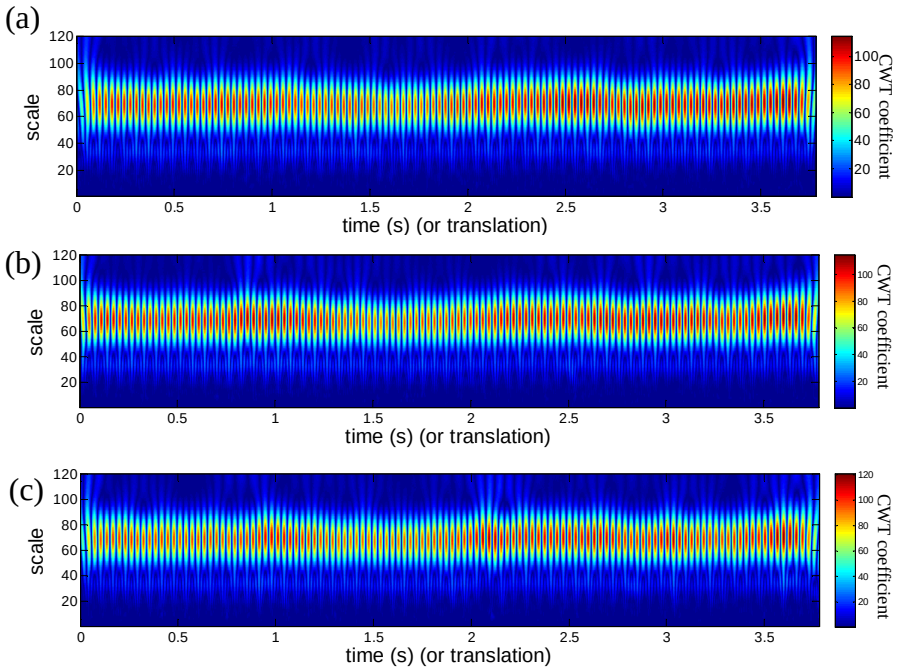

Figure 4.48: Scalograms corresponding to the workpiece profile in Figure 4.40(a)(ii)-(c)(ii)

Figure 4.49 shows the CWT of workpiece profile for the subsequent pass in Figure 4.48 at the time interval of 16.5 s to 22.0 s. When the cutting tool has chipped changes in the higher range of CWT coefficients at high scales are very distinct as seen in the Figures 4.49. A distinct transition of the largest CWT coefficient from lower scale range of around 70 (Figure 4.48) to higher scale range of around 110 was observed from the beginning of the scalograms of workpiece profile. In addition, the CWT coefficient at higher scale band of 100 to 120 appears to vary within the profile length. Thus, it can be concluded that the cutting tool starts to chip when it enters the workpiece profile at cutting duration of 16.5 s. Application of the Morlet wavelet in this study allows separation of the different frequencies of the workpiece profile. As the scale increases the transform start to detect the lower frequency components from the workpiece profile. The apparent lower frequencies are mainly due to the tool-workpiece vibration thus causing the formation of longer wavelength waviness along the tool feed direction.

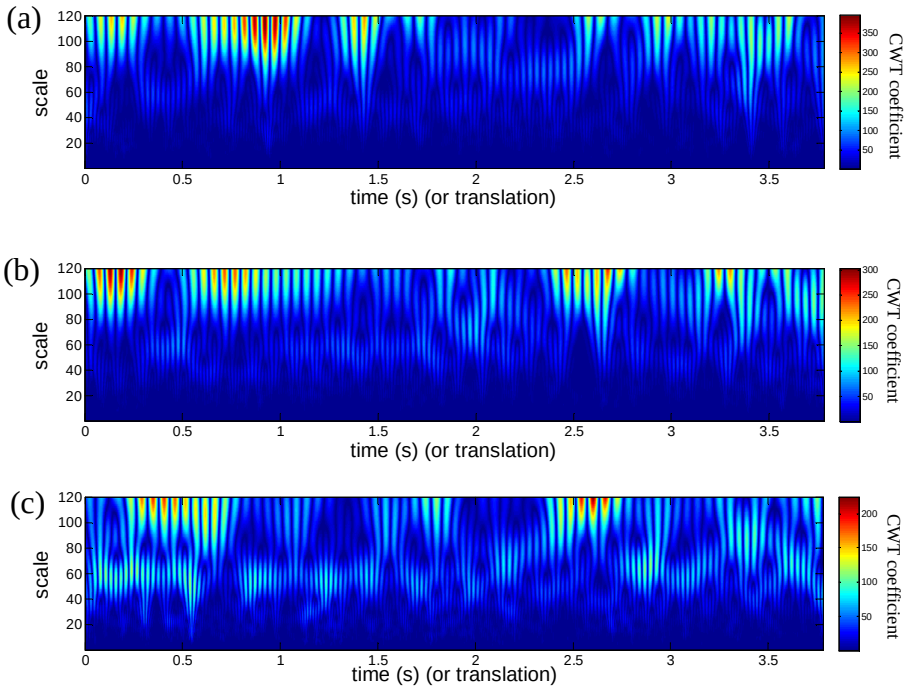

Figure 4.49: Scalograms corresponding to the workpiece profile in Figure 4.41(a)(ii)-(c)(ii)

In order to further extract from the CWT to correlate the tool wear condition, the RMS of CWT coefficient at low, medium and high scales for different cutting duration at various rotational angles was calculated. RMS of CWT coefficients in each scale was determined by:

$$RMSW_a = \sqrt{\frac{\sum_{i=1}^{N}[(CWT_a(i) - \overline{CWT}_a{}^2]}{N}} \qquad (4.1)$$

where a is scale, $CWT_a(i)$ is the values of the individual CWT coefficients, $\overline{CWT}_a$ is the mean value of the CWT coefficients in the particular scale of a. Figures 4.50(a)-(c) show that the variation of RMS of CWT coefficient of workpiece profile at scales of the 20 (low), 60 (medium) and 100 (high) for various rotation angles. From the figures it is clear that the RMS values of CWT coefficients deviate significantly from one rotation angle to another for all selected scales when the tool

has chipped. Figure 4.50(d) shows the maximum deviation of RMS values of CWT coefficients for the various rotation workpiece angles. As seen in Figure 4.50(d), maximum deviation of the RMS values of CWT coefficients at all scales is low during turning with unworn cutting tool. In contrast, high maximum deviation of the RMS values of the CWT coefficient is found after tool chipping. Low RMS values of CWT coefficients is obtained at higher scales and it increased sharply after tool has chipped. It has also been found that compared to other RMS of the CWT coefficients for different scales, the maximum deviation of the RMS of CWT coefficients in scale of 100 is relatively large, indicating that the RMS of CWT coefficient at higher scale is more sensitive to the tool chipping which can be employed as an important indicator to detect the failure of cutting tool.

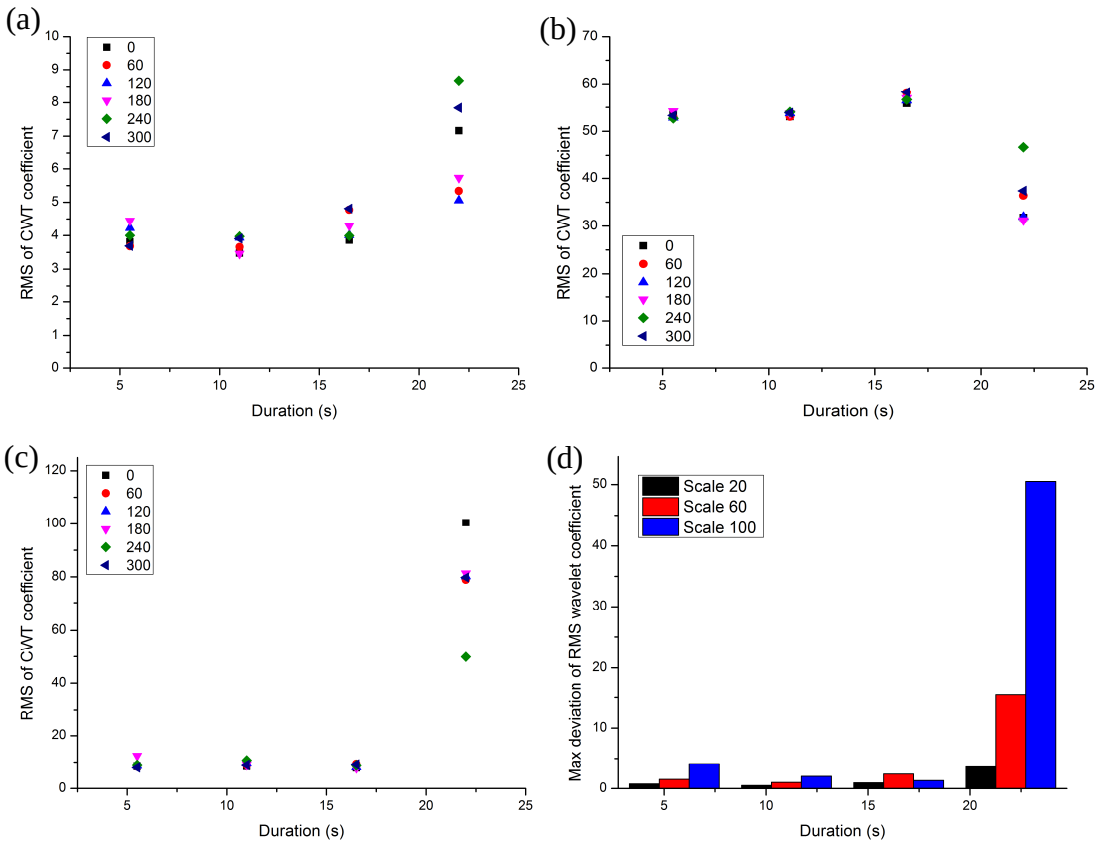

Figure 4.50: RMS of CWT coefficient at different scales (a) 20, (b) 60, (c) 100, and (d) comparison of maximum deviation of RMS of CWT coefficients

Finally, Figure 4.51 shows comparison between the sub-window FFT and CWT method in onset tool chipping detection. In order to demonstrate the advantages of the CWT over the FFT analysis, a periodic workpiece profile generated by unworn cutting tool was jointed with workpiece profile generated by a chipped cutting tool as shown in Figure 4.51(b). The amplitude of spatial frequencies lower than fundamental feed frequencies was found to start to increase significantly within the cutting duration of 1.26-1.89 s as illustrated in Figure 4.51(a). Large CWT coefficients were found in higher scales due to irregular peak-to-peak feed distance peak-to-valley height of workpiece profile as well as presence of significant undulation of surface as shown in Figure 4.51(c). As seen in Figure 4.51(c), CWT method is more effective in detecting the onset tool chipping approximately to 1.6 s instead of 1.89 s using sub-window FFT method.

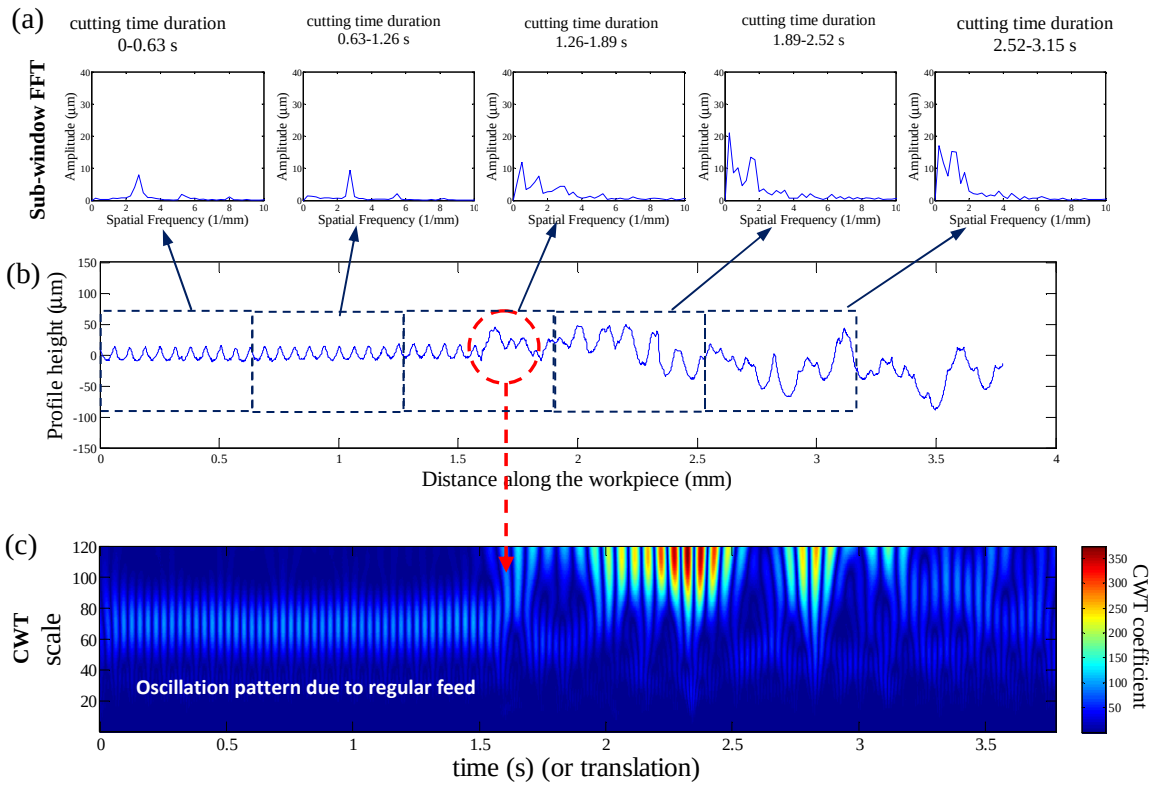

Figure 4.51: Comparison of the sub-window FFT and CWT in onset tool chipping detection (a) sub-window FFT analysis, (b) workpiece profile, and (c) CWT analysis

4.4.1 Results of repeat experiment

Figure 4.52 shows the example of zoomed-in FFT plot while Figure 4.53 shows sub-window of the FFT for the workpiece profile before and after tool chipping at workpiece rotation angle of 120^o for the repeat experiment with the following cutting condition: rotational speed 950 rpm, feed rate 0.4 mm/rev and depth-of-cut 0.5 mm (Appendix A and Appendix B). The repeat results is consistent with the results aforementioned. The amplitude of spatial frequencies lower than fundamental feed frequencies was found to increase significantly when the tool has chipped as illustrated in Figure 4.52(b) and Figure 4.53(b)(i). Figure 4.54 shows the scalograms corresponding to the workpiece profile in Figure 4.53(a)(ii) and Figure 4.53(b)(ii) respectively (Appendix C). As illustrated in Figure 4.54(b), when tool chipping occurred, large CWT coefficients were found in higher scales due to presence of waviness due to tool-workpiece vibration (low frequency). Once again, Figure 4.55 shows the RMS of CWT coefficient at higher scale is more sensitive to detect the tool chipping.

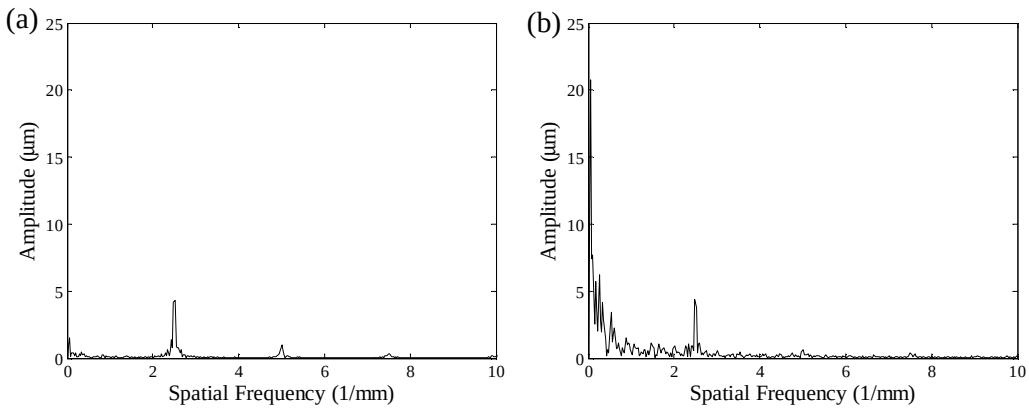

Figure 4.52: Examples of zoomed-in FFT plot (a) before, and (b) after tool chipping at workpiece rotation angle of 120^o for repeat experiment

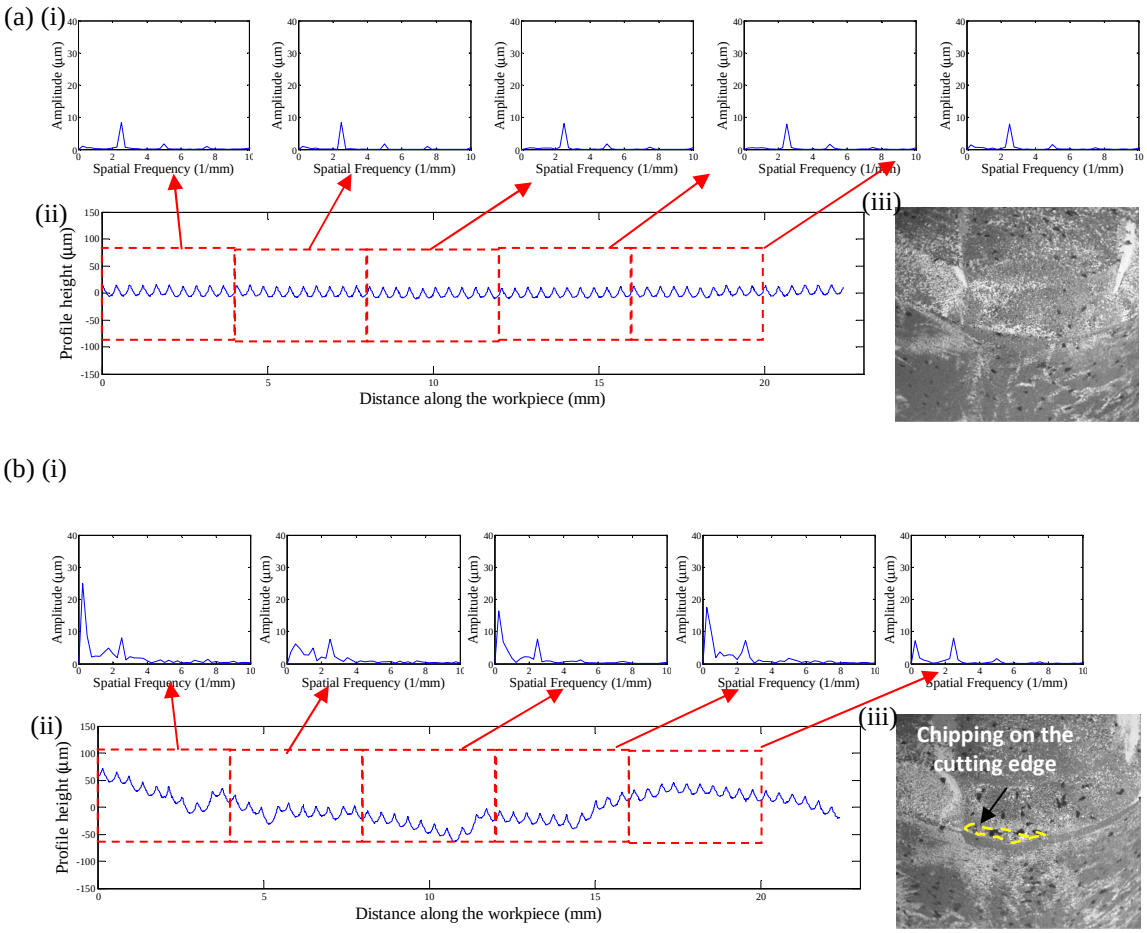

Figure 4.53: Sub-window of the FFT along the workpiece (a) before, and (b) after tool chipping at workpiece rotation angle of 120^{o} for repeat experiment

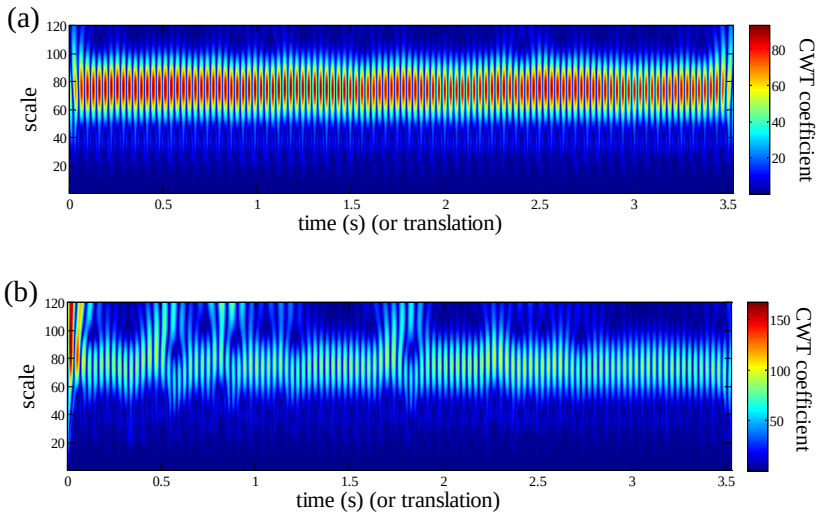

Figure 4.54: Scalograms corresponding to the workpiece profile in Figure 4.53(a)(ii) and Figure 4.53(b)(ii)

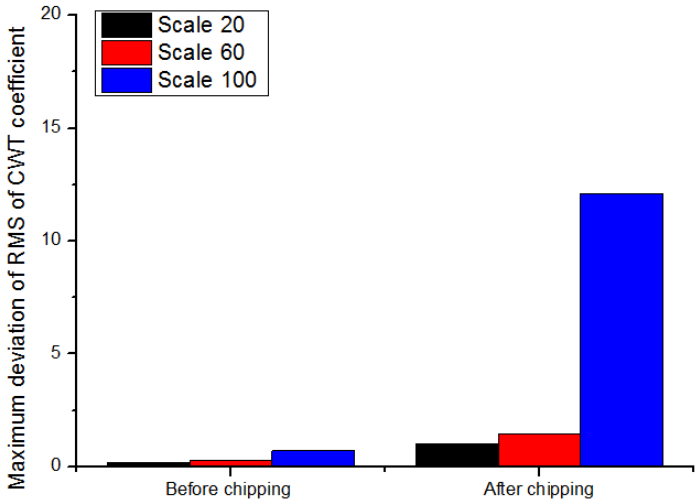

Figure 4.55: Comparison of maximum deviation of RMS of CWT coefficients (a) before, and (b) after tool chipping at scales of 20, 60 and 100 for various workpiece rotation angles

4.5 Chapter summary

This chapter presented the simulation and experimental results for the detection of tool chipping in ceramic cutting insert based on the workpiece profile signature using machine vision during turning process. Detail analysis and discussions for the obtained results were presented.

In the first part, the ACF was applied to detect the randomness features in the workpiece profile to predict the occurrence of tool chipping during turning operation. ACF method enabled the effects of the failure in ceramic insert on the workpiece profile to be observed by examining the peak of the ACF of the workpiece profile.

The application of FFT to detect tool chipping from turned workpiece profile was discussed in second part. As the tool chips, significant changes occurs in the

amplitude of spatial frequencies of the workpiece profile. The tool chipping can be detected by using the amplitude of fundamental feed frequency and the amplitude of spatial frequencies lower than the fundamental feed frequency. An attempt to solve the window function problem in STFT has been made through the development of a novel sub-window FFT method. From the result in this chapter, it can be concluded that the proposed sub-window FFT is capable of detecting the tool chipping around a cutting time of 17.13 s based on the statistical features of spatial frequencies lower than fundamental feed frequency in each sub-window.

The accuracy of the time resolution in sub-window FFT method is, however, highly dependent of the size of the window and the cutting process parameter. Thus the application of the CWT analysis method was chosen to be extended in onset tool chipping detection. From the detailed discussion, it can be concluded that the CWT method has shown its applicability over the sub-window FFT method in detecting the onset of chipping in ceramic inserts from the workpiece profile signature.

CHAPTER FIVE

CONCLUSIONS AND FUTURE RECOMMENDATIONS

5.1 Introduction

This chapter concludes the study with highlight of the main contributions made in this research and the objectives achieved. The chapter ends with the future research recommendations.

5.2 Conclusions

The following conclusions can be drawn from the present study:

i. A machine vision system consists of DSLR camera with aid of backlighting for capturing the images of the workpiece profile during turning is developed. The developed in-process tool chipping detection method using machine vision is shown to be effective in detecting the tool chipping based on workpiece profile signature in ceramic cutting tools during turning of difficult-to-cut materials.

ii. The effect of tool chipping in ceramic cutting insert on the surface profile using ACF and FFT is studied. The peaks of ACF of the workpiece profile generated by the ceramic cutting insert decreased rapidly as the lag distance increased when the tool has chipped. The envelope of the peaks of the ACF was found to deviate significantly from one another at different workpiece rotation angles when the tool has chipped. Chipping has significantly influence the amplitude of fundamental feed frequency of workpiece profile

and the amplitude of spatial frequencies lower than fundamental feed frequency. The amplitude of the fundamental feed frequency increased gradually as the tool wear (gradual) increased. When tool chipping occurred, the amplitude of fundamental feed frequency shows significant random fluctuations with the cutting time. In addition, the FFT plots of the workpiece profile clearly showed the appearance of significant spatial frequencies lower than the fundamental feed frequency after chipping. This is because the tool-workpiece vibration causes waviness in both the cutting and the tool feed directions. Presence of the long wavelength of waviness along the tool feed direction leads to existence of the sharp peak in the spectrum at lower spatial frequencies due to tool-workpiece vibration when the tool has chipped. ACF allows to represent the spatial variation over entire length of workpiece to find the random features buried in periodic surface profile while FFT allows to identify certain spatial frequency components of interest to associate with the tool chipping.

iii. Detection of onset tool chipping from the workpiece profile signature is accomplished by using sub-window FFT and CWT. The proposed sub-window FFT method based on the statistical features of spatial frequencies lower than fundamental feed frequency enable tool chipping to be detected from the workpiece signature around a cutting time of 17.13 s. CWT method was found to be more effective in detecting the exact onset of chipping of the cutting tool. Significant changes in the CWT coefficients at the larger scale band were observed at cutting time of 16.5 s. The larger CWT coefficient at higher scales band (low frequencies) is due to the long wavelengths of the waviness of the workpiece profile caused by tool chipping. The large

deviation in the RMS of CWT coefficients for scale of 100 shows that the RMS of CWT coefficient at higher scale are sensitive to tool chipping and can be potentially used as an important indicator for detecting the onset of chipping in the ceramic cutting tool insert.

5.3 Contributions of the study

The main contribution of this study is a novel in-process tool chipping detection method in ceramic cutting insert based on the 2-D images of the edge of the workpiece using machine vision method. This research provides a new algorithms to process 2-D digital images of workpiece profile to detect the occurrence of tool chipping by distinguishing the sign of chipping in workpiece profile from those originating from tool wear. The study has gone some way towards enhancing the understanding of the effect of tool chipping on workpiece profile.

The findings show that features such as the amplitude of the FFT of fundamental feed frequency, the amplitude of spatial frequencies lower than fundamental feed frequency and the CWT coefficients at higher scale are useful to identify the occurrence of tool chipping. These indicators would be a great help as an important input for pattern recognition techniques in a future tool chipping monitoring system.

5.4 Future recommendations

From the investigations conducted in this research work, a number of possible avenues for future work can be suggested. The biggest obstacle facing the

implementation of in-process tool condition monitoring is the need for experimentation to determine threshold values to develop direct quantitative relationship which relates to tool state to implement effective tool changing strategies in unmanned manufacturing. More research work is needed for advances in pattern recognition and machine learning techniques to overcome this obstacles.

The use of machine vision for in-process tool condition monitoring has not yet been explored in micromachining as it rotates at a very high speed which requires a high shutter speed or speed frame grabber camera. This kind of cameras usually work at low illumination but require high light intensity which can damage the CMOS sensor in the camera (Mandal, 2014). A future study investigating the application of vision-based method on in-process tool condition detection in micromachining would be very interesting.

REFERENCES

Abellan-Nebot, J.V., & Subirón, F.R. (2010). A review of machining monitoring systems based on artificial intelligence process models. *International Journal of Advanced Manufacturing Technology, 47(1),* 237-257.

Aich, U., & Banerjee, S. (2017). Characterizing topography of EDM generated surface by time series and autocorrelation function. *Tribology International, 111,* 73-90.

Alonso, F.J., & Salgado, D.R. (2008). Analysis of the structure of vibration signals for tool wear detection. *Mechanical Systems and Signal Processing, 22(3),* 735-748.

ASME B46.1 (2009) *Surface texture (surface roughness, waviness and lay).* The American Society of Mechanical Engineers: New York.

Azhar, A.Z.A., Mohamed, H., Ratnam, M.M., & Ahmad, Z.A. (2010). The effects of MgO addition on microstructure, mechanical properties and wear performance of zirconia-toughened alumina cutting inserts. *Journal of Alloys and Compounds, 497(1-2),* 316-320.

Babouri, M.K., Ouelaa, N., & Djebala, A. (2016). Experimental study of tool life transition and wear monitoring in turning operation using a hybrid method based on wavelet multi-resolution analysis and empirical mode decomposition. *International Journal of Advanced Manufacturing Technology, 82(9),* 2017-2028.

Balsamo, V., Caggiano, A., Jemielniak, K., Kossakowska, J., Nejman, M., & Teti, R. (2016). Multi sensor signal processing for catastrophic tool failure detection in turning. *Procedia CIRP, 41,* 939-944.

Barreiro, J., Castejón, M., Alegre, E., & Hernandez, L.K. (2008). Use of descriptors based on moments from digital images for tool wear monitoring. *International Journal of Machine Tools and Manufacture, 48(9),* 1005-1013.

Belgassim, O., & Jemielniak, K. (2011). Tool failure detection based on statistical analysis of metal cutting acoustic emission signals. *World Academy of Science, Engineering and Technology, 50(2),* 545-552.

Bendat, J.S., & Piersol, A.G. (1993). *Engineering application of correlation and spectral analysis.* New York: Wiley.

Bhaskaran, J., Murugan, M., Balashanmugam, N., & Chellamalai, M. (2012). Monitoring of hard turning using acoustic emission signal. *Journal of Mechanical Science and Technology, 26(2),* 609-615.

Bhuiyan, M.S.H., Choudhury, I.A., & Dahari, M. (2014). Monitoring the tool wear, surface roughness and chip formation occurrences using multiple sensors in turning. *Journal of Manufacturing Systems, 33(4),* 476-487.

Binsaeid, S., Asfour, S., Cho, S., & Onar, A. (2009). Machine ensemble approach for simultaneous detection of transient and gradual abnormalities in end milling using multisensor fusion. *Journal of Materials Processing Technology, 209(10),* 4728-4738.

Boryczko, A. (2011). Profile irregularities of turned surfaces as a result of machine tool interactions. *Metrology and Measurement Systems, 18(4),* 691-700.

Bushlya, V., Zhou, J.M., Avdovic, P., & Ståhl, J.E. (2013). Performance and wear mechanisms of whisker-reinforced alumina, coated and uncoated PCBN tools when high-speed turning aged Inconel 718. *International Journal of Advanced Manufacturing Technology, 66(9),* 2013–2021.

Cakan, A. (2011). Real-time monitoring of flank wear behavior of ceramic cutting tool in turning hardened steels. *International Journal of Advanced Manufacturing Technology, 52(9),* 897-903.

Cakir, M.K., & Isik, Y. (2005). Detecting tool breakage in turning AISI 1050 steel using coated and uncoated cutting tools. *Journal of Materials Processing Technology, 159(2),* 191-198.

Camargo, J.C., Dominguez, D.S., Ezugwu, E.O., & Machado, A.R. (2014). Wear model in turning of hardened steel with PCBN tool. *International Journal of Refractory Metals and Hard Materials, 47,* 61-70.

Castejón, M., Alegre, E., Barreiro, J., & Hernández, L.K. (2007). Online tool wear monitoring using Geometric Descriptors from digital images. *International Journal of Machine Tools and Manufacture, 47(12-13),* 1847-1853.

Cazaux, J. (2004). Errors in nanometrology by SEM. *Nanotechnology, 15(9),* 1195-1199.

Čerče, L., Pušavec, F., & Kopač, J. (2015). 3D cutting tool wear monitoring in the process. *Journal of Mechanical Science and Technology, 29(9),* 3885-3895.

Chelladurai, H., Jain, V., & Vyas, N. (2008). Development of a cutting tool condition monitoring system for high speed turning operation by vibration and strain analysis. *International Journal of Advanced Manufacturing Technology, 37(5),* 471-485.

Chen, B., Chen, X., Li, B., He, Z., Cao, H., & Cai, G. (2011). Reliability estimation for cutting tools based on logistic regression model using vibration signals. *Mechanical Systems and Signal Processing, 25(7),* 2526-2537.

Chen, H., Huang, S., Li, D., & Fu, P. (2010). Turning tool wear monitoring based on fuzzy cluster analysis. In Zeng, Z., & Wang, J. (Eds.), *Advances in Neural Network Research and Application* (pp. 739-745). Berlin: Springer.

Chen, Q., Yang, S., & Li, Z. (1999). Surface roughness evaluation by using wavelets analysis. *Precision Engineering, 23(3),* 209–212.

Chen, X., & Li, B. (2007). Acoustic emission method for tool condition monitoring based on wavelet analysis. *International Journal of Advanced Manufacturing Technology, 33(9),* 968-976.

Chen, Y.L., Cai, Y., Shimizu, Y., Ito, S., Gao, W., & Ju, B.F. (2016). On-machine measurement of microtool wear and cutting edge chipping using a diamond edge artifact. *Precision Engineering, 43,* 462-467.

Chethan, Y.D., Ravindra, H.V., Krishne, Y.T., & Kumar, S.B. (2015). Machine vision for tool status monitoring in Inconel 718 using Blob analysis. *Materials Today: Proceeding, 2(4-5),* 1841-1848.

Cheung, C.F., & Lee, W.B. (2000). A multi-spectrum analysis of surface roughness formation in ultra-precision machining. *Precision Engineering, 24(1),* 77-87.

Choudhury, S.K., & Bartarya, G. (2003). Role of temperature and surface finish in prediction tool wear using neural network and design of experiment. *International Journal of Machine Tools Manufacture, 43(7),* 747-753.

Colgan, J., Chin, H., Danai, K., & Hayashi, S.R. (1994). On-line tool breakage detection in turning: A multi-sensor method. *Journal of Engineering for Industry, 116(1),* 117-123.

Datta, A., Dutta, S., Pal, S.K., & Sen, R. (2013). Progressive cutting tool wear detection from machined surface images using Voronoi tessellation method. *Journal of Materials Processing Technology, 213(12),* 2339-2349.

Daubeches, I. (1990). The wavelet transformation, time-frequency localization and signal analysis. *IEEE Transactions on Information Theory, 36(5),* 961-1005.

Davoodi, B., & Hosseinzadeh, H. (2012). A new method for heat measurement during high speed machining. *Measurement, 45(8),* 2135-2140.

Dawson, T.G., & Kurfess, T.R. (2005). Quantification of tool wear using light interferometry and three dimensional computational metrology. *International Journal of Machine Tool and Manufacture, 45(4-5),* 591-596.

Devillez, A., Lesko, S., & Mozerc, W. (2004). Cutting tool crater wear measurement with white light interferometry. *Wear, 256(1-2),* 56-65.

Dimla, D.E. (2002). The correlation of vibration signal features to cutting tool wear in a metal turning operation. *International Journal of Advanced Manufacturing Technology, 19(10),* 705-713.

Dimla, D.E., & Lister, P.M. (2000). Online metal cutting tool condition monitoring. I: force and vibration analysis. *International Journal of Machine Tools and Manufacture, 40(5),* 739-768.

Dutta, S., Datta, A., Chakladar, N.D., Pal, S.K., Mukhopadhyay, S., & Sen, R. (2012). Detection of tool condition from the turned surface images using an accurate grey level co-occurrence technique. *Precision Engineering, 36(3),* 458-466.

Dutta, S., Pal, S.K., & Sen, R. (2015). Tool condition monitoring in turning by applying machine vision. *Journal of Manufacturing Science and Engineering, 138(5),* 1-17.

Dutta, S., Pal, S.K., & Sen, R. (2016). On-machine tool prediction of flank wear from machined surface images using texture analyses and support vector regression. *Precision Engineering, 43,* 34-42.

Fadare, D.A., & Oni, A.O. (2009). Development and application of a machine vision system for measurement of tool wear. *ARPN Journal of Engineering and Applied Science, 4(4),* 42-49.

Fang, N., Srinivasa, P., & Mosquea, S. (2011). Effect of tool edge wear on the cutting forces and vibration in high-speed finish machining of Inconel 718: an experimental study and wavelet transform analysis. *International Journal of Advanced Manufacturing Technology, 52(1),* 65-77.

Fang, N., Pai, P.S., & Edwards, N. (2012). Tool-edge wear and wavelet packet transform analysis in high speed machining of Inconel 718. *Journal of Mechanical Engineering, 58(3),* 191-202.

Feng, Z., Liang, M., & Chu, F. (2013). Recent advances in time-frequency analysis methods for machinery fault diagnosis: A review with application examples. *Mechanical Systems and Signal Processing, 38(1),* 165-205.

Fu, P. & Hope, A.D. (2006). *The application of B-spline neurofuzzy network for condition monitoring of metal cutting tool.* Paper presented at PRICAI 2006: Trends in Artificial Intelligence, 9th Pacific Rim International Conference on Artificial Intelligence, Guilin China.

Gajate, A., Haber, R., Toro, R., Vega, P., & Bustillo, A. (2012). Tool wear monitoring using neuro-fuzzy techniques: a comparative study in a turning process. *Journal of Intelligent Manufacturing, 23(3),* 869-882.

Gao, D., Liao, Z.R., Lv, Z.K., & Lu, Y. (2015). Multi-scale statistical signal processing of cutting force in cutting tool condition monitoring. *International Journal of Advanced Manufacturing Technology, 80(9),* 1843-1853.

Gao, R.X., & Yan, R. (2010). From Fourier Transform to Wavelet Transform: A Historical Perspective. In R.X. Gao, & R. Yan (Eds.), *Wavelet: Theory and Application for Manufacturing,* (pp.17-32). United States: Springer.

Ghani, J.A., Rizal, M., Sayuti, A., Nuawi, M.Z., Rahman, M.N., & Haron, C.H.C. (2009). New regression model and I-Kaz method for online cutting tool wear monitoring. *World Academy of Science, Engineering and Technology, 60,* 420-425.

Gong, W., Obikawa, T., & Shirakashi, T. (1997). Monitoring of tool wear states in turning based on wavelet analysis. *JSME International Journal Series C Mechanical Systems, Machine Elements and Manufacturing, 40(3),* 447-453..

Grzesik, W. (2008a) *Advanced Machining Processes of Metallic Materials.* Oxford, UK: Elsevier Publications.

Grzesik, W. (2008b) Influence of tool wear on surface roughness in hard turning using differently shaped ceramic tools. *Wear, 265(3-4),* 327-335.

Grzesik, W., & Brol, S. (2009). Wavelet and fractal approach to surface roughness characterization after finish turning of different workpiece materials. *Journal of Materials Processing Technology, 209(5),* 2522-2531.

Grzesik, W., & Zalisz, Z. (2008). Wear phenomenon in the hard steel machining using ceramic cutting tool. *Tribology International, 41,* 802-812.

Guo, Y.B., & Ammula, S.C. (2005) Real-time acoustic emission monitoring for surface damage in hard machining. *International Journal of Machine Tools and Manufacture, 45(14),* 1622-1627.

Haddadi, E., Shabghard, M.R., & Ettefagh, M.M. (2008). Effect of different tool edge condition on wear detection by vibration spectrum analysis in turning operation. *Journal of Applied Sciences, 8(21),* 3879-3886.

Hase, A., Mishina, H., & Wada, M. (2012). Correlation between features of acoustic emission signals and mechanical wear mechanisms. *Wear, 292-293,* 144-150.

International Organization for Standardization. (1993). *ISO 3685: Tool-life testing with single-point turning tools*. Retrieved from: https://www.asme.org/products/codes-standard/b461-2009-surface-texture-surface-roughness

Jemielniak, K. (1992). Detection of cutting edge breakage in turning. *CIRP Annals, 41(1),* 97-100.

Jemielniak, K., Kossakowska, J., & Urbanski, T. (2011a). Application of wavelet transform of acoustic emission and cutting force signals for tool condition monitoring in rough turning of Inconel 625. *Proceedings of the Institution of Mechanical Engineers, Part B: Journal of Engineering Manufacture, 225(1),* 123-129.

Jemielniak, K., & Othman, O. (1998). Tool failure detection based on analysis of acoustic emission signals. *Journal of Materials Processing Technology, 76(1-3),* 192-197.

Jemielniak, K., & Szafarczyk, M. (1992). Detection of cutting edge breakage in turning. *CIRP Annals-Manufacturing Technology, 41(1),* 97-100.

Jemielniak, K., Urbański, T., Kossakowska, J., & Bombiński, S. (2011b). Tool condition monitoring based on numerous signal features. *International Journal Advanced Manufacturing Technology, 59(1),* 73-81.

Jiang, C.Y., Zhang, Y.Z., & Xu, H.J. (1987). In-process monitoring of tool wear stage by the frequency band energy method. *CIRP Annals-Manufacturing Technology,36(1),* 45-48.

Josso, B., Burton, D.R., & Lalor, M.J. (2002). Frequency normalised wavelet transform for surface roughness analysis and characterisation. *Wear, 252(5-6),* 491-500.

Jurkovic, J., Korosec, M., & Kopac, J. (2005). New approach in tool wear measuring technique using CCD vision system. *International Journal of Machine Tools and Manufacture 45(9):* 1023-1030.

Kalvoda, T., & Hwang, Y.R. (2010). Analysis of signal for monitoring of nonlinear and non-stationary machining process. *Sensors and Actuators A, 161(1-2),* 39-45.

Kassim, A.A., Mannan, M.A., & Mian, Z. (2007). Texture analysis methods for tool condition monitoring. *Image and Vision Computing, 25(7),* 1080-1090.

Kaye, J.E., Yan, D.H., Popplewell, N., & Balakrishnan, S. (1995). Predicting tool flank wear using spindle speed change. *International Journal of Machine Tools and Manufacture, 35(9),* 1309-1320.

Khraisheh, M.K., Pezeshki, C., & Bayoumi, A.E. (1995). Time series based analysis for primary chatter in metal cutting. *Journal of Sound and Vibration, 180(1),* 67-87.

Kim, J.D., & Choi, I.H. (1996). Development of a tool failure detection system using multi-sensors. *International Journal of Machine Tools and Manufacture, 36(8),* 861-870.

Kious, M., Ouahabi, A., Boudraa, M., Serra, R., & Cheknane, A. (2010). Detection process approach of tool wear in high speed milling. *Measurement, 43(10),* 1439-1446.

Korkut, I., Acir, A., & Boy, A. (2011). Application of regression and artificial neural network analysis in modeling of tool-chip interface temperature in machining. *Expert System with Applications, 38(9),* 11651-11656.

Kurada, S., & Bradley, C. (1997). A machine vision system for tool wear assessment. *Tribology International, 30(4),* 295-304.

Kwak, J.S. (2006). Application of wavelet transform technique to detect tool failure in turning operation. *International Journal of Advanced Manufacturing Technology, 28(11),* 1078-1083.

Kwon, Y., & Fischer, G.W. (2003). A novel approach to quantifying tool wear and tool life managements for optimal tool management. *International Journal of Machine Tools and Manufacture, 43(4),*359-368.

Lan, M.S., & Dornfeld, D.A. (1984). In-process tool fracture detection. *Journal of Engineering Materials and Technology, 106(2),* 111-118.

Lanzetta, M. (2001). A new flexible high resolution vision sensor for tool condition monitoring. *Journal of Materials Processing Technology, 119(1-3),* 73-82.

Lauro, C.H., Brandao, L.C., Baldo, D., Reis, R.A., & Davim, J.P. (2014). Monitoring and processing signal applied in machining process-A review. *Measurement, 58,* 73-86.

Leavey, C.M., James, M.N., Summerscales, J., & Sutton, R. (2003). An introduction to wavelet transforms: a tutorial approach. *Insight Non-Destructive Testing and Condition Monitoring, 45(5),* 344-353.

Lee, K.J., Lee, T.M., Yang, M.Y. (2007). Tool wear monitoring system for CNC end milling using a hybrid approach to cutting force regulation. *International Journal of Advanced Manufacturing Technology, 32,* 8-17.

Li, D., & Mathew, J. (1990). Tool wear and failure monitoring techniques for turning- A review. *International Journal of Machine Tools and Manufacture, 30(4),* 579-598.

Li, L., & An, Q. (2016). An in-depth study of tool wear monitoring technique based on image segmentation and texture analysis. *Measurement, 79,* 44-52.

Li, X. (2002). A brief review: Acoustic emission method for tool wear monitoring during turning. *International Journal of Machine Tools and Manufacture, 42(2),* 157-165.

Li, X. (2005). Development of current sensor for cutting force measurement in turning. *IEEE Transactions on Instrumentation and Measurement, 54(1),* 289-296.

Li, X.Q., Wong, Y.S., & Nee, A.Y.C. (1998). Comprehensive identification of tool failure and chatter using a parallel multi-ART2 neural network. *Journal of Manufacturing Science and Engineering, 120(2),* 433-442.

Liao, Y., & Stephenson, D.A. (2010). A multifeature approach to tool wear estimation using 3D workpiece surface texture parameters. *Journal of Manufacturing Science and Engineering, 132(6),* 1-7.

Liao, Z., Gao, D., Lu, Y., & Lv, Z. (2016). Multi-scale hybrid HMM for tool wear condition monitoring. *International Journal of Advanced Manufacturing Technology, 84(9),* 2437-2448.

Lima, J.G., Avila, R.F., Abrao, A.M., Faustino, M., & Davim, J.P. (2005). Hard turning: AISI 4340 high strength low alloy steel and AISI D2 cold work tool steel. *Journal of Materials Processing Technology, 169(3),* 388-395.

Lin, W.S. (2008). Modeling the surface roughness for fine turning of AISI stainless steel. *Key Engineering Materials, 364-366,* 644-648.

Liu, T.I., Song, S.D., Liu, G., & Wu, Z. (2013a). Online monitoring and measurements of tool wear for precision turning of stainless steel parts. *International Journal of Advanced Manufacturing Technology, 65(9),* 1397-1407.

Liu, C., Wu, J., Li, G., & Tan, G. (2013b). Frequency-spectrum characteristics of force in end milling with tool wear and eccentricity. *International Journal of Advanced Manufacturing and Technology, 67(1),* 925-938.

Maia, L.H.A., Abrao, A.M., Vasconcelos, W.L., Sales, W.F., & Machado, A.R. (2015). A new approach for detection of wear mechanism and determination of tool life in turning using acoustic emission. *Tribology International, 92,* 519-532.

Manda, S. (2014). Applicability of tool condition monitoring methods used for conventional milling in micromillig: A comparative review. *Journal of Industrial Engineering, 2014,* 1-8.

Mallat, S.G. (1989). A theory of multiresolution signal decomposition: the wavelet representation. *IEEE Transactions on Pattern and Machine Intelligence, 11(7),* 674-693.

Marinescu, I., & Axinte, D. (2008). A critical analysis of effectiveness of acoustic emission signal to detect tool and workpiece malfunction in milling operations. *International Journal of Machine Tools and Manufacture, 48(10),* 1148-1160.

Marinescu, I., & Axinte, D. (2009). A time-frequency acoustic emission-based monitoring technique to identify workpiece surface malfunction in milling with multiple teeth cutting simultaneously. *International Journal of Machine Tools and Manufacture, 49(1),* 53-65.

Mazzeo, A.D., Stein, A.J., Trumper, D.L., & Hocken, R.J. (2009). Atomic force microscope for accurate dimensional metrology. *Precision Engineering, 33(2),* 135-149.

Meddour, I., Yallese, M.A., Khattabi, R., Elbah, M., & Boulanouar, L. (2015). Investigation and modeling of cutting forces and surface roughness when hard turning of AISI 52100 steel with mixed ceramic tool: cutting conditions optimization. *International Journal of Advanced Manufacturing Technology, 77(5),* 1387-1399.

Mook, W.K., Shahabi, H.H., & Ratnam, M.M. (2009). Measurement of nose radius wear in turning tools from a single 2D image using machine vision. International *Journal of Advanced Manufacturing Technology, 43(3),* 217-225.

Nabil, B.F., & Mabrouk, M. (2006). Effects of random aspects of cutting tool wear on surface roughness and tool life. *Journal of Materials Engineering and Performance, 15(5),* 519-524.

Nakao, Y., & Dornfeld, D.A. (2003). Diamond turning using position and AE dual feedback control system. *Precision Engineering, 27(2),* 117-124.

Neslušan, M., Mičieta, B., Mičietová, A., Čilliková, M., & Mrkvica, I. (2015). Detection of tool breakage during hard turning through acoustic emission at low removal rates. *Measurement, 70,*1-13.

Oraby, S.E., & Alaskari, A.M. (2008). Surface topography assessment techniques based on an in-process monitoring approach of tool wear and cutting force signature. *Journal of Brazilian Society of Mechanical Sciences and Engineering, 30(3),* 221-230.

Oraby, S.E., Al-Modhuf, A.F., & Hayhurst, D.R. (2005). A diagnostic approach for turning tool based on the dynamic force signals. *Journal of Manufacturing Science and Engineering, 127(3),* 463-475.

O'Sullivan, D., & Cotterell, M. (2001). Temperature measurement in single point turning. *Journal Material Processing Technology, 118(1-3),* 301-308.

Otsu, N. (1979). A Threshold Selection Method from Gray-Level Histogram. *IEEE Transactions on Systems, Man and Cybernetics, 9(1),* 62-66.

Özel, T. & Davim, J.P. (2009). *Intelligent Machining*. London, UK: Wiley.

Özel, T., Karpat, Y., Figgueria, L., & Davim, J.P. (2007). Modelling of surface finish and tool flank wear in turning of AISI D2 steel with ceramic wiper inserts. *Journal of Materials Processing Technology, 189(1-3),*192–198.

Özel, T., Tsu-Kong, H., & Zeren, E. (2005). Effect of cutting edge geometry, workpiece hardness, fed rate and cutting speed on surface roughness and forces in finish turning of hardened AISI H13 steel. *International Journal of Advanced Manufacturing Technology, 25(3),* 262–269.

Pampu, N.C. (2011). Study the effect of the short time Fourier transform configuration on EEG spectral estimates. *Electronics and Telecommunications, 52(4),* 26-29.

Patil, S.P., & Tilekar, D.M. (2014). Tool wear detection of cutting tool using Matlab software. *International Journal of Engineering and Technical Research, 2 (11),* 362-366.

Pavel, R., Marinescu, J., Dei, M., & Pillar, J. (2005). Effect of tool wear on surface finish for a case of continuous and interrupted hard turning. *Journal of Materials Processing Technology, 170(1-2),* 341-349.

Penedo, F., Haber, R.E., Gajate, A., & Toro, R.M. (2012). Hybrid incremental modeling based on least square and fuzzy NN for monitoring tool wear in turning processes. *IEEE Transactions on Industrial Informatics, 8(4),* 964-973.

Penalva, M.L., Arizmendi, M., Diaz, F., & Fernandez, J. (2002). Effect of tool war on roughness in hard turning. *CIRP Annals-Manufacturing Technology, 51(1),* 57-60.

Pfeifer, T., & Wiegers, L. (2000). Reliable tool wear monitoring by optimized image and illumination control in machine vision. *Measurement, 28(3),* 209-218.

Rad, J.S., Zhang, Y., Aghazadeh, F., & Chen Z.C. (2014). *A study on tool wear monitoring using time-frequency transformation techniques.* Paper presented at International Conference on Innovative Design and Manufacturing, Montreal, Quebec, Canada.

Rafiee, J., & Tse, P.W. (2009). Use of autocorrelation of wavelet coefficients for fault diagnosis. *Mechanical Systems and Signal Processing, 23(5),* 1554-1572.

Rehorn, A.G., Jiang, J., & Orban, P.E. (2005). State-of-the-art methods and results in tool condition monitoring: a review. *International Journal of Advanced Manufacturing Technology, 26(7),* 693–710.

Ren, Q., Balazinski, M., Baron, L., & Jemielniak, K. (2011). TSK fuzzy modeling for tool wear condition in turning processes: An experimental study. *Engineering Applications of Artificial Intelligence, 24(2),* 260-265.

Roy, S., Bhattacharyya, A., & Banerjee, S. (2007). Analysis of effect of voltage on surface texture in electrochemical grinding by autocorrelation function. *Tribology International, 40(9),* 1387-1393.

Runola, J.P., Moon, K.S., & Sutherland, J.W. (1994). The effects of tool wear on the wavelength structure of a turned surface profile. *Transactions of NAMRI/SME, 22,* 105-109

Salgado, D.R., & Alonso, F.J. (2007). An approach based on current and sound signals for in-process tool wear monitoring. *International Journal Machine Tools and Manufacture, 47(14),* 2140-2152.

Samraj, A., Sayeed, S., Raja, J.E., Hossen, J., & Rahman, A. (2011). Dynamic clustering estimation of tool flank wear in turning process using SVD models of the emitted sound signals. *World Academy Science Engineering Technology, 56,* 1151-1155.

Sandvik Coromant Catalogue, 2015. Available in: http://www.sandvik.coromant.com

Sanjanwala, A., Choudhury, S.K., & Jain, V.K. (1990). Online tool wear sensing and compensation during turning. *Precision Engineering, 12(2),* 81-84.

Sata, T., Li, M., Takata, S., Hiraoka, H., Li, C.Q., Xing, X.Z., & Xiao, X.G. (1985) Analysis of surface roughness generation in turning operation and its application. *Annals of CIRP, 34(1),* 473-476.

Shahabi, H.H., & Ratnam, M.M. (2009a). In-cycle monitoring of tool nose wear and surface roughness of turned parts using machine vision. *International Journal of Advanced Manufacturing Technology, 40(11),* 1148-1157.

Shahabi, H.H., & Ratnam, M.M. (2009b). Assessment of flank wear and nose radius wear from workpience roughness profile in turning operation using machine vision. *International Journal of Advanced Manufacturing Technology, 43(1),* 11-21.

Sharma, V.S., Sharma, S.K., & Sharma, A.K. (2008) Cutting tool wear estimation for turning. *Journal of Intelligent Manufacturing,* 19(1), 99-108

Shi, D.F., & Gindy, N.N. (2007). Development of an online machining process monitoring system: Application in hard turning. *Sensors and Actuators A, 135(2),* 405-414.

Sick, B. (2002). Online and indirect tool wear monitoring in turning using artificial neural networks: a review of more than a decade of research. *Mechanical Systems and Signal Processing, 16(4),* 487-546.

Siddhpura, A., & Paurobally, R. (2013). A review of flank wear prediction methods for tool condition monitoring in a turning process. *International Journal of Advanced Manufacturing Technology, 65(1),* 371-393.

Sikdar, S.K., & Chen, M. (2002). Relationship between tool flank wear area and component forces in single point turning. *Journal of Materials Processing Technology, 128(1-3),* 210-215.

Silva, R.G., Reuben, R.L., Baker, K.J., & Wilcox, S.J. (1998). Tool wear monitoring of turning operations by neural network and expert system classification of a feature set generated from multiple sensors. *Mechanical Systems and Signal Processing, 12(2),* 319-332.

Sivasakthivel, P.S., & Sudhakaran, R. (2013). Optimization of machining parameters on temperature rise in end milling of Al 6063 using response surface methodology and genetic algorithm. *International Journal of Advanced Manufacturing and Technology, 67(9),*2313-2323.

Sobiyi, K., Sigalas, I., Akdogan, G., & Turan, Y. (2015). Performance of mixed ceramics and CBN tools during hard turning of martensitic stainless steel. *International Journal of Advanced Manufacturing and Technology, 77(5),* 861-871.

Sortino, M. (2003). Application of statistical filtering for optical detection of tool wear. *International Journal of Machine Tools and Manufacture, 43(5),* 493-497.

Tabatabai, A.J., & Mitchell, R. (1984). Edge location to sub-pixel values in digital imagery. *IEEE Transactions on Pattern Analysis and Machine Intelligence, 6(2),* 188-201.

Tekiner, Z., & Yesilyurt, S. (2004). Investigation of the cutting parameters depending on process sound during turning of AISI 304 austenitic stainless steel. *Materials and Design, 25(6),* 507-513.

Teti, R., Jemielniak, K., O'Donnell, G., & Dornfeld, D. (2010). Advanced monitoring of machining operations. *CIRP Annals-Manufacturing Technology, 59(2),* 717-739.

Thomas, M., Beauchamp, Y., Youssef, A.Y., & Masounave, J. (1996). Effect of tool vibrations on surface roughness during lathe dry turning process. *Computers and Industrial Engineering, 31(3/4),* 637-644.

Tsao, C.C. (2002). Prediction of flank wear of different coated drills for JIS SUS 304 stainless steel using neural network. *Journal of Materials Processing Technology, 123(3),* 354-360.

Wang, H.L., Shao, H., Chen, M., & Hu, D.J. (2003). Online tool breakage monitoring in turning. *Journal of Materials Processing Technology, 139(1-3),* 237-242.

Wang, L.H., & Gao, R.X. (2006). *Condition Monitoring and Control for Intelligent Manufacturing.* Germany: Springer.

Wang, W.H., Hong, G.S. & Wong, Y.S. (2006). Flank wear measurement by a threshold independent method with sub-pixel accuracy. *International Journal of Machine Tools and Manufacture, 46(2),* 199-207.

Wheeler, A.J., & Ganji, A.R. (2010). *Introduction to Engineering Experimentation*. New Jersey: Pearson Education.

Yesilyurt, I. (2006). End mill breakage detection using mean frequency analysis of scalogram. *International Journal of Machine Tool and Manufacture, 46(3-4),* 450-458.

Yin, Z., Huang, C., Yuan, J., Zou, B., Liu, H., & Zhu, H. (2015). Cutting performance and life prediction of an Al_2O_3 /TiC micro-nano-composite ceramic tool when machining austenitic stainless steel. *Ceramics International, 41(5),* 7059-7065.

Youn, J.W., Yang, M.Y., & Park, H.Y. (1994). Detection of cutting tool fracture by dual signal measurements. *International Journal Machine Tools and Manufacture, 34(4),* 507-525.

Zhang, J., Zhang, C., Guo, S., & Zhou, L. (2012). Research on tool wear detection based on machine vision in end milling process. *Production Engineering, 6(4),* 431-437.

Zhang, K.F., Yuan, H.Q., & Nie, P. (2015). A method for tool condition monitoring based on sensor fusion. *Journal of Intelligent Manufacturing, 26(5),*1011–1026.

Zhou, J.M., Andersson, A., & Stahl, J.E. (2003). The monitoring of flank wear on the CBN tool in the hard turning process. *International Journal of Advanced Manufacturing Technology, 22(9),* 697-702.

Zhu, K., Wong, Y.S., & Hong, G.S. (2009). Wavelet analysis of sensor signals for tool condition monitoring: A review and some new results. *International Journal of Machine Tools and Manufacture, 49(7-8),* 537-553.

Zubaydi, A., Haddara, M.R., & Swamidas, A.S.J. (2000). On the use of autocorrelation function to identify the damage in the side shell of a ship's hull. *Marine Structures, 13,* 537-551.

APPENDICES

APPENDIX A: REPEATED EXPERIMENTAL RESULTS OF FFT

Repeat experiment with cutting condition: spindle speed 950 rpm, feed rate 0.4 mm/rev, depth of cut 0.5 mm

FFT plot for before tool chipping (a, b) and after tool chipping (c) at various workpiece rotation angles

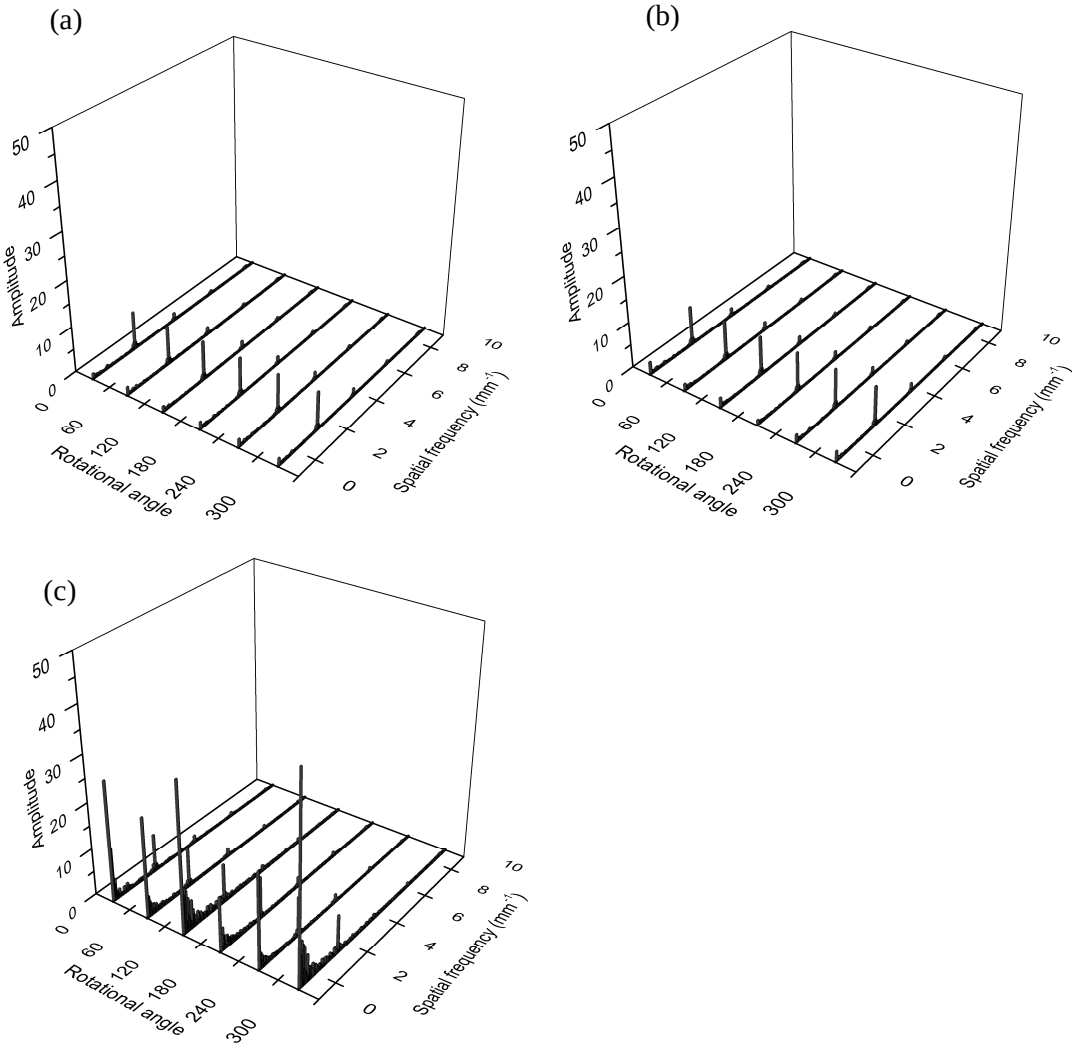

APPENDIX B: REPEATED EXPERIMENTAL RESULTS OF SUB-WINDOW FFT

Sub-window FFT along the workpiece profile at different rotational angles (a) 0^o, (b) 120^o, (c) 240^o in cutting time duration of 5.5 s corresponding to Appendix A

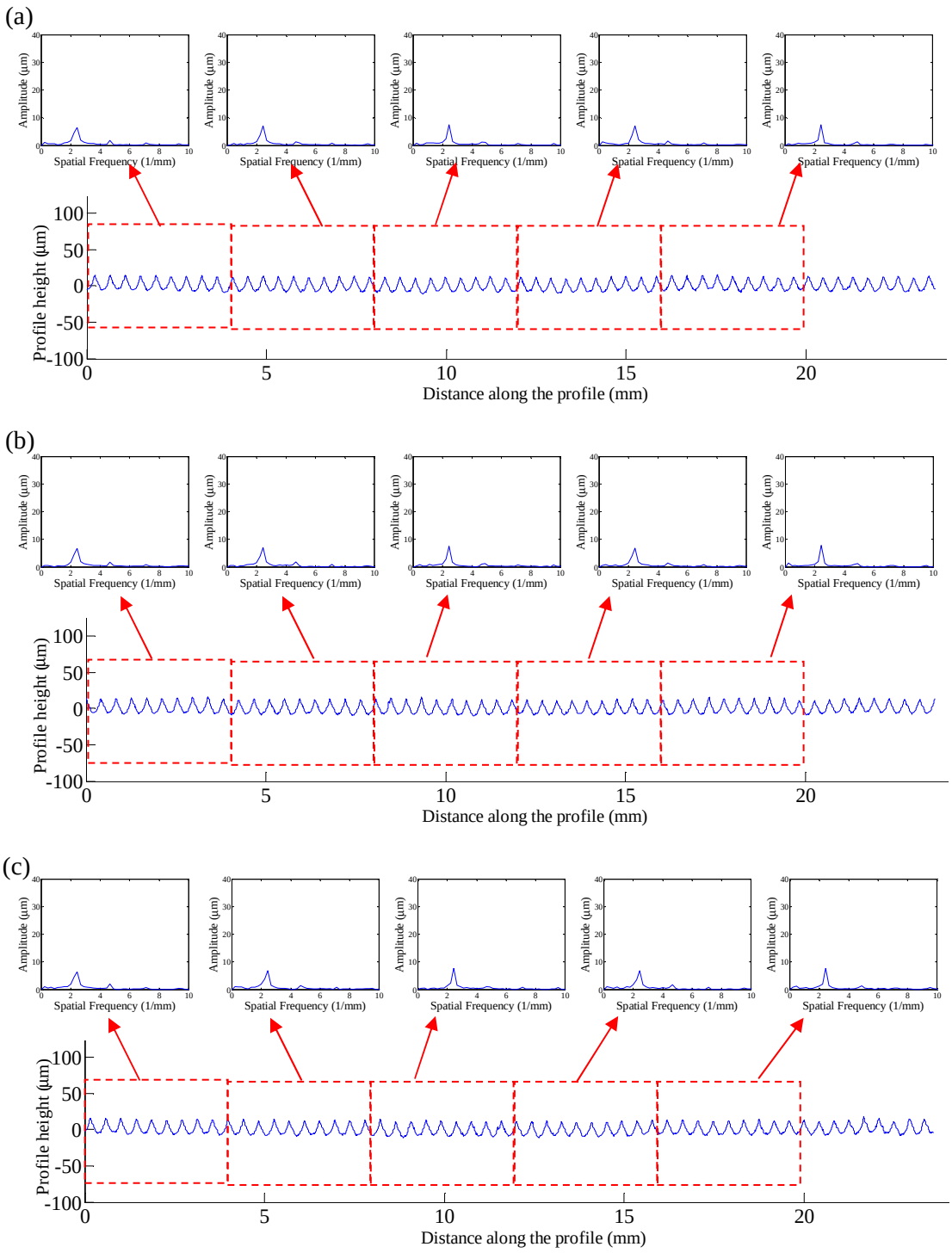

Sub-window FFT along the workpiece profile at different rotational angles (a) 0^o, (b) 120^o, (c) 240^o in cutting time duration of 5.5-11.0 s corresponding to Appendix A

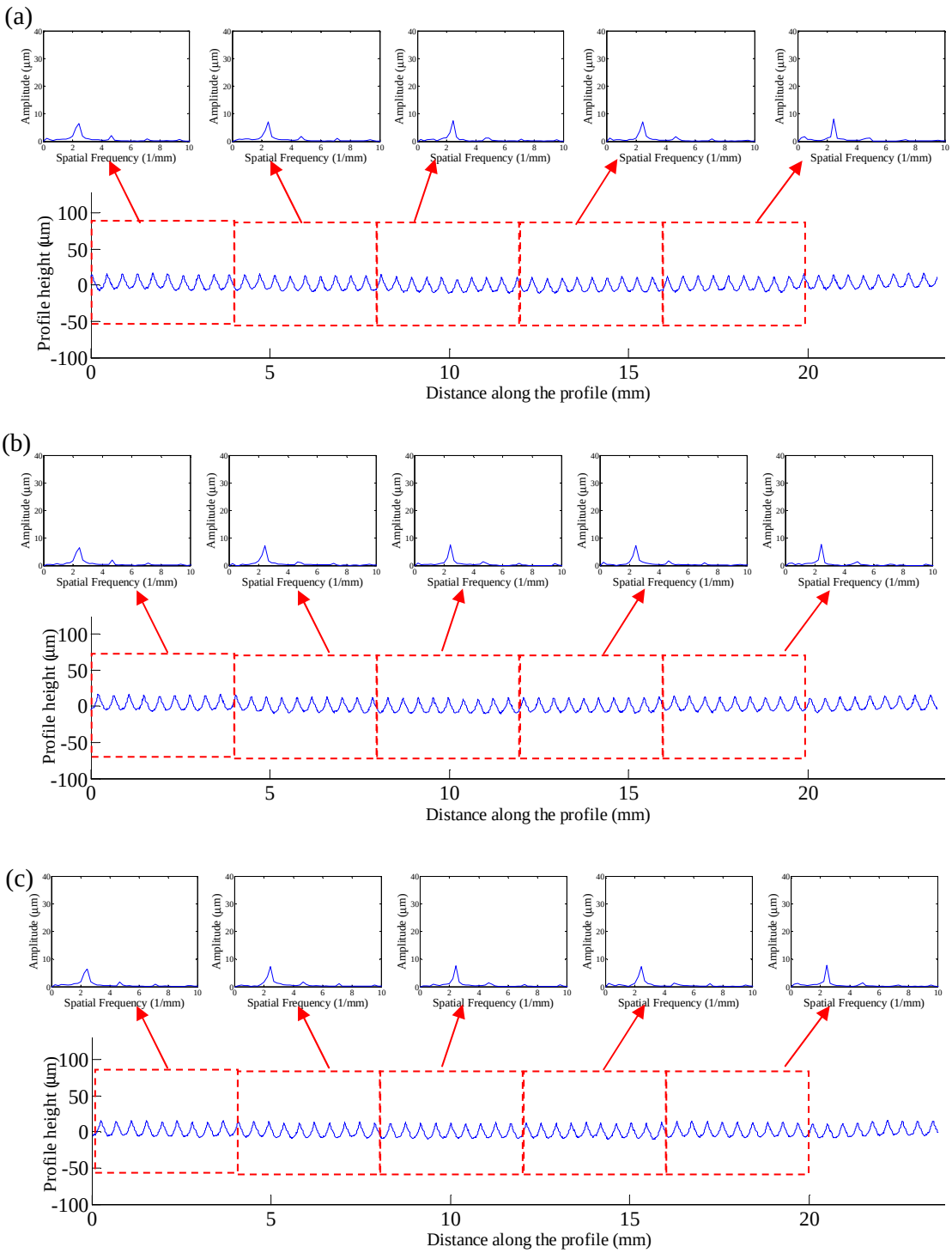

Sub-window FFT along the workpiece profile at different rotational angles (a) 0^o, (b) 120^o, (c) 240^o in cutting time duration of 11.0-16.5 s corresponding to Appendix A

(a)

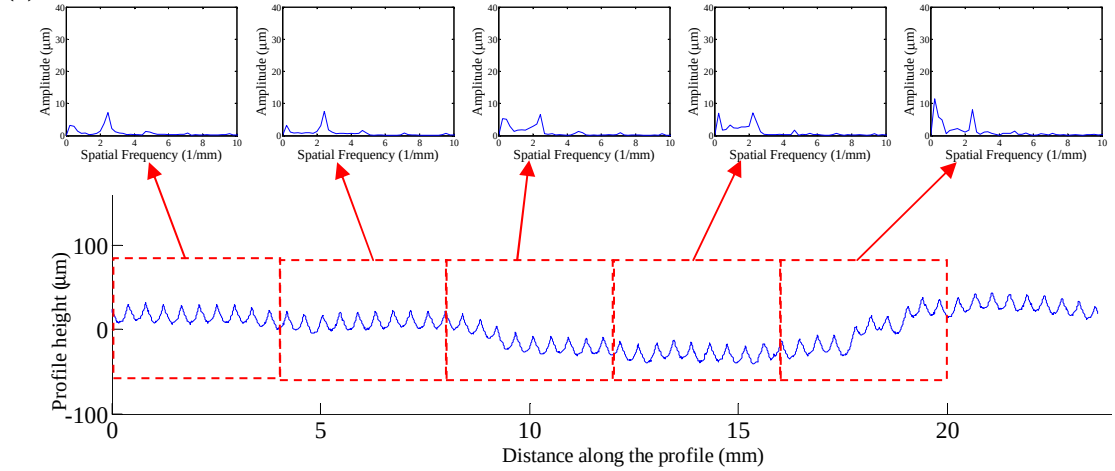

(b)

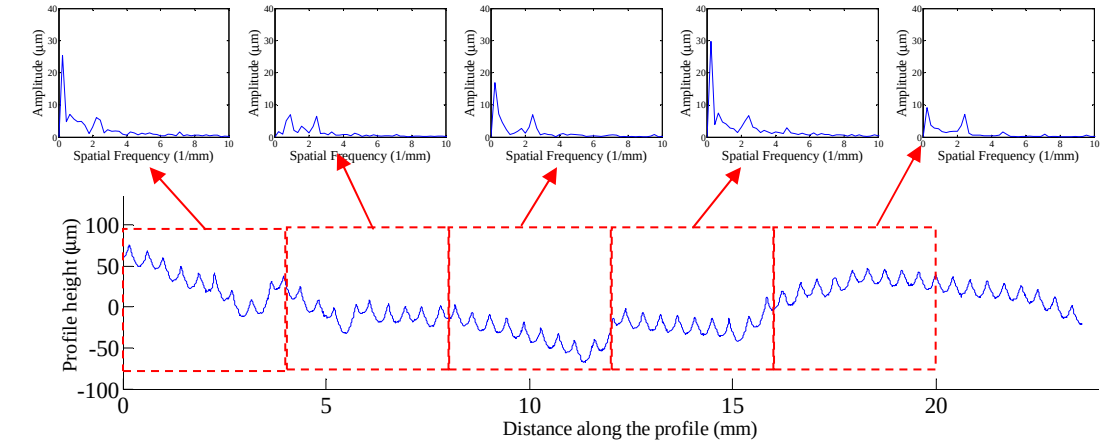

(c)

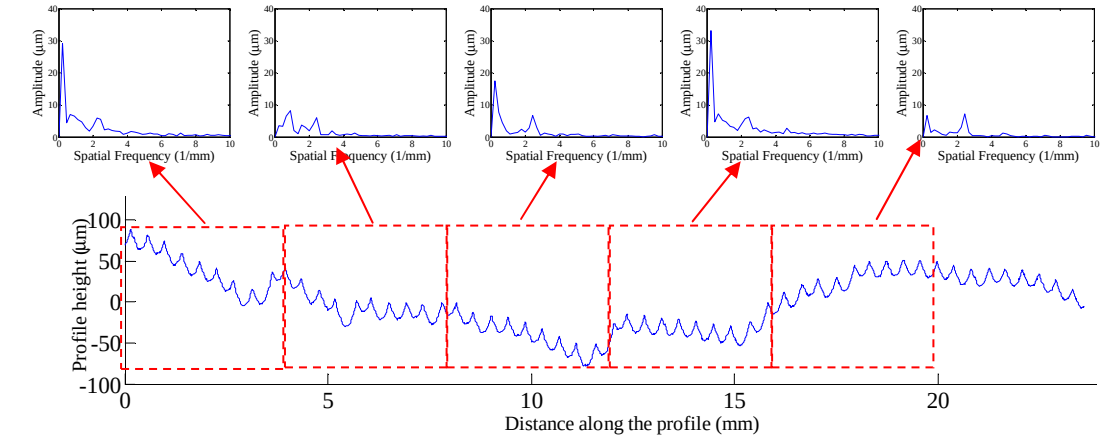

APPENDIX C: REPEATED EXPERIMENTAL RESULTS OF CWT

Corresponding CWT to sub-window FFT along the workpiece profile at different rotational angles (a) 0^o, (b) 120^o, (c) 240^o in cutting time duration of 5.5 s

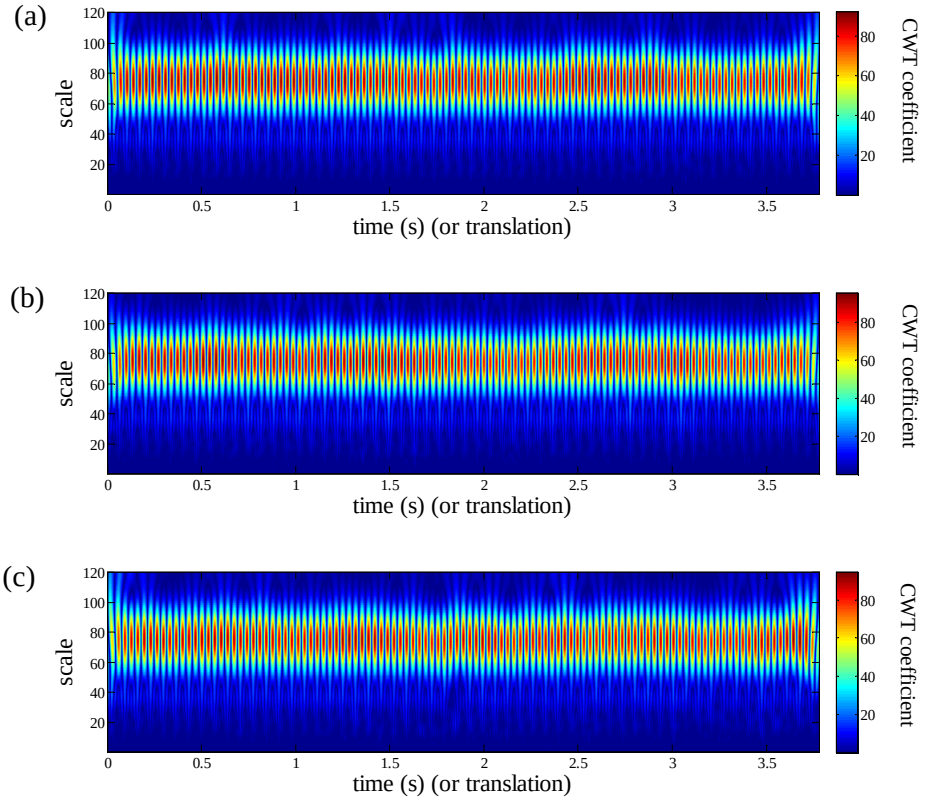

Corresponding CWT to sub-window FFT along the workpiece profile at different rotational angles (a) 0^o, (b) 120^o, (c) 240^o in cutting time duration of 5.5-11.0 s

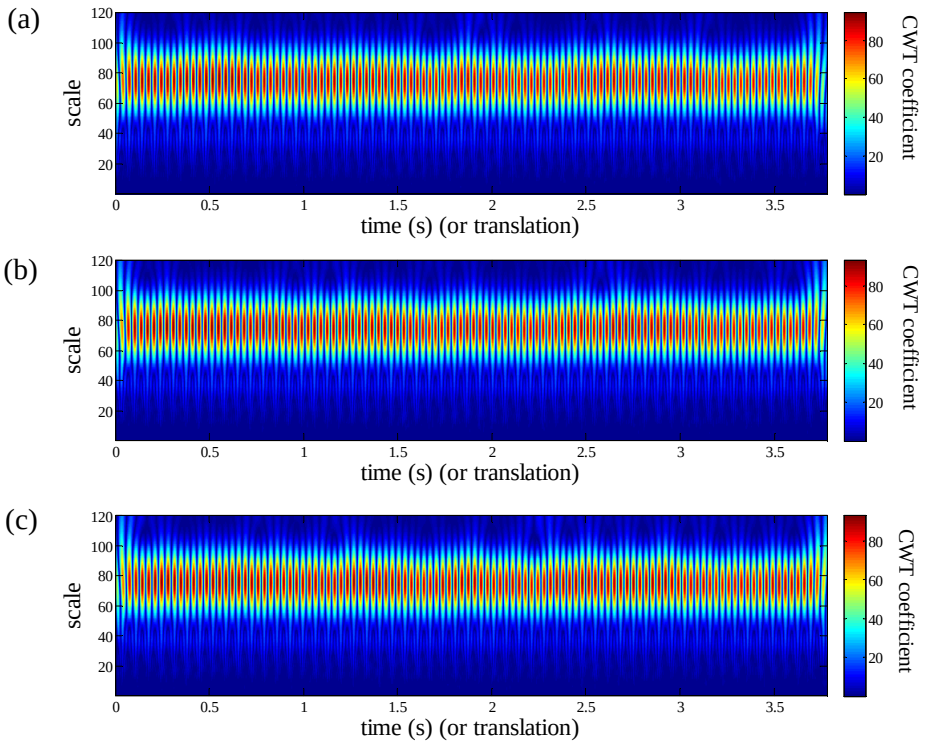

Corresponding CWT to sub-window FFT along the workpiece profile at different rotational angles (a) 0^o, (b) 120^o, (c) 240^o in cutting time duration of 11.0-16.5 s

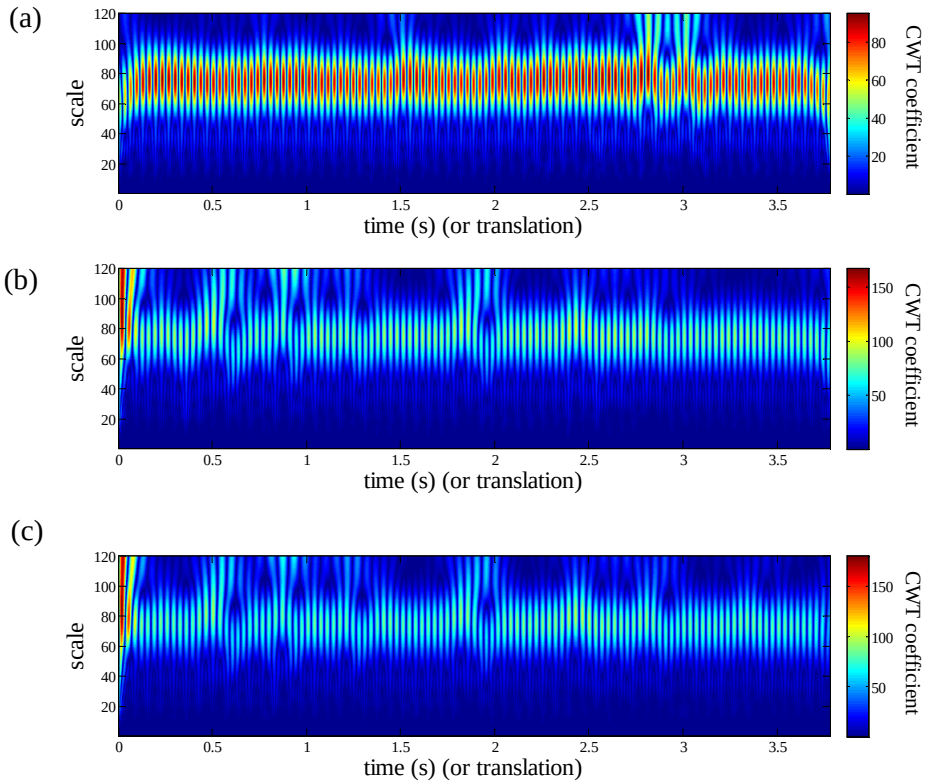

LIST OF PUBLICATIONS

Lee, W.K., Ratnam, M.M., & Ahmad, Z.A. (2017). Detection of chipping in ceramic cutting inserts from workpiece profile during turning using fast Fourier transform (FFT) and continuous wavelet transform (CWT). *Precision Engineering,47,* 406-423. http://dx.doi.org/10.1016/j.precisioneng.2016.09.014

Lee, W.K., Ratnam, M.M., & Ahmad, Z.A. (2016). Detection of fracture in ceramic cutting tools from workpiece profile signature using image processing and fast Fourier transform. *Precision Engineering, 44,* 131-142. http://dx.doi.org/10.1016/j.precisioneng.2015.11.001

Lee, W.K., Ratnam, M.M., & Ahmad, Z.A. (2016). In-process detection of chipping in ceramic cutting tools during turning of difficult-to-cut material using vision-based approach. *The international Journal of Advanced Manufacturing Technology, 85(5),* 1275-1290. doi:10.1007/s00170-015-8038-6

Lee, W.K., Ratnam, M.M., & Ahmad, Z.A. (2015). *Tool breakage detection from 2D workpiece profile using vision method.* Paper presented at 2nd International Manufacturing Engineering Conference iMEC and 3rd Pacific Conference on Manufacturing System (APCOMS 2015), Kuala Lumpur, Malaysia
(Published in IOP conf. Series: Materials Science and Engineering 114 (1), doi:10.1088/1757-899X/114/1/012132)

Lee, W.K., Ratnam, M.M., & Ahmad, Z.A.(2014). *Detection of fracture in ceramic cutting tools from workpiece image using sub-pixel edge location*. Paper presented at International Conference on Control Automation Robotics & Vision (ICARCV), 2014, Singapore.